UNIVERSITY OF CAMBRIDGE
INSTITUTE OF ASTRONOMY

UNDERSTANDING X-RAY REFLECTION AS A PROBE OF ACCRETING BLACK HOLES

DANIEL RICHARD WILKINS

JESUS COLLEGE

Supervisor:
PROF. ANDREW C. FABIAN

This dissertation is submitted for the degree of Doctor of Philosophy

May 2013
Cambridge, United Kingdom

Declaration

I hereby declare that my thesis entitled *Understanding X-ray Reflection as a Probe of Accreting Black Holes* is not substantially the same as any that I have submitted, or, is being concurrently submitted for a degree or diploma at the University of Cambridge or any other University or similar institution. I further state that no substantial part of my dissertation has already been submitted, or, is being concurrently submitted for any such degree, diploma or other qualification at the University of Cambridge or any other University or similar institution. I also declare that this thesis is the result of my own work and incudes nothing which is the outcome of work done in collaboration except where specifically indicated in the text. Various figures in the thesis are reproduced from the work of other authors for illustration or discussion. Such figures are clearly credited in the text.

The following parts have been published or accepted for publication:

- Chapter 4 was published as

  Determination of the X-ray reflection emissivity profile of 1H0707-495
  Wilkins, D.R. and Fabian, A.C., 2011, MNRAS 414, 1269-1277

- Sections of Chapter 4 were also published as parts of

  Long XMM observation of the narrow-line Seyfert 1 galaxy IRAS 13224-3809: rapid variability, high spin and a soft lag
  Fabian, A. C., Kara, E., Walton, D. J., **Wilkins, D. R.**, Ross, R. R., Lozanov, K., Uttley, P., Gallo, L. C., Zoghbi, A., Miniutti, G., Boller, T., Brandt, W. N., Cackett, E. M., Chiang, C.-Y., Dwelly, T., Malzac, J., Miller, J. M., Nardini, E., Ponti, G., Reis, R. C., Reynolds, C. S., Steiner, J. F., Tanaka, Y., Young, A. J., 2013, MNRAS 429, 2917-2923

  and

  On the determination of the spin of the black hole in Cyg X-1 from X-ray reflection spectra
  Fabian, A. C., **Wilkins, D. R.**, Miller, J. M., Reis, R. C., Reynolds, C. S., Cackett, E. M., Nowak, M. A., Pooley, G. G., Pottschmidt, K., Sanders, J. S., Ross, R. R., Wilms, J., 2012, MNRAS 424, 217-223

- Chapter 6 was published as

Understanding X-ray reflection emissivity profiles in AGN: Locating the X-ray source
Wilkins, D.R. and Fabian, A.C., 2012, MNRAS 424, 1284-1296

- Chapter 7 was published as part of

  1H0707-495 in 2011: An X-ray source within a gravitational radius of the event horizon
  Fabian, A.C., Zoghbi, A., **Wilkins, D.R.**, Dwelly, T., Uttley, P., Schartel, N., Miniutti, G., Gallo, L., Grupe, D., Komossa, S. and Santos-Lleo, M., 2011, MNRAS 419, 116-123

- Chapter 8 was published as

  The origin of the lag spectra observed in AGN: Reverberation and the propagation of X-ray source fluctuations
  Wilkins, D.R. and Fabian, A.C., 2012, MNRAS 430, 247-258

This dissertation contains fewer than the limit of 60,000 words.

D.R. Wilkins
Cambridge, May 2013

Summary

The reflection of the X-rays emitted from a corona of energetic particles surrounding an accreting black hole from the accretion disc is investigated in the context of probing the structure of the central regions as well as the physical processes that power some of the brightest objects seen in the Universe.

A method is devised to measure the emissivity profile of the accretion disc, that is the reflected flux as a function of radius in the disc. This method exploits the variation in the Doppler and gravitational redshift of emission from different radii in the disc to fit the observed reflection spectrum as the sum of contributions from successive radii and is applied to X-ray spectra of the narrow line Seyfert 1 galaxies 1H 0707-495, IRAS 13224-3809 and MCG–6-30-15 as well as the Galactic X-ray binary, Cygnus X-1. This illumination pattern of the accretion disc is a sensitive probe of the geometry of the corona that is illuminating the disc.

A formalism is developed in which systematic ray tracing simulations can be run between X-ray emitting coronae and the accretion disc for a range of source geometries and other physical parameters, allowing observable data products to be simulated that can be directly compared to data from astrophysical black holes, in order to determine how these parameters affect the observed data, allowing them to be constrained observationally. The measured emissivity profiles are found to be in agreement with those expected theoretically and it is also discovered that the measured emissivity profile can be used to determine the radial extent of the X-ray emitting corona above the accretion disc.

The X-ray emitting coronae are located and their radial extents constrained in 1H 0707-495, IRAS 13224-3809 and MCG–6-30-15, while the insight gained into accretion disc emissivity profiles from ray tracing simulations allows the low flux state that 1H 0707-495 was seen to drop in to in January 2011 to be explained in terms of a collapse of the X-ray emitting corona to a confined region around the central black hole.

The rapid variability of the X-ray emission from accreting black holes is exploited in the use of reverberation time lags, where variability in the continuum is seen to lead that in its reflection from the accretion disc, to measure the distances between the X-ray emitting corona and the reflector.

Ray tracing calculations are developed to simulate lag spectra that can be measured in X-ray observations to provide a means of constraining the extent and geometry of the corona, complimentary to the use of the emissivity profiles. Combining these methods, the X-ray emitting coronae are constrained to extend radially outward a few tens of gravitational radii over the accretion disc, while extending vertically a few gravitational radii above the plane of the disc. Furthermore, it is demonstrated how measured lag spectra can be used to understand the propagation of luminosity fluctuations through the extent of the corona and techniques are developed for analysing energy-resolved variability analysis that will be possible with future generations of X-ray telescopes.

Finally, these methods, along with theoretical insight gained form ray tracing simulations, are applied to X-ray spectra extracted from 1H 0707-495 during periods of low and high flux during the observations. Evidence is found for the expansion of the corona along with a drop in the average energy density as the X-ray luminosity increases followed by its contraction as the luminosity decreases on timescales of hours.

Acknowledgements

First and foremost, I am indebted to my supervisor, Prof. Andy Fabian, for the inspiration, encouragement and support he has provided in the course of this thesis. A large part of this work grew out of what, at the time, seemed like a relatively short 'starter project' and his amazing intuition for how the Universe works, even right next to a black hole has been invaluable. Thanks must also go to my colleagues, Giovanni Miniutti, Chris Reynolds, Ed Cackett, Phil Uttley and Erin Kara for what have been insightful and extremely interesting discussions, helping this work develop and encouraging me to explore new directions from time to time.

I would like to thank Roderick Johnstone and Jeremy Sanders for their help with computing-related issues, Becky Canning and Roderick for giving me the chance to use a 'real' telescope and the rest of the X-ray group (past and present) for their help and, of course, friendship — Julie, Jack, Dom, Abdu, Chia-Ying, to name but a few. I wish also to thank Carolin Crawford for helping hone my passion for public outreach and communicating with audiences of all ages about the wonders of astronomy. And on a slightly less academic note, I am extremely grateful to Siân Owen and Margaret Harding as well as Paul Hewett for their support and always being on hand to help, right from the moment I arrived for my interview.

Finally, thanks must go to my family, in particular my parents and grandparents for supporting me throughout my University career as well as to my friends from the Institute of Astronomy, College and JCBC and elsewhere for keeping me sane. Special mentions go to Lucy Fielding who always advised me to be careful of those blackish holeish things, Poul Alexander for the high table dinners, Jo Baines, always providing a reason to escape the Cambridge 'bubble' and last, but certainly by no means least, Jonathan Crass for, well, everything.

Contents

1

Introduction

Active galactic nuclei (AGN) are some of the brightest and most extreme objects in the Universe. In fact, they are the most luminous, continuous sources of electromagnetic radiation known. Powered by matter spiralling into a supermassive black hole (up to a billion times the mass of the Sun) in the centre of a galaxy, they are extremely luminous in their emission of visible light through to ultraviolet and all the way up to X-rays.

As well as the supermassive black holes found in the centres of galaxies, smaller, stellar mass black holes are found to be abundant in our own galaxy. Due to the mass-length scale-invariance of Einstein's theory of General Relativity, these stellar mass black holes are almost perfect analogues of their supermassive counterparts. When they are found in a binary system with a companion star, these black holes are able to accrete material from the companion liberating similarly large amounts of energy, becoming luminous astrophysical sources of X-rays.

The first astrophysical black holes were discovered as point sources in some of the early rocket flights carrying X-ray detectors into the upper atmosphere. Over the last decade, high-resolution observations with the large X-ray observatories (XMM Newton, Chandra and Suzaku) have yielded an unprecedented amount of information about these objects. These instruments are able to detect the high energy radiation from material right down to the last stable orbit and even the event

horizon (the limit from which nothing can escape), just moments before it plunges into the black hole.

Much of the physics at work in these impressive objects remains a mystery. It is not fully understood how gravitational energy is liberated from the accretion flow into the energetic corona around the black hole to produce the powerful X-ray source. Neither is it properly understood why these objects are seen to go through different states: Galactic black hole binaries are seen to go from states in which the emission is dominated by thermal emission from the accretion disc of material spiralling into the black hole to states dominated by non-thermal X-ray emission from a corona of energetic particles surrounding the black hole. But why should the behaviour and accretion disc of the corona change so much? AGN are also seen to be highly variable with the emitted luminosity varying by factors of a few in just a couple of hours.

Finally, turning our attention to AGN, the energy emitted by accretion onto the black hole in the centre of a galaxy is comparable, if not an few orders of magnitude greater than the gravitational binding energy holding the stars in that galaxy. If the black hole in the centre of the galaxy is assumed to co-evolve with the galaxy as primordial material condenses onto dark matter haloes, then one might expect that at some stage an equilibrium will be reached where the increasing radiation pressure from the accreting (and growing) black hole is so great that it prevents more material condensing into the galaxy and forming stars. If we are to fully understand the formation and evolution of galaxies, it is vital to understand how this enormous power source in the centre of a galaxy operates and how it feeds back to its surroundings.

In this thesis, I look in detail at the X-ray observations we can make of accreting black holes; mostly AGN but examples of Galactic X-ray binaries are also explored. Developing a theoretical framework and simulations of accreting black holes based upon the observations we are able to make with current and future instruments, I ask how we can really understand the X-ray observations and what are they really telling us about the physical processes at work in some of the brightest objects in the Universe.

2

Background

Energy is liberated in the accretion of material onto a black hole; both solar mass black holes formed by gravitational collapse at the ends of the lives of massive stars accreting material from their binary companions and supermassive black holes, a million to a billion times the mass of the Sun in active galactic nuclei (AGN) accreting material in the centres of galaxies.

Accretion under the force of gravity is the most efficient means of releasing energy from matter, liberating as much as six per cent of the rest mass energy for accretion onto a non-spinning black hole and up to 42 per cent in the case of a spinning black hole as radiation. The accreting matter will typically form a flattened accretion disc around the central black hole to conserve its angular momentum, which is conserved as it spirals inwards. Angular momentum is transported outward through the disc by viscous friction between material at neighbouring radii orbiting at their respective Keplerian velocities, most likely arising from the magneto-rotational instability; the dragging of magnetic field lines between two parts of the disc.

2.1 The Central Black Hole

Black holes exist where material is sufficiently dense According to the 'no hair' theorem, a black hole is characterised by just three parameters, its mass, spin and electrical charge (which will tend to be zero in astrophysical black holes as accreted charges neutralise each other).

The spacetime geometry surrounding a stationary point mass is described by the Schwarzschild metric while that around a rotating point mass is described by the Kerr metric (Kerr, 1963), the spherically symmetric and axisymmetric solutions to the empty-space Einstein field equations around a spinning point mass. As well as the singularity at the centre, corresponding to the point mass, there is a co-ordinate singularity forming the *event horizon* at a radius of $\frac{2GM}{c^2}$ in the case of a non-spinning mass and $\frac{GM}{c^2}$ for a maximally spinning mass. Worldlines of particles may only pass through the event horizon in one direction (inwards), thus it represents a point of no return for both massive particles and light which, on crossing the horizon, must fall into the singularity. Black holes exist when an object is so dense that its event horizon lies outside its surface, such that the mass itself is hidden beyond the horizon and will be formed in the gravitational collapse of a star or gas cloud when the force of gravity is sufficiently strong that it overcomes any other force (electromagnetic or degeneracy pressures of fermions) that would be able to support the object, thus the collapse continues until a black hole is formed.

If mass of the black hole is M, the spin is defined by the parameter a which is related to the angular momentum of the black hole by $J = Mac$. In units of $\frac{GM}{c^2}$, the maximum value for the spin parameter is 1, at which point the rotational energy becomes too great for the black hole to be stable. Calculations of the infall of gas to form the black hole suggest that astrophysical black holes have a maximum value of $a \approx 0.998$. In the limit of a non-spinning black hole ($a = 0$), the Kerr metric reduces to the Schwarzschild metric, the solution for the spacetime around a non-spinning point mass.

Rotation of the black hole itself causes 'frame dragging' where inertial frames (observers with essentially zero angular momentum) are caused to rotate about the black hole. There exists a *stationary limit surface* at $\frac{2GM}{c^2}$ around a maximally spinning black hole (this coincides with the horizon for a non-spinning black hole), inside which no massive particle may be at rest with respect to a stationary observer at infinity. Unlike classical gravity, in general relativity, there exists an innermost stable circular orbit with radius $\frac{6GM}{c^2}$ around a non-spinning black hole and $1.235\frac{GM}{c^2}$ when $a = 0.998$. Inside this radius, there are no circular orbits and all particles fall in to the black hole, limiting the inner extent of any accretion disc.

2.2 Observations of AGN

All galaxies are believed to harbour supermassive black holes at their centres. Active galactic nuclei occur where this black hole continuously accretes material from an inspiralling disc, causing vast amounts of energy to be released such that the nucleus of the galaxy lights up to outshine the stars in that galaxy. In *unification models*, active galactic nuclei are observed as a number of classes of source, depending on the direction from which they are observed.

Among the first detections of AGN were *quasi-stellar radio sources*, or *quasars*, where compact radio sources were found to correlate in position with optical sources that appeared to be stars with prominent emission lines. The emission lines did not, however, appear at the expected wavelengths, but were the Balmer series of emission lines from hydrogen that had been redshifted. These redshifts implied great distances to these sources which meant they were far too luminous to be stars. Quasars possess a smooth optical continuum spectrum that is described by a power law extending into the ultraviolet and display variability on the timescale of years.

Radio-loud AGN possess powerful jets roughly along the rotation axis of the black hole. These jets contain highly relativistic material launched from the nucleus, possibly through the twisting of magnetic fields around the black hole, collimating material into the jet while accelerating it to high velocities (Blandford & Rees, 1974), extraction of energy from the spin of the black hole by the frame-dragging of electromagnetic fields by a rotating black hole (Blandford & Znajek, 1977) or magneto-cenrifugal accleration of material by rotating magnetic field lines anchored to the accretion disc (Blandford & Payne, 1982). Such jets are capable of depositing vast amounts of energy in lobes in the intergalactic medium. If the galaxy is observed edge-on, the view of the central region is obscured by a thick dusty torus enshrouding the nucleus, so the most obvious feature are the lobes emitting radio waves through synchrotron emission and the source appears as a *radio galaxy*.

The most extreme examples of AGN are *BL Lacertae* (*BL Lac*) objects, seen when the line of sight looks down the jet into the core of the galaxy. These objects are extremely compact and are highly variable in their radio and optical emission over timescales from less than a day to a few weeks. Their optical spectrum is smooth and featureless, however they are not as luminous as the brightest quasars.

In addition to these radio-loud objects, there are radio quiet AGN that display little synchrotron emission of radio waves and do not launch jets. Radio-quiet quasars are much more common than their radio loud counterparts.

While quasars are seen at such great distances that only the bright nucleus of the galaxy is detected, in more nearby AGN, the host galaxy can be seen as well. *Seyfert 1* (*Sey 1*) galaxies are spiral galaxies with a star-like active nucleus. This nucleus displays very intense spectral lines, including the Balmer series of hydrogen and the forbidden lines of oxygen, nitrogen and sulphur

in addition to a smooth power law continuum spectrum. The lines resulting from permitted transitions are broadened through Doppler shifts implying velocities of around $5000\,\mathrm{km\,s^{-1}}$ and are emitted from the *broad line region* (*BLR*) close to the nucleus where the gas density is very high (suppressing forbidden transitions). The forbidden lines are much narrower, implying velocities around $500\,\mathrm{km\,s^{-1}}$ and originate from the much less dense *narrow line region* (*NLR*) further from the nucleus. In Seyfert galaxies, the starlight is overwhelmed by non-thermal emission from the nucleus.

If these objects are observed closer to edge-on, the view to the nucleus and the broad line region is obscured by the dusty torus, so all lines are seen to originate from the narrow line region which is further out, so not obscured in these *Seyfert 2* (*Sey 2*) galaxies. In Seyfert 2 galaxies, emission from the nucleus is seen via reflection from more distant clouds and as a result is seen to be polarised.

A schematic of a typical model AGN (including radio loud and quiet) and how the various classes of observed source fit into the unification scheme is shown in 2.1.

2.3 X-ray Emission from Accreting Black Holes

The X-ray spectra of accreting black holes are dominated by a continuum, taking the form of power law extending up to energies of 100 keV. These hard X-rays are produced in a corona of energetic particles surrounding the central black hole through the process of Comptonisation. Soft, thermal seed photons originating from the accretion disc are inverse-Compton scattered to higher energies multiple times by energetic electrons (whose energy follows a Maxwell-Boltzmann distribution), giving rise to a power law spectrum (Sunyaev & Trümper, 1979). It is possible that the corona is heated through the acceleration of particles by reconnection of magnetic fields. Magnetic field lines are stretched and amplified by differential rotation of material at different radii in the accretion disc as well as by convective motions within the disc, causing loops of magnetic field to rise buoyantly from the disc. These loop structures result in a very hot ($T \sim 10^8$ K), magnetically confined corona around the accretion disc (often referred to as an *accretion disc corona* and may reconnection events analogous to the solar corona causing rapid variability in the characteristics of the emission (Galeev et al., 1979; Haardt & Maraschi, 1991; Merloni & Fabian, 2001).

Thermal emission is detected from the accretion disc. Accretion disc models due to Shakura & Sunyaev (1973), for a classical disc with material in Keplerian orbits around the black hole, and Novikov & Thorne (1973), giving a full general relativistic treatment of accretion discs around black holes, liberate energy through viscous friction in the disc as material at neighbouring radii must orbit at different velocities to remain on stable circular orbits. The emission from each position in the disc is that of a pseudo-black body where the temperature is determined by the flux emitted at each location. In AGN, the thermal emission from the accretion disc peaks in the ultraviolet

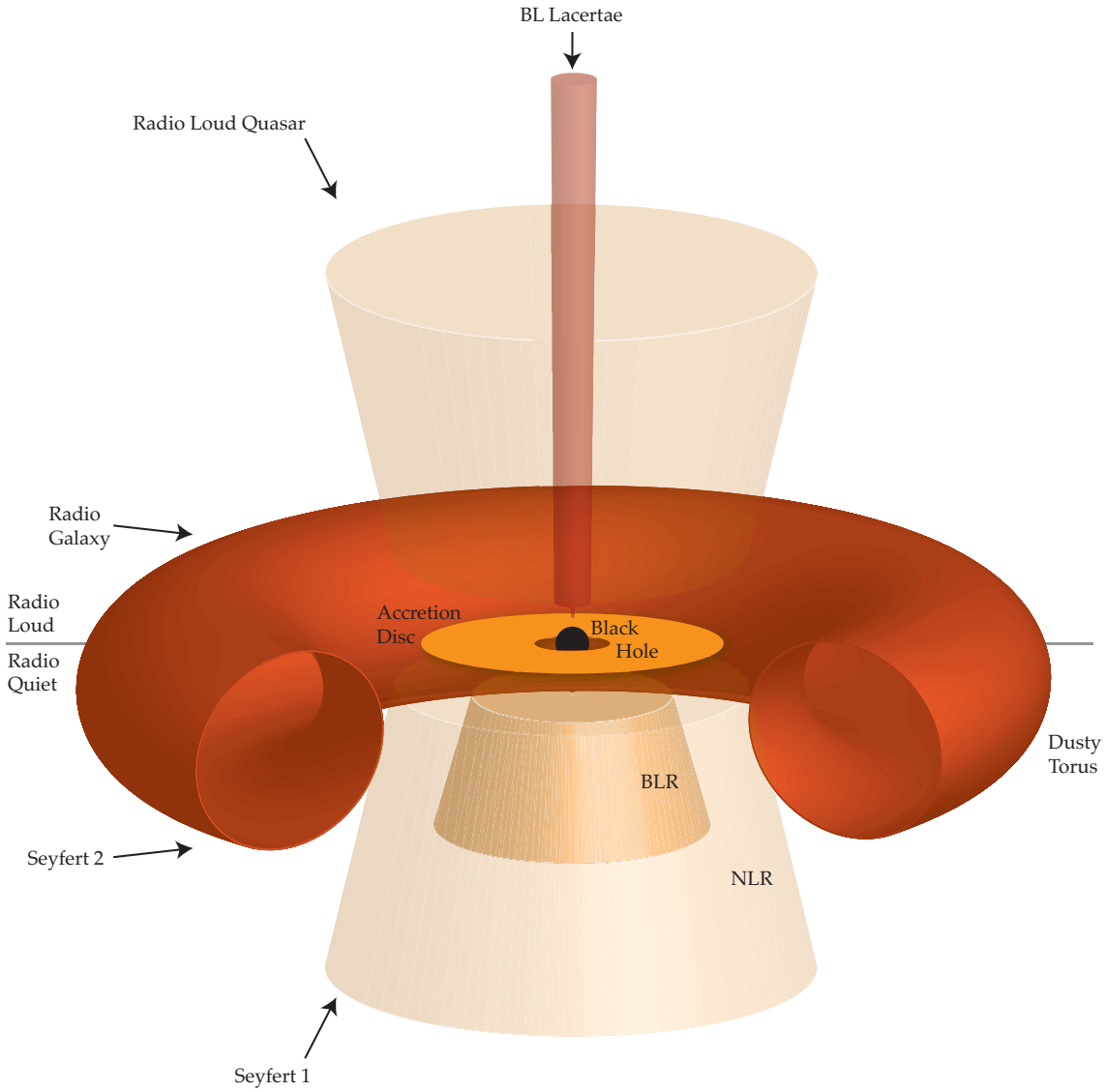

Figure 2.1: Schematic of an AGN showing how the different classes of observed source fit in to the unification model depending on the inclination of the line of sight.

part of the electromagnetic spectrum, with the Wien tail extending just into the X-ray range while the thermal emission from the accretion discs surrounding stellar mass black holes peaks at X-ray energies.

In addition to the thermal emission from the disc itself, the X-rays emitted from the corona incident on the disc will be reflected (Guilbert & Rees, 1988). This gives rise to a reflection spectrum upon which a number of features are imprinted, most notably emission and absorption lines by the atoms and ions found in the disc which have, to date, been observed in the X-ray spectra in a large number of AGN. The concept of the reflection by the accretion disc has led to the 'lamppost model' of emission from AGN (George & Fabian, 1991), where hard X-rays with a power law spectrum are produced by some localised source in the corona (Fig. 2.2).

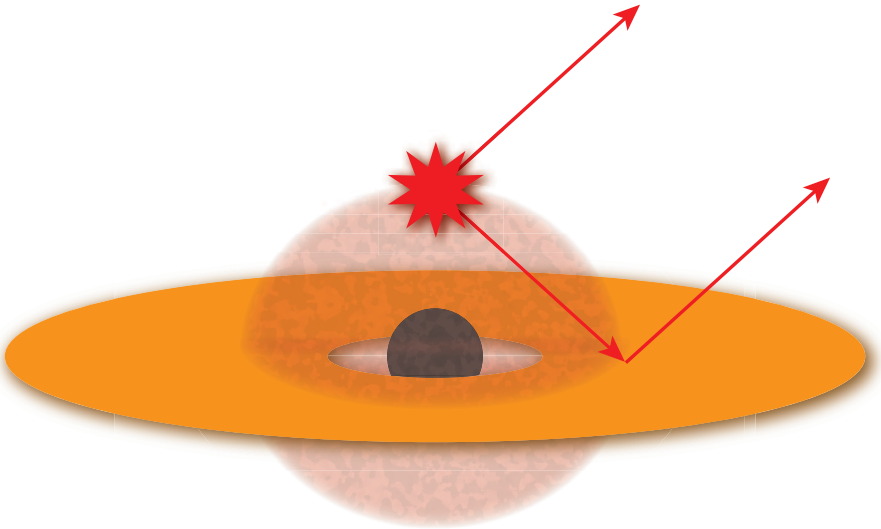

Figure 2.2: X-rays are emitted from a corona of energetic particles surrounding the central black hole, which, as well as being observed directly, can then be reflected off the accretion disc, imprinting a features on the spectrum including atomic emission and absorption lines.

2.4 Reflection from the Accretion Disc

When X-ray photons are incident upon the material in the accretion disc, they may interact with it in a number of ways. They can be Compton scattered by electrons in the disc, as is more likely for harder X-ray photons. Those photons whose energy is in excess of the characteristic Compton temperature of the scattering material will tend to be scattered to lower energies, while those whose

energy is less than the Compton temperature will increase in energy, leading to a characteristic 'Compton hump' in the reflection spectrum; an excess of photons around $20 \sim 30$ keV, the energy corresponding to the Compton temperature.

Alternatively, softer photons can undergo photoelectric absorption by the material in the accretion disc. Once absorbed, photons are re-emitted through one of two processes. One possibility is Auger de-excitation, where the absorbed photon causes an electron from an inner shell to be ejected from the atom allowing an electron from a higher shell to fall in to the vacancy emitting a photon as it does so. This emitted photon can then be absorbed by another electron in the atom, ejecting this so-called 'Auger electron'. The alternative is the emission of a fluorescent line where an electron is ejected from an inner shell as the incident photon is absorbed, allowing an electron from a higher shell to fall into the vacancy, emitting a photon as it does so. Fluorescent lines are emitted at specific energies corresponding to the separation of the energy levels in the atom or ion.

Matt et al. (1997) argue that the strongest X-ray emission line expected from accretion discs around black holes is the Kα line of iron, owing to the abundance of iron and the large absorption cross-section for K shell electrons. For neutral iron, this is a doublet emission line centred at 6.4 keV, however the current generation of X-ray spectrometers cannot resolve the doublet, so a single line is seen at 6.4 keV. The Kα line arises where an X-ray photon at 7.1 keV is absorbed, removing an electron from the K shell ($n = 1$), allowing the transition of an electron from the L ($n = 2$) shell to fill the vacancy, emitting an X-ray photon at 6.4 keV as it does so.

In order to determine the spectrum of the reflected X-rays, it is necessary to take into account a number of factors. The reflection spectrum will depend upon the spectrum of the incident radiation as well as the temperature of the disc and the abundances and ionisation states of atomic species (iron, oxygen and nitrogen to name a few of the significant contributors to the observed X-ray spectra). The atomic abundances will affect the intensities of the various fluorescent lines in the spectrum and the ionisation states determine the energies as well as the intensities of the lines.

The ionisation of the material is characterised by the ionisation parameter, $\xi = \frac{4\pi F}{n}$. Increasing the incident flux, F will serve to further ionise atoms in the disc while increasing the density of the disc material, characterised by the number density of atomic hydrogen, n will increase collisions between ions and electrons leading to more recombination. Weakly ionised material, characterised by $\xi < 100\,\mathrm{erg\,cm\,s^{-1}}$ shows strong absorption below X-ray energies of 10 keV, weak Compton scattering of the continuum and a number of prominent emission lines including the Kα emission line of iron and a weak absorption edge at 7.1 keV corresponding to absorption of photons by the K shell of neutral iron. As the material becomes more ionised, with ξ increasing to $100 \sim 500\,\mathrm{erg\,cm\,s^{-1}}$, iron is found as the more ionised FeXVII-FeXXIII species. These ions have a vacancy in their L shells allowing them to absorb the emitted K line photons (when their K shell electrons absorb the 6.4 keV photons to be promoted to the L shell), reducing the intensity of the Kα line as the ionisation increases. Highly ionised material, however, with ξ in the range $500 \sim 5000\,\mathrm{erg\,cm\,s^{-1}}$ shows only

weak atomic features as all low-Z elements are found in their hydrogenic states. Iron is found in its hydrogenic (FeXXVI) and helium-like (FeXXV) states with $K\alpha$ emission lines at 6.97 and 6.67 keV respectively and the corresponding absorption edges increased to 9.28 and 8.85 keV (with more energy being required to remove electrons from more highly ionised atoms).

Such a model must also be self-consistent since the ionisation state of the material will be dependent on the temperature of the material and also the flux and spectrum of the ionising radiation incident on the disc produced by the corona (the radiation that is reflected also heats and ionises the disc material). Such a model is the REFLIONX code of Ross & Fabian (2005) for X-ray reflection from an ionised slab illuminated by a power law X-ray continuum. REFLIONX computes the reflection spectrum in the equilibrium state in which energy incident on and emitted from the slab is conserved, producing a reflection spectrum such as that shown in Fig. 2.3.

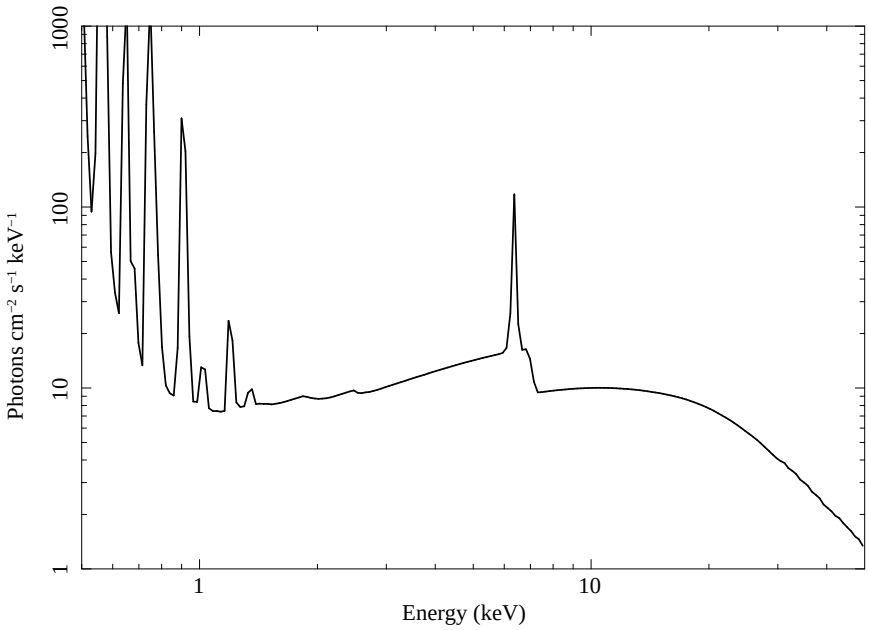

Figure 2.3: The X-ray reflection spectrum of an accretion disc (as measured in the rest frame of the emitting material) predicted by the REFLIONX model of Ross & Fabian (2005). The notable features include the Kα emission line of iron at 6.4 keV and its corresponding absorption edge at 7.1 keV. Also note the characteristic 'Compton hump' around 20 keV as well as a number of emission lines from other species at lower energies.

2.4.1 Relativistic Emission Line Profiles

Atomic emission lines are emitted at specific frequencies or energies that correspond to the gaps between energy levels in the atom. Radiation is emitted in narrow spectral lines at these specific

energies in the *local rest frame* of the emitting material, but will be shifted by a number of factors if measured by an external observer. If the line is emitted from material orbiting the black hole in the accretion disc, the shift in observed energy is a function of emitting location in the disc and typically the accretion disc cannot be spatially resolved, so the observed line profile will be the integral of the radiation emitted over the entire disc, leading to a line profile extended over a range of energies. The weighting of each contribution is, of course, determined by the projected area of that part of the disc as seen by the observer.

Firstly, an observer at rest at infinity will see the radiation Doppler shifted due to the orbital motion of the material. The inclination of the source is defined as the angle subtended between the line of sight and the rotation axis (*i.e.* an inclination of zero corresponds to viewing the disc face-on). If the disc is viewed at high inclination (*i.e.* almost edge-on), the single emission line will be split into a double-peak owing to the redshift from material moving away from the observer and blueshift from material moving towards the observer on the other side of the disc. Classically, this leads to a double-peaked profile symmetric about the rest-frame energy of the line.

The material in the disc is travelling at a high velocity (material on the innermost stable circular orbit will be travelling at half the speed of light), so special relativistic effects will be significant. Emission will be further redshifted owing to time dilation of the moving source with respect to the stationary observer (the 'transverse Doppler shift') and emission will be beamed into the direction of motion, enhancing the blueshifted peak as the observer is 'in front' of the emitting material so more radiation will received from this part of the disc than that moving away from the observer, whose emission will be beamed away from the observer.

Finally, the strong gravitational field around the black hole leads to gravitational redshift of the emission as the proper time of the material closer to the black hole runs more and more slowly. This leads to an extended 'red wing' in the line profile, shifting to lower and lower energy as material gets closer to the black hole. The combination of these effects in the formation of the observed relativistically broadened line profile is illustrated in Figure 2.4.

The relativistic effects on the emission from an accretion disc around a black hole were considered by Cunningham (1975) and relativistic line profiles were initially calculated for emission from the accretion disc around a non-spinning Schwarzschild black hole by Fabian et al. (1989) who reported that the broad iron emission line detected in the spectrum of the galactic black hole X-ray source Cygnus X-1 is well described by this model.

Laor (1991) extended this calculation to the case of a spinning, Kerr black hole, formulating a mathematical description of the line profile (the flux observed at a given frequency) as the convolution of the rest-frame spectrum emitted from the accretion disc, $I_e(r_e, \frac{\nu_0}{g})$ with a *transfer function* $T(r_e, g)$ that describes the transport of the radiation to the observer, including the effects of relativistic

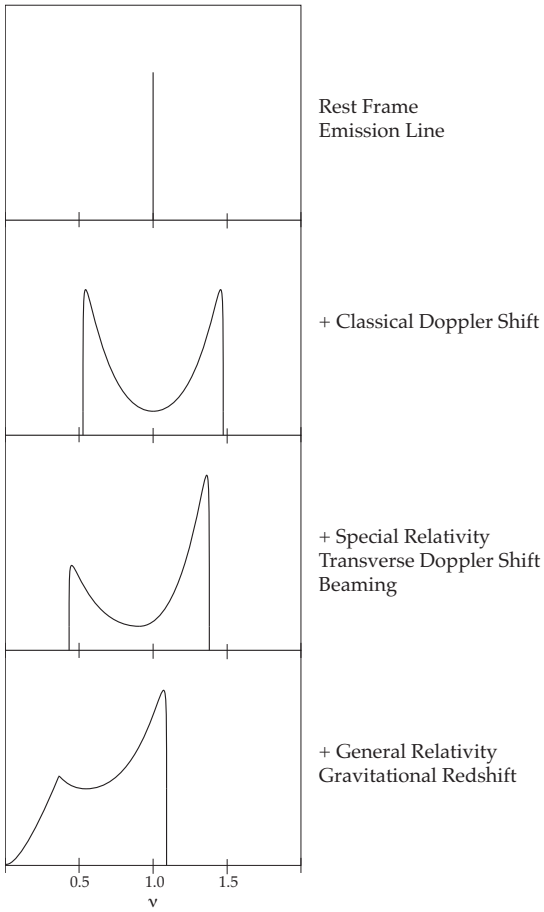

Figure 2.4: The combination of Doppler shift, special relativistic transverse Doppler shift and beaming and gravitational redshift in the formation of the relativistically broadened emission line profile.

beaming, Doppler shift and gravitational redshift.

$$F_0(\nu_0) = \int I_e(r_e, \frac{\nu_0}{g}) T(r_e, g) dg r_e dr_e$$

Dovčiak et al. (2004) present an extended framework for fitting the spectral profiles of relativistically broadened emission lines with a suite of models including KYLINE. The profile of the emission line is affected by the assumed *emissivity profile*, that is the reflected flux as a function of radius on the disc. The emissivity profile is often assumed to take the form of a power law.

To reproduce the enhanced emission from the inner regions of the disc due to relativistic effects, in order to correctly model the observed iron Kα emission line in the Seyfert 1 galaxy MCG–6-30-15, Fabian et al. (2002) found that a once broken power law form was required for the emissivity profile in the LAOR2 broadened emission line model, with the emissivity profile falling off more steeply over the inner regions of the disc before tending to approximately the classically-expected index of

around 3 over the outer part of the disc.

Relativistically broadened emission lines from the accretion disc can be used to measure the spin of accreting back holes. The extremal redshift observed in an emission line from the accretion disc will depend upon the proximity of the innermost orbit in the disc to the black hole; emission is further redshifted from orbits closer to the black hole. The location of the innermost stable circular orbit depends upon the spin of the black hole with the accretion disc able to extend down closer to a more rapidly rotating black hole (the innermost stable orbit and thus the innermost extent of the disc lies at $1.235\,r_{\rm g}$ for a maximally rotating black hole with $a = 0.998$ compared to $6\,r_{\rm g}$ for a non-spinning black hole). Hence, if the location of the innermost stable orbit can be located by measuring the extremal redshift seen in an emission line (assuming the accretion disc extends to the ISCO), the spin of the black hole may be inferred. Brenneman & Reynolds (2006) developed a method for measuring the spin of the black hole using the observed profile of the iron Kα spectral line (the KERRDISK model) and the RELLINE model of Dauser et al. (2010) extends this calculation to emission line profiles from accretion discs with retrograde orbits with respect to the spin of the black hole.

In reality, the entire reflection spectrum (as would be measured in the rest frame of the disc material) will be shifted by these relativistic effects which vary as a function of position in the disc, blurring the whole reflection spectrum. Each energy in the emission spectrum can essentially be treated as a single emission line, thus the blurred reflection spectrum can be obtained by convolving the rest frame reflection spectrum with the profile of a relativistically broadened emission line as shown in Fig. 2.5.

The Detection of Relativistic Lines

The first convincing detection of the relativistically broadened iron K line from an AGN was in the Seyfert 1 galaxy MCG–6-30-15 using the ASCA satellite (Tanaka et al., 1995). Since this first detection, relativistically broadened emission lines have been detected from the accretion discs surrounding many supermassive black holes in AGN as well as around a multitude of stellar mass black holes in our own galaxy. The X-ray spectrum of another narrow line Seyfert 1 galaxy, 1H 0707-495, showing particularly prominent broadened emission lines is shown in Fig. 2.6

The detected emission lines are fit to models of relativistically broadened emission lines detailed above. These models have a number of variable parameters that affect the profile of the emission line seen by the observer and fitting to observed line profiles allows a number of parameters to be constrained including the inclination of the accretion disc to our line of sight (which varies the range of Doppler shifts measured, with accretion discs observed close to edge-on showing broader emission lines as orbital velocities almost parallel to the line of sight produce greater Doppler shifts than those observed face-on) and the inner extent of the extent of the accretion disc around the black

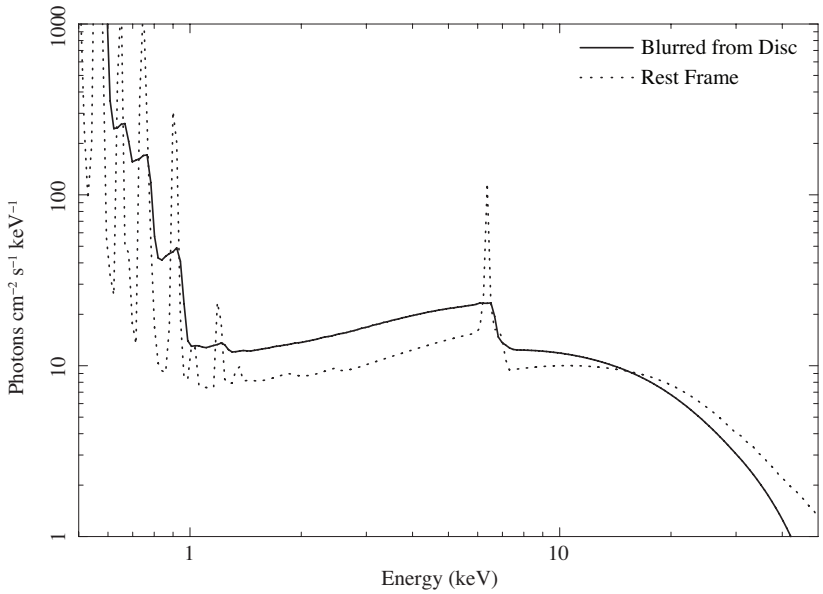

Figure 2.5: The reflection spectrum of the accretion disc blurred by relativistic effects, compared to the spectrum as would be observed in the rest frame of the reflecting material.

hole. Fitting relativistically blurred self-consistent models of reflection from the ionised accretion disc to the observed spectrum allows constraints to be placed on the properties of the material in the accretion flow including elemental abundances and their ionisation states, looking at the energies and intensities of known emission and absorption features. With so many parameters affecting the profile of emission lines in the reflection spectrum, there will inevitably be a number of degeneracies which are explored in great detail in the literature in the context of correlations seen in the fit statistics, though in perhaps a surprising number of cases, examining the fit statistics reveals that some parameters are incredibly well constrained.

While the broad profiles of the emission lines observed with the (relatively low resolution) CCD spectrometers probe the innermost parts of the accretion disc, details of the narrow cores of the emission lines emitted far from the black hole (hence with negligible relativistic effects shifting the emission) can be probed with high resolution grating spectrometers, such as the Reflection Grating Spectrometer (RGS) on board XMM Newton or the transmission gratings on board Chandra. These instruments only range up to 2-3 keV so are unable to probe the iron Kα emission line in great detail, though Blustin & Fabian (2009) find that evidence for features arising from a number of species in the disc (including oxygen, nitrogen and carbon as well as iron, hydrogen and helium) that are consistent with reflection from an accretion disc extending as far out as 1600 $r_{\rm g}$ from the black hole.

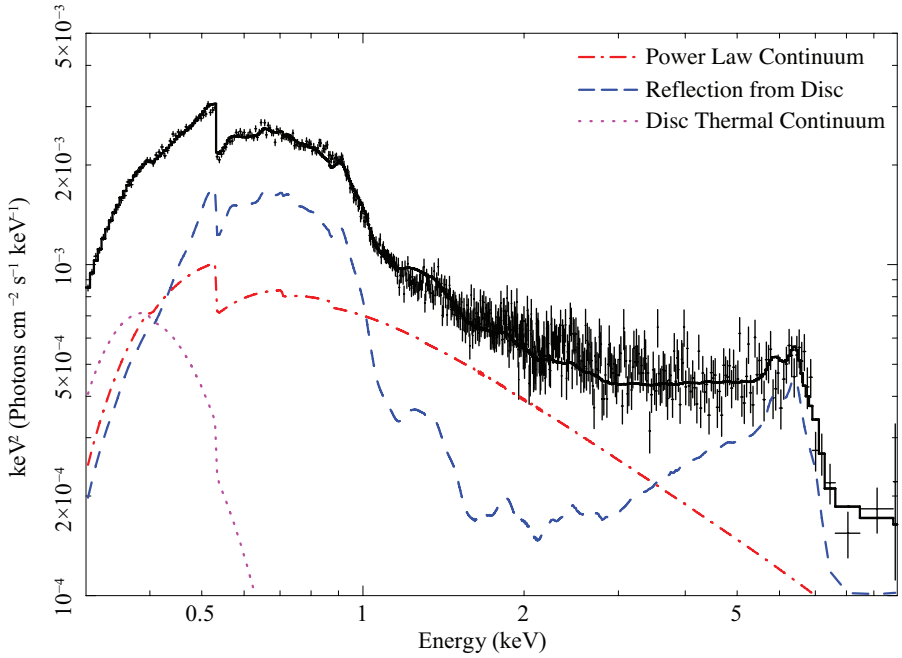

Figure 2.6: The X-ray spectrum of the narrow line Seyfert 1 galaxy, 1H 0707-495 measured by the EPIC pn instrument on board XMM Newton, modelled as the sum of a power law continuum, reflection from the accretion disc (described by the REFLIONX model of Ross & Fabian 2005) and thermal, black body emission from the accretion disc. The broadened Kα emission line of iron can clearly be seen at 6.4 keV as well as the 'soft excess' above the power law continuum between 0.5 and 1.0 keV resulting from the reflection. The drop at low energies is due to absorption of X-rays by material along the line of sight in our own Galaxy.

2.5 Variability and Reverberation

The X-ray emission from accreting black holes is highly variable and recent studies of this variability have added a further dimension to the studies of these systems.

Studying the change in the X-ray spectrum of MCG–6-30-15 (Fabian & Vaughan, 2003a) and 1H 0707-495 (Zoghbi et al., 2010) over time reveals that the power law continuum is highly variable between the observations while the intensity of the reflected X-rays remained almost constant. Naïvely, one would expect that the intensity of the reflection varies with that of the primary continuum that is illuminating the reflector, however if the variation in the continuum is due to movement of X-ray source in relation to the black hole with the continuum flux seen by the observer at infinity dropping as the source moves closer to the black hole (so more of the emitted X-rays are focussed into the black hole), the reflection component does not show such a significant change as the drop in flux is compensated for by the fact that more radiation is focussed towards the black hole and on

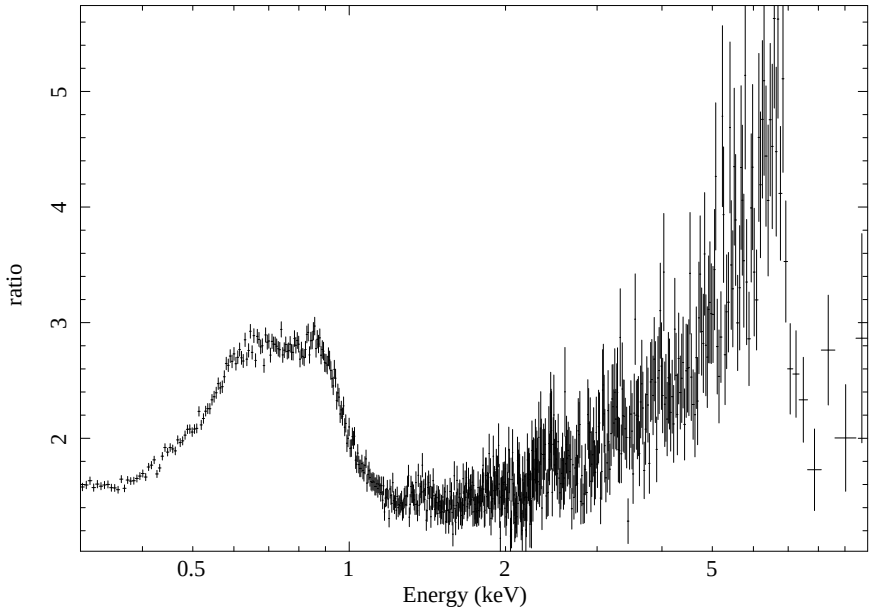

Figure 2.7: The relativistically broadened iron K (6.4 keV) and L (0.9 keV) emission lines in 1H 0707-495, revealed by taking the ratio of the observed spectrum to the powerlaw continuum and black body.

to the disc, enhancing reflection (Miniutti et al., 2003).

Some of the greatest insights about the structure of accreting black hole systems have come through the detection of reverberation lags, where the (more subtle) variability in the spectral band dominated by reflection from the accretion disc is found to lag behind correlated variations in the spectral band corresponding to direct emission from the coronal X-ray source by tens to hundreds of seconds. Such reverberation lags were first detected in the narrow line Seyfert 1 galaxy 1H 0707-495 (Fabian et al., 2009; Zoghbi et al., 2010). Since then, reverberation lags have been discovered in a multitude of other AGN (Emmanoulopoulos et al., 2011; de Marco et al., 2011; Zoghbi & Fabian, 2011; Zoghbi et al., 2012; de Marco et al., 2012) and even in Galactic stellar mass X-ray binaries where the black hole mass and length scale invariance gives equivalent reverberation lags of the order milliseconds (Uttley et al., 2011).

Measuring these phase lags measures the additional light travel time between the source and reflector and allows us to probe scales as small as 10 light-seconds in AGN. The reverberation of X-rays from the accretion disc is characterised by the lag spectrum (Nowak et al., 1999) which shows the time lag of variability at different frequencies between the energy bands. The lag spectrum of 1H 0707-495 was first obtained from a 500 ks lightcurve by Zoghbi et al. (2010) and then in more detail after compiling observations with XMM Newton totalling 1.3 Ms by Kara et al. (2012) and shows a maximum time lag of 30 s between the arrival of the X-ray continuum and the reflection from the accretion disc.

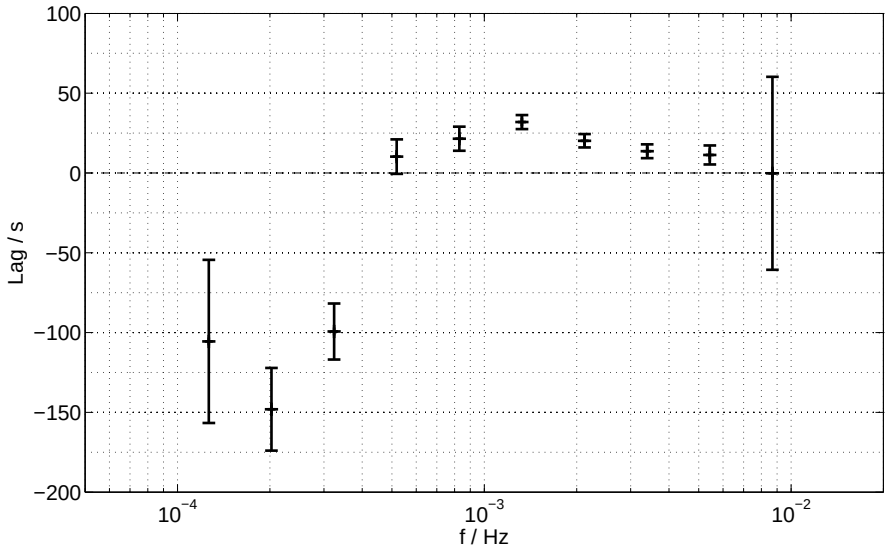

Figure 2.8: The lag spectrum from a 1 Ms lightcurve of 1H 0707-495 from Kara et al. (2012) showing the time lag for the variability at different Fourier frequencies between the hard (1.0-4.0 keV) band corresponding to the primary continuum emission and the soft (0.3-1.0 keV) band corresponding to reflection from the accretion disc. A positive lag indicates that variability in the soft (reflected) band lags behind that in the hard (primary) band.

Examining the reverberation signal in more detail, Zoghbi et al. (2010) and Kara et al. (2012) obtain the time lag as a function of energy for 1H 0707-495, while Fabian et al. (2013) carry out a similar analysis for IRAS 13224-3809. These lag-energy spectra clearly show changes in the power law continuum leading with the variability in both the reflected iron K (6.4 keV) and iron L (0.9 keV) lines responding later. Zoghbi et al. (2012) analyse the reverberation signals detected in the Seyfert galaxy NGC-4151 and find that the reverberation lag at energies corresponding to the redshifted wing of the broadened emission line is significantly shorter and is seen at higher variability frequencies (and thus on smaller spatial scales) than that in the blue peak of the line. Such a result is consistent with the accretion disc being illuminated by a spatially confined X-ray source above the black hole and the more redshifted emission arising from the innermost regions of the accretion disc in the stronger gravitational field close to the black hole.

2.6 Absorption

The presence of warm gas surrounding the nucleus in AGN will add additional features to the X-ray spectrum (Halpern, 1984). This gas is photoionised by the X-ray continuum, whose power law spectrum allows for a range of possible ionisation states within the gas.

The most significant effect of the warm ionised gas is absorption of the continuum. The dominant process, photoelectric absorption, is energy-dependent and the cross section is much greater for soft photons, leading to a drop in continuum flux in the soft part of the spectrum, below around 1 keV with the effect increasing at higher energies as the column density is increased. The warm gas will also contribute emission features to the spectrum, however these are not readily detectable except in high resolution spectra obtained using gratings as they are lost in the continuum emission.

In Seyfert 2 galaxies, the high inclination angle means that emission from the nucleus is heavily obscured by the dusty torus, greatly reducing the continuum emission seen, meaning emission features from the warm gas are more readily visible. This torus is optically thick to Compton scattering, meaning that some emission from the nucleus is visible through reflection off more distant clouds.

It has been argued that the observed spectra of AGN can be explained entirely by the absorption of the X-ray continuum by an optically thick system of absorbing material (perhaps an outflow of material) that completely obscures emission from the accretion disc and whose absorption spectrum mimics the appearance of the relativistically broadened iron Kα emission line (*e.g.* Miller et al., 2008). Such models require multiple absorbers with different column densities and outflowing velocities, each of which partially covers a different fraction of the emission from the X-ray source. These models do not, however, naturally explain the observed reverberation time lags suggesting short light travel times between the primary X-ray source and reflector without invoking further

assumptions about absorbing clouds with sharp edges (Miller et al., 2010), that have, so far, not been demonstrated to be consistent with the properties required to produce the spectrum (while the model of coronal emission reflecting from the accretion disc naturally explains these both of these observations). Further more, the observed reflection spectra from the accretion discs in AGN are analogous to those seen from the accretion disc in X-ray binaries in which any obscuration such as this would be obvious (and is not seen).

2.7 Accreting Black Holes of Interest

2.7.1 1H 0707-495

1H 0707-495 (RA $07°08'41.532''$, Dec $-49°33'06.6''$) is a narrow line Seyfert 1 galaxy, characterised by optical emission lines with widths less than 2000 $\mathrm{km\,s^{-1}}$ at a redshift of 0.041. It was first detected as an X-ray source in the all sky survey made with the HEAO-1 X-ray satellite whose source catalog was published in 1984.

Since its initial discovery, 1H 0707-495 has been observed several times including many observations with XMM Newton. The X-ray spectrum can be understood fairly simply in terms of thermal emission from the accretion disc with continuum emission arising from an energetic corona around the black hole with the reflection of this continuum from the accretion disc.

The X-ray emission from 1H 0707-495 implies a high iron abundance (more then eight times the Solar abundance), giving the X-ray spectrum prominent relativistically broadened emission lines from the accretion disc. There is little absorbing material shrouding the X-ray emission from the central regions, which combined with the strong iron emission lines makes 1H 0707-495 an ideal target for studying the processes at work in the innermost regions of accreting black holes in AGN. Reverberation lags between variability in the primary continuum emission from the corona and the reflection of this from the accretion disc were first detected in 1H 0707-495.

2.7.2 IRAS 13224-3809

Like 1H 0707-495, IRAS 13224-3809 (RA $13°25'19.373''$, Dec $-38°24'52.44''$ at a redshift of 0.066) is a radio-quiet narrow line Seyfert 1 galaxy with a high abundance of iron (in this case around 13 times the Solar abundance). There is again little intrinsic absorption of X-rays giving a clear detection of prominent, relativistically broadened emission lines from the accretion disc.

IRAS 13224-3809 was originally detected in the Infrared All-Sky Survey (IRAS) as a luminous infrared starburst galaxy and was identified as an X-ray source during the ROSAT all-sky survey in 1992. It is one of the most X-ray variable Seyfert 1 galaxies known, making it the ideal target for

studying mechanisms of variability in accretion onto black holes and for the measurement of X-ray reverberation.

2.7.3 MCG–6-30-15

While 1H 0707-495 and IRAS 13224-3809 show prominent broadened emission lines from the accretion disc, the first detection of such a relativistically broadened emission line was made by the ASCA satellite in MCG–6-30-15 (RA $13^\circ 35' 53.800''$, Dec $-34^\circ 17' 43.78''$ at a redshift of 0.0078). Also a Seyfert 1 galaxy, MCG–6-30-15 was first observed to be an X-ray source with HEAO-1.

While interpretation of X-ray observations of MCG–6-30-15 is complicated by the presence of a number of systems of absorbing material, each imprinting features on the spectrum and in fact leading to speculation that the entire form of the X-ray spectrum can be explained by absorption, as well as its lower iron abundance (only around twice the Solar abundance), MCG–6-30-15 is found to have many spectral and variability features in common with 1H 0707-495 and MCG–6-30-15.

2.7.4 Cygnus X-1

Cygnus X-1 (RA $19^\circ 58' 21.68''$, Dec $+35^\circ 12' 05.78''$) is a high mass X-ray binary in our own galaxy in which the envelope of a companion star is accreting onto a black hole with which it is in a binary orbit. Cygnus X-1 is one of the brightest X-ray sources observed from Earth, first discovered by X-ray detectors launched into the upper atmosphere on sounding rockets before being studied in detail by Uhuru, the first astronomical X-ray satellite. Cygnus X-1 was the first discovered astrophysical black hole candidate owing to its large mass (about $14\,\mathrm{M}_\odot$) and small size inferred from its rapid variability that limits the light-crossing time.

Cygnus X-1, like many stellar mass black hole binaries, is seen to transition between a number of states, most notably a high flux state in which the X-ray spectrum is soft and dominated by thermal emission from the accretion disc and a low flux state in which the thermal emission from the accretion disc is seen to drop as the X-ray spectrum becomes dominated by a hard power law originating from a corona of energetic particles around the central black hole. Cygnus X-1 has also been found to possess collimated jets of highly relativistic particles accelerated perpendicular to the plane of the accretion disc.

3

X-ray Observations of Accreting Black Holes

Following the discovery of the first astronomical X-ray point source, the accreting neutron star binary Scorpius X-1 and further sources including Cygnus X-1, Cygnus X-1 was inferred to be a the first astrophysical black hole candidate following detailed observations with Uhuru, the first X-ray detector in orbit on board a satellite, rather than being launched into the upper atmosphere on a sounding rocket. X-rays are strongly absorbed by the Earth's atmosphere, necessitating space-based X-ray detectors. Uhuru was launched in 1970 and performed the first X-ray all-sky survey, detecting 339 sources including Cygnus X-1, which was later confirmed to be a black hole binary, emitting X-rays as the envelope of the massive companion star is accreted onto the black hole.

X-ray astronomy advanced rapidly through the 1970s and 80s with the NASA *High Energy Astrophysics Observatory (HEAO)* programme; *HEAO-1* surveyed the sky three times, while the *Einstein Observatory* (designated *HEAO-2* before launch) was the first imaging X-ray telescope launched into space, allowing for spatially resolved X-ray spectra and located around 7000 astronomical X-ray sources. The final mission of the HEAO programme, *HEAO-3* surveyed the sky in hard X-rays and gamma rays and carried instruments to make measurements of cosmic rays. The European mission *Exosat*, launched in 1983, made detailed observations of a wide variety of objects, including AGN and X-ray binaries as well as clusters of galaxies and supernova remnants. It made a comprehensive study of AGN variability and its transmission gratings meant it would obtain high-resolution

spectra at low X-ray energies. This development culminated with the launch of the German, US and British mission, *ROSAT*, in 1990. ROSAT was sensitive to X-rays in the energy band 0.1-2 keV and could resolve spatially down to 5 arcsec (though was limited by spacecraft jitter to 10 arcsec for prolonged exposures). As well as providing detailed images and spectra of specific sources with its high resolution imager, it completed an all-sky survey cataloguing 60,000 sources.

The 1990s saw refinements to the technology of X-ray detectors. The Japanese satellite *ASCA* was launched in 1993 and carried the first charged-coupled devices (CCD) for X-ray detection. CCD detectors revolutionised X-ray astronomy, due to their high sensitivity and high degree of linearity in their response to incoming radiation. They allow for simultaneous imaging and spectroscopy. ASCA made great progress in the X-ray spectroscopy of AGN, X-ray binaries and clusters of galaxies. While ASCA advanced X-ray spectroscopy, the Rossi X-ray Timing Explorer *RXTE* (US, launched 1995) allowed the X-ray variability of AGN and black hole binaries to studied in unprecedented detail.

Arguably, some of the greatest scientific advances came with the advent of the two major X-ray observatories, *Chandra* (US) and the *X-ray Multi-Mirror Mission*, *XMM-Newton* (European), both launched in 1999. The Chandra X-ray Observatory orbits between 16,000 km and 133,000 km altitude and is able to resolve spatialy down to 0.5 arcsec. Such high resolution imaging is provided by a telescope consisting of nested *Wolter type 1* X-ray mirrors made from the high-Z metal iridium. X-rays are reflected off a parabolic followed by a hyperbolic reflector at grazing incidence, bringing incoming X-rays to a focus.

Chandra has two instruments in its focal plane array; the *high resolution camera* which has produced a large number of high resolution images of X-ray sources, including AGN, X-ray binaries and galaxy clusters and the *Advanced CCD Imaging Spectrometer* (*ACIS*), capable of producing images while measuring the energy of incoming photons. In addition to the focal plane detectors, Chandra is equipped with two transmission grating spectrometers, which can produce high resolution spectra when used in combination with one of the focal plane detectors.

While XMM-Newton does not match Chandra in spatial resolution (only achieving 6 arcsec), its greater collecting area means it can achieve greater spectral resolution. X-rays are collected and focussed by three Wolter type 1 grazing incidence telescopes with gold reflecting surfaces. The three focal plane CCD detector arrays form the *European Photon Imaging Camera* (*EPIC*). Two of the telescopes illuminate metal oxide semiconductor (MOS) CCDs and are mounted behind reflection gratings. The reflection gratings deflect around 44 per cent of the incoming flux to the *reflection grating spectrometer (RGS)* cameras rather than the EPIC MOS detectors to produce high resolution spectra ($E/\Delta E$ of 150-800) over the range 0.33-2.5 keV. The third telescope illuminates the pn CCD which receives an unobstructed beam. This CCD is fabricated from a p-n junction rather than a metal oxide semiconductor and is back-illuminated, so the number of photoelectrons produced is proportional to the energy of the incoming photon, allowing for production of spectra with energy

resolution $E/\Delta E$ of 20-50).

Suzaku is a joint Japanese and US X-ray observatory in a low Earth orbit at 550 km altitude. It receives a much lower background than Chandra and XMM Newton being below the van Allen belts so is shielded more by the Earth's magnetic field. Suzaku is designed to obtain high spectral resolution over a large energy range combining the CCD *X-ray Imaging Spectrometer (XIS)* and PIN and GSO instruments comprising the *hard X-ray detector* (*HXD*). Suzaku is able to obtain X-ray spectra extending up to 600 keV.

X-ray telescopes capable of obtaining high resolution spectra mean that while spatially resolved images of such distant and/or compact objects that are accreting black holes cannot be obtained, a lot can be learned about the physics and models of their operation can be tested by studying their spectra and variability. X-rays are ideal for studying accreting black holes, since they make up a significant fraction of the light emitted and originate from the innermost regions, allowing for a relatively unobstructed view of these extreme environments.

3.1 X-ray CCD Spectroscopy

Much of the observational data used in this thesis was collected using X-ray CCD spectrometers; the European Photon Imaging Camera (EPIC) on board XMM Newton and the X-ray Imaging Spectrometer (XIS) on board Suzaku. The CCD detectors are mounted in the focal plane of the X-ray telescopes such that an image of the sky is formed in the X-rays incident on the detectors. They are behind blocking filters to prevent optical photons reaching the detector. Accreting black holes are observed as unresolved point sources on the sky, which will be smeared onto the imaging plane of the detector by the telescope's *point spread function (PSF)* as shown in Fig. 3.1.

The surface of the CCD itself is a semiconductor substrate, divided into discreet pixels. An incident X-ray may undergo photoelectric absorption in the substrate in order to produce electron-hole pairs which are held in the pixel by an electric field applied through electrodes. Thus, each pixel behaves essentially like a capacitor, storing the charge produced by the incoming photon. Once charge has been collected in the pixels during an exposure, the detector is read-out. Each pixel is coupled to the neighbouring pixels and applying a varying voltage to the electrodes on the pixels allows charge to be transferred from one pixel to the next. The 'frame' is read out by transferring charge sequentially along the detector until it reaches one of the edges. On the EPIC CCDs, each pixel along that edge is connected to a readout amplifier, or alternatively the charge may be transferred along that edge to a single readout amplifier on the last pixel. By measuring the pulses detected in the readout amplifier and knowing how far the charge has been transferred at that stage, it is possible to determine how much charge was collected in each pixel.[1]

[1]In reality, the CCD is split into two; an 'image' section and a 'framstore' section which is shielded from incoming

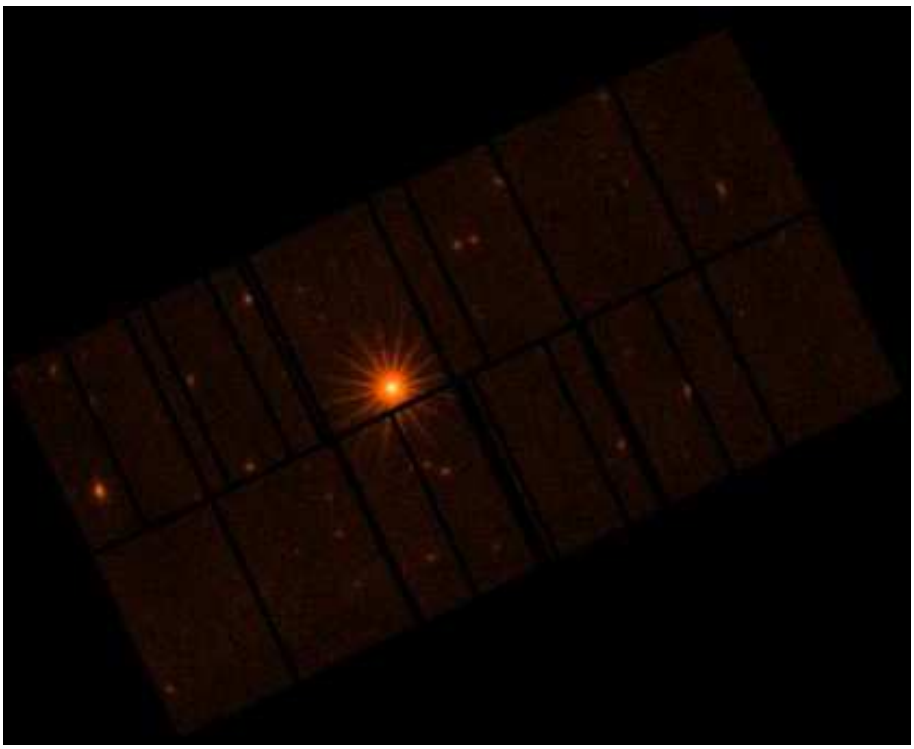

Figure 3.1: Image of the narrow line Seyfert 1 galaxy 1H 0707-495 (an accreting black hole in an AGN) observed with the EPIC pn CCD detector on board XMM Newton. The source is seen as an unresolved point on the sky, though the image is spread out by the telescope's point spread function (PSF). The pn detector is divided into 12 separate CCD chips. The source spectrum is extracted from a 35 arcsec circular region centred on the core of the PSF and the background is extracted from a 35 arcsec circular region on the same chip. Bad pixels (and dead rows on chips) are blacked out in the image.

The number of electrons collected per photon is essentially a linear function of the energy of the incoming photon; the number of electrons freed is the energy of the incoming photon divided by the energy required to free each electron, around 3.7 eV for silicon. Typically, the X-ray arrival rate from the source is sufficiently low and the signals are read from the detector sufficiently quickly that in each 'frame,' only one photon will have struck each pixel, therefore, the voltage peak when that pixel is read, known as the *pulse height amplitude (PHA)*, gives the energy of the incident photon. The charges produced by a single incident photon may be spread over multiple pixels, therefore to obtain the total signal from one photon, the signals detected in neighbouring pixels are summed (assuming that a group of pixels recording signals from one photon is sufficiently isolated from other groups of pixels with charge corresponding to other photons). The detector is operated in 'photon counting' mode and is able to detect each individual incident photon.

CCDs may output data at a very high rate, exceeding the telemetry available to transmit data from the spacecraft. It is therefore not possible to obtain entire CCD readouts from X-ray telescopes. Rather, the data are processed into a list of 'events' corresponding to discreet detections. An event is defined on a pixel whose signal is higher than its neighbours and also exceeds some threshold to remove the bias level in the detector. The total pulse height amplitude is recorded for the event, along with the number of pixels in which the event was detected, the shape of the event on the CCD and also the time and position of the detection.

To maximise efficiency and capability for a set of observations, CCD detectors can be operated in a number of different modes. For instance, the EPIC detectors on XMM Newton may be operated in one of four science modes for any given observation. There are two imaging modes; full frame mode, reading out all pixels of the CCD or partial window mode, reading out only some of the pixels to give either the so-called large or small window mode. Reading out only some of the pixels on the CCD decreases the time taken to read out the detector. This means that the exposure time of each frame before it is read out can be reduced while maintaining the total live time of the detector, improving the time resolution (from 2.6 s in full frame mode to 0.9 s and 0.3 s in large and small window modes respectively) and decreasing the risk that two or more photons will strike the same pixel per frame, meaning brighter sources may be observed. Finally, XMM Newton's EPIC cameras have a timing mode as well as a burst mode. The image is only recorded in one dimension and the charge is constantly transferred down the detector columns to the readout amplifier. This offers time resolution as good as 0.03 ms in timing mode or 7μ s in burst mode (though burst mode offers only 3 per cent live time for observing bright flaring phenomena compared to almost constant observation in timing mode).

radiation. The frame is transferred relatively quickly from the image section to the framestore section, then read out more slowly through the readout amplifiers connected to the framestore section. Reading out slowly reduces the noise picked up in the amplifier and reading out from the framestore while the image section is exposed for another frame reduces the dead time of the detector during readout.

An important assumption made in CCD spectroscopy is that only one photon is detected in each pixel per frame that is read out from the detector. If two or more photons were to strike the same pixel, or neighbouring pixels such that they are interpreted as the distributed cloud of charge produced in a single event, rather than recording the two events separately, they will be recorded as one photon with the combined energy of the original photons, referred to as *pile-up*. For low flux sources, it is sufficiently unlikely that events will be piled up on the detector so this phenomenon will not affect the shape of the total spectrum, however when observing bright sources, pile-up becomes sufficiently likely that it will skew the shape of the recorded spectrum. It is therefore important to assess if the events in an observation are piled up before analysing spectra. The charge cloud produced in the detector through the interaction with a photon will be spread through a number of neighbouring pixels, though the majority of X-rays will be detected in a single pixel. The risk of pile-up can be assessed by comparing the number of double-pixel detection events compared to the number of single pixel detections. If this deviates significantly from the expected values derived from calibrations, there is a risk that the observation is piled up. Pile-up can be mitigated for bright sources either by exposing each frame for a shorter time before read-out in small window or timing mode (though this must be planned before the observations are made) or by only analysing spectra from an annular region, excluding the brightest part of the PSF in the centre.

3.1.1 Data Reduction

Before the data are usable, the event list must be processed in a number of ways. Firstly, the Cartesian co-ordinates of the detection on the square grid of the CCD must be translated initially into 'detector co-ordinates' if the detector is made up of multiple, separate CCD chips to get events from all of the chips into the same co-ordinate system. These detector co-ordinates are then translated into the position on the sky using knowledge of the pointing direction of the telescope and its roll angle (which are found from an image of known stars and constellations from an optical star tracker telescope mounted on the spacecraft such as the *optical monitor, OM* on XMM Newton). This conversion must also take into account any flexure in the focussing optics. The time of the event (which is recorded using the spacecraft's on-board clock) is also converted to a time on Earth relative to the modified Julian date such that the dataset can be compared with other observations.

Further more, the response of the CCD detector to incoming photons is not constant across all of the pixels (or constant in time for that matter). As such, calibration data of the detector, either obtained from astrophysical X-ray sources or from X-ray emitting radioactive sources on board the spacecraft are used to provide a position- and time-dependent conversion from the recorded pulse height amplitude (PHA) to the so-called *PHA invariant (PI)*. This PI value is comparable between detections made in different pixels and at different times and is what is used to characterise the energy of each incident photon. Finally, before the data can be used, 'hot pixels' (which always

record a signal), 'dead pixels' which record no signal and other defects are detected and these bad pixels and those adjacent are either excluded from the event list or 'flagged' as bad events.

3.1.2 Background Removal

In addition to X-rays from the source of interest, the detector will record a number of background signals. The most significant background detections fall broadly into two categories; X-rays from other cosmic sources (including the cosmic X-ray background) and cosmic rays, the solar wind and other energetic particles striking the detector.

Cosmic ray protons and other energetic particles will ionise the semiconductor in the CCD causing charge to accumulate in the pixels and will thus cause a signal to be detected in the readout. While X-ray photons typically produce a very localised charge cloud, spanning only one or two pixels (so-called single and double pixel events), particles will spread charge over many more pixels, so the vast majority are quite easily filtered from the event list by demanding only single and double pixel events.

The particle background is extremely variable, particularly in XMM Newton and Chandra's highly elliptical orbits that pass through the Earth's radiation belts. The background particles from the solar wind go through flaring periods which can last between minutes and hours and are evident in observations by a high count rate in the uppermost energy channels. Events detected during these flaring intervals are filtered out of the event list using a *good time interval (GTI)* filter, which selects only events detected in time periods when specified criteria are met (in this case, when the count rate in the high energy bands is below a threshold). In XMM Newton, the requirement to avoid flares in the background are that the count rate between PI channels 10,000 and 12,000 (approximately 10-12 keV) is below $0.4\,\mathrm{ct\,s^{-1}}$.

Once the particle background has been filtered from the event list, the X-ray background must be subtracted from observations of the astrophysical object of interest. X-rays from the target of interest are analysed by selecting only events recorded at the required location on the image, typically a circular region. The background is assumed to be uniform across the region of sky in the vicinity of the object of interest and it can be subtracted from the observations by analysing photons detected in an area the same size as the source region (so background photons are detected at the same rate in both the source and background regions), just on a different part of the same detector chip.

3.1.3 Extracting X-ray Spectra

In principle, the energy of each incoming photon is given by the amount of charge it produces when it is absorbed by the semiconductor in each pixel, characterised by the pulse height amplitude

invariant (PI) recorded for the detection event. In order to extract the spectrum of the source, X-ray detection events matching some filtering criteria (typically single and double pixel events with none of the data reduction pipeline's bad event flags set) are selected from the event list based upon their location in the image. Events are selected from a circular region encompassing the majority of the X-rays detected from the source, typically 30-35 arcsec for point sources detected with XMM Newton. To produce the spectrum, at the simplest level, the detected events are counted into energy bins (PI channels).

In reality, the response of the detector to incident photons of a single energy is a little more complicated than a voltage pulse being produced proprotional to the energy of the incident photon. If the incoming photon is absorbed by removing an inner-shell electron from an atom, the atom will then de-excite. It may do this by producing further electrons by Auger de-excitation, however it may also de-excite by emitting a photon which can escape from the detector. In this case, the recorded pulse height amplitude corresponds to the energy of the original incident photon less the energy that escapes with this emitted photon. As such, it is necessary to understand the probability distribution characteristic of the detector of the production of different PI signals for a given incident photon energy in order to recreate the energy spectrum of incident X-rays from the recorded distribution of pulse height signals. This is characterised by the *photon redistribution matrix* (also known as the *response matrix file or RMF*.

In addition to response of the detector, the observed spectrum is also influenced by the sensitivity of the focussing optics. X-ray reflection by grazing incidence mirrors is a strong function of the incoming X-ray energy as well as the position of the source on the sky and whether the X-rays approach along the optical axis of the telescope. The sensitivity of the telescope coupled with the sensitivity of the detector itself as a function of energy (the probability a photon of a given energy being detected at all, for instance photons with energies greater than around 10 keV are likely to pass through a silicon detector without interaction) is characterised by the *effective area* and is stored in the *ancillary response file* as a function of energy.

As the spectrum is measured from the random arrival of photons of different energies, the probability distribution of the number of photons received per unit time is a Poisson distribution about the mean arrival rate over all times. Therefore, the error associated with each spectral bin, the standard deviation, σ, is $\sqrt{N}$ where N is the number of photons detected. In the limit of high count rates (in fact more than around 10 photons detected per spectral bin since the Poisson distribution rapidly converges to a normal distribution), under the central limit theorem, this distribution will tend to Gaussian. In order to improve the signal to noise (to reduce the fractional error in each bin), neighbouring spectral bins may combined, summing their photon counts. This is typically done to satisfy the criterion of a minimum number of counts in each bin, usually 20-25 detections depending on the dataset (the energy bin size becomes variable).

XMM Newton completes one orbit of the Earth in 48 hours (173 ks), limiting the total time it can be

focussed on any one object to just over 100 ks per orbit, while Suzaku completes a low Earth orbit in just 96 minutes (5.8 ks). As such, longer observations must be composed of a number of separate observations made on separate orbits. The data from each orbit are reduced independently; spectra are extracted from each and RMF and ARFs are computed separately. These may be combined into a total spectrum offering a longer observation and more counts, thus a greater signal to noise ratio by summing the counts detected in each energy bin from the orbits. The overall response matrices (the RMF and ARF) are computed as weighted averages of the responses from the separate orbits, though care must be taken to ensure the source was on a similar region of the detector for each orbit to ensure the response matrices for each are similar. Combining photon counts in PI channels under an average response when in reality some of the photons in each PI channel correspond to a very different response will produce a misleading spectrum that is unrepresentative of the real source.

The spectrum of the X-ray background is computed by analysing photons from a separate region on the detector chip, the same size as the region used to select the object of interest. The background spectrum is computed in the same way as the source spectrum and is then subtracted from the observed spectrum of the source.

3.1.4 Extracting Lightcurves

In the same way that the spectrum of a source can be extracted from the event list by binning photons according to their energy (or PI channel), a lightcurve, characterising the variation in flux received from the the source over time, may be extracted by binning the photons according to their arrival time.

A lightcurve may be constructed either using all of the photons received from the source, or the photons counted in the lightcurve may be filtered by their energy to obtain the lightcurve in a specific energy band, which can be useful in probing mechanisms of variability. When computing lightcurves in specific energy bands, events are typically filtered based upon their PI channels. While a proper separation of events by photon energies should account for the detector response and the probabilistic distribution of photons of a given energy into multiple PI channels (characterised by the RMF), present analysis techniques use lightcurves in relatively broad energy bands (0.5-1 keV in width). The width of the energy bands is much wider than the distribution of events between PI channels, thus filtering simply by PI channel is sufficient.

Like extracting a spectrum, the corresponding lightcurve from a background region, the same area as the source region, but in a different region of the chip is subtracted from the source lightcurve.

3.2 Analysing X-ray Spectra

X-ray spectra are analysed in the context of models of the emission from the object of interest. These models may be phenomenological descriptions of the shape of the spectrum, such as a simple power law continuum with a collection of emission lines and absorption edges that are put in 'by hand,' or may be physically motivated, for example, an X-ray continuum arising from the Comptonisation of thermal seed photons or a self-consistent model of the X-ray reflection from material in the accretion disc. Typically, the X-ray emission from an accreting black hole will be modelled as the sum of a (pseudo) black body component for the thermal emission from the accretion disc, a (cut off) power law arising from the corona by Comptonisation and a reflection spectrum from the accretion disc convolved with the profile of a relativistically blurred emission line. Spectral models must also account for any absorption by intervening material along the line of sight, both in the host galaxy of an AGN and in our own galaxy. The absorption is most significant below 1 keV. Any instrumental features that are not removed by calibration of the instrument response (for example absorption edges arising from the materials in the telescope and detector) must also be modelled, or the corresponding energies should be excluded from the spectrum.

Spectral models will possess a number of free parameters that correspond to physical properties of the emitter, for example the characteristic temperature of the black body emission, the innermost radius of the accretion disc or the inclination of our line of sight to the plane of the accretion disc. The values of these parameters are determined by finding the combination thereof providing the best fit by the model to the observed spectrum. The goodness of fit is quantified by the *likelihood function*, the probability of obtaining the given data set (within the errors) given the model. Assuming the errors to be Gaussian (applying the central limit theorem in the limit of high enough count rates of X-ray photons), the probability of obtaining each, independent data point follows a normal distribution, thus the likelihood function for a set of data points, x_i with errors σ_i and the expected values of the data points from the model μ_i is

$$\mathcal{L} = \prod_i \frac{1}{\sqrt{2\pi\sigma_i^2}} \exp\left(\frac{(x_i^2 - \mu_i^2)}{2\sigma_i^2}\right) \tag{3.1}$$

The likelihood is maximised when the model best fits the data.

Taking the logarithm of the likelihood function, we obtain

$$-2\ln\mathcal{L} = \sum_i \frac{(x_i - \mu_i)^2}{\sigma_i^2} - 2\sum_i \frac{1}{\sqrt{2\pi\sigma_i^2}} \tag{3.2}$$

This function is minimised when the model best fits the data. The second term is independent of the model, therefore the goodness of fit as the model parameters are varied is given by the first term, which is often referred to as the χ^2 statistic.

$$\chi^2 = \sum_i \frac{(x_i - \mu_i)^2}{\sigma_i^2} \tag{3.3}$$

The χ^2 statistic is minimised for the best fitting model. When the model describes the data perfectly, the mean deviation of the data points from the model, $\langle x_i - \mu_i \rangle$ is equal to the error in the measurement, σ_i, so each term in the sum reduces to around unity and χ^2 is equal to the number of data points. The goodness of fit (*i.e.* the probability that the model describes the data) is characterised by the *reduced* χ^2; the χ^2 value divided by the number of *degrees of freedom*, where the number of degrees of freedom is the number of data points less the number of free parameters in the model (to account for the fact that models with more free parameters are better-able to fit any dataset and if there are more free parameters than data points, one or more of the parameters will be unconstrained by the data).

The response matrices mapping the energy distribution of incoming photons to the PI channels recorded in the detector may be complicated and singular, such that the instrument response is not readily unfolded from the recorded data.[2] Therefore, in order to fit a model to an observed spectrum, the model is folded through the instrument response and this 'folded model' is fit to the data. When the spectrum is obtained using an imaging detector, such as a CCD, such that a background spectrum may be extracted from a separate region of the detector to the source, the background spectrum is subtracted from the data before fitting the model.

Numerical algorithms are employed to find the best-fitting set of parameters for any given model to the data in question, that is the minimum value of the fit statistic across the entire parameter space. The spectral fits in this thesis employ the Levenberg-Marquardt algorithm for numerical minimisation of a function in the spectral analysis software, XSPEC (Arnaud, 1996) to achieve this.

As well as determining the values of model parameters best fitting the data, it is also important to assess the confidence limits or errors on these values to understand how well constrained they are by the data and the range of values the data will admit. The confidence limits of a parameter are determined in a maximum likelihood fitting procedure by stepping through the values of the parameter in question. At each step, the values of all other free parameters are varied to give the best fit given the current value of the parameter whose confidence limits are to be estimated and the χ^2 statistic is evaluated to assess the goodness of this fit. Comparing each step of the parameter value, the best fit will, of course, be when the value of χ^2 is the least, though the values will follow the chi-squared distribution. The 1σ confidence limit of the parameter corresponds to the step when the value of χ^2 has increased by 1 from its minimum. Similarly, the 90 per cent confidence interval corresponds to 2.706σ.

In exactly the same way as estimating errors, it is possible to step through values of one or two parameters, find the best fit of the other parameters given those values and then evaluate the overall

[2]It is possible to produce 'unfolded' spectra using spectral analysis software, in which the flux or spectral energy distribution is plotted rather than the count rate, though these are produced by assuming the spectral model is correct, then plotting the data points around the model according to their errors. These unfolded spectra are useful for illustrative purposes though can be misleading if the assumed model is incorrect.

goodness of fit those values provide in order to plot either the χ^2 statistic as a function of a parameter to assess the values admitted by the data or to plot contours of constant χ^2 to assess both how those two parameters fit into the data and if there is any correlation between two 'free' model parameters or if they are truly independent.

4

Determining the Accretion Disc Emissivity Profile

Considering the scenario in which X-rays originate from a source in an energetic corona surrounding the central black hole and are reflected off the accretion disc, with photons being either Compton-scattered or undergoing photo-electric absorption which will lead to Auger de-excitation or the emission of a fluorescent line (§2.3), the incident flux varies as a function of position on the disc. This variation causes the reflected flux (the *emissivity profile*) to vary across the disc.

In the simplest case of a point source in flat, Euclidean spacetime, the emissivity at a point on the disc is proportional to the inverse-square of the distance from the source, multiplied by the cosine of the angle at which the ray hits the disc from the normal, giving a form r^{-3} at large radius out from the source. In general relativity, however, rays will be focussed towards the black hole (and the inner disc) so naively one would expect a steeper fall-off in emissivity with distance from the black hole. The details of the emissivity profile will depend upon the location, spatial extent and geometry of the source.

When modelling the X-ray reflection spectrum from the accretion disc around a black hole, a (broken) power law emissivity profile ($\epsilon \propto r^{-\alpha}$) describing the reflected power per unit area from

the disc, is typically assumed and its parameters fit to the observed spectra. Power law forms of the emissivity profile are motivated by calculations tracing rays from coronal X-ray sources in the spacetime around the central black hole on to the accretion disc (Miniutti et al., 2003; Dabrowski & Lasenby, 2001; Suebsuwong et al., 2006). These calculations suggest a very steeply falling profile in the inner regions of the disc, then flattening off before tending to a constant power law slightly steeper than the r^{-3} law one would expect in the classical case.

If the emissivity profile of an accretion disc can be determined from observations without *a priori* assumption of its form, this will allow for testing of the light-bending hypothesis and could place constraints on the location and geometry of the coronal X-ray source.

4.1 Relativistic Emission Line Profiles

From a given region of the accretion disc, the energy of an emission line as measured by an observer at infinity will be altered from the rest-frame frequency by relativistic effects including Doppler shift, beaming and gravitational redshift, characterised by the transfer function (Laor, 1991), defined such that the spectrum of the line seen by the observer at infinity is given by

$$F_0(E_0) = \int I_e(r_e, \frac{E_0}{g}) T(r_e, g)\, dg\, r_e dr_e \tag{4.1}$$

Where subscripts '0' denote quantities measured by the observer at infinity and 'e' those measured in the rest frame of the emitter. The redshift parameter is $g = \frac{E_0}{E_e}$ and is a function of position in the disc, while $T(r_e, g)$ is the transfer function encoding all relativistic effects from the emission of the radiation around the black hole to the observer at infinity. For a narrow emission line line at energy E_e, the rest-frame spectrum is simply

$$I_e(r_e, E) = \delta(E - E_e)\epsilon(r_e) \tag{4.2}$$

The emissivity profile, $\epsilon(r)$, gives the variation in reflected power as a function of radius, measured in the disc frame.

It is clear from the form (4.1) that the observed emission line can be considered as the sum of contributions from successive radii in the disc, with the number of photons received by the observer at infinity from an annulus of the accretion disc radius r_e and thickness dr_e

$$N_0(r_e, dr_e) = A'(r_e, dr_e)\epsilon(r_e) \tag{4.3}$$

Where $A'(r_e, dr_e)$ is the projected area of the annulus as seen by the observer, which from (4.1) is the integral of the transfer function over all frequencies (or over redshifts, g, after a change of variables) that are seen from a given radius in the disc (the range of Doppler shifts) and is equivalent to integrating around the disc in φ. The transfer function is defined to give photon counts per unit

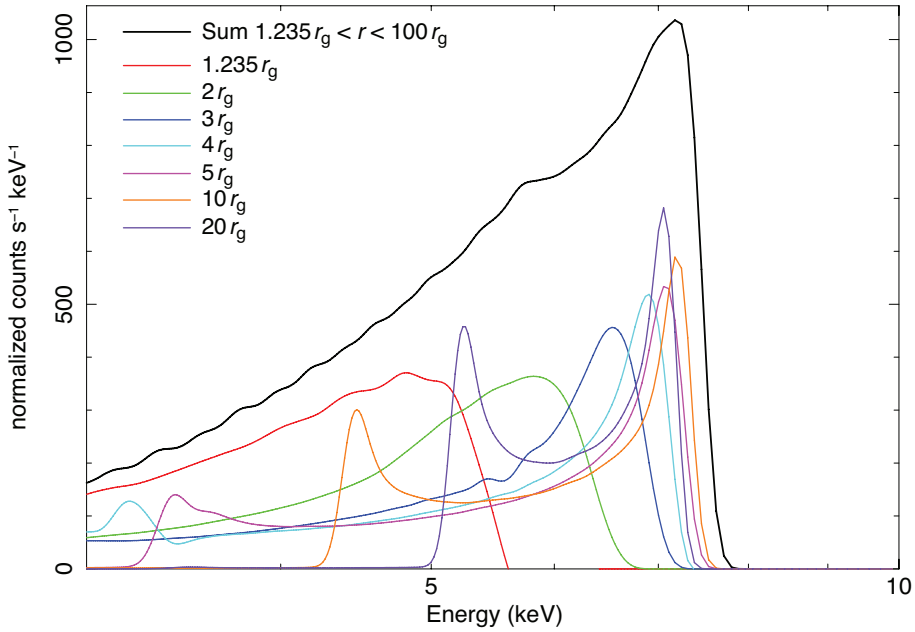

Figure 4.1: Relativistically broadened emission line profiles emitted from successive radii in the accretion disc ranging from 1.235 r_g to 20 r_g and the integrated line over the disc out to 100 r_g, calculated using the LAOR line model.

energy, rather than fluxes, which is relevant here as when fitting to the reflection spectrum, the contribution from each region of the disc is given by its contribution to the total photon count.

4.2 Emissivity Profile Determination

In order to determine the emissivity profile of the accretion disc from the observed reflection spectrum, the relativistically broadened iron Kα emission line (which has a rest frame energy of around 6.4 keV, though varies slightly with the ionisation state of the disc) is considered, as above, to be the sum of contributions from successive radii in the disc. A relativistically broadened line will have a different profile if emitted from annuli of different radius, due to different orbital velocities and gravitational redshifts across the disc, which can be seen in Fig. 4.1. Therefore if the observed line can be broken down into contributions from different annuli and the relative weightings of these found, the reflected flux from each part of the disc (*i.e.* the emissivity profile) can be determined.

In the 3-10 keV region of the spectrum where the Kα line lies, the spectrum is well described as the sum of a power law (the directly observed continuum emission) and the reflection spectrum containing the emission line and corresponding absorption edge, described by the REFLIONX model (Ross & Fabian, 2005), once convolved with the KDBLUR model to apply the relativstic blurring in

the accretion disc. The spectrum is modelled in XSPEC as

$$\text{powerlaw} + \sum_{r_e} \text{kdblur} \otimes \text{reflionx} \tag{4.4}$$

The radial intervals are selected to coincide with the radial binning of the transfer function used in the LAOR model (when fitting the model to the data, XSPEC looks up the transfer function from a pre-calculated table rather than evaluating it on-the-fly at each point, which would be computationally intensive) as it would be inappropriate to subdivide the disc further, since the resulting line profiles from these subdivided bins would be essentially the same as the same transfer function is used.

Only the 3-10 keV region of the spectrum is considered when determining the emissivity profile as this band contains a single emission line which can be decomposed into contributions identifying successive radii in the accretion disc according to the observed redshifts. When fitting for the emissivity, it is necessary to have a single emission line profile from which these contributions can be distinguished and as such the iron L region (0.5-1.0 keV), which contains multiple emission lines (including those from oxygen and nitrogen) whose annular components will overlap in energy once relativistic blurring is applied, is not suitable as emission from different regions of the disc cannot be distinguished here. Once the emissivity profile has been determined, however, it can be applied to a reflection spectrum covering the full energy range. Furthermore, the EPIC pn detector on board XMM-Newton has a spectral resolution of 150 eV (FWHM) at 6 keV meaning there are 46 energy bins in the 3-10 keV band but between 0.3 and 1 keV a resolution of 100 eV (FWHM) results in only nine bins, with only three before emission lines from oxygen appear below 0.65 keV, thus in the iron L band, there are insufficient spectral bins available to fit for the emissivity profile.

All model parameters are frozen to values which have been previously found to give the best fit to the overall spectrum, except for the normalisations (photon counts) of the REFLIONX components, which are free parameters and are fit by minimising χ^2 to find the relative weightings of the components. The inner and outer radius of each annulus is set in the blurring kernel KDBLUR. Each annulus has constant emissivity (the `index` parameter is set to zero) such that there is no variation in emitted flux across each annulus and the overall emissivity profile is given by the variation in photon counts between the annuli.

The projected area of each annulus as seen by the observer at infinity is found from the transfer function in the LAOR model (which is used by KDBLUR for the convolution), by summing the photon count over all energies at a given radius with a constant, flat emissivity. The emissivity profile is then calculated by dividing the normalisations of the REFLIONX components by these areas as per Equation 4.3.

4.2.1 Testing the Method

It is not immediately obvious that a given emissivity profile will lead to a unique emission line profile which then gives a unique annular decomposition, particularly once folded through the response function of a real X-ray detector, since the contributions to the line from different radii are not, strictly speaking, orthogonal functions. Before applying the method to real data, it is therefore important to carry out preliminary tests, applying it to synthetic spectra whose emissivity profiles are known and checking that these profiles can be recovered correctly.

This method has been applied to synthetic spectra in which relativistically broadened emission lines with known emissivity profiles, formed from the LAOR emission line model, were folded through the response matrix of the EPIC pn detector on board XMM-Newton, using the `fakeit` command in XSPEC to simulate the spectra that would be observed if sources emitting such lines were observed with this instrument. Synthetic spectra were calculated for an exposure time of 300 ks and the incident flux in the emission line was normalised to unity, since here we are interested only in the overall shape of the line spectra with no background. The response matrix of the detector maps only incident energies onto detector channels. It is independent of the incident flux which will just provide an overall scaling that is irrelevant here since we are interested in whether the contributions from successive annuli can be recovered from the overall shape of the spectrum.

A variety of line profiles were tested, with single power law emissivity profiles with indices ranging from 2.0 to 6.0. In addition to this, once-broken power law profiles were tested (these model line spectra are created using the LAOR2 variant of the model). It can be seen from Fig. 4.2 that these profiles were successfully recovered.

Scatter at larger radius appears where the radial step is finer than the binning used in the LAOR line model where the transfer function is evaluated. As a result, the line profiles from neighbouring radii in the same bin are essentially the same. They cannot be distinguished in the fitting procedure, leading to multiple points with essentially equal weighting rather than following the true emissivity profile as illustrated in Figure 4.2(b). This scatter is reduced when the radial interval in the fit is chosen to coincide with the radial binning of the LAOR transfer function.

4.3 The Emissivity Profile of 1H 0707-495

The emissivity profile of the accretion disc in the Narrow Line Seyfert 1 galaxy 1H 0707-495 was determined using the above method applied to the spectrum obtained using the EPIC pn detector on board XMM-Newton during four consecutive orbits with a total exposure time of 500 ks (Zoghbi et al., 2010). The values of the frozen parameters (*i.e.* those other than the photon counts from the reflection components) were taken from the best fit model of Zoghbi et al. (2010) and are shown in

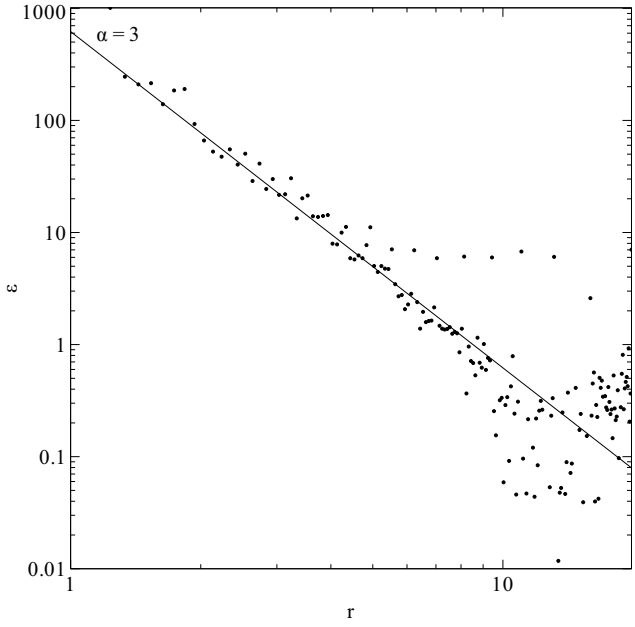

(a)

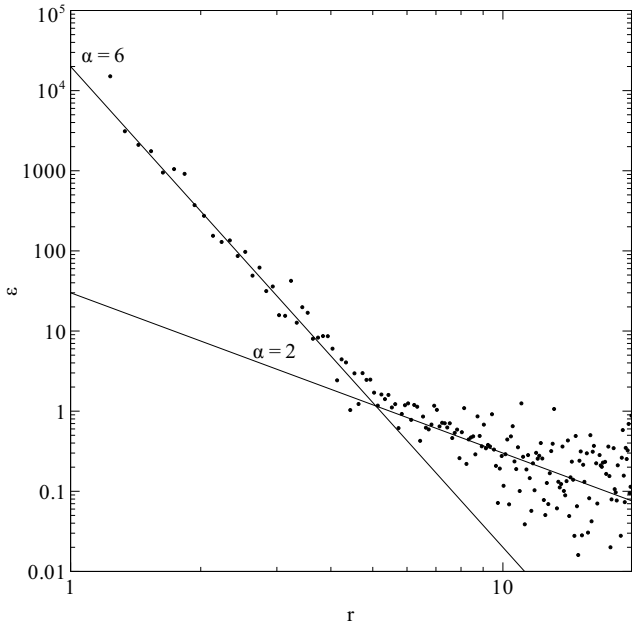

(b)

Figure 4.2: Recovered emissivity profiles from synthetic spectra to test the method, each consisting of a single emission line with (a) a single power law emissivity profile, index 3 and (b) a once-broken power law emissivity profile, indices 6 and 2 with the break at a radius of $5\,r_{\rm g}$. Scatter occurs in regions where the radial points are more finely spaced than the radial bins in the LAOR model.

Table 4.1: Values of frozen model parameters used in emssivity profile determination.

Component	**Parameter**	**Value**
powerlaw (PLC)	Photon index, Γ	3.09
	Photon count, *norm*	1.50×10^{-3}
kdblur (RDC)	Inclination, i	$53.96\,\mathrm{deg}$
reflionx (RDC)	Photon index, Γ	= `powerlaw:`Γ
	Iron abundance / solar	8.88
	Ionisation parameter, ξ	$53.44\,\mathrm{erg\,cm\,s^{-1}}$
	Redshift, z	4.10×10^{-2}

Table 4.1.

The normalisations of the reflection components were initially fit in the energy range 3-10 keV, which encompasses the entire iron Kα line. The resulting fit is shown in Fig. 4.3 and gives the a reduced χ^2 value of $255.48/227 = 1.1255$, indicating that the model describes the data well and that there are no significant components other than the power law continuum and reflection from the disc contributing to the spectrum in this energy range.

The emissivity profile found from this fit by dividing the best-fit REFLIONX normalisations by the projected areas of the annuli is shown in Fig. 4.4(a).

The model was also fit to the spectrum in the restricted energy range 3-5 keV. This energy range includes contributions to the 6.4 keV emission line from regions of the disc out to $20\,r_\mathrm{g}$with contributions to the line emitted from radii beyond this mostly excluded, with only their redshifted wings included. Since the majority of the line flux is in the energy range above this and originates from the outer disc, the fit over the full line will be weighted heavily towards these radii, so fitting to the restricted 3-5 keV range will give better detail of the inner regions of the disc. The emissivity profile determined from the results of this restricted fit is shown in Fig. 4.4(b).

From the above fits, a steep emissivity profile is apparent in the inner regions of the disc, with the 3-10 keV fit indicating a power law index of 6.0 out to a radius of around $3\,r_\mathrm{g}$ and tending to a value of around 3.3 at large radius.

In the 3-10 keV fit, the points in the region 4-20 r_g are missing, with the best fit values to these normalisations being zero. However the 1σ error limits on these points are very large (on the arbitrary scale in Fig. 4.4(a), these points could be as high as 10^{-6}), showing that the photon counts from this region of the disc are poorly constrained by these data. This is most likely due to the χ^2 statistic in a fit over this energy range being dominated by the line flux from the outer regions of the disc which is much greater than that received from the inner region. The line profiles from the innermost regions out to $4\,r_\mathrm{g}$ account for the shape of the line at low energy (and have a relatively

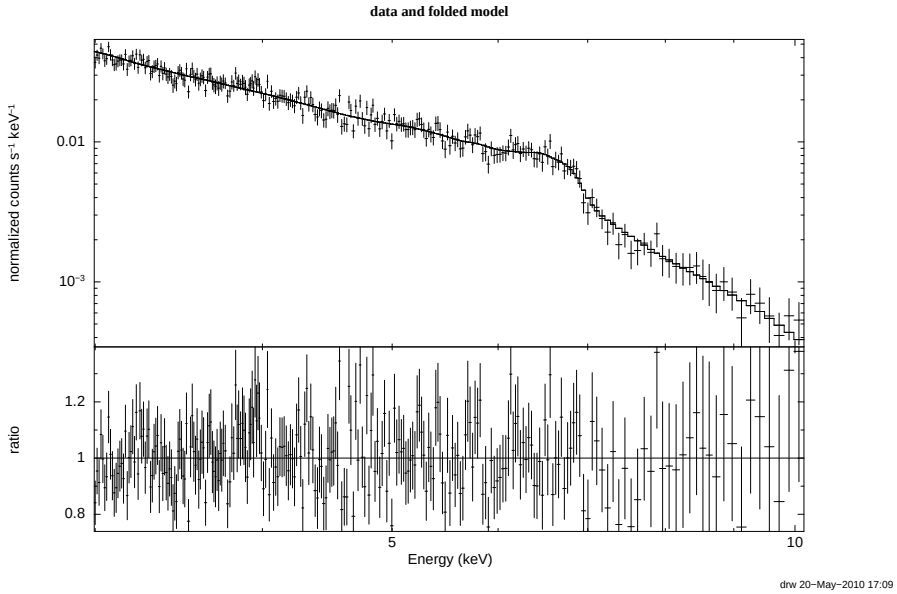

Figure 4.3: Fit to the iron Kα edge (3-10 keV) of 1H 0707-495 with the disc reflection considered as the sum of components from successive radii. $\chi^2/\mathrm{DoF} = 255.48/227 = 1.1255$.

high photon count due to the apparent steepness of the emissivity profile). Once these contributions and those from the outer disc are accounted for, the 4-20 r_{g} region corresponding to the middle band of the emission line is not well constrained. This is remedied in the 3-5 keV fit where the outer region of the disc (outside 20 r_{g}) which dominated the line flux is removed and more detail of the inner disc is seen.

Fitting to the energy band 3-5 keV steepens the index of the emissivity profile to around 7.8 out to a radius of 5 r_{g}. This fit also indicates a flattening of the emissivity profile in the region 5-30 r_{g} with a power law index of between 0 and 1. These points do not appear in the 3-10 keV fit because the contributions from these regions lie in the middle of the line profile so are masked by the contributions from either side. Note that in this fit, the points in the outer disc are poorly constrained and have large error bars because the energy range of their contributions to the line is omitted.

The determined emissivity profile can be used to construct a pseudo-image of the accretion flow in 1H 0707-495, showing the reflected flux (measured in the rest frame of the disc) as a function of position in the disc (Figure 4.5).

While this analysis was completed using the KDBLUR model which convolves the reflection spectrum with the LAOR line model for efficiency of computation, the analysis can be completed using other relativistic disc convolution models. One such model is the RELCONV model of Dauser et al. (2010) which convolves the reflection spectrum with the RELLINE profile, providing finer radial

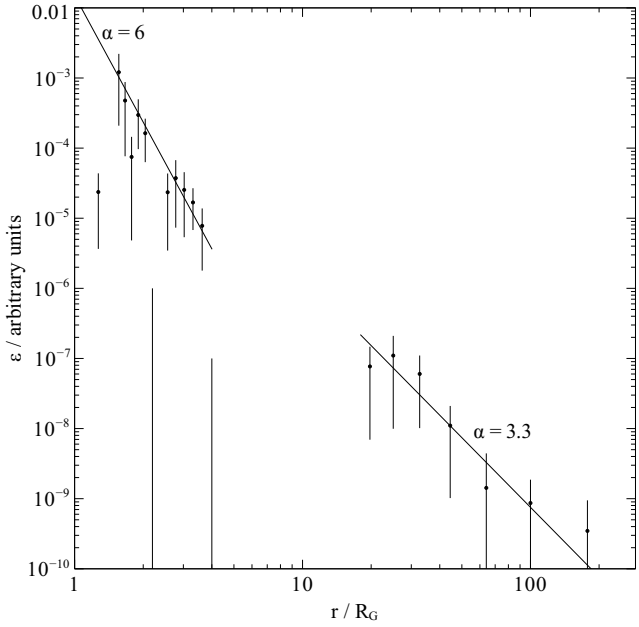

(a) 3-10 keV

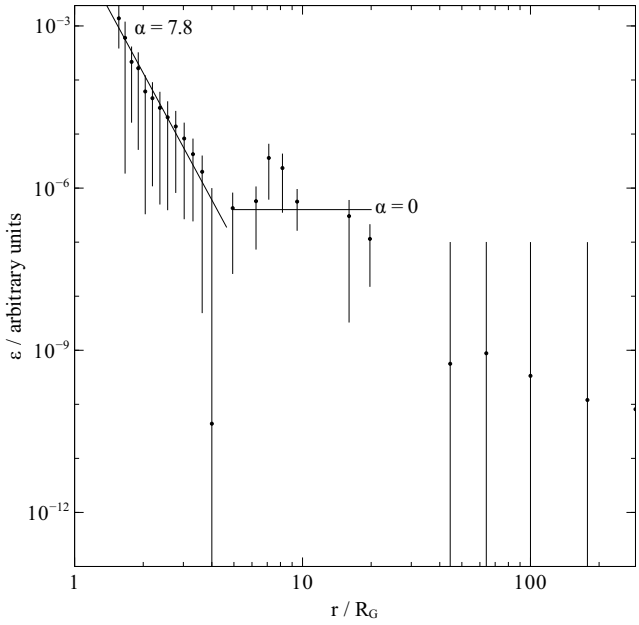

(b) 3-5 keV

Figure 4.4: Emissivity profile of 1H 0707-495 recovered from fitting to the spectrum in the energy ranges (a) 3-10 keV and (b) 3-5 keV. Error bars show 1σ confidence limits corresponding to $\Delta\chi^2 = 1$. Lines show power laws of index 6.0 and 3.3 in (a) and 7.8 for the inner disc as well as a flat profile, for reference, through the middle region in (b). In the 3-5 keV fit, error bars are large at radii beyond $30\,r_{\rm g}$ as emission in the iron Kα line from these radii is excluded from the fit range, so the points are unconstrained.

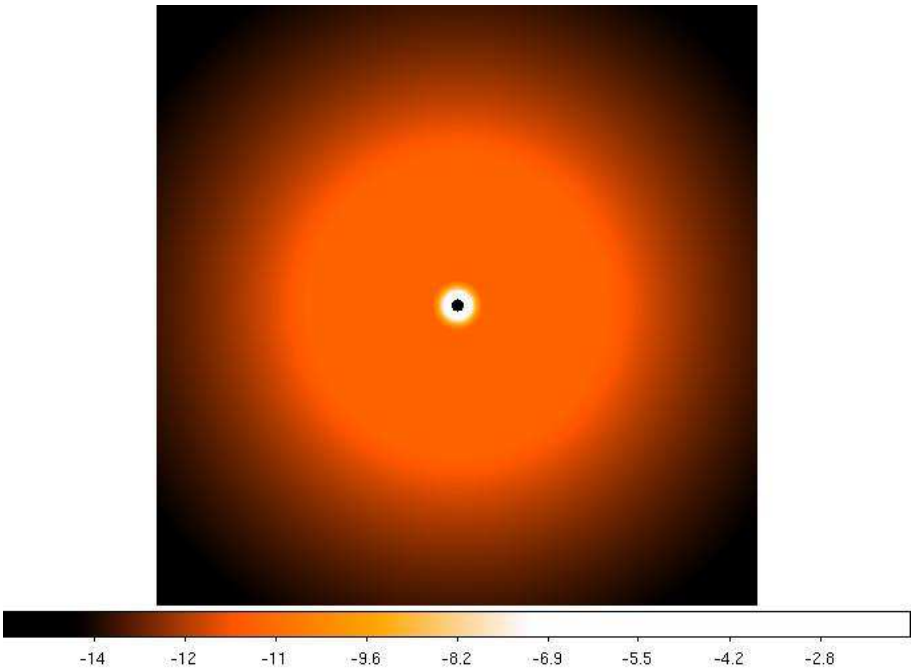

Figure 4.5: Pseudo-image of the inner regions of the accretion flow in 1H 0707-495 out to 60 $r_{\rm g}$ formed from the observed emissivity profile. Shading corresponds to reflected flux in the disc frame on a logarithmic scale.

binning than the LAOR model. Using RELCONV yields very much the same result as is obtained here. A couple of further data points are obtained in the flat 5-30 $r_{\rm g}$ region of the emissivity profile when performing the fit over the full 3-10 keV range consistent with the above result, however this region is still largely unconstrained until the 5-10 keV band is excluded from the fit. This indicates that this is not due to systematics in the LAOR model but is rather the masking of this region by the high flux from the outer disc in the observed spectrum.

4.4 Testing the Result

It is important to test these results for the emissivity profile, in particular the flattened region of the profile from 5 to 30 $r_{\rm g}$, by fitting one continuous reflection spectrum with the appropriate emissivity profile over the entire disc. It would appear from the above that the closest analytic form for the profile is a twice-broken power law.

In XSPEC, the emissivity profile of the disc is applied by the relativistic blurring kernel, KDBLUR (with a single, unbroken power law emissivity profile) or KDBLUR2 (once-broken power law), to the rest-frame reflection spectrum REFLIONX. The blurred spectrum is obtained by convolving the original spectrum with the profile of a relativistically broadened line (delta-function spectrum in the rest frame) from the LAOR or LAOR2 models.

Modified versions of these models were written to give a relativistically blurred reflection spectrum from the disc corresponding to a twice-broken power law emissivity profile: The model KDBLUR3, which provides the blurring kernel based upon the line profile LAOR3, with which XSPEC may convolve the rest frame spectrum. These models have the three power law indices and two break radii for the emissivity profile as input parameters.

The spectrum was fit in the region 3-10 keV (the iron Kα line, with no significant spectral components other than the power law continuum and reflection component) with the model

$$\mathrm{powerlaw} + \mathrm{kdblur3} \otimes \mathrm{reflionx} \tag{4.5}$$

with the power law indices and break radii of the emissivity profile fit as free parameters, within limits to constrain them to roughly the values observed (*i.e.* a steeper index tending to a moderate index, with a flat profile in the middle region) but sufficiently broad not to place any particular bias on the results. Other parameters of the models were again set to the best-fit values of Zoghbi et al. (2010). The results of this fit are shown in Table 4.2.

Table 4.3 shows this fit compared to an equivalent fit using only a once-broken power law as had been assumed in previous work in the analysis of the spectra.

Modelling the emissivity profile as a twice-broken power law fits the data substantially better than

Table 4.2: Fit to the emissivity profile of 1H 0707-495 (3-10 keV) using the KDBLUR3 model (twice-broken power law emissivity). Errors quoted are 1σ.

Parameter	**Fit Range**	**Value**
Index 1	2 – 12	$7.83^{+3.97}_{-0.66}$
Break radius 1	1.235 – 10 $r_{\rm g}$	$5.60^{+0.15}_{-0.48}\,r_{\rm g}$
Index 2	0 – 2	$7.84 \times 10^{-5}{}^{+0.38}_{-7.8\times10^{-5}}$
Break radius 2	5 – 400 $r_{\rm g}$	$34.75^{+4.42}_{-4.72}\,r_{\rm g}$
Index 3	1.5 – 10	$3.30^{+0.43}_{-0.32}$

Table 4.3: Comparison between fits to the iron Kα line (3-10 keV) of 1H 0707-495 using models with once- and twice-broken power law emissivity profiles (KDBLUR2 and KDBLUR3, respectively).

	kdblur2	**kdblur3**
Index 1	4.82	7.83
Break radius 1	6.85 $r_{\rm g}$	5.60 $r_{\rm g}$
Index 2	2.09	7.84×10^{-5}
Break radius 2	—	34.75 $r_{\rm g}$
Index 3	—	3.30
χ^2	287.52	264.32
χ^2/DoF	1.1144	1.0365

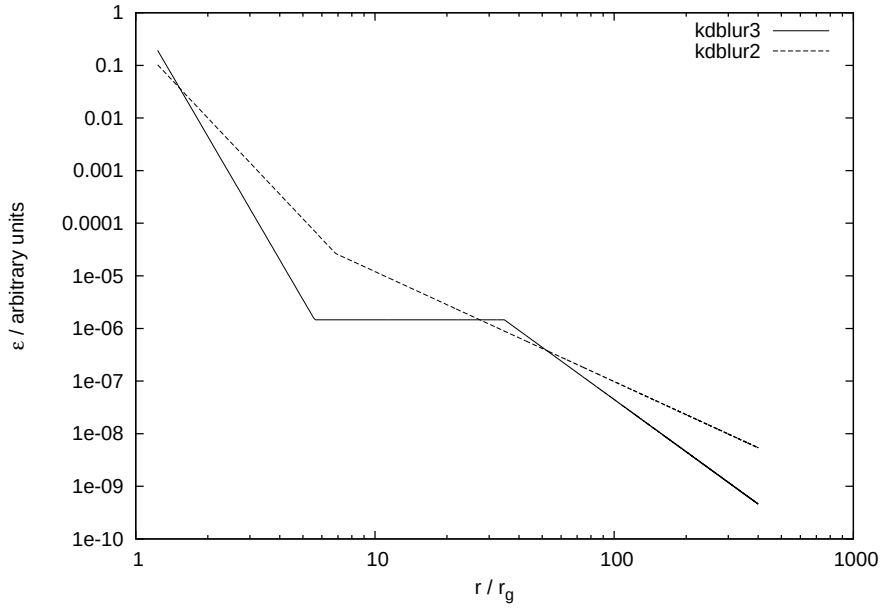

Figure 4.6: Comparison between the best fit emissivity profiles obtained for 1H 0707-495 using the KDBLUR3 ($\chi^2/\mathrm{DoF} = 1.037$) and KDBLUR2 ($\chi^2/\mathrm{DoF} = 1.114$) models.

using a once-broken power law, giving a reduction in χ^2 of 23.2 (a reduction from 1.11 per degree of freedom to 1.04 per degree of freedom). The best-fit parameters obtained using the KDBLUR3 model agree well with the emissivity profiles recovered from the sum of reflection components, with a power law index of 7.8 in the inner disc out to $5\,r_{\mathrm{g}}$ and flattening to a very low index of 8×10^{-5} from here to $35\,r_{\mathrm{g}}$ before tending to an index of 3.3 over the outer regions of the disc. The best fit emissivity profiles obtained using the KDBLUR3 and KDBLUR2 models are shown in Fig. 4.6.

The parameters are well constrained to these values by the 1σ confidence limits, with the exception of the index in the middle, flattened region, where the lower limit is not well constrained by the data but an upper limit of 0.4 is placed on the index here. Likewise, the lower limit of the power law index for the inner disc is found, yet the upper bound is less well constrained with a confidence limit of $+3.97$. This is likely due to the low flux received from the inner disc since photons originating from here are more likely to fall into the black hole, thus increasing the emission from the inner disc by steepening the emissivity profile will have less of an effect on the line profile detected at infinity.

The fits to the spectrum using the two models are shown in Fig. 4.7. The form of the edge between 6.5 and 7 keV is reproduced much better by the KDBLUR3 model than by KDBLUR2.

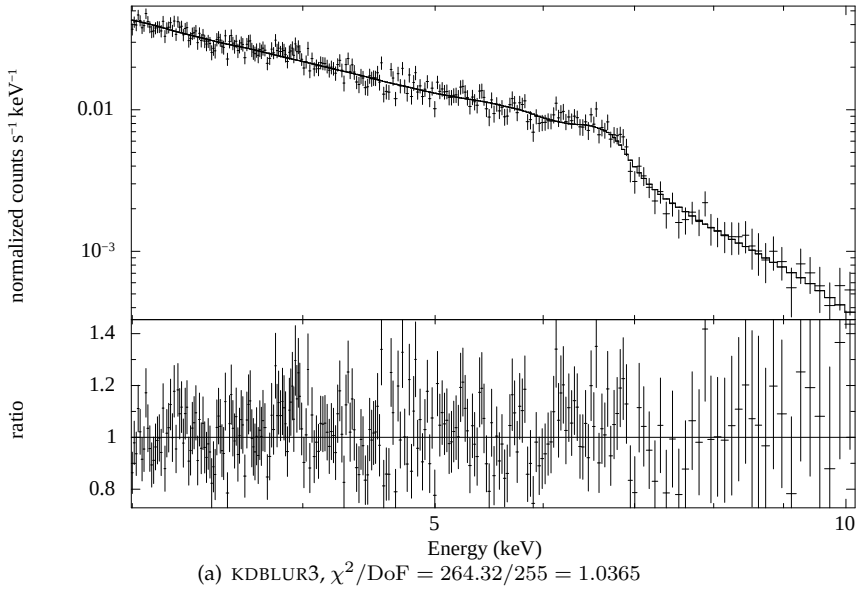

(a) KDBLUR3, $\chi^2/\mathrm{DoF} = 264.32/255 = 1.0365$

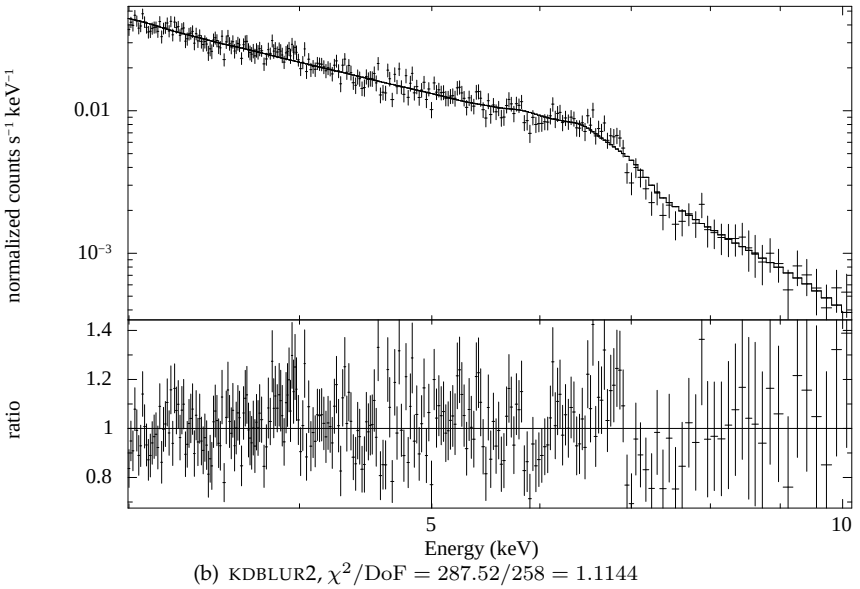

(b) KDBLUR2, $\chi^2/\mathrm{DoF} = 287.52/258 = 1.1144$

Figure 4.7: Best fits to the iron Kα edge of 1H 0707-495 using (a) twice-broken and (b) once-broken power law emissivity profiles (KDBLUR3 and KDBLUR2 respectively).

4.4.1 Further Spectral Components

Adding a narrow (Gaussian) line at 6.4 keV (fitting for the line width, σ, and photon count as free parameters) to account for X-ray emission from a more distant reflector from which relativistic blurring is not seen does not significantly improve the fit to the data. The reduced χ^2 changes to only 1.01 (compared with 1.03) when the emissivity profile is frozen at the values determined above. The flux in the narrow line is 100 times less than that seen in the broad line from the disc, indicating that this component is not significant. Allowing the parameters of the KBLUR3 emissivity profile to vary also in the fit yields a similar result with the observed emissivity profile not changing greatly (it is steepened slightly over the outer disc to compensate for the extra flux in the narrow line coinciding with energies from the outer disc, but the fit is not improved with a reduced χ^2 of 1.03).

Adding a second ionisation component in the disc (either simply adding a second component that is co-spatial with the first, or dividing the disc into two ionisation components for the inner and outer disc and fitting for the break point) does not improve the fit. The reduced χ^2 statistic is unchanged at 1.03 when the disc from $45\,r_{\rm g}$ outwards has the ionisation parameter reduced to $\xi = 28$ (while that in the inner disc is still found to be around $\xi = 53$). The best fit emissivity profile for the disc with two ionisation components is found to be essentially unchanged from the previous result using one component.

4.5 The Emissivity Profiles of Further Black Hole Accretion Discs

Following development of the method for measuring the emissivity profile of the accretion discs around black holes due to X-ray reflection from a power law continuum source in the corona, it was applied to the further X-ray sources; both AGN and accreting Galactic black holes.

4.5.1 IRAS 13224-3809

The X-ray source IRAS 13224-3809 is an accreting supermassive black hole in an AGN, with spectral characteristics very similar to 1H 0707-495. The X-ray spectrum is dominated by a power law continuum with strong reflection from the accretion discs with bright iron emission lines indicating an iron abundance around 13 times the Solar value (Fabian et al., 2013).

Parameters of the continuum and rest-frame reflection model used to find the emissivity profile, determined by fitting to entire spectrum over the 0.3-10.0 keV range using a single reflection component, are shown in Table 4.4 and the observed emissivity profile obtained by decomposing the reflection spectrum between 3.0 and 10.0 keV into the contributions from successive radii is shown

Table 4.4: Values of frozen model parameters used in the determination of the emissivity profile of the accretion disc in IRAS 13224-3809.

Component	Parameter	Value
powerlaw (PLC)	Photon index, Γ	2.82
	Photon count, *norm*	1.58×10^{-3}
kdblur (RDC)	Inclination, i	$64\,\mathrm{deg}$
reflionx (RDC)	Photon index, Γ	= `powerlaw:`Γ
	Iron abundance / solar	13.4
	Ionisation parameter, ξ	$336\,\mathrm{erg\,cm\,s^{-1}}$
	Redshift, z	6.58×10^{-2}

in Fig. 4.8.

The emissivity profile of the middle section of the accretion disc can be recovered by fitting to the spectrum over the energy band 4-10 keV instead of by fitting over the 3-5 keV band. Omitting the 3-4 keV range will exclude the reflection from the very innermost part of the accretion disc (here seen to be that within $2\,r_{\mathrm{g}}$ of the black hole), requiring the statistical contribution from the middle section of the disc to reproduce the observed emission line, while keeping the contribution from the outer parts of the accretion disc.

The emissivity profile of the accretion disc in IRAS 13224-3809 is qualitatively very similar to that in found in 1H 0707-495, with the reflected flux falling off steeply over the innermost regions of the disc, with a best-fitting power law index of around 8 out to a radius of 4 to $5\,r_{\mathrm{g}}$. The profile again flattens over the middle part of the disc, before turning over to a fall-off slightly steeper than r^{-3} over the outer part of the accretion disc, in this case at a radius of around 15-20 r_{g}.

4.5.2 MCG–6-30-15

Like 1H 0707-495 and IRAS 13224-3809, the Seyfert 1 galaxy MCG–6-30-15 shows a strong, relativistically broadened iron Kα emission line at 6.4 keV (Tanaka et al., 1995). In contrast to 1H 0707-495 and IRAS 13224-3809 however, the X-ray emission from MCG–6-30-15 is obscured by a complex system of absorbers.

Chiang & Fabian (2011) show that is is possible to explain the X-ray spectrum from 0.5 to 20 keV using data obtained with XMM-Newton, Chandra, Suzaku and Beppo-SAX as arising from the reflection of a power law continuum spectrum from the accretion disc, obscured by three or four systems of absorbing material, all completely covering the source. Most notably, there is a highly ionised fast outflow of material, imprinting blueshifted absorption lines on the observed spectrum. The absorber models of Chiang & Fabian (2011) are computed using the radiative transfer code XS-

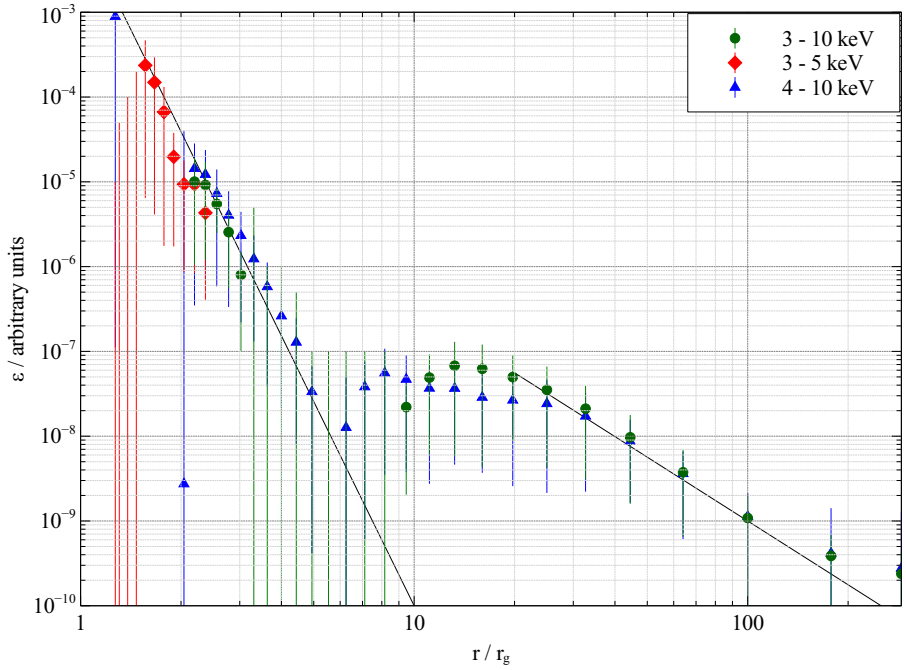

Figure 4.8: The emissivity profile of the accretion disc in the narrow line Seyfert 1 galaxy, IRAS 13224-3809 obtained by fitting to the profile of the iron Kα emission line in the energy ranges 3.0-10.0 keV, 4.0-10.0 keV and 3.0-5.0 keV.

TAR and fit to the observed spectra, including the energies and equivalent widths of absorption and emission lines detected using the high resolution reflection grating spectrometer (RGS) on XMM Newton and the medium and high energy transmission grating (METG and HETG) spectrometers of Chandra.

These absorption models were applied to power law continuum emission as well as its unblurred reflection detected from distant material and relativistically blurred reflection from the accretion disc with parameters as shown in Table 4.5. Parameters of the absorbers (their abundances, ionisation states, velocities and column densities) as well as the narrow iron Kα line and reflection from distant material were frozen at the best-fit values for the high resolution grating spectra found by Chiang & Fabian (2011), since when the constraints of high resolution spectra are not applied to the absorbers, at significant column densities they can change the shape of the spectrum around 3 keV and thus skew the emissivity profile determined for the reflected iron Kα line. The emissivity profile was then determined by fitting the relativistically blurred contributions from successive radii in the accretion disc to the remaining reflection spectrum recorded from three orbits (totalling 250 ks) using the EPIC pn detector and is shown in Fig. 4.9.

While the lower iron abundance, hence the weaker emission line, combined with the affect of the

Table 4.5: Values of frozen parameters of the continuum and reflection models used in the determination of the emissivity profile of the accretion disc in MCG–6-30-15.

Component	**Parameter**	**Value**
powerlaw (PLC)	Photon index, Γ	1.99
	Photon count, *norm*	1.33×10^{-2}
kdblur (RDC)	Inclination, i	$33.5\,\mathrm{deg}$
Relativistically blurred reflionx (RDC)	Photon index, Γ	= `powerlaw:`Γ
	Iron abundance / solar	1.45
	Ionisation parameter, ξ	$523\,\mathrm{erg\,cm\,s^{-1}}$
	Redshift, z	7.75×10^{-3}
Distant, unblurred reflionx (RDC)	Photon index, Γ	= `powerlaw:`Γ
	Iron abundance / solar	1.45
	Ionisation parameter, ξ	$1\,\mathrm{erg\,cm\,s^{-1}}$
	Redshift, z	7.75×10^{-3}

X-ray absorption up to around 4 keV mean the emissivity profile is not constrained so well as it was in 1H 0707-495 and IRAS 13224-2809, the results are again consistent with an emissivity profile falling off steeply over the inner part of the accretion disc with a power law index of ~ 8.5 before flattening over the middle part of the accretion disc and finally turning over to a fall-off approximately following r^{-3} at a radius of $10\,r_\mathrm{g}$. This emissivity profile is affirmed by fitting a twice-broken power law to the emissivity using the KDBLUR3 convolution kernel, finding an outer break radius of $9 \pm 2\,r_\mathrm{g}$.

4.5.3 Cygnus X-1

As well as AGN, relativistically blurred emission lines are detected from the accretion discs around stellar mass black holes in Galactic X-ray binaries, including Cygnus X-1. Analogous to an AGN, the X-ray spectrum from an X-ray binary consists of a power law continuum emitted from a corona of energetic particles around the black hole and the reflection of this emission from the accretion disc. Compared to AGN, however, the temperatures of the accretion discs in Galactic X-ray binaries are around a factor of ten hotter, peaking above 1 keV in the X-ray spectrum, due to their smaller size (Novikov & Thorne, 1973) and unblurred reflection, particularly a narrow iron Kα emission line at 6.4 keV is seen from the surface of the companion star.

The emissivity profile of the accretion disc is, again, determined by fitting a model to the spectrum in the region of the iron Kα emission line although, in addition, a narrow (Gaussian) emission line is included at 6.4 keV corresponding to the iron Kα line in the X-ray reflection spectrum from the surface of the companion star also illuminated by the X-ray continuum from around the black hole.

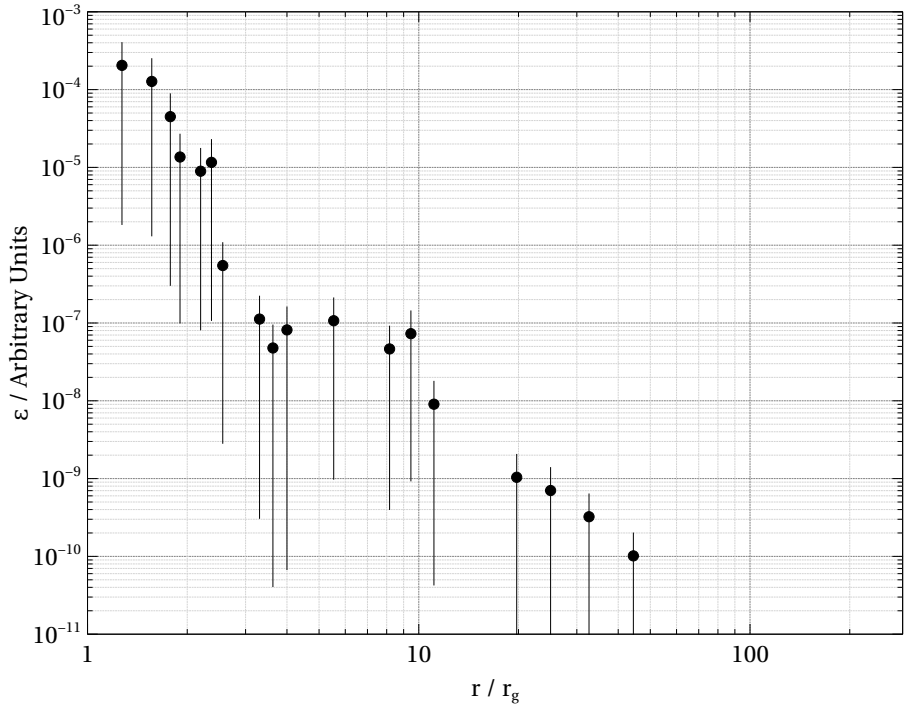

Figure 4.9: The emissivity profile of the accretion disc in MCG–6-30-15 obtained by fitting to the spectrum obtained with the EPIC pn instrument on XMM Newton in the energy range 3-5 keV (hence the outer part of the accretion disc, $r > 20\,r_{\rm g}$, is unconstrained).

The emissivity profile is not affected by the inclusion of the pseudo-black body thermal emission from the accretion disc in the spectral model as this does not extent to high enough energies to overlap with the relativistically broadened iron Kα emission line, however failure to include the narrow emission line results in the emissivity profile dropping to a sharp narrow trough at around $5\,r_{\rm g}$ as the emissivity profile adjusts to bets reproduce the narrow emission feature on top of the broad line. Fig 4.10 shows the emissivity profile obtained for the accretion disc in Cygnus X-1, using a spectrum obtained during a 13 ks observation using the XIS instrument on board Suzaku.

As for the accretion discs in AGN, the emissivity profile falls off steeply over the inner parts of the accretion disc, in this case following the relation r^{-8}, though turns over to r^{-3} much closer to the centre a radius of around $5\,r_{\rm g}$. There is evidence for a slight flattening of the profile with power law index $q < 3$ in the region $3 \sim 5\,r_{\rm g}$.

Reflection from the accretion disc is detected from radii as small as $1.5\,r_{\rm g}$, implying the accretion disc extends down to this radius and hence the innermost stable orbit around the black hole lies at a radius less than $1.5\,r_{\rm g}$. Such a small radius of the innermost stable circular orbit requires the spin of the black hole, $a > 0.98$.

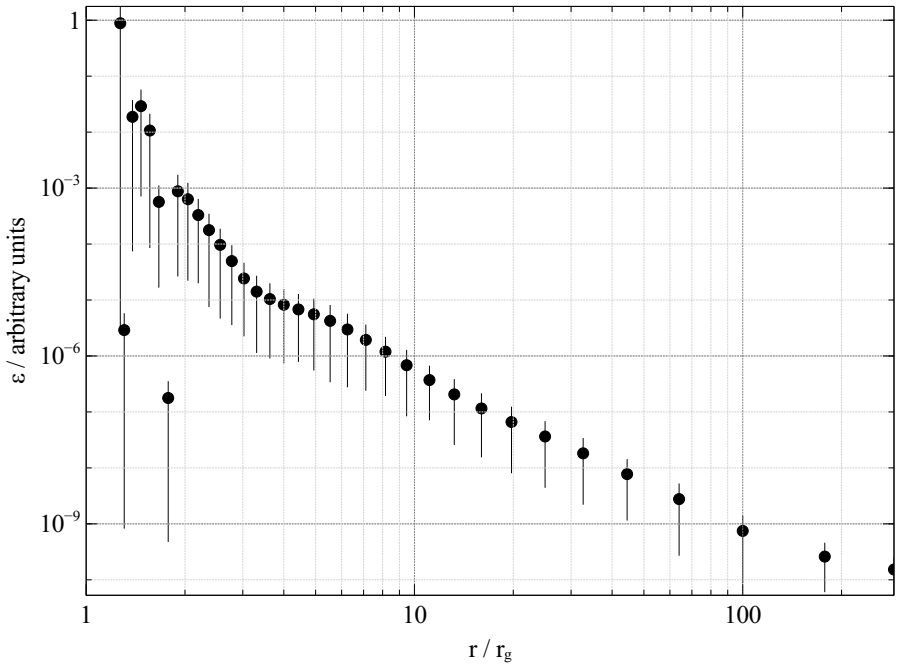

Figure 4.10: The emissivity profile of the accretion disc in the Galactic black hole binary Cygnus X-1 obtained by fitting to the profile of the broadened iron Kα emission line detected by the XIS instrument on Suzaku in the energy range 3.0-10.0 keV, accounting for the narrow iron Kα line seen from the reflection of X-rays from the surface of the companion star.

4.6 The Effect of the Length of Observation

It is useful to understand the quality of data that is required in order to recover the emissivity profile of the accretion disc by decomposing the reflection spectrum into contributions from successive radii in the accretion disc. Clearly the emission line that is used must be clearly detected above the errors in the surrounding continuum and the detection of the emission line will become more significant in spectra including more counts from longer observations.

Fig 4.11 shows the emissivity profile that is obtained for the accretion disc in 1H 0707-495 using the data from one, two, three and four orbits (with each orbit giving around 120 ks of exposure) compared to the full four orbits used originally.

We see that finding the emissivity profile by fitting the decomposed reflection spectrum to the 3-10 keV energy band yields consistent results when as few as two orbits with XMM Newton (240 ks) are used, however looking at the emissivity profiles from the 3-5 keV energy band, we see that reducing the exposure time to two orbits causes the middle parts of the accretion disc to be less well constrained, with two data points detected anomalously low between 4 and 9 $r_{\rm g}$. Finally, reducing

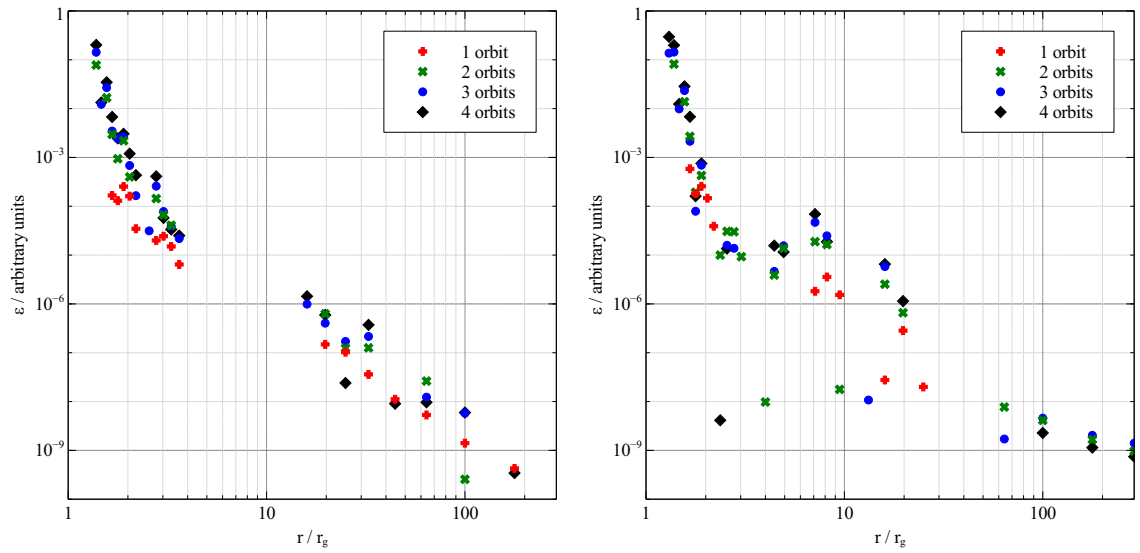

(a) 3-10 keV (b) 3-5 keV

Figure 4.11: The emissivity profiles obtained for 1H 0707-495 using the data from one, two, three and four orbits, fitting to the reflection spectrum in the (a) 3-10 keV and (b) 3-5 keV energy bands.

the exposure time to one orbit (120 ks) means that the emissivity profile is not well measured, with emission from the innermost parts of the disc (within $2\,r_{\rm g}$ of the black hole) as well as the middle region and outer break point at $20 \sim 30\,r_{\rm g}$ not being well reproduced.

The possibility of recovering the emissivity profile from the iron Kα line with varying exposure times can be understood in terms of the quality of the detection of this emission line. The significance of the detection can be quantified by fitting the emission line as a single relativistically broadened emission line (using the LAOR model) on top of the power law continuum spectrum. The normalisation of this component is compared to its own standard deviation, σ, computed by reducing the normalisation until the value of χ^2 characterising the goodness of fit the model gives to the spectrum is increased by $\Delta\chi^2 = 1$. We find that the normalisation of the emission line has reduced to 27σ in the spectrum taken from two orbits, from 42σ when data from all four orbits are used. We therefore conclude that the relativistically broadened emission line should be detected with greater than 27σ significance in order to find the emissivity profile of the accretion disc by fitting the contributions to the reflection spectrum from successive radii.

4.7 Dependence on Other Parameters

In determining the emissivity profile of the accretion disc, a number of properties of the both the black hole and reflecting material in the accretion disc were pre-determined through preliminary fitting to the X-ray spectrum as a whole, using a single relativistically-blurred emission spectrum over the whole disc with a power-law emissivity profile. These properties include the spin of the black hole and inclination of the accretion disc to the line of sight as well as the metallicity and ionisation state of the reflecting material and their values when fitting reflection from successive annuli were frozen at the values determined in the preliminary fits.

Each of these parameters affects the reflection spectrum (either the intrinsic reflection spectrum of the disc material or the relativistic blurring as seen by an external observer) and the assumed value may influence the emissivity profile that is found for the accretion disc. If the emissivity profile is to be used to infer the intrinsic properties of the X-ray source, it is important to understand how each of these parameters and errors therein affect the measured emissivity profile.

In order to test the effects of these parameters on the measured emissivity profile, a synthetic spectrum was constructed, taking a model for the X-ray emission from 1H 0707-495, consisting of a power law continuum and reflection from the accretion disc with the twice-broken power law emissivity profile determined previously as well as the parameters of the reflection spectrum as shown in Table 4.1, folded through the response of the EPIC pn detector on XMM Newton for a 500 ks observation (including the effect of counting statistics on the errors in the observation). The real emissivity profile is known, though is also measured as it would be for a real observation, but assuming incorrect values for various parameters, allowing the robustness of the method to be tested.

4.7.1 The Spin of the Black Hole

While the profiles of emission lines originating from annuli in the accretion disc are calculated using the LAOR model and thus implicitly assume a maximally spinning Kerr metric ($a = 0.998$), the profile of the line from any given annulus does not vary significantly with the spin parameter. This can be demonstrated by computing line profiles outwards of $6\,r_{\mathrm{g}}$ (*i.e.* the innermost stable orbit of a non-spinning, Schwarzschild black hole) for varying values of the spin parameter using a relativistic emission line model such as RELLINE (Dauser et al., 2010) which includes the black hole spin as a variable parameter.

The effect of varying the spin parameter is to move the innermost stable orbit, defining the innermost possible extent of the accretion disc and thus the extremal gravitational redshift, as illustrated in Figure 4.12. As each annulus is considered independently, varying the black hole spin will de-

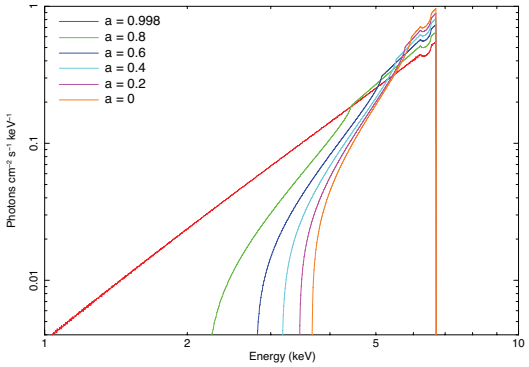

(a) $r_{\mathrm{ISCO}} < r < 400 r_{\mathrm{g}}$

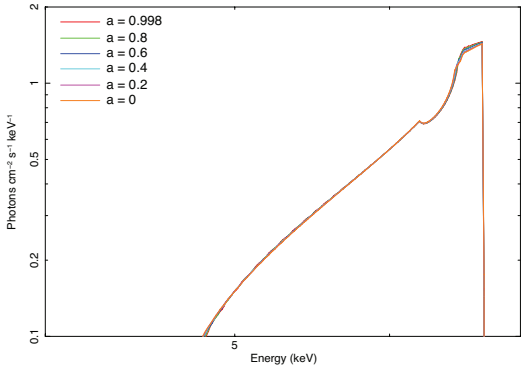

(b) $10 r_{\mathrm{g}} < r < 400 r_{\mathrm{g}}$

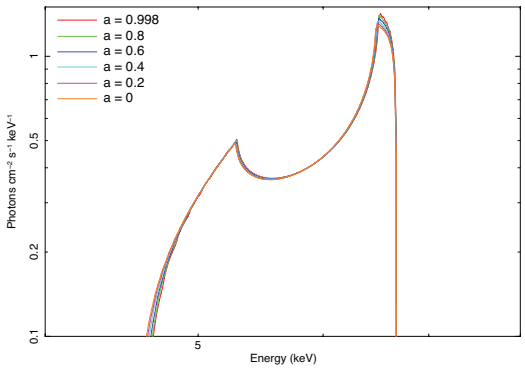

(c) $10 r_{\mathrm{g}} < r < 20 r_{\mathrm{g}}$

Figure 4.12: Theoretical line profiles for varying values of the black hole spin parameter, a, calculated using the RELLINE model. (a) shows emission lines emitted from a region of the disc extending from the relevant innermost stable orbit (ISCO) for the value of a out to 400 r_{g}, with the extended redshifted wing of the line for higher values of a resulting from the accretion disc (and thus emission) extending down to an ISCO closer to the black hole. (b) and (c), showing lines emitted from the regions of the disc 10-400 r_{g} and 10-20 r_{g} respectively, demonstrate that the effect of the spin on the emission from a given radius is small. The effect of spin decreases in significance further from the black hole.

termine whether contributions are detected from the inner annuli whose existence depends on the location of the ISCO. As such, the spin of the black hole will not affect the determined emissivity profile for the outer disc and the inference of emission from regions of the disc down to $1.235\,r_{\rm g}$ implies a spin of the black hole close to maximal.

If the emissivity profile can be determined by fitting to the reflection spectrum in this way, it provides a means of measuring the spin of the black hole that is not biased by the emissivity profile assumed for the accretion disc. Finding the spin of the black hole by fitting for the inner edge of the accretion disc in the computation of the entire relativistic line profile can be biased by an incorrect emissivity profile. For instance, if the emissivity of the inner parts of the disc were to be overestimated, fitting to the profile of the emission line will tend to shift the inner radius of the accretion disc outwards in attempt to reduce the emission seen from the inner disc relative to the outer parts to better match the observed spectrum and thus will underestimate the spin of the black hole. We see, however, that the emissivity profile falls off steeply over the inner parts of the accretion disc, so a conservative emissivity profile, r^{-3} as is typically used (*e.g.* Brenneman & Reynolds, 2006) will not adversely affect the result in this way.

4.7.2 Iron Abundance

Given that the emissivity profile of the accretion disc is determined from the profile of the relativistically broadened iron Kα emission line, it is conceivable that the assumed iron abundance in the reflector will affect the measured emissivity. When fitting to the spectrum in the energy band 3-10 keV, there are two key spectral features. The Kα emission line around 6.4 keV and the corresponding absorption at 7.1 keV. Fig. 4.13 shows the reflection spectra of accretion discs with increasing abundances of iron.

Increasing the iron abundance produces a stronger emission line as well as a deeper absorption trough, though the overall shape of the spectrum between 3 and 10 keV is not altered. As such, a change in the iron abundance is manifested as a change in overall normalisation of the reflected component of the spectrum and the shape of the emissivity profile (which is of interest in determining the properties of the X-ray source) is not affected, as demonstrated in Fig. 4.14.

Attempting to recover the emissivity profile of the synthetic spectrum assuming different iron abundances does not affect the overall shape of the emissivity profile that is obtained, though as the iron abundance is reduced, the weaker iron emission line means the emissivity profile is less well constrained, particularly over the middle part of the accretion disc between radii of 4 and $20\,r_{\rm g}$ (previously found to be the least well constrained) where it can be seen that some of the data points are lost. This is particularly notable when the spectrum is fit in the energy range 3-5 keV in order to reveal the structure of the emissivity profile on the middle part of the disc. There are clearly fewer photons detected in the range 3-5 keV than in the range 3-10 keV and reducing the (assumed) iron

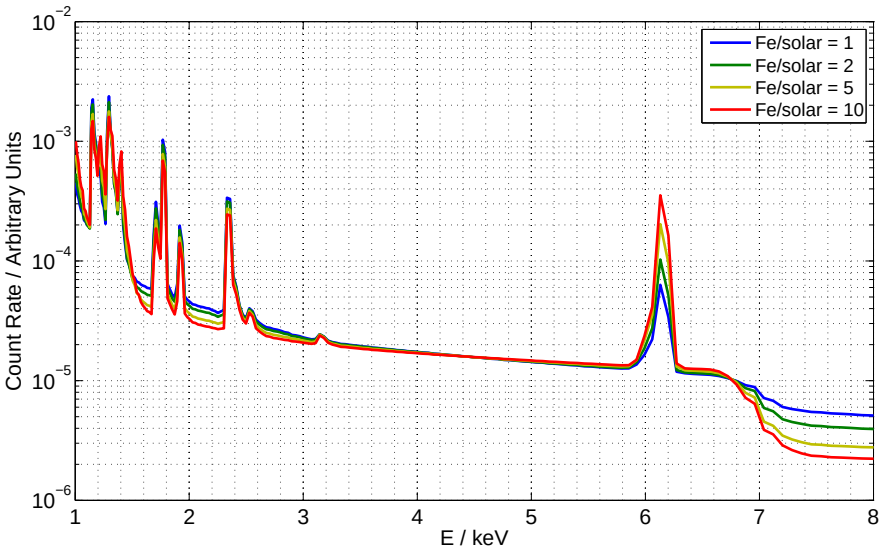

Figure 4.13: The reflection spectrum of the material in the accretion disc measured in the rest frame of the reflecting material (computed by the REFLIONX code) for varying iron abundances. All other elements are taken to be at the solar abundance. The spectrum is computed for the redshift of 1H 0707-495, $z = 4.11 \times 10^{-2}$.

abundance to merely the solar value results on there being no constraint on the emissivity profile at all. The smooth curve seen in this case is simply the inverse of the projected area of each annulus (obtained from the relativistic blurring model), since when there are not enough photons detected to constrain the emissivity profile of only the redshifted wing of the emission line, the best fit found to the data is when each annulus contributes equally to the observed reflection spectrum, though this is easily noticed since the observed emissivity profile in the 3-5 keV band is not consistent with that in the 3-10 keV band in this case.

The robustness of the determined emissivity profile with respect to the assumed iron abundance is demonstrated in the confidence contours between the iron abundance and the radius of the outer break point of the twice-broken power law emissivity profile for 1H 0707-495, shown in Fig. 4.15. In this case, the outer break point is taken as a representative parameter for the emissivity profile as we shall see in Chapter 6 that this radius can be used to infer the extent of the coronal X-ray source (though all three slopes and both break points are free parameters here). There is no correlation between the parameters in the confidence contours. The lower limit to the iron abundance is constrained by the ratio of the emission line to the underlying continuum in the observed spectrum. In this fit, the upper limit is not constrained because only the 3-10 keV energy band is used. The upper limit to the iron abundance is found when additional constraints are imposed by the iron L emission line around 0.9 keV.

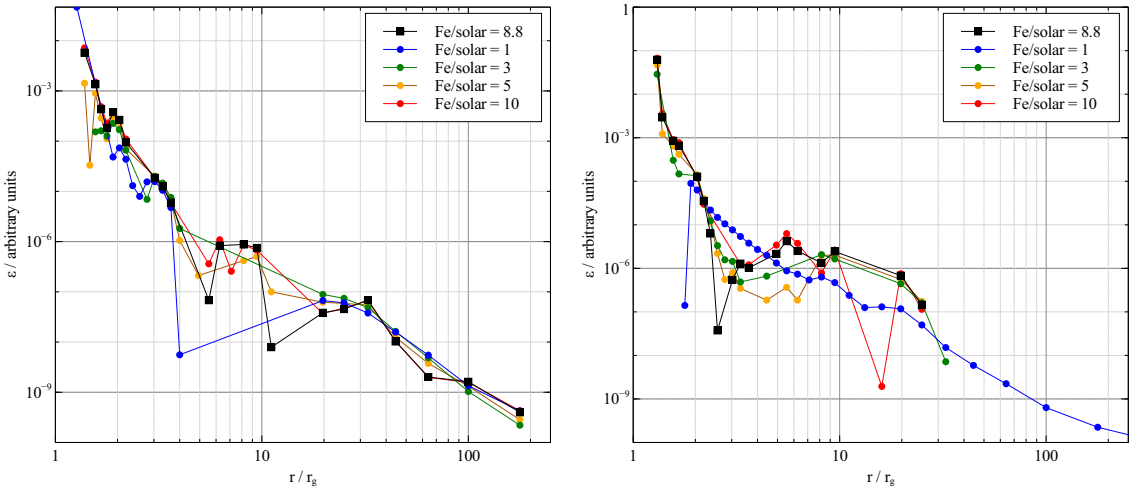

(a) 3-10 keV (b) 3-5 keV

Figure 4.14: The results of fitting for the emissivity profile of the synthetic spectrum assuming different abundances of iron (relative to the solar abundance) in the accretion disc, ξ, fitting over the energy range (a) 3-10 keV and (b) 3-5 keV. The real iron abundance is 8.8 times the solar value, shown in black. Plots are illustrative. Data points are joined by lines to aid the reader in comparing the different values of the iron abundance though points with a large degree of scatter such that they are outside the axes are omitted. Deviation from the black line indicates errors in the recovered emissivity profile.

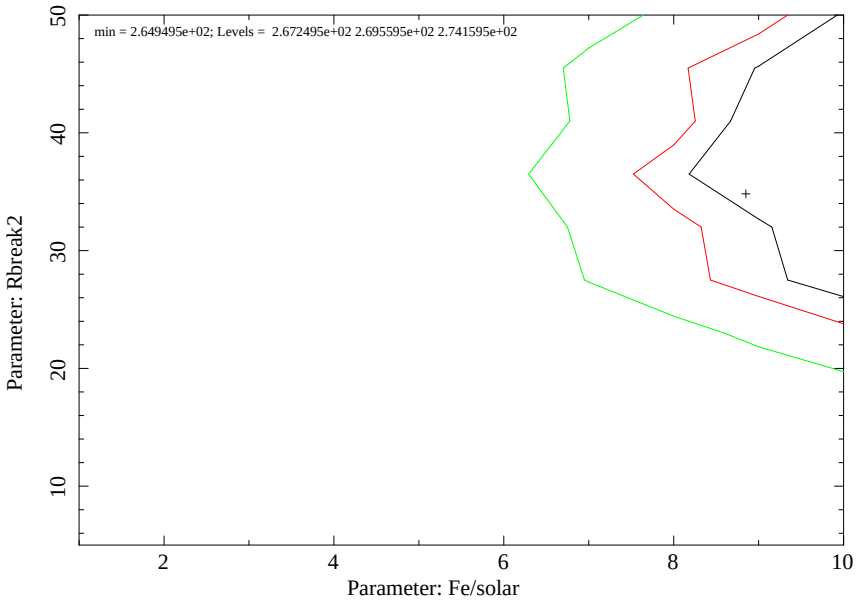

Figure 4.15: Confidence contours between the assumed iron abundance and the radius of the outer break point of the twice-broken power law emissivity profile for 1H 0707-495 in the energy band 3-10 keV. The best fit values are marked with a cross. The REFLIONX model extends only as far as an iron abundance of 10 times the solar value.

It is interesting to note here that sources with a naturally higher iron abundance are better candidates for determination of the accretion disc emissivity profile. The reflection spectra will show stronger emission lines with an improved signal to noise ratio, providing better statistical constraints on the relative contributions of successive parts of the accretion disc to the observed spectrum.

4.7.3 Ionisation

The material in the accretion disc will be ionised by the incident X-ray flux. The ionisation state of the material is characterised by the ionisation parameter, defined as $\xi \equiv \frac{4\pi F}{n}$, where F is the incident ionising flux and n the number density of hydrogen. The ionisation state of the material making up the accretion disc will again affect the reflection spectrum to which the emissivity profile is fit.

Fig. 4.16 shows the effect of the assumed ionisation parameter on the recovered emissivity profile. Underestimating the ionisation of the reflecting material in the accretion disc, while changing the overall normalisation of the emissivity profile, does not affect the shape of the emissivity profile that is recovered (which is of interest in inferring properties of the X-ray source). Even overestimating

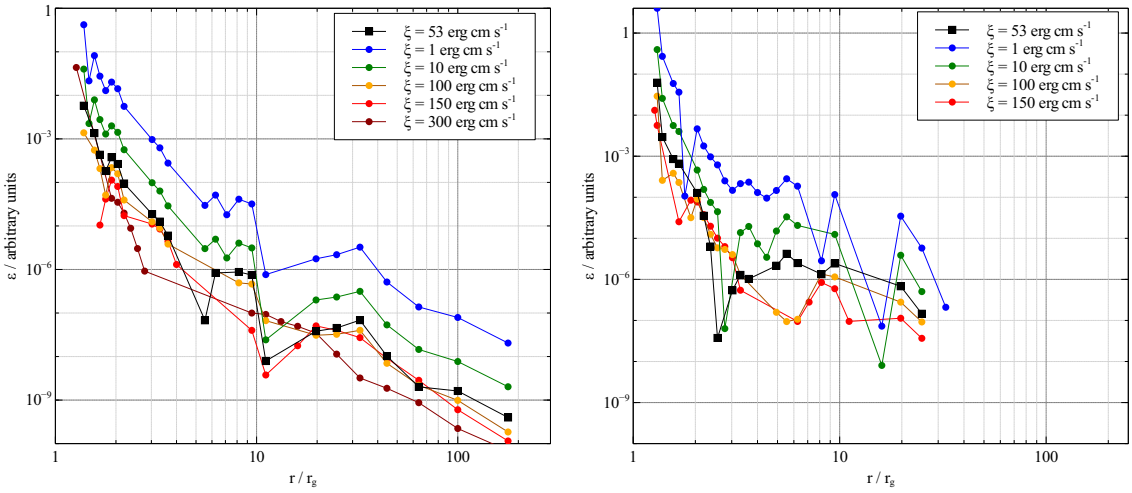

(a) 3-10 keV

(b) 3-5 keV

Figure 4.16: The results of fitting for the emissivity profile of the synthetic spectrum assuming different values of the ionisation parameter of the material in the accretion disc, ξ, fitting over the energy range (a) 3-10 keV and (b) 3-5 keV. The real value of ξ is $53\,\mathrm{erg\,cm\,s^{-1}}$, shown in black. Plots are illustrative. Data points are joined by lines to aid the reader in comparing the different values of ξ though points with a large degree of scatter such that they are outside the axes are omitted. Deviation from the shape of the black line indicates errors in the recovered emissivity profile.

the ionisation of the accretion disc by as much as a factor of three in this relatively low ionisation state , such that $\xi < 150\,\mathrm{erg\,cm\,s^{-1}}$ does not change the shape of the measured emissivity profile, though the emissivity profile is becoming less well constrained as the assumed ionisation parameter is increased with the contribution from annuli in the middle parts of the accretion disc between radii of 3 and $10\,r_\mathrm{g}$ not being well determined.

This can be understood in the context of the changes to the intrinsic reflection spectrum from material with an increasing ionisation parameter shown in Fig. 4.16. As the ionisation state of the material increases, the number of more highly ionised species, including FeXVII to FeXXIII is increased relative to the number of lesser-ionised species. These ions have a vacancy in the M shell, meaning the L shell is able to absorb the emitted iron Kα photons, causing the emission line to become weaker when $\xi > 100\,\mathrm{erg\,cm\,s^{-1}}$. The weaker emission line means the observed spectrum becomes less sensitive to the emissivity profile (hence at higher ionisation states, the contributions from fewer annuli in the disc are well constrained). Once $\xi > 500\,\mathrm{erg\,cm\,s^{-1}}$, the emissivity profile will not be recovered, since the hydrogenic and helium-like iron will display iron Kα lines at 6.97 and 6.67 keV, thus the fitting procedure will be attempting to fit the profile of an emission line at the wrong energy.

As well as the diminishing emission line, increasing the ionisation state of the reflecting material shifts the energy of iron K absorption feature around 7.1 keV to higher energies as more energy is required to eject the K shell electrons from more highly ionised atoms. While this shift changes the shape of the reflection spectrum, it is less important in determining the emissivity profile of the accretion disc since the emissivity is determined by fitting the contributions of the reflection from successive annuli in the disc to minimise the χ^2 statistic. The value of χ^2 is dominated by parts of the spectrum in which the signal is stronger relative to the error (assuming Poisson counting statistics for the errors on the number of photons detected in each energy channel), so will therefore depend more upon the emission line (an excess in detected photons) than an absorption feature (a decrement in the detected photons). In addition, the change in shape of the absorption feature with increasing ionisation parameter becomes less pronounced when considering the blurred reflection spectrum that has been integrated over the whole accretion disc, accounting for relativistic effects (Fig. 4.18), so the change in shape of this feature does not greatly affect the determination of the emissivity profile from the observed reflection spectrum.

Fig. 4.19 shows the confidence contours between the ionisation parameter of the accretion disc against the radius of the outer break point in the emissivity profile and it again can be seen that there is no correlation between these two parameters in the range that satisfies the data. In this case, a lower limit to the ionisation parameter is not found from the observed spectrum between 3 and 10 keV, though this can be determined by including the region of the spectrum below 1 keV since this will provide further constraints through a large number of emission lines, including the L line of iron and those of oxygen, though here we are only interested in the effect of the ionisation parameter on the measured emissivity profile.

Like sources with high iron abundances, this method to determine accretion disc emissivity profiles favours sources with discs in relatively low ionisation states (specifically $\xi < 150\,\mathrm{erg\,cm\,s^{-1}}$), since these will display the strongest broadened emission lines to fit the profile to. That is not to say, however, that it is impossibe to determine the emissivity profiles of more highly ionised accretion discs as we see from the spectrum of IRAS 13224-3809 with a best-fitting ionisation parameter of around $300\,\mathrm{erg\,cm\,s^{-1}}$.

It should also be noted that the ionisation parameter is assumed to be constant across the entire accretion disc. In reality, this is unlikely to be the case; if the X-ray source is located above the central parts of the accretion disc, those parts further out will be illuminated by less X-ray flux and thus will be less highly ionised. We see from Fig. 4.16 that underestimating the ionisation state of the reflector, while maintaining the shape of the emissivity profile, shifts the normalisations of the annuli in the accretion disc to higher values. Assuming a constant ionisation parameter over the whole accretion disc will select an average value to best fit the reflection spectrum from the entire disc and if the ionisation is greater than the average on the inner parts of the disc, the emissivity will be overestimated in this region. This will mean the measured emissivity profile will fall off

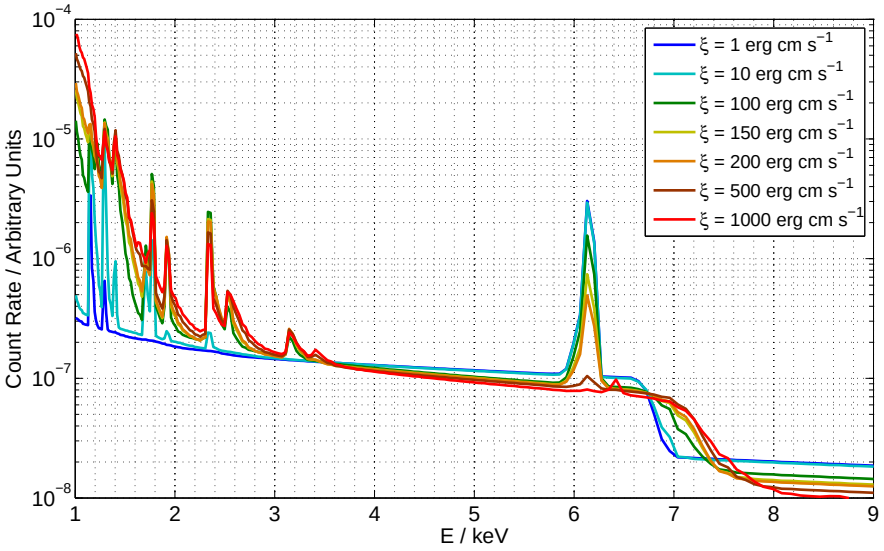

(a)

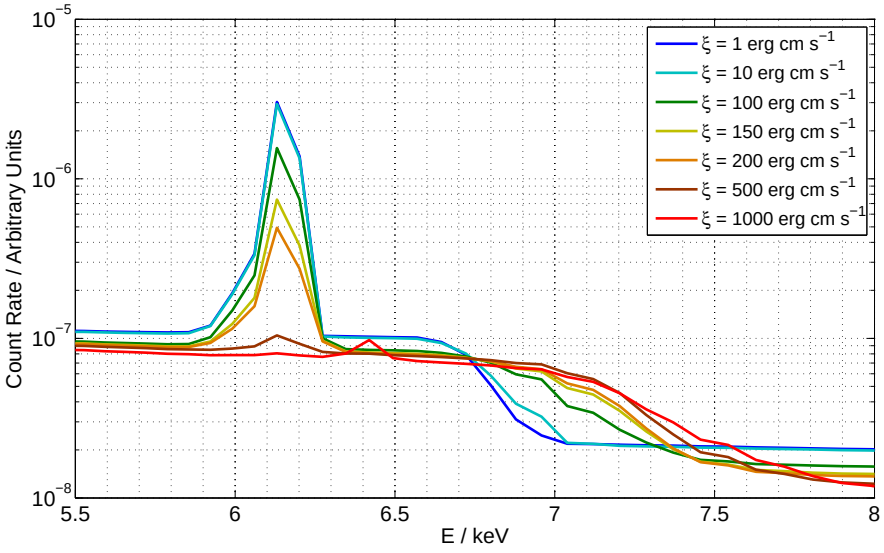

(b)

Figure 4.17: (a) The rest-frame reflection spectrum of the material in the accretion disc for varying ionisation parameter, $\xi \equiv \frac{4\pi F}{n}$ and (b) zoom-in on the iron K absorption and emission region of the spectrum.

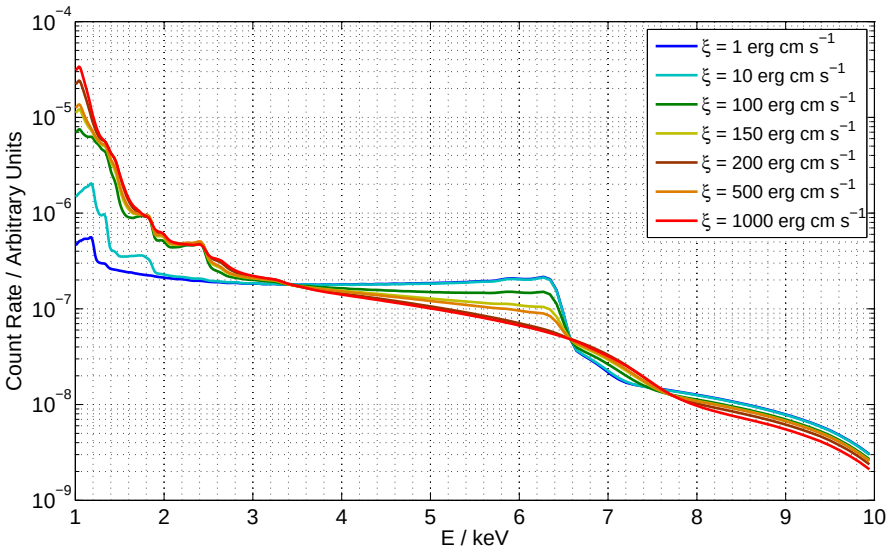

Figure 4.18: The relativistically blurred reflection spectrum observed from the orbiting material in the accretion disc by an observer at infinity with varying ionisation parameter. The emissivity profile of the disc is taken to fall off as r^{-3} in each case.

more steeply over the inner parts of the accretion disc. Svoboda et al. (2012) explore the effect of such a gradient in ionisation parameter, assuming illumination of a constant-density disc by a point source above the black hole, though rather than determining the emissivity profile directly, they fit a once-broken power law emissivity profile over the surface of the accretion disc.

They indeed find that assuming a constant ionisation parameter overestimates the emissivity of the inner accretion disc by 5 to 10 per cent, within around $13\,r_{\mathrm{g}}$ of the black hole. This means that while the emissivity profiles determined here are robust over the outer part of the accretion disc, it is possible that the power law slope over the inner accretion disc is not quite as steep as r^{-8}, though it is still much steeper than the classical r^{-3} fall-off. It should be noted, however, that the computations of Svoboda et al. (2012) assume a constant-density reflector. In reality, it is difficult to compute accurately how the ionisation parameter will vary across the disc, because while the illuminating flux can, in principle, be computed for an X-ray source in a curved spacetime, the density structure of the accretion disc is unknown. Rather than following the fairly simple density profile of Novikov & Thorne (1973) for material in relativistic circular orbits in the Kerr spacetime, it is likely that the energetics of the accretion disc are magnetically dominated, particularly if magnetic field lines anchored to the accretion disc give rise to a 'disc corona.' Further more, Fabian et al. (2013) find evidence for two cospatial reflectors in the accretion disc in the X-ray spectrum of IRAS 13224-3809 with different ionisation parameters, suggesting that the accretion disc may have a complicated, perhaps 'clumpy' density structure.

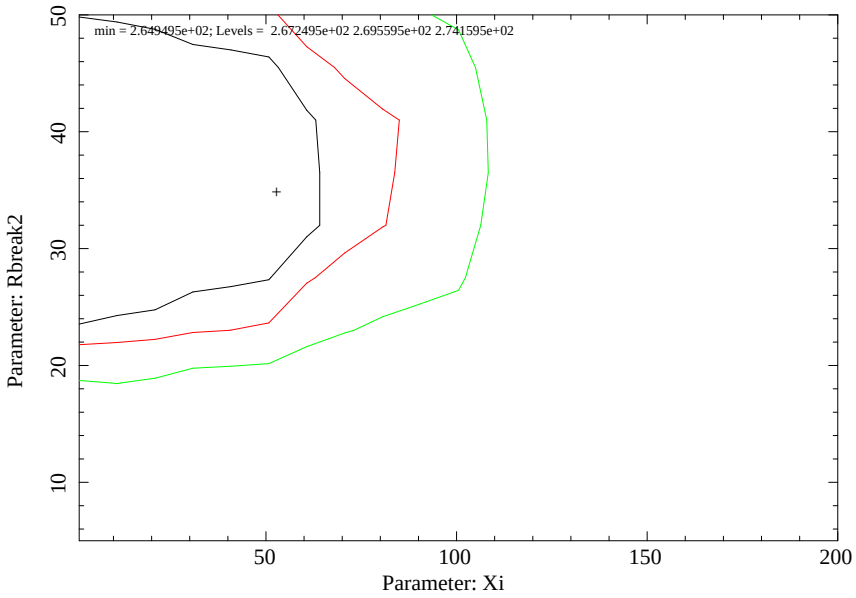

Figure 4.19: Confidence contours between the assumed ionisation parameter, ξ, and the radius of the outer break point of the twice-broken power law emissivity profile for 1H 0707-495 in the energy band 3-10 keV. The best fit values are marked with a cross.

4.7.4 Inclination

Varying the inclination of the accretion disc to the line of sight changes the range of observed Doppler shifts of the emission from the material in the accretion disc. Increasing the inclination (*i.e.* viewing the accretion disc closer to edge-on) increases the observed range of line-of-sight velocities as well as increasing the maximal projected line-of-sight velocity, which is greatest for a disc viewed completely edge-on). The most notable effect of increasing the inclination angle is the shift of the blueshifted peak of the emission line to higher energies (Fig. 4.20).

In order to understand how the shift in the blueshifted peak of the emission line due to the inclination influences the measured emissivity profile of the accretion disc, it is necessary to understand where photons observed at different energies originate from in the accretion disc. Fig. 4.21 shows the observed energy of photons, shifted due to Doppler shifts from the orbital motion of the material as well as the gravitational redshift in the vicinity of the black hole, as a function of the location at which they were reflected off the accretion disc for discs observed at different inclinations. As one might expect, the extended, redshifted wing of the emission line (those photons seen at the lowest energies) originate from the innermost regions where the gravitational redshift is the strongest. The most blueshifted photons (highest observed energies) also originate from the regions close to the black hole with the energy peaking at radii within $7\,r_{\mathrm{g}}$, because the orbital velocity of the accretion disc (assumed to follow circular geodesics, the relativistic equivalent of Keplerian orbits)

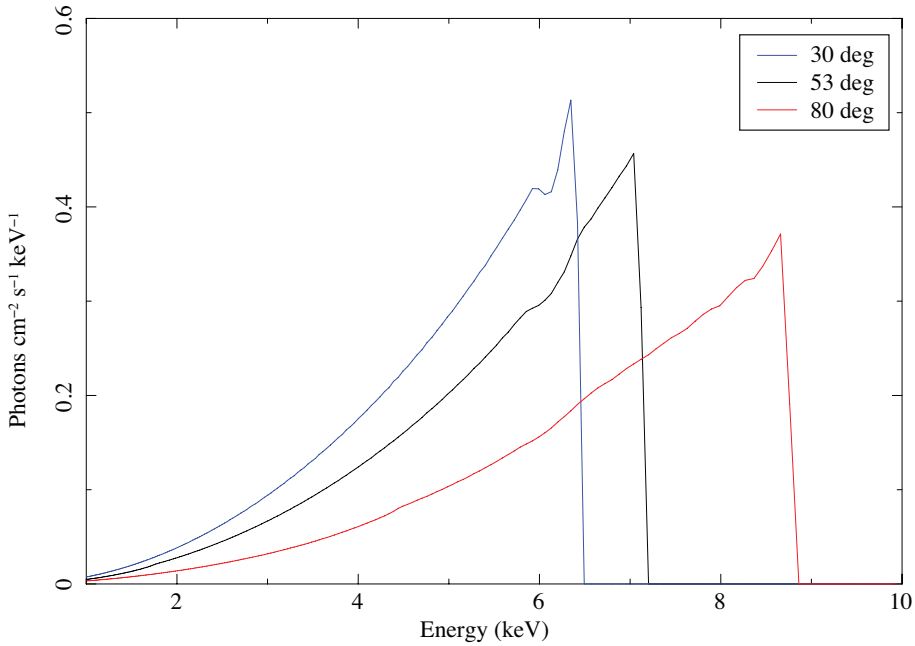

Figure 4.20: The profiles of relativistically blurred emission lines emitted from the material orbiting in the accretion disc, with varying inclination (defined as the angle between the line of sight and the rotation axis of the black hole).

is substantially greater closer to the black hole. This blueshifted emission is also enhanced in its observed intensity due to the relativistic beaming of the emitted radiation into the line of sight.

To see the effect of the assumed inclination on the measured emissivity profile, we turn our attention to Fig. 4.22, showing recovered emissivity profiles from the test spectra as well as the confidence contours between the radius of the outer break point in the power law index against the assumed inclination of the disc, shown in Fig. 4.23. When underestimating the inclination, it is impossible to reproduce the extremal blueshift and thus the high energy peak of the emission line. Looking at Fig. 4.7, the shape of the peak of the emission line is determined by the shape of the emissivity profile between around 5 and 30 $r_{\rm g}$ (in this case, whether there is a flattened region). Fig. 4.21 demonstrates that it is within these radii, the observed energy of the reflected photons starts to increase towards the peak energy, determined by the inclination. We therefore see, in Fig. 4.22, that when the inclination is underestimated, the flattened part of the emissivity profile as well as the outer break point become less well defined and, indeed, that it is less well constrained by the data as demonstrated by the expanding confidence contours towards lower inclination in Fig. 4.23.

When the inclination of the accretion disc is overestimated, the spectral model contains too much emission at higher energies compared to the observed spectrum due to the increase in energy of the

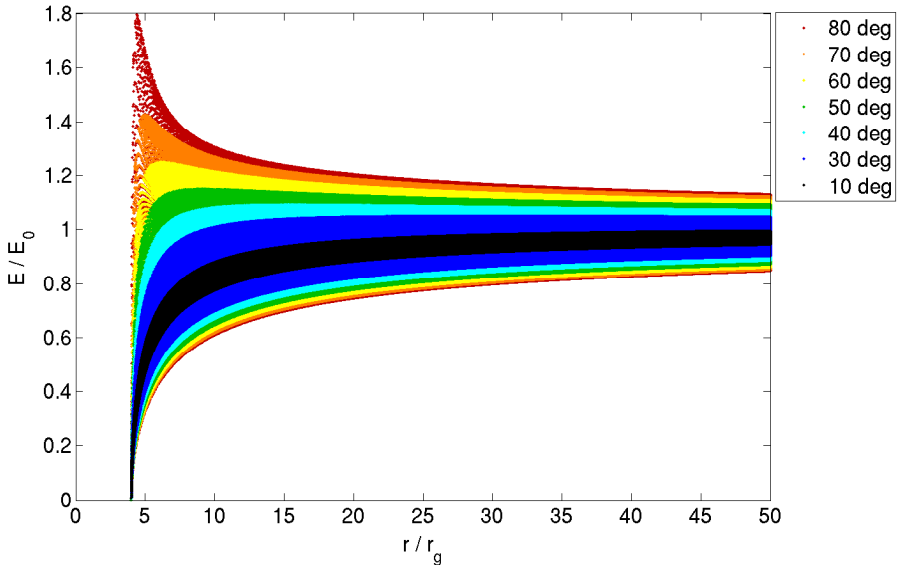

Figure 4.21: The observed energy of reflected photons (relative to the energy at which they were emitted in the rest frame of the disc) as a function of the radius on the accretion disc at which they were reflected for accretion discs viewed at different angles of inclination (measured between the rotation axis and the line of sight such that $0\,\mathrm{deg}$ represents a disc viewed face-on and $90\,\mathrm{deg}$ a disc viewed edge-on).

blueshifted peak of the emission line. In order to compensate for this, a dip occurs in the emissivity profile between around 3 and $10\,r_{\mathrm{g}}$, to artificially reduce the emission in the line at higher energies when fitting to the spectrum in the range 3-10 keV. Such a dip does not occur, however, when only considering the 3-5 keV range since this excludes the high energy peak of the emission line, though it does result in the contributions from annuli in this region not being constrained (the data points are not shown).

While we see that uncertainty in the inclination at which the accretion disc is viewed can lead to uncertainties in the shape of the emissivity profile, with an underestimate in the inclination leading to poor constraints on the flattened region and outer break point in the emissivity profile and an overestimate in the inclination causing a dip in the measured emissivity, this does not greatly affect the certainty of the emissivity profile we measure. Looking at Fig. 4.23, we see that the observed spectrum of 1H 0707-495 constrains the inclination within $10\,\mathrm{deg}$ at the 3σ level and indeed Fabian et al. (2013) show that the inclination of the accretion disc in IRAS 13224-3809 is constrained within $\pm 0.4\,\mathrm{deg}$ at 90 per cent confidence. Fig. 4.22 shows that an error of this size in the inclination does not adversely affect the determined emissivity profile.

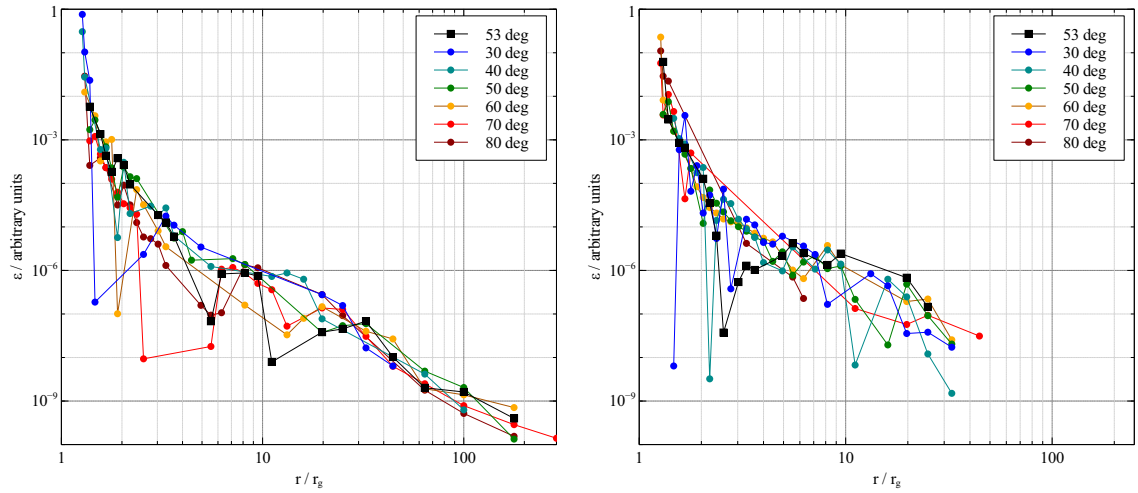

(a) 3-10 keV (b) 3-5 keV

Figure 4.22: The results of fitting for the emissivity profile of the synthetic spectrum assuming different inclinations of the accretion disc to the line of sight. fitting over the energy range (a) 3-10 keV and (b) 3-5 keV. The emissivity profile for real inclination is 53 deg, shown in black, deviations from which indicate errors in the recovered profile.

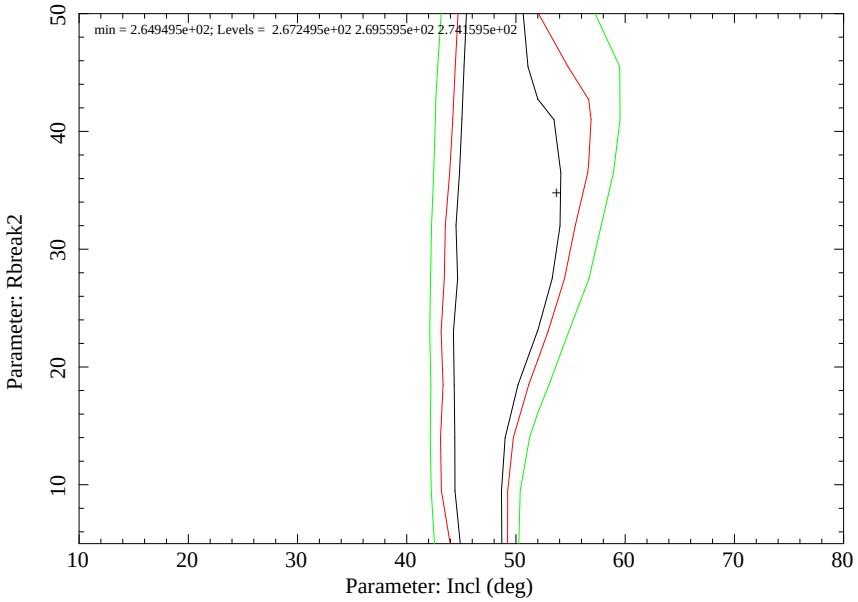

Figure 4.23: Confidence contours between the assumed inclination and the radius of the outer break point of the twice-broken power law emissivity profile for 1H 0707-495 in the energy band 3-10 keV.

4.8 Discussion

It is evident from the results here that the emissivity profile of 1H 0707-495 resembles the form predicted by Miniutti et al. (2003), with a steep power law ($\epsilon \propto r^{-\alpha}$) in the inner regions of the disc, found to have an index of around 7.8, flattening to a very shallow index, close to zero, before tending to a constant index of 3.3, slightly steeper than the Euclidean case, at large radius. Similar results are obtained for the emissivity profiles of the AGN IRAS 13224-3809 and MGC–6-30-15 as well as the Galactic black hole binary Cygnus X-1, albeit with the outer break radius located at smaller radii in these sources.

Such an emissivity profile suggests that 90 per cent of the X-ray flux reflected from the accretion disc (where $F(< r) = \int_{r_{\rm in}}^{r} \epsilon(r')\, r' dr'$, measured in the local disc frame) is reflected from the innermost regions of the disc, within $2\, r_{\rm g}$ of the central black hole as shown in Fig. 4.24 (the solid line shows the cumulative flux distribution measured in the disc frame and the dashed line that measured by an observer at infinity where the outer disc is more dominant due to the larger solid angle subtended and the tendency of photons emitted from the inner regions of the disc to fall into the black hole — as seen at infinity, only around 66% of the reflected flux originates from the inner disc, within $4\, r_{\rm g}$).

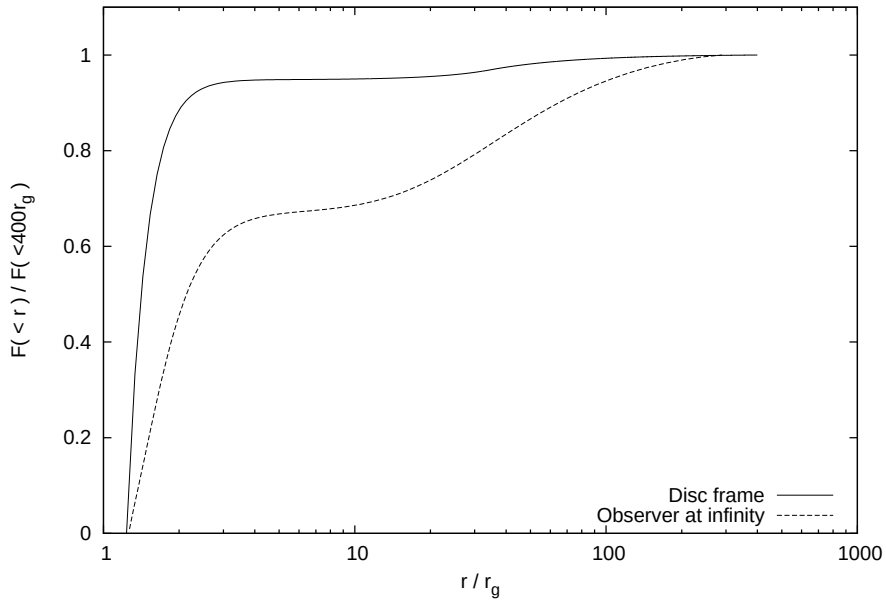

Figure 4.24: Cumulative reflected X-ray flux distribution, $F(< r)$, as a function of radius in the disc as implied by the determined emissivity profile for 1H 0707-495 measured in the disc frame compared with that as measured by an observer at infinity (taking into account the transport of radiation from the disc to the observer around the black hole for 1H 0707-495 which is observed at an inclination angle of $53\,\deg$).

Qualitatively, this form of the emissivity profile can be understood by considering an isotropic point source above the disc in a flat, Euclidean spacetime. The flux received from the source at each point on the disc, and thus the reflected power from that point (the emissivity) will vary simply as the inverse square of the distance from the primary X-ray source, projected into the direction normal to the disc plane, *i.e.* if the source is at a height h above $r = 0$ in the disc, the emissivity will go as $(r^2 + h^2)^{-1} \cos\vartheta$, with $\cos\vartheta = \frac{h}{\sqrt{r^2+h^2}}$, the angle from the normal at which the ray hits the disc. This will be constant (a flat profile) in the limit $r \ll h$ (the inner disc) and tending to r^{-3} at large radius (a power law emissivity profile with index 3).

In the presence of the black hole, gravitational light-bending will act to focus light rays from the point source towards the black hole and will increase the flux incident on the inner regions of the disc relative to the outer regions. This will cause the emissivity to fall off more steeply in the central regions of the accretion disc as is observed in the sources studied here, before reaching a power law index of around 3.3 at large radius, slightly steepened from the classical value of of 3.0.

In addition to gravitational light bending focussing the light rays on to the disc, the emissivity profile will be affected by relativistic effects on the disc itself. While the classical area of an annulus radius r and thickness dr is $2\pi r dr$, the proper area as measured in the rest frame of the disc for a given dr is increased as r decreases, as the space is warped close to the black hole and proper radial distances increase at small r as described by the Kerr metric. As the disc orbits the black hole (which on the last stable orbit will be at half the speed of light), the disc material will be length-contracted by a factor of γ, the Lorentz factor according to a stationary observer, so the area of the radial bins is increased further in the disc frame by a factor of γ. These effects increase the proper area of a radial bin closer to the black hole so will tend to reduce the steepness of the emissivity profile (as the incident flux is divided by the disc area).

The best fit to the spectrum with reflection components originating from successive radii indicates a non-zero contribution to the spectrum from photons originating from the inner regions of the disc right down to the innermost stable orbits for a rapidly spinning Kerr black holes at $1.235 \sim 1.5\,r_{\rm g}$. This suggests that the black holes are rapidly spinning (with $a > 0.95$ in all of these cases) and that the accretion disc extends down to the innermost stable orbit. The contribution received from the innermost regions of the accretion disc by an observer at infinity is, however, small once the projected area of the annuli (including the effect of the propagation of rays around the black hole to the observer) is accounted for. As such, the drop in the observed emissivity over several decades across the innermost regions may not be as significant to the observed line profile as first it seems.

The steep power law emissivity profile determined here without *a priori* assumption of its form and the agreement of this form with theoretical emissivity profiles calculated for point sources around the black hole show that the steep emissivity profiles previously required to explain the emission seen in terms of reflection of X-rays from a hard X-ray source near the black hole off of the accretion disc are indeed plausible.

It should be noted that if this twice-broken power law for the emissivity profile is averaged over the disc to a single-slope power law (averaging the index over radius, weighted by the annular area, $r\,dr$), the single power law index is found to be around 3.3. This would be found if a reflection component blurred using a single-slope emissivity profile is fit to the spectra and is only slightly steeper than the classical case, masking the significant steepening over the inner disc by relativistic effects. Merely measuring the slope of a single power law emissivity profile fit over the entire disc is not a good indicator of the importance of relativistic effects in the formation of the emission lines.

Throughout the preceding analysis, the standard limb-darkening of emission from the accretion disc (Laor, 1991) is assumed where rays emitted close to parallel to the disc plane will be intercepted by neighbouring material. Work by Svoboda et al. (2010) suggests that the disc emission due to reflection can in fact be limb-brightened or at least isotropic from the innermost regions of the disc close to the central black hole as photons on curved trajectories strike the disc at grazing angles. This will lead to an enhanced red wing of the emission line over the typical limb-darkened profile as can be seen in the RELLINE model of Dauser et al. (2010), and as such will lead to an apparently steeper emissivity profile. Thus, in reality the power law slope over the inner disc may be less than 7.8 in 1H 0707-495, while the effect on the emissivity profile obtained will be less relevant for the outer disc regions where these light bending effects are weaker. The power law slope over the inner parts of the accretion disc may also be overestimated by assuming a constant ionisation parameter over the surface of the disc.

4.9 Conclusions

The X-ray reflection emissivity profiles of the accretion discs in 1H 0707-495, IRAS 13224-3809, MCG–6-30-15 and Cygnus X-1 have been determined from the profile of the iron Kα emission line in the X-ray spectrum without *a priori* assumption of their form, by considering independently the relative contributions from successive radii in the disc.

The emissivity profiles were found to agree with theoretical predictions; a steeply falling profile in the inner regions of the disc with a power law index of around 8, then flattening to constant emissivity between $5\,r_{\rm g}$ and $10 \sim 35\,r_{\rm g}$ before tending to a constant power law slightly steeper than r^{-3} over the outer regions of the disc. The profile obtained suggests emission right down to the last stable orbit for rapidly rotating Kerr black holes.

The emissivity profiles obtained are consistent with fitting a relativistically blurred reflection spectrum from a disc with a continuous twice-broken power law emissivity profile, which provides a better fit than the previously assumed once-broken power law. The measurements are robust with regard to errors in the assumed iron abundance, ionisation state and inclination within the ranges permitted by the data.

The observed profile can be understood in the context of gravitational light bending as rays travel around the black hole from the source to the disc before being reflected, as well as relativistic effects on the disc and agrees with forms predicted by ray tracing simulations, indicating that reflection from an accretion disc with a steep central emissivity profile is plausible.

The results can be compared to theoretical emissivity profiles computed for a range of locations and geometries of the X-ray source as well as disc geometries in order to place constraints on the properties of the coronal X-ray sources in AGN.

5

General Relativistic Ray Tracing

In order to understand the physical implications of the observed accretion disc emissivity profiles as well as other features of the X-ray spectrum and variability and use them to place constraints on the source of X-rays in the nucleus of an active galaxy or from a Galactic black hole binary, it is necessary to understand how these observables arise and how they are affected by the properties of the X-ray source. In order to do this, simulations were run in which rays originating from a source in the corona around the black hole, above the disc plane are traced in the Kerr spacetime around the black hole to the disc and finally to an observer or telescope.

5.1 Ray Tracing in the Kerr Spacetime

The spacetime around a spinning black hole (spin parameter $a = \frac{J}{Mc}$) is described by the Kerr metric (Kerr, 1963). In Boyer-Lindquist co-ordinates, the Kerr metric is written

$$ds^2 = c^2\left(1 - \frac{2\mu r}{\rho^2}\right)dt^2 + \frac{4\mu acr\sin^2\theta}{\rho^2}dtd\varphi - \frac{\rho^2}{\Delta}dr^2 - \rho^2 d\theta^2 - \left(r^2 + a^2 + \frac{2\mu a^2 r\sin^2\theta}{\rho^2}\right)\sin^2\theta d\varphi^2$$

where

$$\begin{aligned}\mu &\equiv \frac{GM}{c^2}\\ \rho^2 &\equiv r^2 + a^2\cos^2\theta\\ \Delta &\equiv r^2 - 2\mu r + a^2\end{aligned}$$

In this spacetime, photons propagate along null geodesics satisfying the condition

$$g_{ab}\dot{x}^a\dot{x}^b = 0 \tag{5.1}$$

and the geodesic equation

$$\ddot{x}^a + \Gamma^a_{\ bc}\dot{x}^b\dot{x}^c = 0 \tag{5.2}$$

Where $\{x^a\}$ are some co-ordinates corresponding to basis vectors $\{\mathbf{e}_a\}$. g_{ab} is the metric tensor defined such that $ds^2 = g_{ab}dx^a dx^b$, and $\Gamma^a_{\ bc}$ are the connection co-efficients, defining the derivatives of the basis vectors such that $\frac{\partial \mathbf{e}_a}{\partial x^c} = \Gamma^b_{\ ac}\mathbf{e}_b$.

Solving this, the geodesic equations that characterise the propagation of photons can be written in terms of the first derivatives of the co-ordinates, $\dot{\mathbf{r}} = (\dot{t}, \dot{r}, \dot{\theta}, \dot{\varphi})$. Working in units such that $\mu = c = 1$:

$$\dot{t} = \frac{\left[(r^2 + a^2\cos^2\theta)(r^2 + a^2) + 2a^2 r\sin^2\theta\right]k - 2arh}{r^2\left(1 + \frac{a^2\cos^2\theta}{r^2} - \frac{2}{r}\right)(r^2 + a^2) + 2a^2 r\sin^2\theta} \tag{5.3}$$

$$\dot{\varphi} = \frac{2ark\sin^2\theta + (r^2 + a^2\cos^2\theta - 2r)h}{(r^2 + a^2)(r^2 + a^2\cos^2\theta - 2r)\sin^2\theta + 2a^2 r\sin^4\theta} \tag{5.4}$$

$$\dot{\theta}^2 = \frac{Q + (ka\cos\theta - h\cot\theta)(ka\cos\theta + h\cot\theta)}{\rho^4} \tag{5.5}$$

$$\dot{r}^2 = \frac{\Delta}{\rho^2}\left[k\dot{t} - h\dot{\varphi} - \rho^2\dot{\theta}^2\right] \tag{5.6}$$

Where the dots denote derivatives with respect to some affine parameter, σ. k, h and Q are conserved constants of the motion which distinguish the geodesics.

Given the starting point of a photon and the values of the constants of motion, the ray can be traced simply as the affine parameter advances by integration of the geodesic equations.

$$\mathbf{r}(\sigma + d\sigma) = \mathbf{r}(\sigma) + \dot{\mathbf{r}}(\sigma)d\sigma \tag{5.7}$$

Expressed in these natural units, distances are measured in gravitational radii, $r_{\mathrm{g}} = \mu = \frac{GM}{c^2}$ and scale with the black hole mass. The corresponding units of time are $\frac{GM}{c^3}$.

5.2 The X-ray Source

The coronal X-ray source is taken to be an isotropic point source. This means that it emits equal power into equal solid angle in its own local instantaneous rest frame. In the source's local rest frame, the solid angle element is written

$$d\Omega' = d(\cos\alpha)d\beta$$

where α is the declination from the polar axis and β the azimuthal angle of the ray as measured in the source's frame.

The source frame is defined by a tetrad of orthogonal basis vectors. The timelike tetrad basis vector, $\mathbf{e}'_{(t)}$ is, by definition of the instantaneous rest frame, parallel to the source's 4-velocity, $\mathbf{u}_0$ (since in its rest frame its own 4-velocity must have no spacelike component as its 3-velocity is zero). By the equivalence principle, which states that in a local, freely-falling laboratory the laws of physics reduce to those of special relativity, the local spacetime in the source frame is flat and when working in Cartesian co-ordinates, the tetrad basis vectors satisfy

$$\mathbf{e}'_{(a)} \cdot \mathbf{e}'_{(b)} = \eta_{(a)(b)} \tag{5.8}$$

$$g_{\mu\nu} e^{\mu}_{(a)} e^{\nu}_{(b)} = \eta_{(a)(b)} \tag{5.9}$$

Note that bracketed subscripts indicate directions in the tetrad basis and those not bracketed directions in the Boyer-Lindquist co-ordinate basis. $\eta_{(a)(b)} = \mathrm{diag}(1, -1, -1, -1)$ is the Minkowski (flat) space metric.

When considering the dynamics of inertial frames and constructing tetrad basis vectors, it is often convenient to re-write the metric in the form (following Chandrasekhar 1983)

$$ds^2 = e^{2\nu}c^2dt^2 - e^{2\psi}(d\varphi - \omega dt)^2 - e^{2\mu_1}dr^2 - e^{2\mu_2}d\theta^2$$

Where

$$\begin{aligned} e^{2\nu} &= \frac{\rho^2\Delta}{\Sigma^2} \\ e^{2\psi} &= \frac{\Sigma^2 \sin^2\theta}{\rho^2} \\ e^{2\mu_1} &= \frac{\rho^2}{\Delta} \\ e^{2\mu_2} &= \rho^2 \\ \omega &= \frac{2ar}{\Sigma^2} \end{aligned}$$

With

$$\Sigma^2 = (r^2 + a^2)^2 - a^2\Delta\sin^2\theta$$

This rewriting of the metric co-efficients as exponentials allows their square roots, products and ratios to be easily written.

5.2.1 Stationary Source

The simplest, idealised case is that of an isotropic point source, stationary at some point in the Kerr spacetime (Fig. 5.1). This will allow us to explore the effects of ray propagation in the Kerr spacetime with the fewest free parameters and assumptions about the nature of the source itself. A localised source, however, may be expected if the X-ray emission results from magnetic reconnection events within the corona (Galeev et al., 1979; Merloni & Fabian, 2001).

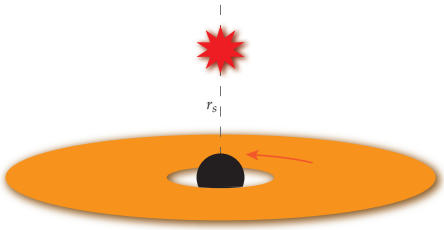

Figure 5.1: The geometry of an isotropic point source located on the rotation axis above the black hole.

If the source is stationary in the Boyer-Lindquist co-ordinate system, the local time-like basis vector (the frame's 4-velocity, $\mathbf{u}_0$) will be parallel to the co-ordinate time-like basis vector.

$$\begin{aligned} \mathbf{e}'_{(t)} &= \mathbf{u}_0 = (u^t, \dot{\vec{r}}) = \left(u^t, \frac{d\vec{r}}{dt}\dot{t}\right) = u_0\left(1, \frac{d\vec{r}}{dt}\right) \\ \mathbf{e}'_{(t)} &= (u^t, 0, 0, 0) \end{aligned}$$

Now, applying the condition (5.9)

$$\begin{aligned} g_{\mu\nu}e^{\mu}_{(t)}e^{\nu}_{(t)} &= \eta_{(t)(t)} = 1 \\ g_{tt}(u^t)^2 &= 1 \\ u^t &= g_{tt}^{-\frac{1}{2}} \end{aligned}$$

Thus,

$$\begin{aligned} u^t &= \left(e^{2\nu} - \omega^2 e^{2\psi}\right)^{-\frac{1}{2}} \\ u^t &= \frac{e^{-\nu}}{\sqrt{1 - \omega^2 e^{2(\psi-\nu)}}} \end{aligned}$$

$$\mathbf{e}'_{(t)} = \left(\frac{e^{-\nu}}{\sqrt{1 - \omega^2 e^{2(\psi-\nu)}}}, 0, 0, 0\right) \tag{5.10}$$

Now the timelike basis vector is determined, one is free to define the directions of the three space-like basis vectors that are orthogonal to it. Here, we will define the polar axis, $\mathbf{e}'_{(3)}$, such that it is radial in the co-ordinate frame, *i.e.* parallel to $\mathbf{e}_r = (0, 1, 0, 0)$. $\mathbf{e}'_{(2)}$ will be defined to be parallel to

$\mathbf{e}_\theta = (0, 0, 1, 0)$. This is permitted since the Kerr metric is diagonal in the co-ordinates r and θ, so condition (5.9) is satisfied so long as $g_{rr}e^r_{(3)}e^r_{(3)} = -1$ and $g_{\theta\theta}e^\theta_{(2)}e^\theta_{(2)} = -1$.

$$\mathbf{e}'_{(3)} = \left(0, \frac{\sqrt{\Delta}}{\rho}, 0, 0\right) \tag{5.11}$$

$$\mathbf{e}'_{(2)} = \left(0, 0, \frac{1}{\rho}, 0\right) \tag{5.12}$$

Finally, the third tetrad basis vector must, due to the $g_{t\varphi}$ cross-term in the Kerr metric, take the form

$$\mathbf{e}'_{(1)} = \left(e^t_{(1)}, 0, 0, e^\varphi_{(1)}\right)$$

and satisfy the conditions (5.9):

$$\mathbf{e}'_{(t)} \cdot \mathbf{e}'_{(1)} = 0 \tag{5.13}$$

$$\mathbf{e}'_{(1)} \cdot \mathbf{e}'_{(1)} = -1 \tag{5.14}$$

From (5.13),

$$g_{tt}e^t_{(t)}e^t_{(1)} + g_{t\varphi}e^t_{(t)}e^\varphi_{(1)} + g_{\varphi t}e^\varphi_{(t)}e^t_{(1)} + g_{\varphi\varphi}e^\varphi_{(t)}e^\varphi_{(1)} = 0$$

$$e^\varphi_{(1)} = -\frac{(e^{2\nu} - \omega^2 e^{2\psi})}{\omega e^{2\psi}} e^t_{(1)} \tag{5.15}$$

And using (5.14),

$$g_{tt}e^t_{(1)}e^t_{(1)} + 2g_{t\varphi}e^t_{(1)}e^t_{(1)}\varphi + g_{\varphi\varphi}e^\varphi_{(1)}e^\varphi_{(1)} = -1$$

Where the factor of 2 in the cross-term arises due to the symmetry of the metric of any (pseudo-) Riemannian manifold, where $g_{t\varphi} = g_{\varphi t}$.

Substituting using (5.15) and solving gives

$$e^t_{(1)} = \frac{-\omega e^{\psi-\nu}}{\sqrt{e^{2\nu} - \omega^2 e^{2\psi}}} \tag{5.16}$$

$$e^\varphi_{(1)} = \frac{e^{-\nu-\psi}(e^{2\nu} - \omega^2 e^{2\psi})}{\sqrt{e^{2\nu} - \omega^2 e^{2\psi}}} \tag{5.17}$$

The signs of the components have been selected to form a right-handed basis.

$$\mathbf{e}'_{(1)} = \left(\frac{-\omega e^{\psi-\nu}}{\sqrt{e^{2\nu} - \omega^2 e^{2\psi}}}, 0, 0, \frac{e^{-\nu-\psi}(e^{2\nu} - \omega^2 e^{2\psi})}{\sqrt{e^{2\nu} - \omega^2 e^{2\psi}}}\right) \tag{5.18}$$

Putting this together, the tetrad basis vectors in the stationary source's local instantaneous rest

frame are, expressed in the Boyer-Lindquist co-ordinate basis,

$$\begin{aligned}
\mathbf{e}'_{(t)} &= \left(\frac{e^{-\nu}}{\sqrt{1-\omega^2 e^{2(\psi-\nu)}}}, 0, 0, 0\right) \\
\mathbf{e}'_{(1)} &= \left(\frac{-\omega e^{\psi-\nu}}{\sqrt{e^{2\nu}-\omega^2 e^{2\psi}}}, 0, 0, \frac{e^{-\nu-\psi}(e^{2\nu}-\omega^2 e^{2\psi})}{\sqrt{e^{2\nu}-\omega^2 e^{2\psi}}}\right) \\
\mathbf{e}'_{(2)} &= \left(0, 0, \frac{1}{\rho}, 0\right) \\
\mathbf{e}'_{(3)} &= \left(0, \frac{\sqrt{\Delta}}{\rho}, 0, 0\right)
\end{aligned}$$

These Cartesian tetrad vectors may then be used as the (t', x', y', z') basis, in which the initial momentum of the photon may be expressed. The photon is to start travelling along the spatial directions defined by the polar angles α (declination from the polar axis defined by $\mathbf{e}'_{(3)}$) and β (azimuth). In the tetrad basis, the initial photon momentum, if its energy in the source frame is E_0 (taking $c = 1$), is written (noting that to give a right-handed co-ordinate system with $\mathbf{e}'_{(3)}$ as the polar axis, $\mathbf{e}'_{(2)}$ corresponds to the x-axis and $\mathbf{e}'_{(1)}$ the y-axis)

$$\mathbf{p}' = (E_0, E_0 \sin\alpha \sin\beta, E_0 \sin\alpha \cos\beta, E_0 \cos\alpha)$$

This is then re-expressed the Boyer-Lindquist co-ordinate basis by expressing each of the tetrad basis as a linear combination of the co-ordinate basis vectors.

$$\mathbf{p} = \left(\dot{t}, \dot{r}, \dot{\theta}, \dot{\varphi}\right)$$

$$\mathbf{p} = \left(p^{(t)} e^t_{(t)} + p^{(1)} e^t_{(1)}, p^{(3)} e^r_{(3)}, p^{(2)} e^\theta_{(2)}, p^{(1)} e^\varphi_{(1)}\right)$$

i.e.

$$\dot{t} = p^{(t)} e^t_{(t)} + p^{(1)} e^t_{(1)} \tag{5.19}$$
$$\dot{r} = p^{(3)} e^r_{(3)} \tag{5.20}$$
$$\dot{\theta} = p^{(2)} e^\theta_{(2)} \tag{5.21}$$
$$\dot{\varphi} = p^{(1)} e^\varphi_{(1)} \tag{5.22}$$

Given this, the values of the constants of motion k, h and Q are trivially calculated from the geodesic equations (5.3), (5.4) and (5.5).

$$k = \left(1 - \frac{2r}{\rho^2}\right)\dot{t} + \frac{2ar\sin^2\theta}{\rho^2}\dot{\varphi} \tag{5.23}$$
$$h = \left(r^2 + a^2 + \frac{2a^2 r \sin^2\theta}{\rho^2}\right)\sin^2\theta\dot{\varphi} - \frac{2ar\sin^2\theta}{\rho^2}\dot{t} \tag{5.24}$$
$$Q = \rho^4\dot{\theta}^2 - (ak\cos\theta - h\cot\theta)(ak\cos\theta + h\cot\theta) \tag{5.25}$$

5.2.2 Rotating Source

While it is conceivable that X-rays originate from a stationary point source close to the rotation axis, one might also consider the case of a point source located elsewhere in the corona. The concept of a stationary object in the corona (if not on the rotation axis) is somewhat unphysical, given that the black hole is considered to have formed from the gravitational collapse of material towards the galactic centre, a process in which it is likely to rotate, conserving angular momentum. Furthermore, without rotation, the material will just fall into the black hole and will not survive for long as a corona (unless it is replenished).

Due to the axisymmetry of the Kerr spacetime, a point source in orbit at a given radius is equivalent to a continuous ring source of that radius (which may be relevant when considering the total emission from many localised flaring events when looking at time-averaged X-ray spectra).

We again consider the idealised case of an isotropic point source (Fig. 5.2) to explore the observed effects in the emissivity profile due to ray propagation to the accretion disc in general relativity with the minimum number of free parameters. Orbiting point sources at various locations in the corona will be the building blocks for extended X-ray sources.

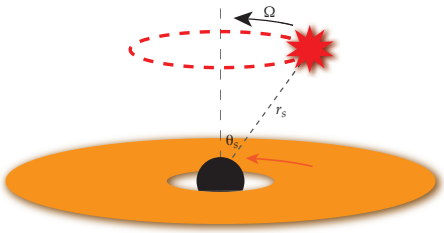

Figure 5.2: The considered geometry of an isotropic point source orbiting the rotation axis above the plane of the accretion disc.

Qualitatively, in addition to the gravitational light-bending focussing light rays towards the central black hole and hence on to the inner regions of the accretion disc, emission will also be 'beamed' forwards into the direction of motion. If the emitting region is in a circular orbit in a plane above the accretion disc, emission will be beamed into a direction tangential to the orbit and hence the emissivity of regions of the disc below this orbit will be enhanced while that of regions outside this band will be reduced. If the source is close to the black hole, this will lead to further steeping of the emissivity profile. The relativistic beaming will be significant for sources close to the black hole as, for instance, material at the inner-most stable orbit ($1.235\,r_{\rm g}$ for a maximally rotating Kerr black hole) will be orbiting at half the speed of light.

The case of a moving source is treated using the same formalism, where the source emits isotropically in its own rest frame described by the tetrad basis vectors. The photon 4-momenta are then transformed into the Boyer-Lindquist co-ordinate basis, and the constants of the photon motion are

calculated.

Once again, the timelike tetrad basis vector is the 4-velocity of the emitting particle orbiting at angular velocity $\frac{d\varphi}{dt} = \Omega$.

$$\begin{aligned} \mathbf{e}'_{(t)} &= \mathbf{u} = (u^t, \dot{\overrightarrow{r}}) = \left(u^t, \frac{d\overrightarrow{r}}{dt}\dot{t}\right) = u^t\left(1, \frac{d\overrightarrow{r}}{dt}\right) \\ \mathbf{e}'_{(t)} &= u^t(1, 0, 0, \Omega) \end{aligned}$$

The time-like component, u^t, is found from the condition for the motion of a massive particle $g_{\mu\nu}u^\mu u^\nu = c^2$ (again taking $c = 1$).

$$g_{tt}u^t u^t + 2g_{t\varphi}u^t u^\varphi + g_{\varphi\varphi}u^\varphi u^\varphi = 1$$

$$(e^{2\nu} - \omega^2 e^{2\psi})(u^t)^2 + 2\omega e^{2\psi}\Omega(u^t)^2 - e^{2\psi}\Omega^2(u^t)^2 = 1$$

$$u^t = \frac{e^{-\nu}}{\sqrt{1 - e^{2(\psi-\nu)}(\Omega - \omega)^2}}$$

Thus,

$$\mathbf{e}'_{(t)} = \left(\frac{e^{-\nu}}{\sqrt{1 - e^{2(\psi-\nu)}(\Omega - \omega)^2}}, 0, 0, \frac{e^{-\nu}\Omega}{\sqrt{1 - e^{2(\psi-\nu)}(\Omega - \omega)^2}}\right) \tag{5.26}$$

As for the case of the static source, since the 4-velocity has no component in either the r or θ directions and the Kerr metric is diagonal in these directions, two of the orthogonal space-like basis vectors are

$$\mathbf{e}'_{(3)} = \left(0, \frac{\sqrt{\Delta}}{\rho}, 0, 0\right) \tag{5.27}$$

$$\mathbf{e}'_{(2)} = \left(0, 0, \frac{1}{\rho}, 0\right) \tag{5.28}$$

Finally, the fourth orthogonal tetrad basis vector must take the form

$$\mathbf{e}'_{(1)} = \left(e^t_{(1)}, 0, 0, e^\varphi_{(1)}\right)$$

and satisfy the conditions (5.9)

$$\mathbf{e}'_{(t)} \cdot \mathbf{e}'_{(1)} = 0 \tag{5.29}$$

$$\mathbf{e}'_{(1)} \cdot \mathbf{e}'_{(1)} = -1 \tag{5.30}$$

Condition (5.29) gives

$$g_{tt}e^t_{(t)}e^t_{(1)} + g_{t\varphi}e^t_{(t)}e^\varphi_{(1)} + g_{\varphi t}e^\varphi_{(t)}e^t_{(1)} + g_{\varphi\varphi}e^\varphi_{(t)}e^\varphi_{(1)} = 0$$

$$e^\varphi_{(1)} = \frac{e^{2\nu} - \omega^2 e^{2\psi} + \Omega\omega e^{2\psi}}{e^{2\psi}(\Omega - \omega)}e^t_{(1)} \tag{5.31}$$

And from (5.30),

$$g_{tt}e^t_{(1)}e^t_{(1)} + 2g_{t\varphi}e^t_{(1)}e^\varphi_{(1)} + g_{\varphi\varphi}e^\varphi_{(1)}e^\varphi_{(1)} = -1$$

Substituting using (5.31) and solving gives

$$e^t_{(1)} = \frac{e^{\psi-\nu}(\Omega-\omega)}{\sqrt{e^{2\nu}-e^{2\psi}(\Omega-\omega)^2}} \tag{5.32}$$

$$e^\varphi_{(1)} = \frac{e^{-\nu-\psi}(e^{2\nu}+\Omega\omega e^{2\psi}-\omega^2e^{2\psi})}{\sqrt{e^{2\nu}-e^{2\psi}(\Omega-\omega)^2}} \tag{5.33}$$

Where, once again, the signs have been selected to form a right-handed basis.

$$\mathbf{e}'_{(1)} = \left(\frac{e^{\psi-\nu}(\Omega-\omega)}{\sqrt{e^{2\nu}-e^{2\psi}(\Omega-\omega)^2}}, 0, 0, \frac{e^{-\nu-\psi}(e^{2\nu}+\Omega\omega e^{2\psi}-\omega^2e^{2\psi})}{\sqrt{e^{2\nu}-e^{2\psi}(\Omega-\omega)^2}}\right) \tag{5.34}$$

To summarise, the tetrad basis vectors in the frame of a massive observer orbiting a Kerr black hole at angular velocity $\frac{d\varphi}{dt} = \Omega$ are

$$\mathbf{e}'_{(t)} = \left(\frac{e^{-\nu}}{\sqrt{1-e^{2(\psi-\nu)}(\Omega-\omega)^2}}, 0, 0, \frac{e^{-\nu}\Omega}{\sqrt{1-e^{2(\psi-\nu)}(\Omega-\omega)^2}}\right) \tag{5.35}$$

$$\mathbf{e}'_{(1)} = \left(\frac{e^{\psi-\nu}(\Omega-\omega)}{\sqrt{e^{2\nu}-e^{2\psi}(\Omega-\omega)^2}}, 0, 0, \frac{e^{-\nu-\psi}(e^{2\nu}+\Omega\omega e^{2\psi}-\omega^2e^{2\psi})}{\sqrt{e^{2\nu}-e^{2\psi}(\Omega-\omega)^2}}\right) \tag{5.36}$$

$$\mathbf{e}'_{(2)} = \left(0, 0, \frac{1}{\rho}, 0\right) \tag{5.37}$$

$$\mathbf{e}'_{(3)} = \left(0, \frac{\sqrt{\Delta}}{\rho}, 0, 0\right) \tag{5.38}$$

Taking $\mathbf{e}'_{(3)}$, $\mathbf{e}'_{(2)}$ and $\mathbf{e}'_{(1)}$ as the z (polar), x and y axes respectively (forming a right-handed co-ordinate system), the 4-momentum of a photon energy E_0 emitted at declination α and azimuth β in the emitter's frame is written

$$\mathbf{p}' = (E_0, E_0\sin\alpha\sin\beta, E_0\sin\alpha\cos\beta, E_0\cos\alpha)$$

And transforming back into the Boyer-Lindquist co-ordinate basis,

$$\dot{t} = p^{(t)}e^t_{(t)} + p^{(1)}e^t_{(1)} \tag{5.39}$$

$$\dot{r} = p^{(3)}e^r_{(3)} \tag{5.40}$$

$$\dot{\theta} = p^{(2)}e^\theta_{(2)} \tag{5.41}$$

$$\dot{\varphi} = p^{(t)}e^\varphi_{(t)} + p^{(1)}e^\varphi_{(1)} \tag{5.42}$$

The constants of motion for the photon are then calculated using Equations (5.23), (5.24) and (5.25).

Co-rotating Source

One might consider the case of an X-ray source that is 'co-rotating' with the accretion disc. The term 'co-rotating' is not particularly meaningful when discussing an X-ray source above the disc, since as the source and disc are in different locations, their velocity vectors lie in separate vector spaces, so they cannot be said to have the same velocity. However, here, we discuss 'co-rotation' in the sense of a source orbiting at a some 'radius' we shall call r from the rotation axis having the same angular velocity $\Omega = \frac{d\varphi}{dt}$ as material at radius r in the accretion disc. While this is a simplifying assumption in modelling a 'generalised' corona whose exact origin is not specified, such a situation could arise in the case of particles accelerated by magnetic field lines that are anchored to the accretion disc below.

Writing the geodesic equation in terms of the derivative of the covariant components of the velocity vector, $\dot{u}_\mu = \frac{1}{2}\left(\partial_\mu g_{\nu\sigma}\right) u^\nu u^\sigma$ and setting $u_r = \dot{u}_r = 0$ for a circular orbit

$$\left(\partial_r g_{tt}\right)\left(u^t\right)^2 + 2\left(\partial_r g_{t\varphi}\right) u^t u^\varphi + \left(\partial_r g_{\varphi\varphi}\right)\left(u^\varphi\right)^2 = 0$$

Defining the angular velocity $\Omega = \frac{d\varphi}{dt}$ and noting that $u^\varphi = \dot{\varphi} = \Omega\dot{t} = \Omega u^t$, we obtain

$$\left(\partial_r g_{tt}\right)\left(\frac{1}{\Omega}\right)^2 + 2\left(\partial_r g_{t\varphi}\right)\left(\frac{1}{\Omega}\right) + \left(\partial_r g_{\varphi\varphi}\right) = 0$$

Substituting in the components of the metric and solving this quadratic in $\frac{1}{\Omega}$ gives

$$\Omega = \frac{1}{a \pm r^{\frac{3}{2}}} \tag{5.43}$$

Where the plus sign represents prograde orbits (in the same sense as the black hole spin) and the minus sign, retrograde orbits.

5.2.3 Extended X-ray Sources

While it is instructive to consider the case of isotropic point sources in the corona to illustrate the factors affecting the emissivity profile of the accretion disc from X-ray reflection, in reality, the source is likely to be extended over a region of the corona where particles are heated and accelerated, Compton up-scattering seed photons to produce the observed X-rays.

In the simplest case, an extended X-ray source can be considered as the sum of point sources assuming the corona is optically thin to the emitted X-rays such that emission from any part of the source can escape without interacting with other parts (as one might expect for an optically thin corona of hot, accelerated electrons that inverse-Compton scatter photons). This simple model will illustrate the behaviour of such systems in determining the accretion disc emissivity profile.

Spatially extended X-ray sources may be studied in more detail through Monte-Carlo ray tracing simulations. Rays are started at random locations (with a uniform probability density function

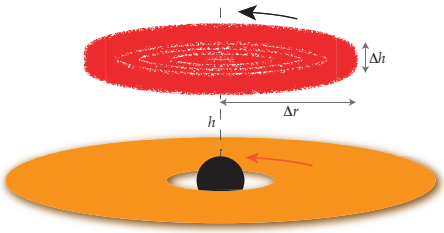

Figure 5.3: Extended X-ray source defined by a lower and upper height from the disc plane as well as an inner and outer radius.

such that all locations are equally likely) within an allowed cylindrical source region (defined by a lower and upper height from the disc plane as well as an inner and outer radius) and are assigned random initial direction cosines $\cos\alpha$ and β, again with uniform probability density (Fig. 5.3. This will simulate the effect of an X-ray source of finite spatial extent that is, again, optically thin to the X-rays it emits. Each local region of the source is taken to be co-rotating with the element of the accretion disc in a relativistic Keplerian orbit at the same radius.

To account for the variation in source luminosity across its extent, the rays reaching the disc can be weighted by power laws in the height and radius of their origin in the source (or indeed weighted by other functions) allowing for simple non-uniform sources to be modelled, however as this introduces a number of free parameters that will not be constrained by the current quality of observations, the simplest case of constant luminosity sources is taken here to explore the effects of spatially extending the source. Matching observations to simulations of a constant luminosity source with a simple cylindrical emitting region with uniform luminosity will represent be representative of the bulk of the coronal emission.

5.3 Ray Tracing Results

Results of raytracing from a stationary point source located above the plane of the accretion disc on the $\theta = 0$ axis (corresponding to the rotation axis of a spinning, Kerr black hole) for non-spinning Schwarzschild and maximally rotating ($a = 0.998$) Kerr black holes are shown in Figure 5.4.

Immediately obvious from these plots is the gravitational bending of the light rays towards the central black hole in the warped spacetime (whereas in a classical, flat spacetime the light rays would follow straight paths). Also visible in the case of the maximally spinning Kerr black hole is the 'frame-dragging,' causing the light rays to be dragged round the black hole azimuthally. These effects are enhanced as the source is moved closer to the black hole, as can be seen in Figure 5.5

Introducing rotation of the X-ray source about the polar axis causes the emission to be 'beamed'

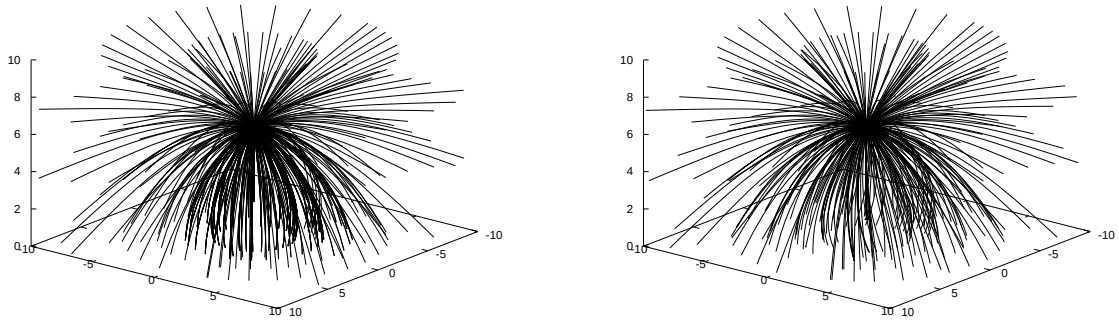

(a) $a = 0$ (b) $a = 0.998$

Figure 5.4: Raytracing from a stationary point source at $\theta = 0$ above the plane of the accretion disc of (a) a non-spinning Schwarzschild black hole and (b) a maximally rotating ($a = 0.998$) Kerr black hole. The black hole is located at the origin, the disc in the equatorial $\theta = \frac{\pi}{2}$ plane and the source at $r = 6\,r_{\rm g}$.

forward into the direction of motion, enhancing emission here and reducing the emission trailing the source. This is illustrated in Figure 5.6 for a source at $3\,r_{\rm g}$ and $\theta = \frac{\pi}{4}$ rotating at co-ordinate angular velocity $\Omega \equiv \frac{d\varphi}{dt} = 0.1c$.

5.4 Redshift

Travelling between two points in a gravitational potential or between observers with different velocities, the observed energy of a photon will be shifted; radiation emitted from closer to a larger mass is redshifted while proper motion of the observers will cause the light to appear Doppler shifted to higher energies if its source is approaching the observer and to lower energies if the source is receding.

It is possible to calculate the observed redshift of a photon between an emitter, E and receiver, R by considering the 4-momentum of the photon, $\mathbf{p}$. Any given observer (the emitter is counted as an observer since they will 'observe' the energy at which they are emitting the photon), by the equivalence principle, has their own reference frame corresponding to a flat, Minkowski spacetime and they will measure the components of the 4-momentum of the photon in their frame $[p^\mu] = \left(\frac{E}{c}, \overrightarrow{p}\right)$ where $E = \hbar\omega$ is the measured energy of the photon and $\overrightarrow{p} = \hbar\overrightarrow{k}$ is its 3-momentum, with 3-wavevector $\overrightarrow{k}$.

To compute the energy of the photon as seen by the observer, the zeroth component of the vector in their frame (*i.e.* the projection of the 4-momentum onto their timelike axis) is taken by calculat-

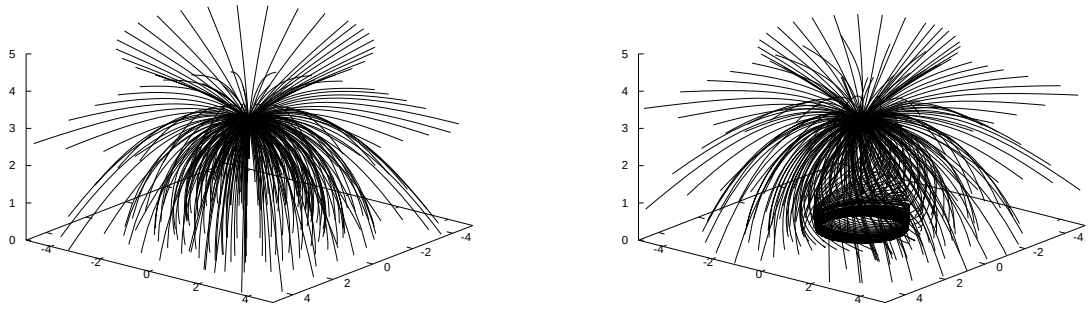

(a) $a = 0$ (b) $a = 0.998$

Figure 5.5: The gravitational light bending and frame-dragging (for the Kerr black hole only) are enhanced for (a) the non-spinning Schwarzschild black hole and (b) the maximally rotating ($a = 0.998$) Kerr black hole. The black hole is located at the origin, the disc in the equatorial $\theta = \frac{\pi}{2}$ plane and the source is now at $r = 3\,r_{\rm g}$.

ing the scalar product of the 4-momentum with their zeroth basis vector. Since, by definition, an observer is stationary in their own rest frame, their 4-momentum must be parallel to their zeroth basis vector, therefore their 4-velocity is used as this basis vector, giving the redshift

$$g^{-1} \equiv \frac{E_R}{E_E} = \frac{\mathbf{u}_R \cdot \mathbf{p}(R)}{\mathbf{u}_E \cdot \mathbf{p}(E)} = \frac{u^\mu_R p_\mu(R)}{u^\mu_E p_\mu(E)} = \frac{g_{\mu\nu} u^\mu_R p^\nu(R)}{g_{\rho\sigma} u^\rho_E p^\sigma(E)} \tag{5.44}$$

5.5 Observing the Accretion Disc

To discover how the accretion disc will be seen by an observer at infinity (or indeed an X-ray telescope in orbit around the Earth), it is necessary to trace every ray that can be emitted by the disc that will end up reaching the telescope, potentially having been deflected by the curved spacetime around the black hole. Tracing every ray originating from the accretion disc, many of which will not end up anywhere near the telescope, however, is computationally very expensive and wasteful.

The telescope images a patch of the sky, henceforth referred to as the *image plane* and will detect rays that are travelling perpendicular to that plane, if the image plane is constructed sufficiently far from the black hole that rays will travel in a straight line after they pass through it (here, the distance from the black hole to the centre of the image plane is taken to be 10,000 $r_{\rm g}$). It is therefore more straightforward to ask which of these rays, passing through, perpendicular to the image plane originated on the accretion disc (or indeed any object that we wish to observe).

The geometry of the Kerr spacetime, including the geodesic equations describing the passage of

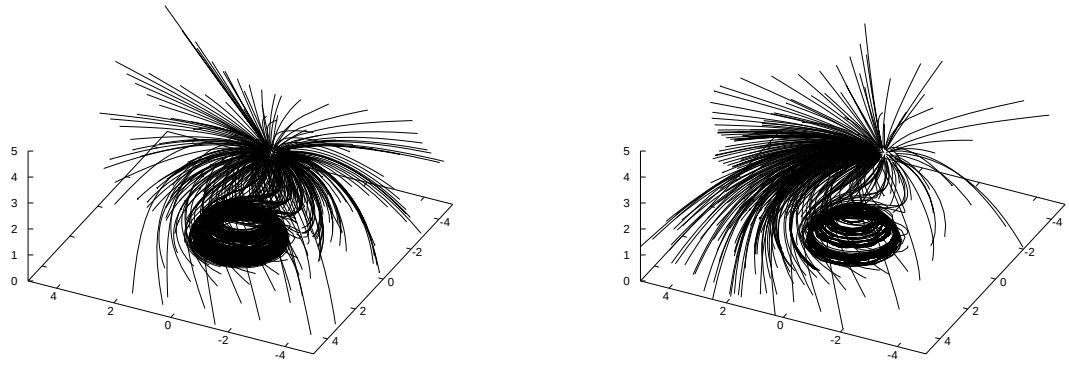

(a) $\Omega = 0$ (b) $\Omega = 0.25c$

Figure 5.6: Comparison of the ray paths from an isotropic point source at $3\,r_{\rm g}$and $\theta = \frac{\pi}{4}$ around a maximally spinning Kerr black hole for (a) a stationary source and (b) a source orbiting the rotation axis at $\Omega \equiv \frac{d\varphi}{dt} = 0.25c$. The source is in a prograde orbit with respect to the source, travelling in an anticlockwise direction in the figures. Note the beaming of emission into the forward direction for the rotating source.

light rays is entirely encoded in the metric, g_{ab} and we see that the Kerr metric is invariant under the reversal of time, $dt \rightarrow -dt$ so long as the spin of the black hole is also reversed $a \rightarrow -a$ (travelling backwards in time, the ray travels back where it came from but the black hole has spun backwards also to 'where it came from').

It is therefore possible to see how the accretion disc is observed by the telescope by starting a regular grid of rays across the disc, travelling perpendicular to the plane. The geometry of the image plane is shown in Fig. 5.7.

Each ray is identified by its (x, y) Cartesian co-ordinates in the plane, from which the impact parameter, b and polar angle in the image plane, β, are calculated.

$$b = \sqrt{x^2 + y^2}$$
$$\beta = \arcsin\left(\frac{y}{b}\right)$$

At sufficient distance from the black hole, the spacetime reduces to flat, Euclidean geometry and the effect of the spin of the black hole is negligible, therefore the constants of motion of the photon may be calculated geometrically. Rays are normalised such that $k = 1$.

The rate of change of the φ co-ordinate is set to counteract the component of the vector joining the ray to the origin in the φ direction such that the ray travels parallel to the image plane and normalising the impact parameter b as a fraction of the distance to the plane, r in order to obtain a

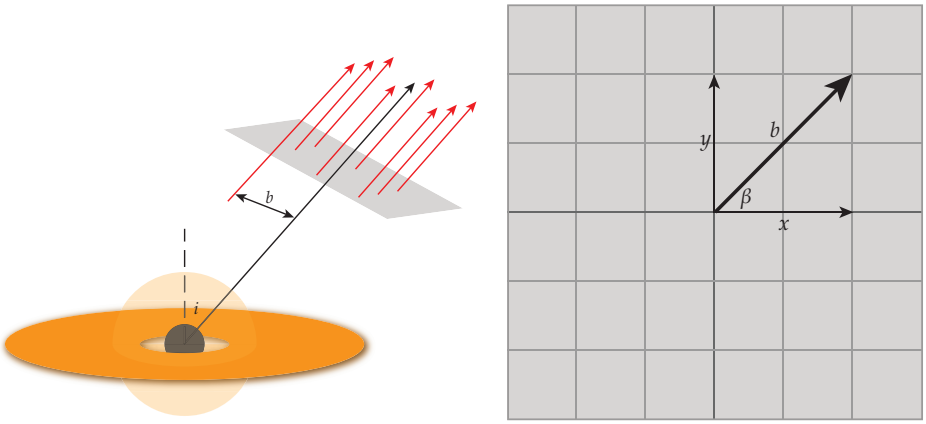

(a) (b)

Figure 5.7: (a) The geometry of an image plane constructed to observe the accretion disc with the line of sight at inclination angle i from the normal to the plane of the disc with each ray crossing the imageplane identified by its (x, y) Cartesian co-ordinates in the plane or alternatively the impact parameter, b and polar angle β as shown in (b).

ray travelling at the speed of light given $k = 1$, *i.e.*

$$\dot{\varphi} = -\frac{b\cos\beta}{r^2\sin i}$$

For the limit of zero spin as experienced at such large distances from the black hole, the geodesic equations give

$$h = r^2\sin^2 i\,\dot{\varphi} = -b\sin i\cos\beta \tag{5.45}$$

Resolving the ray in the θ direction, a similar analysis may be performed

$$r^2\dot{\theta} = b\sin\beta$$

And noting that in the limit $a \to 0$, the co-ordinate $\rho \to r$, so the Carter constant can be written

$$Q = b^2\sin^2\beta - (a\cos\theta - h\cot\theta)(a\cos\theta + h\cot\theta) \tag{5.46}$$

Where θ is the starting point of the ray in Boyer-Lindquist co-ordinates.

The rays are traced by integration of the geodesic equations, with the spin of the black hole reversed, until they reach the equatorial plane. Recording their position and time co-ordinates on the equatorial plane gives the mapping between points in the accretion disc and the image plane showing how the disc will appear to the observer, including the gravitational lensing effects, as well as their travel time from the disc to the observer. The redshift of the ray of the ray is then calculated by, firstly reversing the spatial components of the photon 4-momentum (such that it is travelling towards the observer), flipping the spin of the black hole back to its original value and then taking

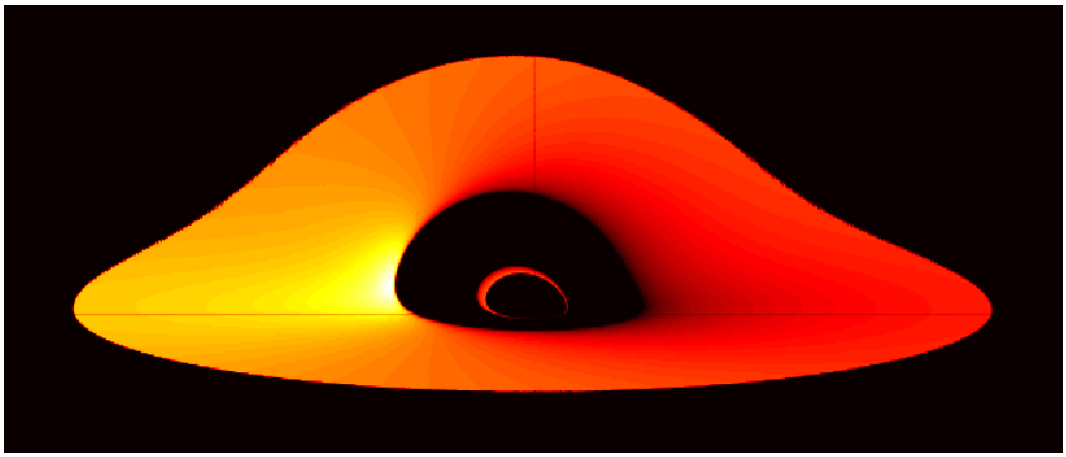

Figure 5.8: Image of a uniformly emitting accretion disc around a Schwarzschild black hole viewed at an inclination angle of $80\,\mathrm{deg}$ to the normal by an observer at infinity. Light from the far side of the disc is lensed around the black hole so appears above. Material in the accretion disc is travelling in geodesic circular orbits (the relativistic equivalent of Keplerian orbits). Emission from the side of the disc approaching the observer appears brighter as the photons are blueshifted and emission is beamed into the line of sight (material on the innermost stable orbit is travelling at half the speed of light), while the emission from receding material is dimmed by beaming out of the line of sight as well as stronger gravitational redshift closer to the black hole. A ring of emission is seen from the (unstable) photon orbit at $3\,r_{\mathrm{g}}$.

the dot products of the photon 4-momentum at either end of its path with the 4-velocity of the material in the accretion disc (as the emitter) and the telescope (as the observer, at rest at infinity) as in Equation 5.44. The effects of the transfer of emission from the accretion disc to the observer are illustrated in Fig. 5.8.

5.6 Implementation

The above ray tracing algorithms are coded to run on Graphics Processing Units (GPUs) using the NVIDIA CUDA programming architecture. A typical GPU at the time of writing has between 256 and 512 processing cores, each capable of computing an independent thread, meaning that parallelised computations can often be sped up by factors of several hundred or more. As an illustration, ray tracing routines to compute high resolution emissivity profiles of accretion discs were sped up from a running time of $24 \sim 48$ hours on a cluster of conventional CPUs to under 10 minutes on a single GPU.

In the CUDA programming model, threads are conceptualised on a two-dimensional grid, meaning each thread can be readily mapped on to a point in the source-frame trajectory $(\cos\alpha, \beta)$ parameter

space in the case of a point source. For ray tracing from an image plane back to the disc, used for simulating the observation of the accretion disc by an X-ray telescope, the threads are mapped to the (x, y) co-ordinates across the image plane while for Monte Carlo simulations of extended X-ray sources, threads are mapped to each of the randomly generated rays.

In order to compute emissivity profiles and other observables arising from an X-ray source from a given set of rays, each ray is traced by an independent computing thread on the GPU. The parameters (starting co-ordinates and constant of motion) are computed by the conventional CPU and copied to the memory on board the GPU, with memory addresses allocated to each thread (*e.g.* for an isotropic point source, all the rays are started at the same spacetime location and the constants of motion are incremented according to equal steps in $\cos\alpha$ and β). The GPU computing threads are then executed, moving each ray as the affine parameter advances according to the equations of motion, until they reach their limits on the disc, at the event horizon or at a maximum allowed radius or number of steps. Once each thread has finished, the final positions of the rays are read back from the GPU memory and binned into locations on the accretion disc, arrival times, energies, *etc.* as appropriate for the problem in hand to allow observables such as X-ray spectra, light curves, emissivity profiles and lag spectra to be computed.

6

Understanding Emissivity Profiles

In order to understand the reflection spectrum emerging from an accretion disc around a black hole, it is necessary to understand the illumination pattern of the accretion disc, that is its *emissivity profile*, the reflected power per unit area as a function of location on the disc. Following Laor (1991), the emissivity, $\epsilon(r)$, is defined as the radial weighting of the reflected radiation from the accretion disc, measured in the rest frame of the disc material, such that the observed spectrum is given by

$$F_0(\nu_0) = \int \epsilon(r_e) I_r \left(\frac{\nu_e}{g}\right) T(r_e, g)\, dg\, r_e dr_e \tag{6.1}$$

where I_r is the rest-frame reflection emerging from the accretion disc, folded through the transfer funtion, $T(r_e, g)$ which projects the rays around the black hole to the observer, integrating over all redshifts g that will shift the emitted photons into the observed energy band at the corresponding radius.

In the simplest case of a point source in flat, Euclidean spacetime, the emissivity at a point on the disc is proportional to the inverse-square of the distance from the source, multiplied by the cosine of the angle at which the ray hits the disc from the normal, giving a form r^{-3} at large radius out from the source. In general relativity, however, rays will be focussed towards the black hole (and the inner disc) so naïvely one would expect a steeper fall-off in emissivity with distance from the black hole.

Previous calculations of the illumination of black hole accretion discs by a point source on the rotation axis above the black hole, *e.g.* Miniutti et al. (2003) and Martocchia et al. (2000), predict emissivity profiles approximating twice-broken power laws, falling steeply over the inner regions of the disc, then flattening before tending to a constant power law index over the outermost radii, while Suebsuwong et al. (2006) extended this work to orbiting point sources offset from the rotation axis, yielding qualitatively similar results.

The emissivity profile of the accretion discs in the narrow line Seyfert 1 galaxies 1H 0707-495, IRAS 13224-3809 and MCG–6-30-15 as well as that in the Galactic X-ray binary, Cygnus X-1 were determined by independently fitting the contributions to the relativistically broadened emission lines from successive radii in the disc (§4). The accretion disc in 1H 0707-495 was found to have a steeply falling emissivity profile (with a power law index 7.8) in the inner region of the disc then flattening off to almost constant emissivity between radii of $5.6\,r_{\rm g}$ and $34.5\,r_{\rm g}$ before tending to a constant power law index of 3.3 (slightly steeper than the classical case) over the outermost parts of the disc, in broad agreement with previously predicted forms, with similar results obtained for the other sources.

Developed here is a formalism in which theoretical emissivity profiles due to point-like and extended X-ray sources located in the corona may be predicted through general relativistic ray tracing simulations. While previous theoretical work derives emissivity profiles of accretion discs for selected cases, mostly for the case of a point sources on the rotation axis above the central black hole, herein emissivity profiles are systematically calculated for varying locations of the primary X-ray source and furthered to include extended sources of different sizes and geometries. This allows the effects of these parameters on the emissivity profile to be studied, such that properties of the X-ray source may be inferred from the observed emissivity profile.

6.1 Calculating Emissivity Profiles from Ray Tracing Simulations

Rays originating from X-ray sources constructed as described in §5.2 are traced until they reach the accretion disc, lying in the equatorial plane in the Kerr spacetime around the black hole. The geodesic equations, 5.3-5.6, are integrated until $\theta \geq \frac{\pi}{2}$, or until the photons escape to a maximum allowed radius (or the maximum number of allowed steps is reached, to prevent the code entering an infinite loop if the step size were to become very small). When the photon hits the disc, its position is assigned to a radial bin and the number of photons hitting the disc in each bin is counted.

Once the number of photons in each radial bin has been counted, the emissivity profile is obtained by dividing these counts by the area of each bin (an annulus). Strictly speaking, that is the proper area of the annulus, as measured in the disc frame, from the definition of the emissivity profile in Equation 6.1. The proper area as measured by a stationary observer is obtained from the metric.

For radial bins on the accretion disc, $dt = d\theta = 0$, so the area element is

$$d^2x = \sqrt{g_{rr}g_{\varphi\varphi}}drd\varphi$$

For the Kerr metric, this gives

$$d^2x = \frac{\rho}{\sqrt{\Delta}}\sqrt{r^2 + a^2 + \frac{2a^2r}{\rho^2}}drd\varphi \tag{6.2}$$

So the proper area of a stationary annulus of co-ordinate thickness dr at radial co-ordinate r is

$$A(r, dr) = 2\pi\frac{\rho}{\sqrt{\Delta}}\sqrt{r^2 + a^2 + \frac{2a^2r}{\rho^2}}dr \tag{6.3}$$

In addition to the warping of spacetime around the black hole, the proper area of an orbiting element of the disc will be length contracted according to a stationary observer, so in the frame of the reflecting material, the area will be increased by a factor of γ, the Lorentz factor of the orbiting disc element.

A further subtlety lies here, and that is the velocity of the 'stationary' observer mentioned above. In the Kerr spacetime, the rotation of the black hole causes 'frame-dragging' of an observer whose angular momentum is zero. Therefore it is more meaningful to define the stationary observer as one who is dragged in this way, rotating at $\frac{d\varphi}{dt} = \omega = \frac{2ar}{\Sigma^2}$ (where $\Sigma^2 \equiv \left(r^2 + a^2\right)^2 - a^2\Delta\sin^2\theta$). In fact, the solution $\frac{d\varphi}{dt} = 0$ is not possible within the stationary limit surface upon which $g_{tt} = 0$ (this lies at $2\,r_{\rm g}$ for a maximally rotating Kerr black hole) — massive particles are forced to orbit the black hole within this region since there is no allowed solution of the geodesic equations which have zero 3-velocity.

The Lorentz factor of the orbiting disc element is calculated from the disc velocity with respect to an observer with $\frac{d\varphi}{dt} = \omega$. Solving the geodesic equations for a massive particle in a circular orbit ($\dot{r} = 0$) in the equatorial plane, the 4-velocity of the disc element is

$$\mathbf{v}_d = (\dot{t}, 0, 0, \dot{\varphi}) = \dot{t}(1, 0, 0, \Omega)$$
$$\Omega = \frac{d\varphi}{dt} = \left(a \pm r^{\frac{3}{2}}\right)^{-1}$$

(with the $+$ and $-$ signs in the denominator corresponding to prograde and retrograde orbits respectively). This is then projected into the frame of the observer (whose tetrad basis is constructed as for the X-ray source) by taking the appropriate scalar products.

$$v^{(a)} = \mathbf{v}\cdot\mathbf{e}'_{(a)} = g_{\mu\nu}v^\mu e^\nu_{(a)}$$

The Lorentz factor is then calculated from the 3-velocity, $\overrightarrow{v} = (v^{(1)}, v^{(2)}, v^{(3)})$ and its squared magnitude, $v^2 = (v^{(1)})^2 + (v^{(2)})^2 + (v^{(3)})^2$.

$$\gamma = \frac{1}{\sqrt{1 - \frac{v^2}{c^2}}}$$

In addition to the relativistic effects on the areas of the radial bins, the energy of individual rays will be red or blueshifted as rays travel further from or closer to the black hole due to the variation in the rates at which the proper times of observers elapse. Since the emissivity is defined as the flux emitted from the disc (proportional to the flux received for reflection) and the flux is the power per unit area, it is proportional to the product of the photon arrival rate and the energy of each photon. The emissivity is enhanced by a factor of g^{-2}, where $g \equiv \frac{\nu_{\rm E}}{\nu_{\rm O}}$ is the ratio of the emitted and observed photon energies. The first factor of g arises from the shifts in the energy of individual photons, while the second is due to the photon arrival rate along each ray. The redshift is calculated by the projection of the photon 4-momentum on its geodesic on to the observers' timelike axes since the photon energy is the p^0 component of the 4-momentum.

$$g^{-1} \equiv \frac{\nu_{\rm O}}{\nu_{\rm E}} = \frac{\mathbf{v}_{\rm O} \cdot \mathbf{p}({\rm O})}{\mathbf{v}_{\rm E} \cdot \mathbf{p}({\rm E})} = \frac{g_{\mu\nu} v_O^\mu p^\nu(O)}{g_{\rho\sigma} v_E^\rho p^\sigma(E)} \tag{6.4}$$

where $\mathbf{v}_{\rm O}$ and $\mathbf{v}_{\rm E}$ are, respectively, the 4-velocities of the observer (the disc element) and emitter (the primary X-ray source), while $\mathbf{p}(x)$ is the photon 4-momentum as a function of position along the geodesic, here taken at observation and emission.

Putting this together, if the photon count in a radial bin at co-ordinate radius r and of thickness dr is $N(r, dr)$, the emissivity profile is given by

$$\epsilon(r) = \frac{N(r, dr)}{g^2 A(r, dr)} \tag{6.5}$$

6.2 Theoretical Emissivity Profiles

6.2.1 Relativistic Effects

Computing the illumination of the accretion disc resulting from an isotropic point source at a height of $10\,r_{\rm g}$ on the rotation axis above the plane of the accretion disc (Fig. 6.1) and specifically the emissivity profile (Fig. 6.2) illustrates the key effects that influence the form of the emissivity profile that will enable observed forms to be explained in terms of the properties of the X-ray source.

In a flat, Euclidean spacetime the flux received from the source at each point on the disc and thus the reflected flux (emissivity) from that point will vary simply as the inverse square of the distance from the primary X-ray source, projected into the direction normal to the disc plane. If the source is at a height h above $r = 0$ in the disc, the emissivity profile will go as $(r^2 + h^2)^{-1} \cos\vartheta$, with $\cos\vartheta = \frac{h}{\sqrt{r^2+h^2}}$, the angle from the normal at which the ray hits the disc. This will be constant (a flat profile) in the limit $r \ll h$ (the inner disc) and tending to r^{-3} at large radius, giving a power law emissivity profile with index 3 as can be seen where the flatter region of the emissivity profile becomes a power law of constant index at the break point, $r \sim 10 r_{\rm g}$ (approximately the height of the X-ray source above the accretion disc).

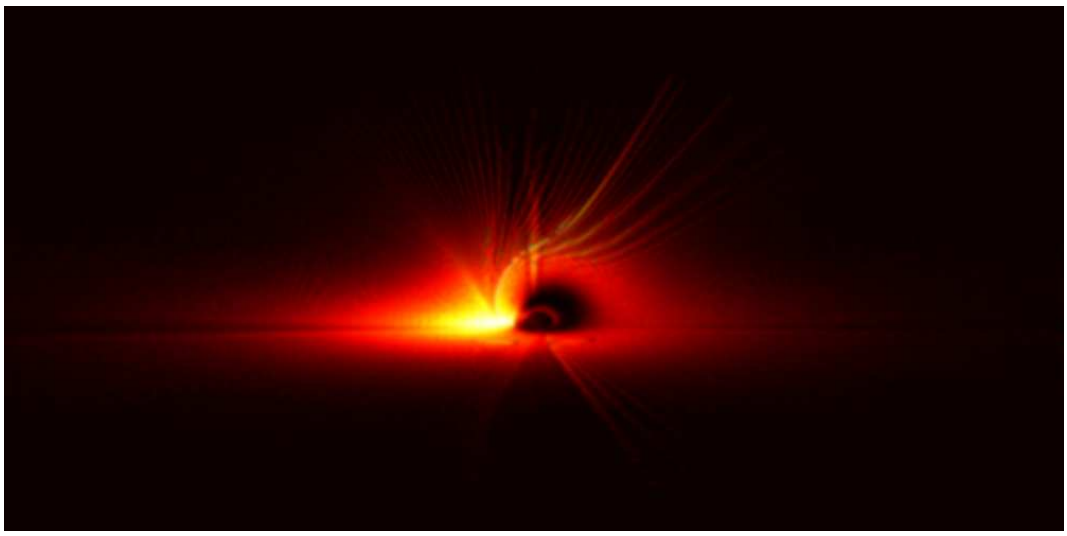

Figure 6.1: Illumination of the accretion disc in the Kerr spacetime by an isotropic point source at a height $10\,r_{\rm g}$ on the rotation axis, as seen by a stationary observer at infinity.

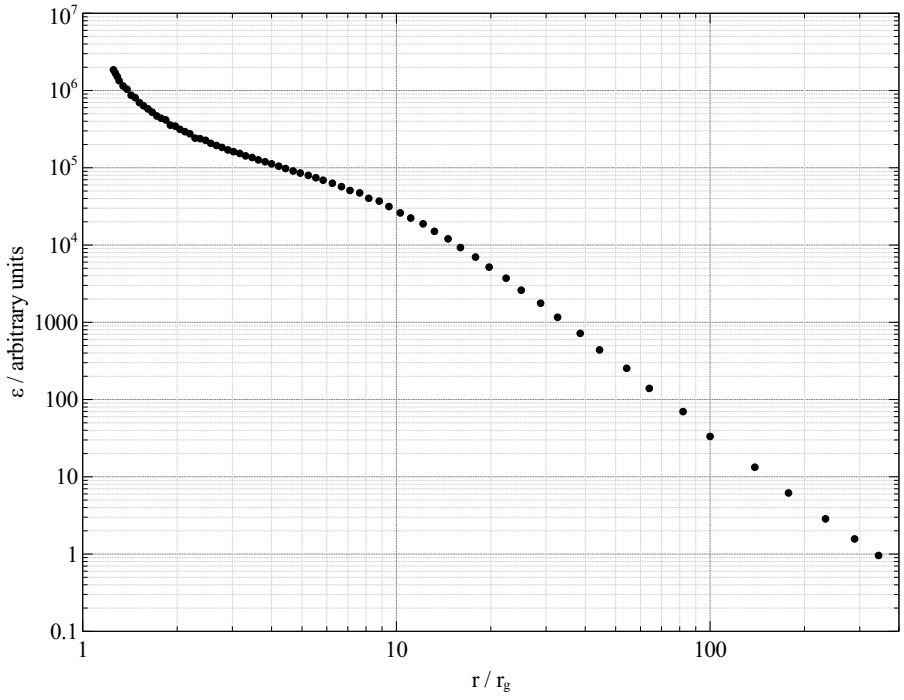

Figure 6.2: Theoretical accretion disc emissivity profile due to a stationary isotropic point source located at a height of $10\,r_{\rm g}$ on the rotation axis.

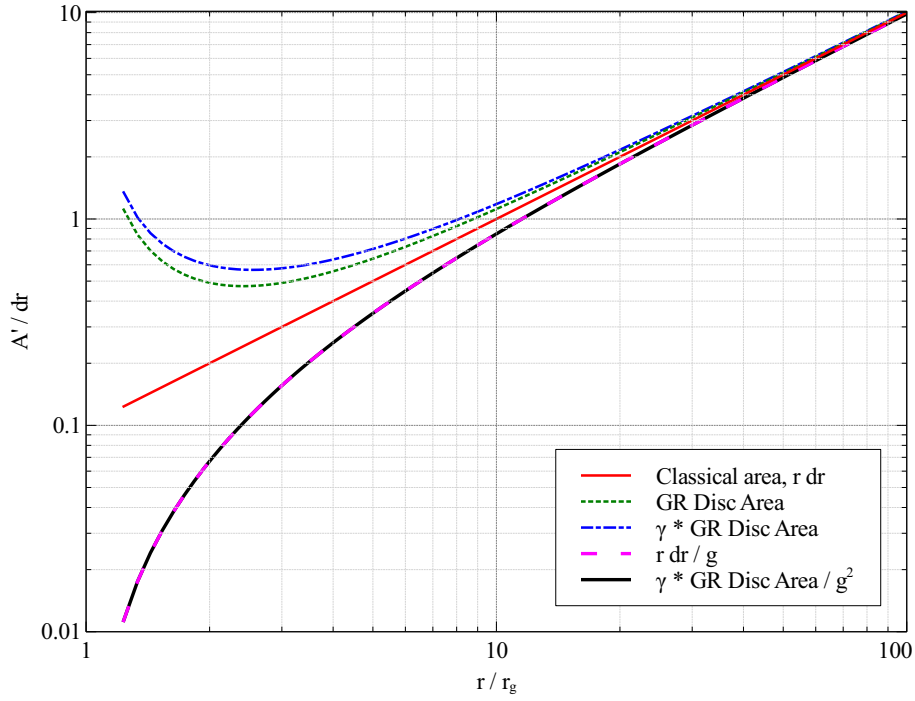

Figure 6.3: The effective area of successive annuli in the accretion disc, that is the total value (per dr) by which the photon count in the radial bin from the ray tracing simulation is divided in order to obtain the emissivity profile in Equation 6.5. The classical area, rdr of the annulus is compared with that in the Kerr spacetime for a stationary area element as well as an orbiting element, multiplying by the Lorentz factor, γ, to take into account Lorentz contraction as observed by a stationary observer. Finally, the effect of redshift on the rays is accounted for. It is noted that the relativistic effects on the area of the disc element exactly cancel one factor of the redshift, g, such that the fully relativistic result is equal to rdr/g.

The index of the power law over the outer region of the disc is, however, slightly steeper than the classical case of 3.0, with a value of around 3.2. In the presence of the black hole, gravitational light-bending will act to focus light rays from the point source towards the black hole and will therefore increase the flux incident on the inner regions of the disc relative to the outer regions causing it to fall off faster, steepening the emissivity profile.

The contributions of the relativistic effects on the accretion disc itself are best illustrated by considering the 'effective area' of the annuli in the accretion disc, that is the total value (per dr) by which the photon count in the radial bin from the ray tracing simulation is divided in order to obtain the emissivity profile in Equation 6.5. Fig. 6.3 shows the classical area, rdr of the annulus, compared with the proper area in the Kerr spacetime for a stationary area element as well as an orbiting element, multiplying by the Lorentz factor, γ, to take into account Lorentz contraction as observed by a stationary observer.

On including the shift in photon energy and arrival rate (the factor of g^{-2} from Equation 6.4) as rays travel towards the black hole, the cause of the steep emissivity profile over the central regions of the disc is apparent. The increase in photon energy as well as the increased photon arrival rate along each ray as measured by observers closer to the black hole with more slowly elapsing proper times, means that the flux received by the disc is greatly enhanced on the inner parts, increasing reflection from these regions (notwithstanding the effects of radiation transport out to the observer at infinity, as the emissivity profile is defined in the local rest frame of the emitting material before the transfer to the observer is included in the formulation of the relativistic reflection spectrum).

It is interesting to note that the the general relativistic effects on the area of orbiting annuli in the accretion disc are cancelled exactly by one factor of the redshift, so in practice the effective area of the annulus is given by dividing the classical area (rdr) by one factor of the redshift. This function is also plotted for comparison.

6.2.2 Axial X-ray Sources

Theoretical emissivity profiles for isotropic point sources, stationary upon the rotation axis (Fig. 6.4, at varying heights above the black hole are shown in Fig. 6.5.

In all cases, the profile tends to a power law with an index slightly steeper than 3 over the outer regions of the disc (from 3.1 for a source at height $10\,r_{\rm g}$ to a steeper index of 3.3 for a source height of $3\,r_{\rm g}$), with the power law indices steepening as high as $6 \sim 7$ over the innermost parts.

It can be seen that as the source is moved higher up the rotation axis, further from the black hole, the region over which the emissivity profile is flattened increases (the region where $r \ll h$). The outer break-point in the power law form of the profile moves to coincide approximately in radius with the height of the source (Fig. 6.6) for sources at heights greater than $12\,r_{\rm g}$ with the outer break

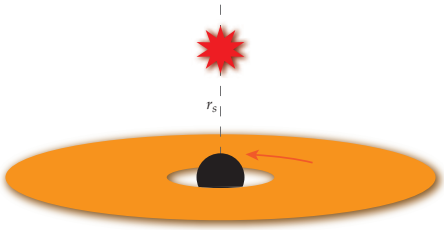

Figure 6.4: The geometry of an isotropic point source located on the rotation axis above the black hole for which accretion disc emissivity profiles are initially computed.

at a radius slightly greater than the height of the source for lower sources (due to the requirement for the break being $r \gg h$ which requires a greater increment in r for smaller h).

As the source is moved closer to the black hole, the steepening over the inner regions is greatly enhanced as more photons are focussed on to the inner regions of the disc while rays are bent towards the central black hole, until the source is lowered to $3\,r_{\rm g}$ at which point the steepening is so severe that it masks the classically-predicted flattened region of the profile (now constrained to a much smaller region of the disc where $r \ll h$). The emissivity profile now more closely resembles a once-broken power law which in the extreme case of a source at only $1.235\,r_{\rm g}$ above the black hole has a very steep power law index of around 8 out as far as a radius of $5\,r_{\rm g}$ before tending towards an index around 3.5 over the outer regions of the disc.

6.2.3 Orbiting Sources

Theoretical emissivity profiles for isotropic point sources, orbiting the rotation axis at varying radii at a height $h = 5r_{\rm g}$ above the disc plane, configured as in Fig. 6.7, are shown in Fig. 6.8.The sources are 'co-rotating' with the element of the accretion disc at the same radius, in the sense that a source at a distance x from the rotation axis as measured along a plane parallel to the accretion disc below is taken to be orbiting at the same velocity as the element of the disc in a (relativistic) Keplerian orbit at radius x. Where the orbiting source is close to the disc, this serves as an approximation to the orbital velocity, however if the X-ray source originates from flaring due to magnetic reconnection in poloidal field lines anchored to the ionised accretion disc, it may also be expected that the coronal material will move along with the orbiting disc.

As for the case of an axial source, the profiles are steepened from the classical case due to gravitational light bending, focussing more rays on to the inner region of the disc as well as the blueshifting of photons as they travel towards the innermost regions. These calculations show that the power law index of the emissivity profile over the innermost regions of the disc ranges from 7 for sources close to the rotation axis and black hole, within $5\,r_{\rm g}$, to 6 where the source located further out between 20 and $25\,r_{\rm g}$ (this central steepening of the emissivity profile is almost entirely due to the

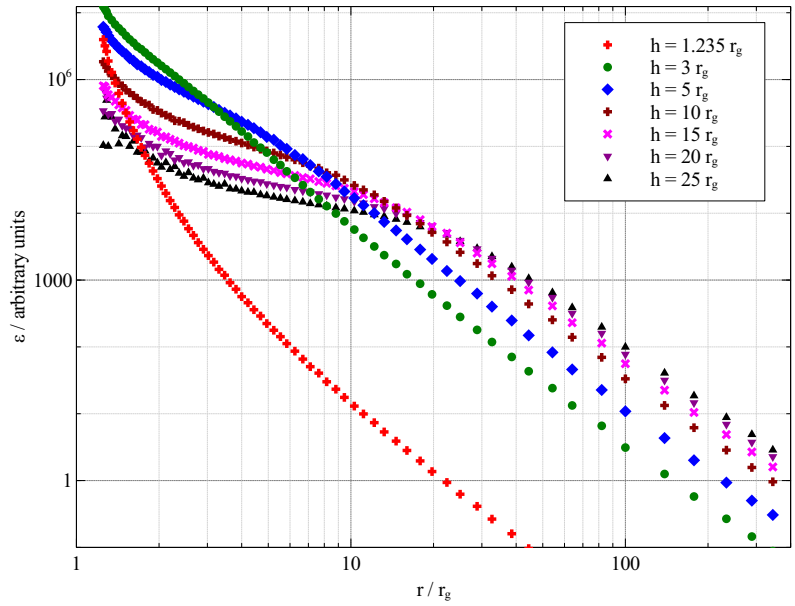

(a)

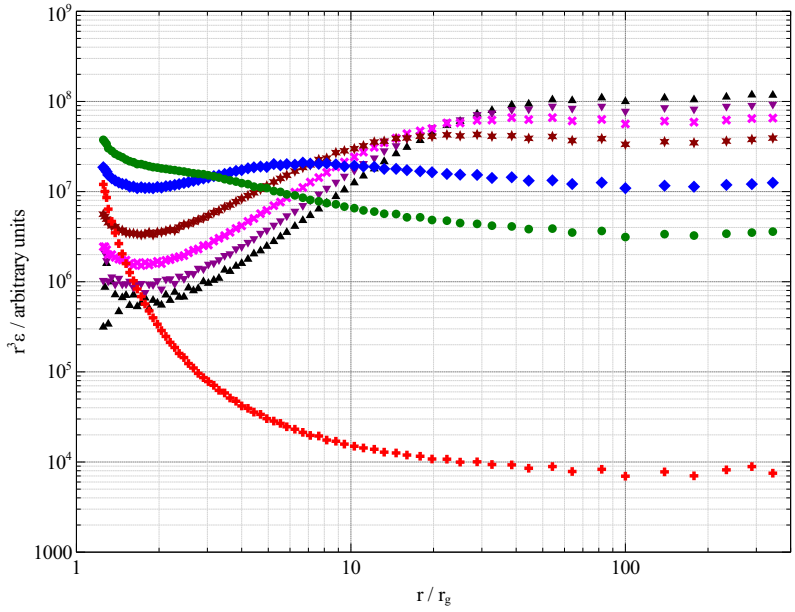

(b)

Figure 6.5: (a) Theoretical accretion disc emissivity profiles due to a stationary isotropic point sources located at varying heights above the black hole on the rotation axis. (b) The emissivity profiles scaled by r^3, illustrating the steepening of the emissivity profile over the inner disc (where the plot decreases) before the profile flattens (plot increasing) and then tends to a constant power law index of around 3 over the outer disc (plot approximately constant). The plot styles in the two plots correspond to one another.

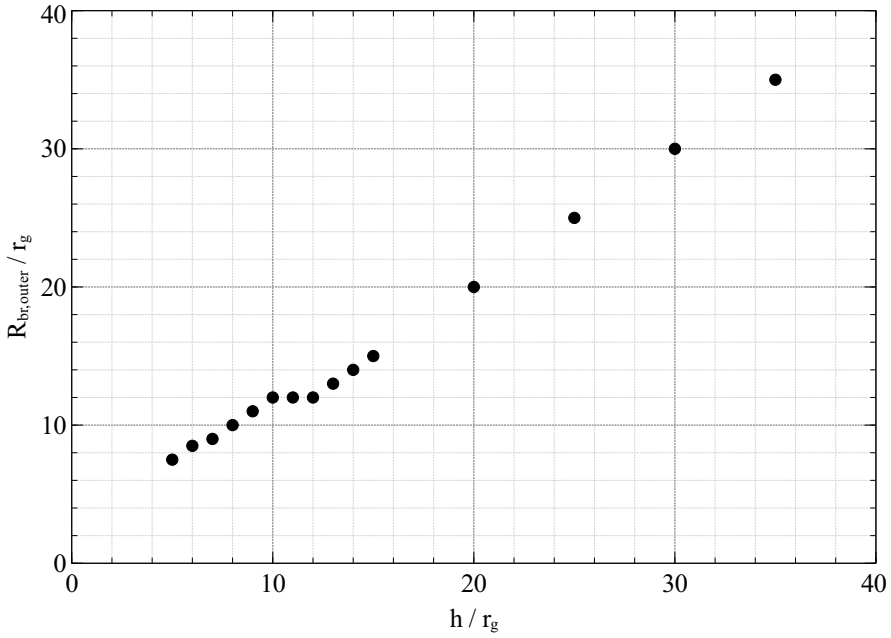

Figure 6.6: Observed location of the outer break point between the flattened region of the emissivity profile and the power law of constant index around 3 over the outer part of the accretion disc (where $r \gg h$) for axial point sources of increasing height above the disc.

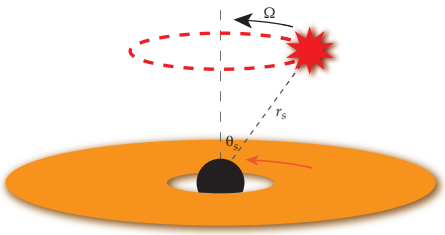

Figure 6.7: The considered geometry of an isotropic point source orbiting the rotation axis above the plane of the accretion disc.

blueshifting of photon energies and arrival rates as the rays travel towards the black hole now the source is located away from the inner parts of the disc). The power law index of the emissivity profile for the outer disc is 3.2 in each case.

The emissivity profiles are flatter over the middle region than for axial sources, owing to the source being located further out from the rotation axis, so the classical region where $h \gg r$ giving a constant flux at the disc is not masked by the relativistic effects steepening the profile over the inner disc.

Since an X-ray source close to the innermost stable orbit will be travelling at relativistic speeds if in a Keplerian orbit, emission will be 'beamed' into the forward direction of source motion. This will enhance the flux in front of the source and (to a lesser extent) on the region of the disc directly below the source locus while reducing the flux received outside of this region. This will serve to further flatten the emissivity profile in the vicinity of the source.

Following this reasoning, increasing the radius of the ring source flattens the profile out to a larger radius. Where the source height is less than or of the order of the source's radius, a small peak is observed in the emissivity profile below the source, where the proximate regions of the disc subtend a large solid angle at the source so a large number of rays are intercepted by this region of the disc before they are able to propagate further out.

6.2.4 Extended Sources

A vertically extended source of X-ray emission can be constructed by summing isotropic point sources at regular intervals above the plane of the accretion disc. This will allow the emissivity profiles of sources of finite height above the disc plane to be investigated. The emissivity profile resulting from a stationary, vertically extended source whose luminosity is constant along its length is shown in Fig. 6.9. These profiles take an almost constant power law index all the way out on the disc as the profiles from sources at successive heights sum together, masking the flattened part of each. There is steepening due to relativistic blueshift on the innermost parts and a very slight break

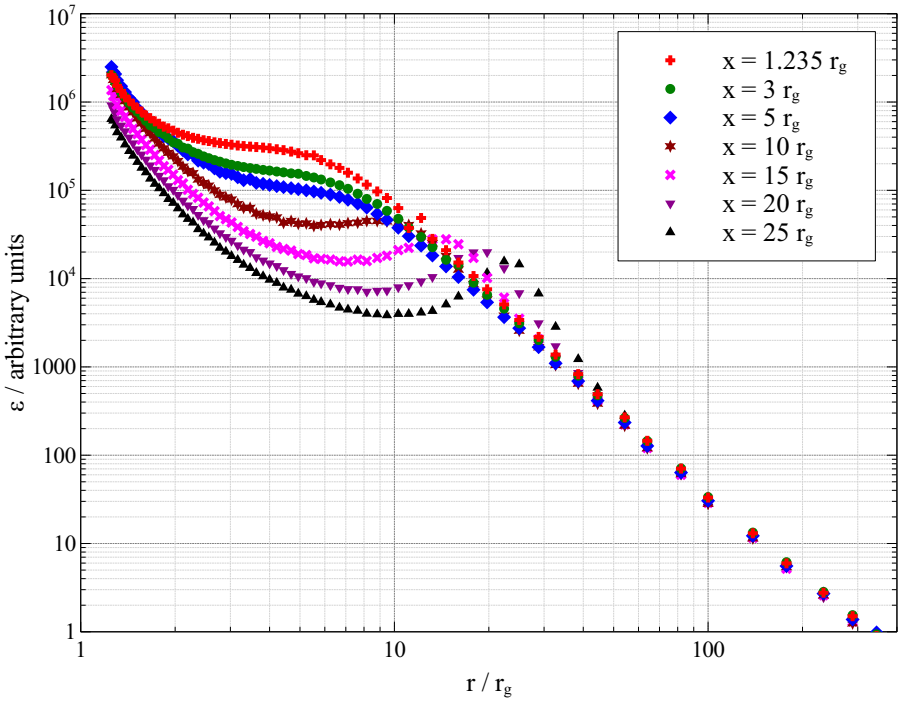

Figure 6.8: Theoretical emissivity profiles for isotropic point sources orbiting the rotation axis at varying radii at a height $h = 5r_g$ above the disc plane. The sources are 'co-rotating' with the element of the accretion disc at the same radius.

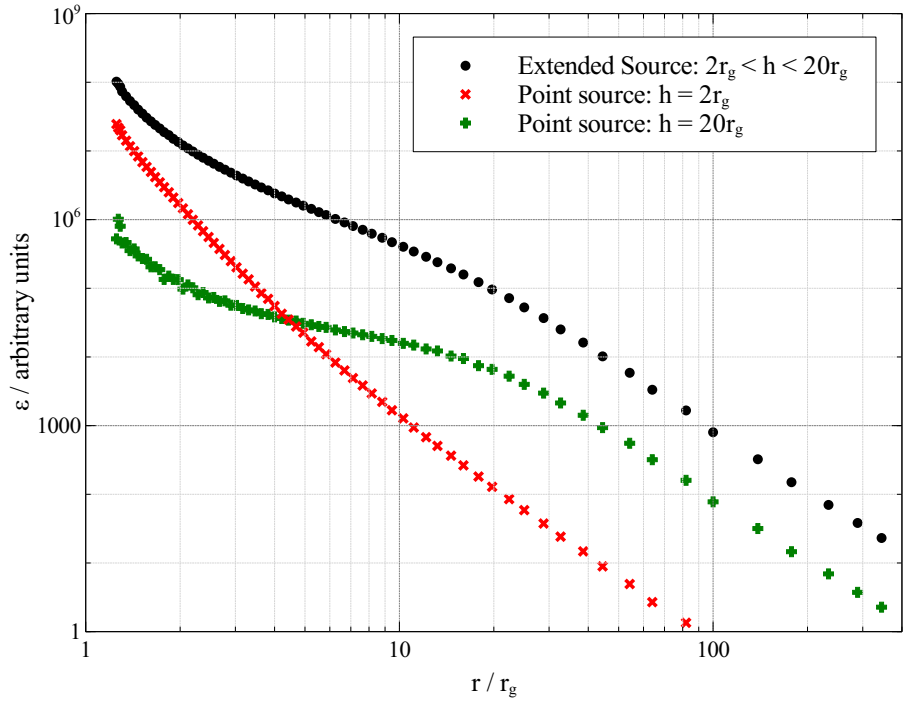

Figure 6.9: Theoretical accretion disc emissivity profile due to a vertically extended stationary source on the rotation axis, extending from $2\,r_{\rm g}$ to $20\,r_{\rm g}$. The emissivity profile compared to those of point sources located at either end of the extended source, illustrating that the overall emissivity profile combines the effects of the more extreme steepening over the inner disc from the source closer to the black hole, with the slight outer break point corresponding to that in the emissivity profile of the highest source (though the effect of summing the sources up the axis is to steepen the middle region of the profile, making the break points in the power law form less pronounced).

to the outermost index of around 3 corresponding to the break point in the emissivity profile of the uppermost point in the source.

Modelling a radially extended source (Fig. 6.10) at a height of $10\,r_{\rm g}$ and extending radially to $25\,r_{\rm g}$ produces an emissivity profile as shown in Fig. 6.11 and, for reference, is compared to a single point source located at the outer extent. It can be seen that the outermost break point in the power law form is determined by the outer extent of the source (when its radial extent is greater than its height), while the existence of X-ray sources within this radius cause the profile to be flattened off within this part before steepening, once again, over the inner regions of the disc.

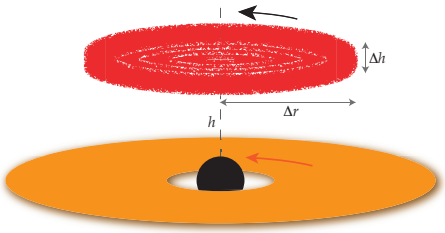

Figure 6.10: Extended X-ray source defined by a lower and upper height from the disc plane as well as an inner and outer radius.

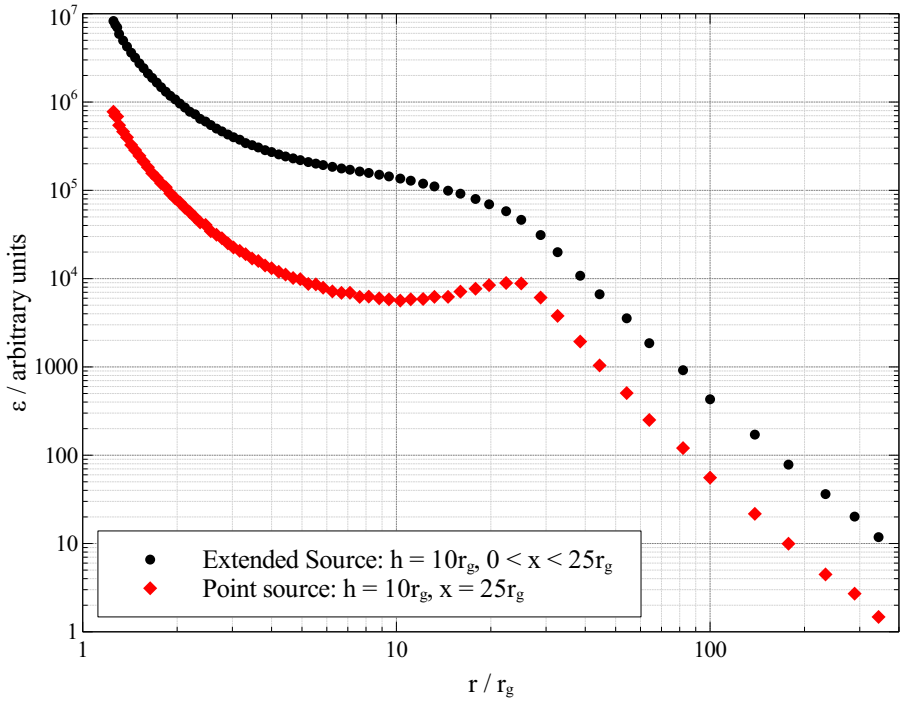

Figure 6.11: Theoretical accretion disc emissivity profiles due to an extended disc of emission located at a height of $10\,r_{\rm g}$ above the disc plane and extending radially to $25\,r_{\rm g}$ from the rotation axis, compared to that arising from a point source orbiting on the outermost edge of this source.

6.2.5 Jet Sources

X-ray emitting jets of collimated particles accelerated to relativistic velocities are observed in a number of galactic black hole binaries such as Cygnus X-1. It is conceivable that it is the X-rays from this jet that illuminate the accretion disc giving rise to the reflection dominated component of the spectrum. A vertically collimated X-ray source could also represent, for example, the X-ray emission from a vertically collimated jet of particles accelerated up along the rotation axis of the black hole seen in radio galaxy including Cygnus A and Centaurus A.

Fig. 6.12 shows the accretion disc emissivity profiles due to illumination by point sources moving radially at a constant velocity up the rotation axis (the point sources are assumed to be isotropic in their instantaneous rest frames) compared to a stationary source. The emissivity profile are computed, as before, by constructing the tetrad basis vectors in the instantaneous rest frame of the X-ray source, now moving radially.

Gravitational light bending and blueshifting of rays still enhances the emission reaching the very inner part of the disc, however the highly relativistic radial motion of the sources causes the emission to be beamed in front of the motion, greatly reducing the emission behind the jet that reaches the middle region of the accretion disc (Fig. 6.13). The emission reaching the accretion disc drops dramatically by $1.5 \sim 2$ orders of magnitude on the middle parts.

The forms of the emissivity profiles greatly differ from observed emissivity profiles. The steep fall-off and low fraction of the initial radiation that is reflected suggests that relativistically moving jet sources are not responsible for the significant reflection components observed in AGN and galactic black hole binaries, rather these more likely occur from a more slowly moving corona.

Accelerating jets of particles do, however, raise the possibility that the observed X-ray continuum and reflected component could be disconnected, with a fairly constant reflection component from a steady base of a jet or extended corona while the observed variable continuum radiation is dominated by fast moving particles in the jet accelerated by a variable mechanism. Weaker variation of the reflection component that is uncorrelated with the variation in the primary continuum was observed by Vaughan & Edelson (2001) and Fabian & Vaughan (2003b) in MCG–6-30-15. Such disconnection of the observed continuum and reflection also relaxes the constraint on the relative fluxes observed in the continuum and reflection components of the spectrum if they are no longer dominated by the same component.

6.2.6 Black Hole Spin

The most significant effect of varying the spin of the black hole is to change the location of the innermost stable circular orbit (ISCO). For a maximally rotating black hole ($a = 0.998$) in the Kerr

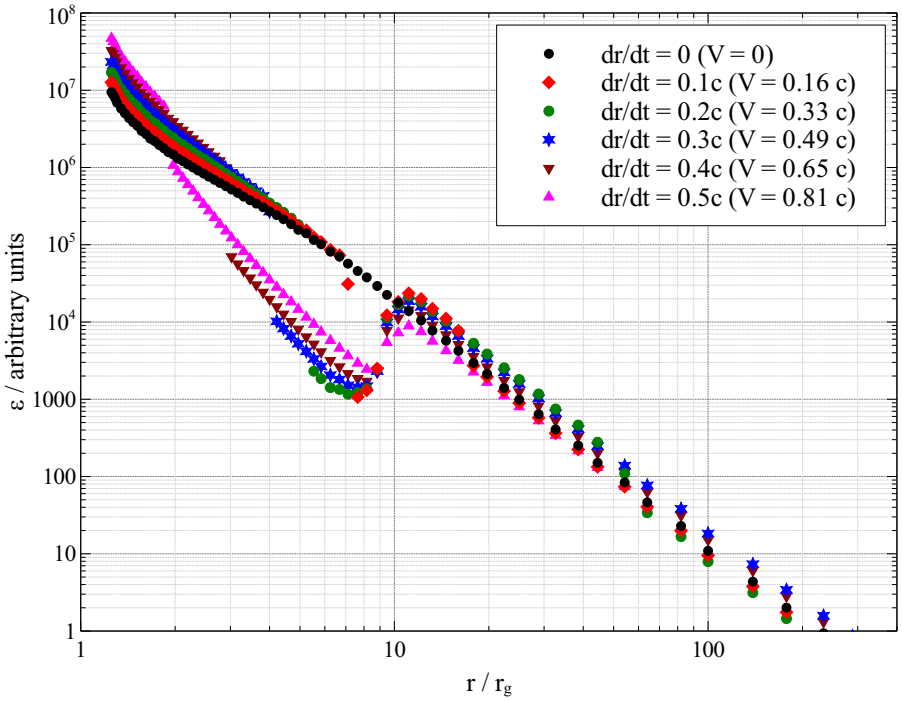

Figure 6.12: Theoretical accretion disc emissivity profiles due to a 'jet' component moving radially up the rotation axis. The moving point source is taken to be at a height of $5\,r_{\rm g}$ and is assumed to be isotropic in its instantaneous rest frame. Velocities are quoted in the global Boyer-Lindquist co-ordinates (dr/dt) as well as those measured by a stationary observer at the same location (V). The rays propagating backwards, towards the black hole, are still focussed onto the inner parts of the accretion disc, however as the relativistic motion of the source outwards causes emission to be beamed away from the accretion disc causing a sudden drop in the emission reaching the disc over the middle region.

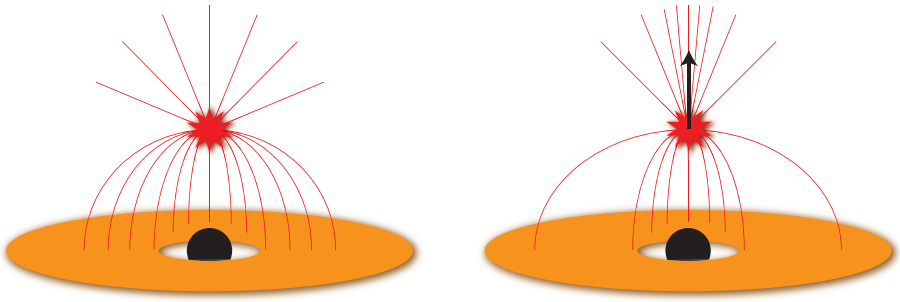

Figure 6.13: Relativistic motion of the jet source causes the emission to be beamed into the forward direction of motion. The black hole still focusses the backward emission onto the innermost regions of the accretion disc, however X-rays are now beamed away from the accretion disc, reducing reflection from the middle region.

spacetime, the ISCO lies at a radial co-ordinate of $1.235\,r_{\rm g}$ while for a non-rotating, Schwarzschild black hole, the ISCO moves out to $6\,r_{\rm g}$. The accretion disc cannot exist stably within the ISCO since material is unable to maintain a stable orbit here and will plunge into the black hole, reducing the density in this region causing little or no reflection to be seen within the ISCO.

Fig. 6.14 shows theoretical emissivity profiles for the accretion disc around black holes with varying (dimensionless) spin parameter, a, for both an axial and orbiting ring sources. It can be seen that the spin parameter has little effect on the emissivity at specific locations upon the disc, with the only notable change in the profiles being the truncation of the disc at greater radii as the spin parameter decreases. As such, the steepening over the inner part of the accretion disc is only seen for rapidly spinning black holes, with no steepened inner part seen for $a \leq 0.8$, though this is due to the lack of reflector at small radius where the spin is low rather than an intrinsic effect of the black hole spin. In the case of the source orbiting with the same angular velocity as the disc element below, reflection is slightly enhanced from the innermost regions for lower values of the spin owing to the angular velocity of a circular orbit being greater for smaller values of the spin parameter, increasing relativistic beaming.

This is, of course, only accounting for the propagation of X-rays around the black hole and assuming 'idealised' reflection off of a razor thin accretion disc extending as close to the black hole as it is able to as defined by the innermost stable orbit. It may be that the accretion disc does not extend this far inwards, in the case of a truncated accretion disc with an advection-dominated hot accretion flow in the inner regions, though this solution would be more applicable to accretion discs around galactic black holes rather than to AGN. For example, Beckwith et al. (2008) find in general relativistic magneto-hydrodynamic simulations that there is significant thermal dissipation within the innermost stable orbit, regardless of the spin of the black hole. The density of the accretion flow will drop greatly in this region (both due to the high temperatures and there being no stable circular orbit such that material plunges into the black hole), so little reflection, with which we are concerned here, will be observed from the accretion flow within the innermost stable orbit.

6.2.7 Returning Radiation

In general relativity, it is conceivable that X-rays reflected from one part of the accretion disc will be bent around the black hole back to the disc to be reflected a second time (Cunningham, 1976). Ross et al. (2002) considered the spectrum of the reflected radiation from an ionised slab (*i.e.* an accretion disc) if a fraction of the reflected radiation is said to return to the reflector as incident radiation. They found that multiple reflection of returning radiation strengthens the broadened absorption and emission features such as the iron K line as well as steepening the softer part of the spectrum below 2 keV. We here simply consider the effects of gravitational light bending returning radiation to the disc in terms of the 'raw' emissivity rather than considering the energy-dependent

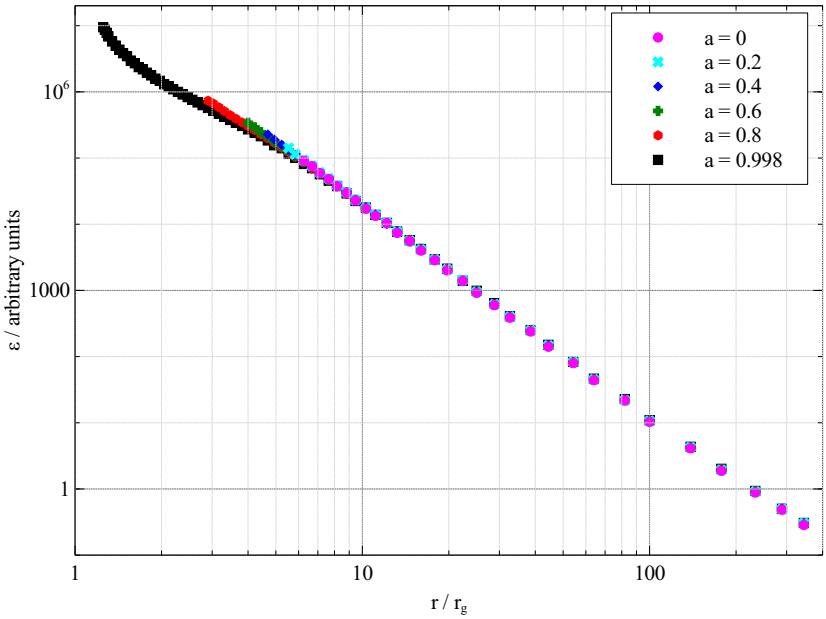

(a)

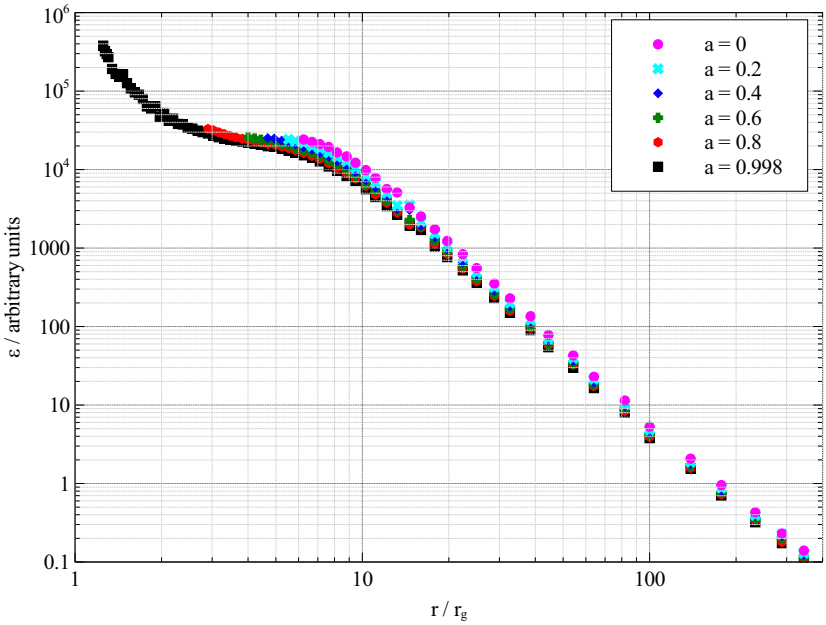

(b)

Figure 6.14: Theoretical emissivity profiles of the accretion disc surrounding black holes with varying (dimensionless) spin parameter, a for (a) a stationary source located at a height $5\,r_{\rm g}$ on the rotation axis and (b) a ring source radius $3\,r_{\rm g}$ located at a height $5\,r_{\rm g}$ co-rotating with the disc below.

details of the reflection spectrum, since the emissivity profile is determined from the emission lines which are enhanced so we determine if this measurement is affected by returning radiation.

In order to compute the emissivity profile due to radiation returning to the accretion disc from the primary reflection component, the emission from the disc is modelled as the sum of isotropic point sources in (relativistic) Keplerian orbits in the disc at regular radial intervals. Due to the axisymmetry of the Kerr spacetime, each of these point sources represents emission (or more specifically reflection) from its respective annulus. The photon count from each source is scaled by the emissivity profile across the disc to account for the variation in incident flux and is multiplied by the (relativistic) area of the annulus.

This, of course, assumes that in the frame of the disc material, the reflected radiation is emitted isotropically while in reality anisotropic emission from atomic processes and Compton scattering will depend on the angle of incidence of the incoming radiation (Svoboda et al., 2010). Assuming isotropic emission, however, provides a simple model which illustrates an upper limit of the effect of returning radiation.

Simulations reveal that as many as 50 per cent of the photons reflected from the accretion disc are returned to the disc (since for a typical X-ray source located above the plane of the accretion disc, the reflected flux will be concentrated on the innermost parts of the disc where the influence of the black hole focusing them back to the disc is the greatest).

Computing the returning radiation from a disc illuminated by a point source at a height $10\,r_{\mathrm{g}}$ above the disc around a maximally spinning black hole yields an emissivity profile with an approximately constant power law slope, steepening over the innermost regions of the disc. Once the photon counts returning to the disc have been divided by the effective areas of the annuli, the emissivity due to returning radiation is an order of magnitude lower than that due to the primary X-ray source and with its almost constant power law slope (with most of the returning photons ending up on the inner parts of the disc), the returning radiation has little effect on the overall shape of the emissivity profile, as shown in Fig. 6.15.

These results are consistent with those of Agol & Krolik (2000) who show that for a maximally spinning black hole, up to 50 per cent of the radiation emitted from the accretion disc can be returned to the disc before finally being observed at infinity, though we here explicitly demonstrate that the distribution of re-reflected emission from the disc means that returning radiation does not greatly affect the observed emissivity profile of the accretion disc. Agol & Krolik (2000) also note that the fraction of the flux returned to the accretion disc for more slowly spinning black holes is less (as many of the returning rays end up within the innermost stable orbit in this case) so as returning radiation in the maximally spinning case does not affect the emissivity profile substantially, it will do so even less for more slowly spinning black holes. Furthermore, we can say that even including the effects of returning radiation, the black hole spin does not greatly affect the form of the emis-

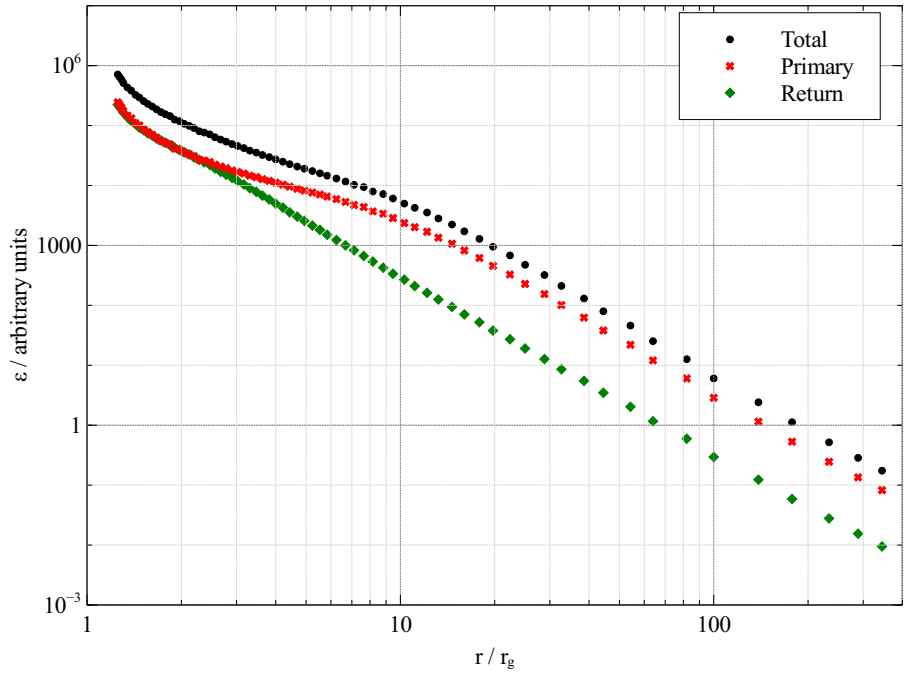

Figure 6.15: The effect of reflected radiation returning to the accretion disc to be reflected again on the overall emissivity profile. The emissivity profiles due to the primary X-ray source and returning X-rays are shown as red crosses and green diamonds, respectively, and the overall profile (the sum of these contributions) is shown as black points. Returning radiation has little effect on the overall emissivity profile.

sivity profile save for the innermost extent of the accretion disc and thus the degree of steepening observed over the inner part of the disc.

6.3 The Incident Spectrum

To this point, the radiative transfer between the X-ray source and the accretion disc has made no assumptions about the spectrum of the radiation emitted from the corona, rather it has computed the shift in the flux received by the disc along single rays, assuming implicitly that all of the photons are emitted at the same energy. This has allowed us to gain insight into the relativistic effects affecting the reflection from the accretion disc and is applicable to 'reflection' of X-rays by any process.

In reality, of course, the reflection spectrum arises from a number of physical processes (Compton scattering, Bremsstrahlung, fluorescent line emission, *etc.*), each of which is energy-dependent. In §4, the emissivity profile of the accretion disc was measured by considering the profile of the rel-

ativistically broadened iron Kα emission which is produced by the de-excitation of an atom after a photon is absorbed at 7.1 keV. The strength of the line emitted from any given part of the accretion disc will depend upon the number of incident photons at 7.1 keV, therefore emission will be enhanced from parts of the accretion disc that see more photons shifted into this energy according to an observer on the surface of the disc and emission will be decreased where photons are shifted out of this energy.

The spectrum from the corona is taken to be a power law, characterised by the photon index, Γ. In the rest frame of the coronal emission,

$$N_S(E)\,dE_S = E_S^{-\Gamma}\,dE_S \tag{6.6}$$

While observers at the source and on the disc will measure the photons to be at different energies and will measure time passing at different rates, the number of photons that passes along a ray to the observer must be conserved:

$$N_D(E)\,dt_D\,dE_D = N_S(E)\,dt_S\,dE_S \tag{6.7}$$

Substituting the spectrum in the emitters frame from Equation 6.6 gives

$$N_D(E) = E_S^{-\Gamma}\,\frac{dt_S}{dt_D}\,\frac{dE_S}{dE_D}$$

Though, of course the energy of the photon measured in each frame is measured by the redshift, $g = \frac{E_S}{E_D}$ so $E_S = gE_D$ and $\frac{dE_S}{dE_D} = g$. Also, the time intervals are related by $\frac{dt_S}{dt_D} = g^{-1}$, so the continuum spectrum seen by an observer at a given location on the disc is given by the redshift from the source to that location:

$$N_D(E)\,dE_D = g^{-\Gamma}E_D^{-\Gamma}\,dE_D \tag{6.8}$$

Therefore, Equation 6.5 for the calculation of the emissivity from the number of photons in the bin is replaced by

$$\epsilon(r) = \frac{N(r,dr)}{g^{\Gamma}A(r,dr)} \tag{6.9}$$

Where, of course, in the case of extended X-ray sources, the redshift contributions should be computed independently and summed for each ray that lands in the bin.

The effect of a more steeply falling continuum spectrum (*i.e.* a greater value of Γ is to cause the emissivity profile to fall off more steeply over the inner part of the accretion disc as shown in Fig. 6.16. Since the photon counts decrease towards higher photon energies, the emissivity is enhanced on the inner part of the accretion disc where the radiation is blueshifted travelling from the corona closer to the black hole, since this will shift more photons from the lower energy part of the spectrum into the required band to excite the Kα line transition. The is emissivity profile outward of $10\,r_{\rm g}$ is unaffected where the blueshifting of photons between the corona and disc becomes less important.

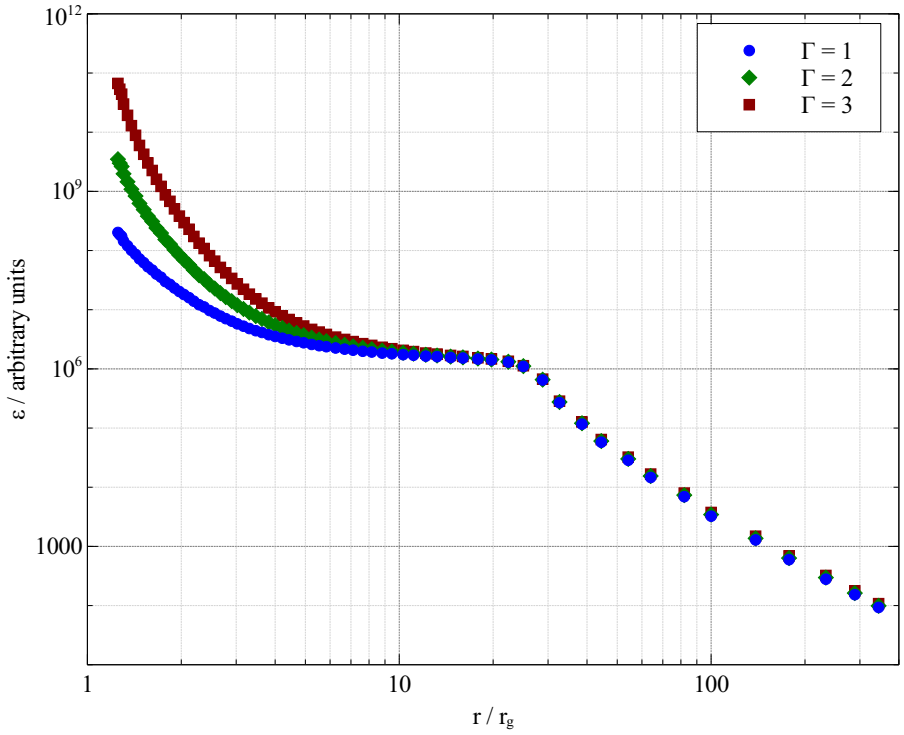

Figure 6.16: The effect of increasing spectral index, Γ (with photon counts in the X-ray continuum given by $N(E)\,dE = E^{-\Gamma}\,dE$) on the emissivity profile of an accretion disc illuminated by an extended corona spanning radially out to $30\,r_{\rm g}$.

6.4 The Case of 1H 0707-495

The emissivity profile of the accretion disc due to X-ray reflection in the narrow line Seyfert 1 galaxy, 1H 0707-495 was determined in §4, considering the relativistically broadened iron K line (whose rest-frame energy is 6.4 keV) to be composed of the sum of independent relativistically-blurred emission line components from successive annuli in the accretion disc and fitting for the relative contributions of these.

The accretion disc was found to have an emissivity profile approximated by a twice-broken power law, with a steep index of 7.8 over the innermost parts then flattening to almost constant emissivity (index zero) between $5.6\,r_{\rm g}$ and $34.8\,r_{\rm g}$ before tending to a constant index 3.3 over the outer parts of the disc (Fig. 6.17).

Fabian et al. (2009) and Zoghbi et al. (2010) report reverberation time lags of around 30 s where variability in the reflection dominated component of the spectrum is seen to respond to that in the power law continuum after a time lag due to the finite light travel time from the primary X-ray source to the reflecting accretion disc. If the mass of the black hole is taken to be $3 \times 10^6\,{\rm M}_\odot$, as quoted in the literature (see *e.g.* Zhou & Wang, 2005), this implies that a significant portion of the observed X-rays originate from a source located within $2\,r_{\rm g}$ of the reflector.

Comparing the observed emissivity profile to the theoretical emissivity profiles computed for a variety of source locations and geometries while applying the constraint that the source is as close to the disc as $2\,r_{\rm g}$ implies that the source is located at a low height close to the disc plane while extending radially outwards to between 25 and $35\,r_{\rm g}$ to account for the location of the outermost break point in the emissivity profile. A theoretical emissivity profile for a disc of emission between $2\,r_{\rm g}$ and $5\,r_{\rm g}$ above the disc, extending radially outward to $35\,r_{\rm g}$ with constant luminosity throughout its extent is shown in Fig. 6.17, accounting for the slope of the continuum spectrum seen in 1H 0707-495 with $\Gamma = 3$. Letting the source region extend to greater heights serves only to flatten the middle section of the emissivity profile. In general, the emissivity profile does not well constrain the vertical extent of the X-ray emitting region above the disc providing that its height is less than its radial extent to simultaneously satisfy the steep inner part and the location of the outermost break point. To account for the 30 s reverberation signal, it is likely that the source will be more luminous in the lower regions closer to the disc, however this is also accounted for in the fact that a larger fraction of the primary emission will reach the disc from lower sources than those further from the disc, as can be seen in Fig. 6.5, although a fully relativistic treatment of reflection time lags is required to quantify this fully and will be explored in §8.

The spectral features contributed to the emission line by the inner regions of the disc out to $10\,r_{\rm g}$ will appear in the energy range 3-5 keV (Fig. 4.1) over which the intrinsic energy resolution (FWHM) of the EPIC pn detector, used to obtain the spectra from which this emissivity profile was determined,

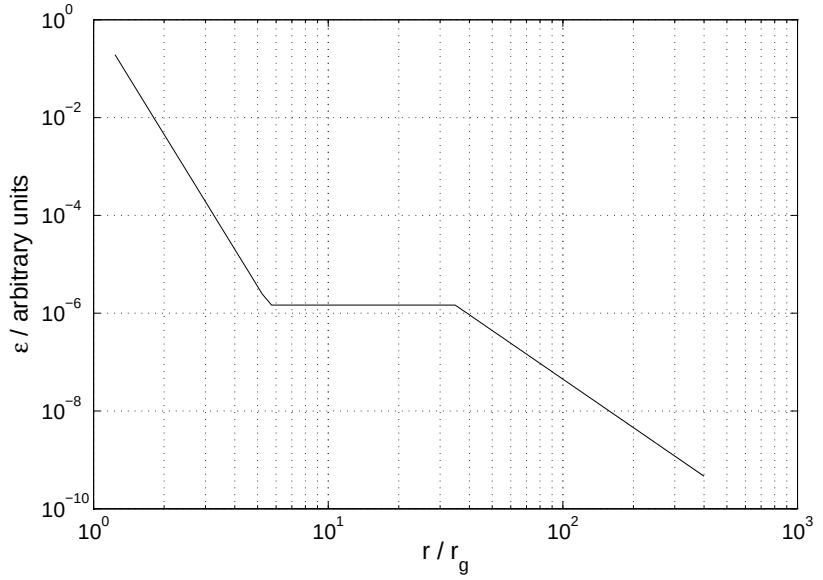

(a)

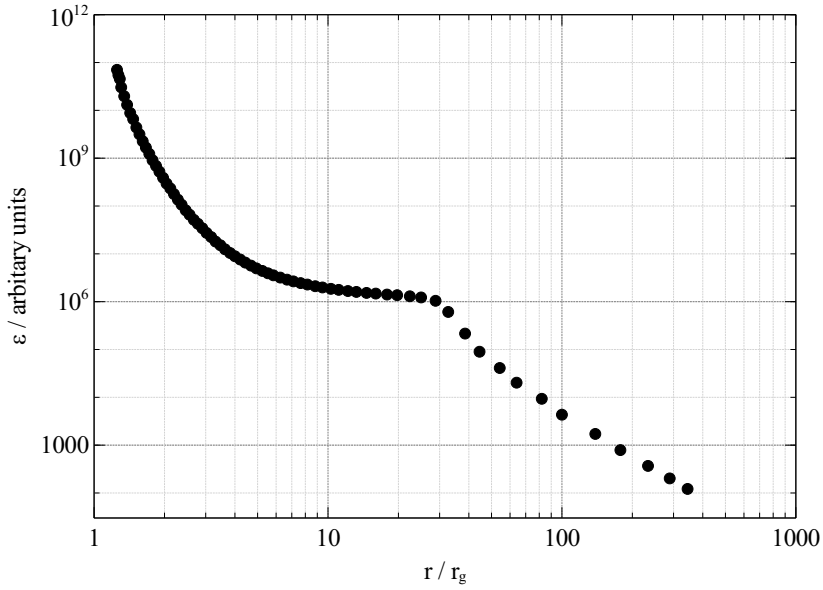

(b)

Figure 6.17: (a) Emissivity profile determined for X-ray reflection from the accretion disc in 1H 0707-495 in January 2008 by fitting for the relative contributions of components of the relativistically broadened iron K emission line from successive radii in the disc (§4), compared with (b) a theoretical emissivity profile due to an extended X-ray source extending radially outwards to $35\,r_{\rm g}$ and between 2 and $5\,r_{\rm g}$ above the plane of the accretion disc accounting for the photon index of the continuum spectrum measured in 1H 0707-495, with $\Gamma = 3$.

is 150 eV. Spectral features distinguishing the emission from these inner annuli of the accretion disc will, to some degree, be smoothed out by the detector such that they will be harder to distinguish above the power law continuum. The curving of the emissivity profile to the flattened middle section is therefore likely not fully resolved, rather a broken power law is fit to the observed emissivity profile.

The results of these ray tracing calculations combined with the observed emissivity profile of 1H 0707-495 and the reverberation time lags appear to suggest an emitting region surrounding the central black hole and covering the central parts of the accretion disc. While the exact geometry of the corona is not specified, modelling a uniform luminosity cylindrical source region allows the bulk of the X-ray emission to be located. This emitting region could consist a corona of hot electrons emitting X-rays through the inverse-Compton scattering of (thermal) seed photons emitted from the accretion disc. If this corona were optically thin to X-rays, as implied by the steep index of the power law continuum after Comptonisation of seed photons, for example a sparse plasma or even a region with emission originating from flares where magnetic reconnection takes place (Galeev et al., 1979; Merloni & Fabian, 2001; Goyder & Lasenby, 2004), rays emitted from any part of it could reach the accretion disc, as modelled in ray tracing simulations here and the corona would not obscure the emission from the regions of the disc below.

Following the same reasoning, the X-ray emitting coronae of IRAS 13224-3809 and MCG–6-30-15 can be inferred to lie in a similar region around the inner part of the accretion disc, extending outwards to radii of around $10\,r_{\mathrm{g}}$ in both cases (identifying the outermost break point in the emissivity profile with the radial extent of the source). In Cygnus X-1, however, the X-ray source appears to be confined in a much more compact region around the black hole, certainly within $4\,r_{\mathrm{g}}$ (with the flattened part of the emissivity profile being less well identified). Such a compact X-ray source could, indeed, correspond to the base of the observed radio jet in Cygnus X-1.

6.5 Conclusions

Numerical ray tracing simulations of the propagation of X-rays from a source in a corona surrounding the central black hole to the accretion disc have yielded theoretical predictions for the emissivity profile of the accretion disc due to X-ray reflection.

These calculations have demonstrated that the forms of the emissivity profiles observed through the profiles of relatively broadened emission lines from accretion discs in AGN (such as those from the narrow line Seyfert 1 galaxies 1H 0707-495, IRAS 13224-3809 and MCG–6-30-15 as well as the Galactic X-ray binary Cygnux X-1) arise naturally from the relativistic effects on the propagation of the rays around the black hole and on the accretion disc itself, with the simplest possible assumptions about the X-ray itself (assuming either an isotropic point source or an extended source

of uniform intensity throughout its volume).

By comparing observed emissivity profiles to those computed theoretically for different locations and geometries of the source along with constraints from the time lags between the continuum emission and reflection components in AGN, it is possible to constrain the location and extent of the primary X-ray source. The outermost radial extent of the corona is identified with the outermost break point in the (twice-broken power law) emissivity profile. In 1H 0707-495, the emissivity profile obtained from the data appears to suggest an X-ray source as low as $2\,r_{\rm g}$ above the plane of the accretion disc and extending outwards from the rotation axis to around $30\,r_{\rm g}$, while IRAS 13224-2809 and MCG–6-30-15 show X-ray sources extending radially out to $10\,r_{\rm g}$. The emissivity profile of the accretion disc in Cygnus X-1 suggests a much more compact corona, extending no further than $4\,r_{\rm g}$ from the black hole.

7

1H 0707-495 in January 2011: A Low Flux State

1H 0707-495 was the subject of a monitoring campaign using the *Swift* satellite from March 2010 to March 2011 to study its long-timescale variability. During this period, the X-ray and ultraviolet emission was observed during a 1 ks exposure approximately every four days with the *X-ray Telescope (Swift-XRT)* and the *Ultraviolet and Optical Telescope (Swift-UVOT)*.

From the Swift monitoring campaign data, it was noticed that 1H 0707-495 had become exceptionally faint in its X-ray emission in January 2011 (around MJD 55570). A target of opportunity (ToO) request was initiated, confirming the low flux state with daily monitoring of 1H 0707-495 with Swift and on 12$^{\text{th}}$ and 13$^{\text{th}}$ January 2011, 1H 0707-495 was observed with XMM Newton for a total of 100 ks. Fig. 7.1 shows the X-ray spectrum of 1H 0707-495 in Januray 2011 compared to that observed with XMM Newton in January 2008. The soft X-ray flux (below 1 keV) dropped by an order of magnitude between the 2008 and 2011 observations, while the flux at 5 keV (corresponding to the relativistically broadened iron Kα line) dropped by a factor of two to three.

It was found that the X-ray spectrum of 1H 0707-495 in the low flux state could be modelled as only consisting of the thermal emission as well as the relativistically blurred reflection from the accretion disc, with little or no contribution from the directly-observed power law X-ray continuum emitted from the corona (Fabian et al., 2011). The power law continuum spectrum required to reproduce

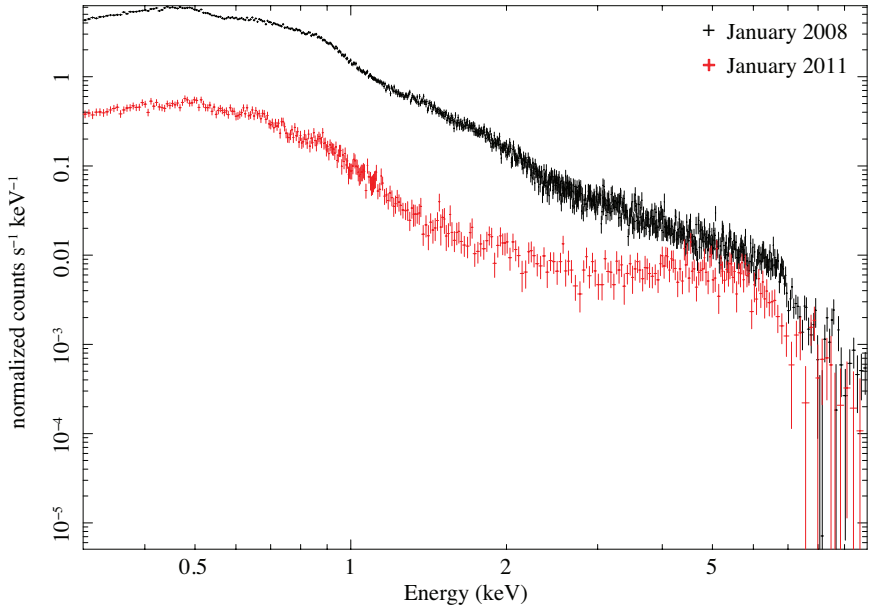

Figure 7.1: The X-ray spectrum, obtained with the EPIC pn detector on board XMM Newton, of 1H 0707-495 during the low flux state of January 2011 (red) compared to that obtained in January 2008 (black).

the observed reflection spectrum from the accretion disc was 'harder' (*i.e.* a less steeply falling spectrum) than in 2008 and taking the ratio of the observed spectrum to the best-fitting power law (fit in the $1.5 - 2.0$ keV band) in each case reveals the profile of the iron Kα emission line, as shown in Fig. 7.2.

7.1 The Accretion Disc Emissivity Profile and the Change to the X-ray Source

The emissivity profile of the accretion disc was obtained for the January 2011 observation of the low flux state of 1H 0707-495 by decomposing the observed relativistically blurred reflection spectrum (specifically the profile of the broad iron Kα emission line) into the contributions from successive radii in the disc and fitting for the relative contribution of each annulus (§4).

In this low flux state, the emissivity profile, Fig. 7.3(a), was found to fall off steeply ($\epsilon \propto r^{-8}$) over the inner regions of the accretion disc, out to around $5\,r_{\rm g}$. Little flux is received from reflection beyond a radius of $5\,r_{\rm g}$owing to the steeply-falling emissivity profile over the inner part and the overall flux simply being low, hence the emissivity profile of these regions is poorly constrained, however the data are consistent with the emissivity falling off with a power law index of $3 \sim 4$

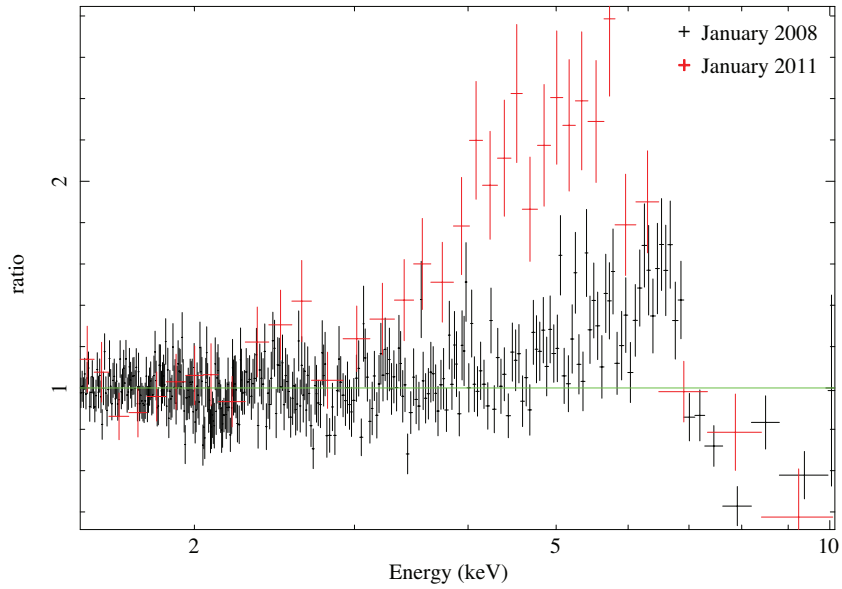

Figure 7.2: The ratio of the observed X-ray spectrum to the best-fitting power law (fit in the $1.5-2.0$ keV band) of 1H 0707-495 in the low flux state of January 2011 (red) compared to that in January 2008 (black), revealing the profile of the relativistically broadened iron Kα emission line in each case.

outward of $5\,r_{\rm g}$. The emissivity profile changed substantially from that found in January 2008, where fitting reflection from successive annuli in the accretion disc suggested a twice-broken power law form for the emissivity profile, with a steep index of 7.8 out to a radius of $5\,r_{\rm g}$, where the profile flattened to an index of zero out to around $30\,r_{\rm g}$ before tending to an index of 3 over the outer regions of the disc. This steepening of the emissivity profile can be seen in the shape of the iron Kα emission line in Fig. 7.2, with the line turning over at lower energy in 2011 rather than displaying the sharp peak just above 6.4 keV as it did in 2008. Now more than 90 per cent of the observed emission originates from within $2\,r_{\rm g}$, compared with 50 per cent from that region in 2008.

This dramatic change in the emissivity profile can be understood in terms of a change in the size of the coronal X-ray source by comparing the observed emissivity profile to theoretical predictions of the emissivity profile due to isotropic point sources located at varying heights above the black hole, as shown in Fig. 7.4. The observation of the low flux state reveals an emissivity profile explained by a compact source, confined to a small region around the rotation axis and close to the black hole. The source is now required to be at a height less than $1.5\,r_{\rm g}$ above the disc plane to explain the observed steepening over the inner region as shown in Fig. 7.3(b). With the source this close to the black hole, there is no flattened region in the emissivity profile. Rather, the relativistic effects close to the black hole steepen the inner region of the profile out as far as the region where $r \gg h$, so the emissivity profile takes the form of a once-broken power law from the steep inner profile to a

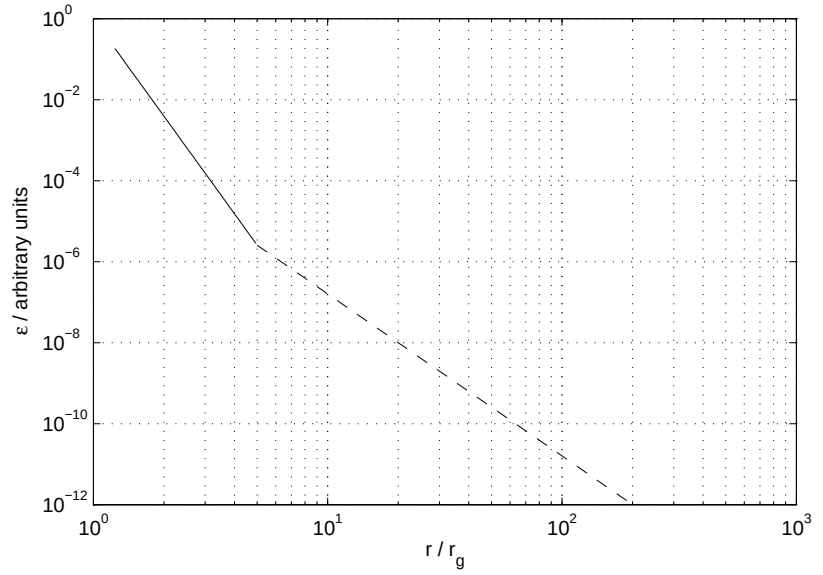

(a)

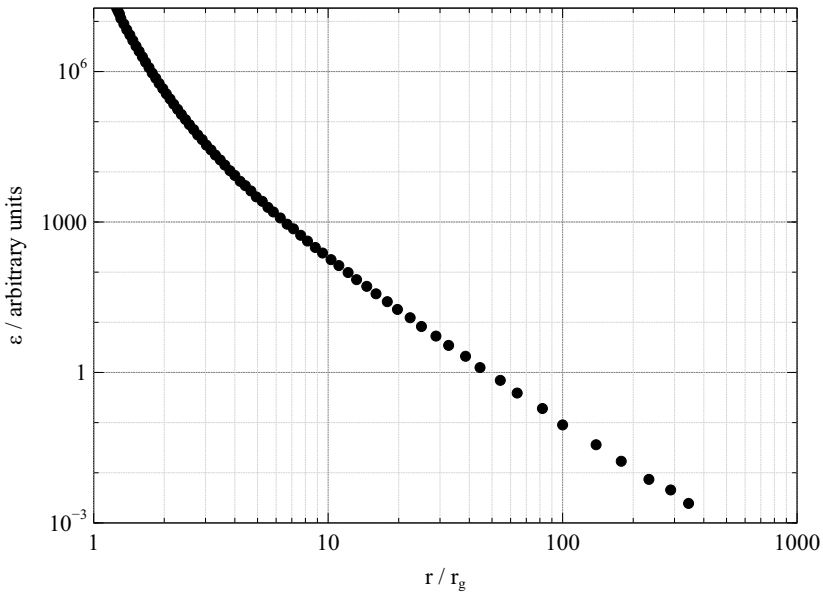

(b)

Figure 7.3: (a) Emissivity profile determined for X-ray reflection from the accretion disc in 1H 0707-495 in January 2011 by fitting for the relative contributions of components of the relativistically broadened iron K emission line from successive radii in the disc (Fabian et al., 2011), compared with (b) a theoretical emissivity profile due to a compact X-ray source located on the X-ray source 1.5 $r_{\rm g}$ above the plane of the accretion disc.

profile slightly steeper than r^3 (with the slight steeping from the classical case due to rays being focussed towards the black hole) over the outer regions of the disc.

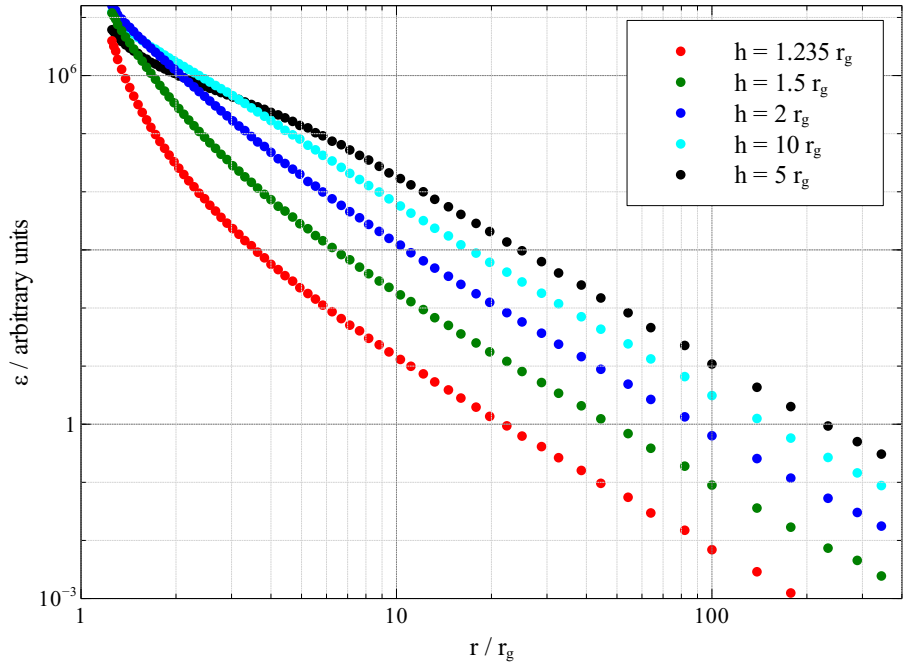

Figure 7.4: Theoretical emissivity profiles due to isotropic point sources located close to the central black hole at varying height above the accretion disc.

Fig. 7.5 shows the energy at which photons are observed from different locations in the accretion disc (with red corresponding to higher energies and blue corresponding to lower, redshifted energies) as well as the intensity of the incident (and hence reflected) radiation as a function of radius (the emissivity profile). From this illustration, it is clear that in the low flux state of January 2011, the vast majority of the emission is seen from the very innermost region of the accretion disc, with the blueshifted emission from the approaching side of the accretion disc is not seen, explaining the apparent shift in the peak of the emission line in Fig. 7.2.

7.2 The Disappearance of the Continuum

Ray tracing simulations also illustrate the variation in the reflected flux observed compared to that in the power law continuum as a function of the source height, by counting the photons in the simulation that hit the accretion disc compared to those which are able to escape to infinity to be detected in the coronal continuum (in practice, they are counted upon reaching a limiting radius of $1000\,r_{\rm g}$ in the simulation). The results are shown in Fig. 7.6. A similar result is obtained when

considering the variation in reflected and continuum flux as a function of source radius from the rotation axis.

As the X-ray source is moved closer to the black hole, the gravitational light bending becomes more extreme and more photons are focussed downwards towards the black hole and hence onto the disc to be reflected. The reflection fraction declines at the lowest source heights due to the hole in the centre of the accretion disc within the innermost stable orbit. Within this region, photons are lost inside the event horizon of the black hole.

The substantial drop in the observed power law continuum between the January 2008 observation and that of January 2011 supports the hypothesis that the primary X-ray source has collapsed down to a region close to the black hole such that these relativistic effects focus the majority of the rays towards the black hole and on to the disc, so a greater fraction of the emitted X-rays are reflected from the disc, while very few are able to escape as part of the continuum.

7.3 Conclusions

In January 2011, 1H 0707-495 was seen to drop into a state of low X-ray emission in which the observed spectrum was dominated by the reflection from the accretion disc with no discernible contribution detected from the directly observed power law continuum. Obtaining the emissivity profile of the accretion disc in this state by fitting the reflection spectrum as the sum of contributions from successive radii in the disc and comparing to theoretical predictions obtained from ray tracing simulations allows this low flux state to be interpreted as the coronal X-ray source collapsing down to a confined region close to the central black hole. Extreme gravitational light bending from such a source close to the black hole means that almost all of the emitted radiation is focussed down onto the accretion disc to be reflected or into the event horizon of the black hole. As such, little or no direct emission from the corona is observed.

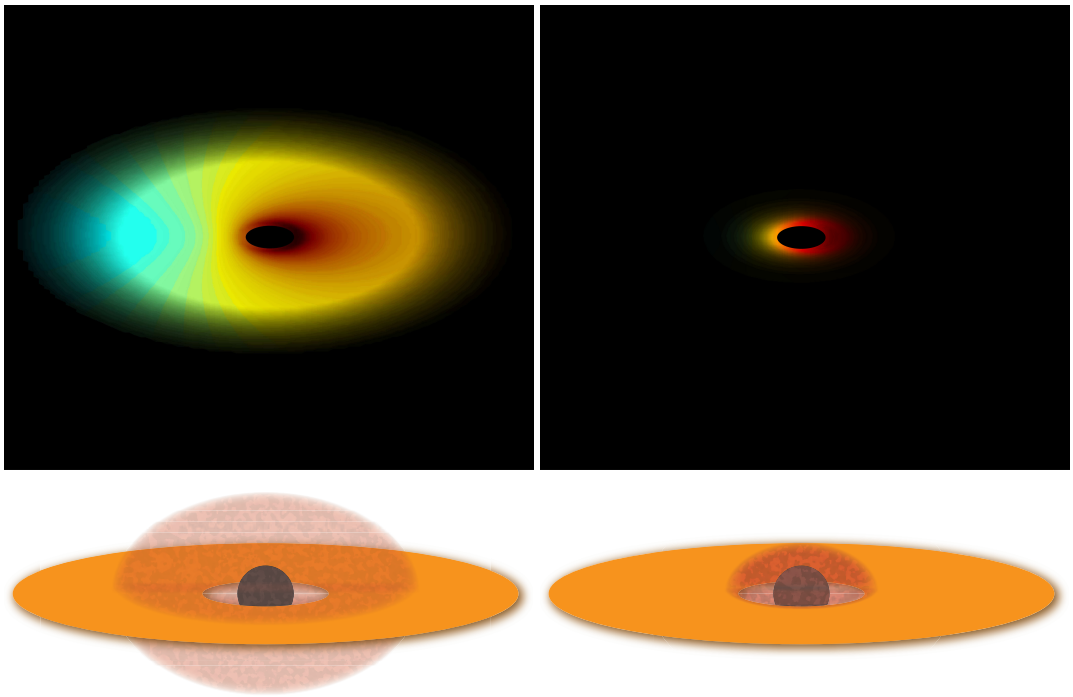

(a) January 2008 (b) January 2011

Figure 7.5: The changing emissivity profile of the accretion disc between the January 2008 and the low-flux state January 2011 observations can be interpreted as a change in the extent of the coronal X-ray source. Colours represent the observed energy of the reflected photons (due to the Doppler shifts and gravitational redshifts), with red corresponding to lower energies and blue corresponding to higher energies. The intensity of the image shows the emissivity profile of the accretion disc (measured in the frame of the emitter). When 1H 0707-495 dropped into a low flux state in January 2011, the emissivity profile is consistent with the X-ray source having collapsed down to a confined region close to the central black hole.

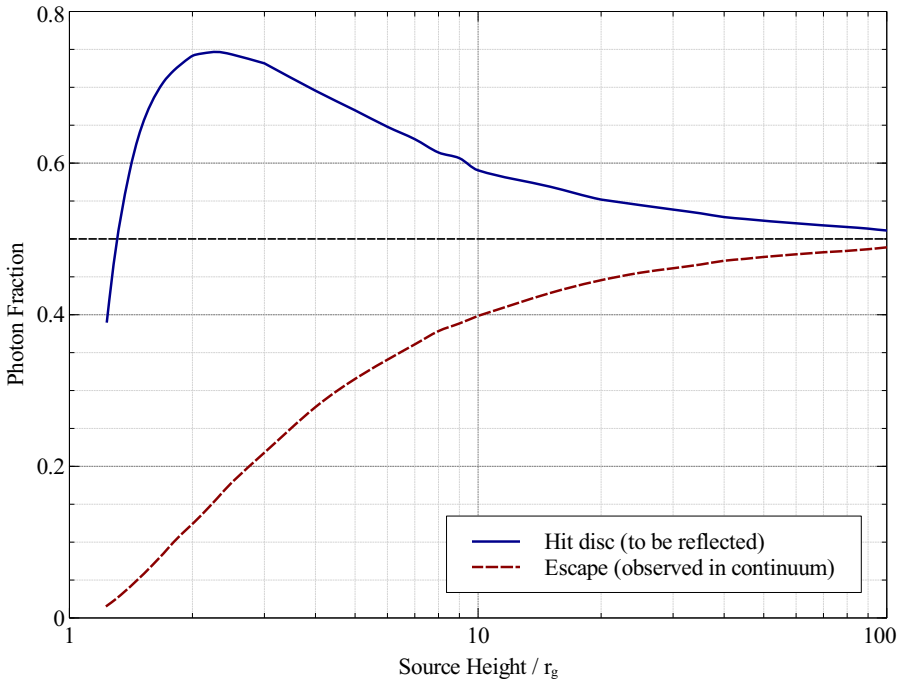

Figure 7.6: The fraction of the total number of photons emitted from an isotropic point source at varying height above the accretion disc that are reflected off of the disc and that are able to escape to infinity to be observed directly as the continuum emission.

8

Probing Accreting Black Holes Through X-ray Variability

High resolution X-ray spectra from long observations of accreting black holes, both in active galactic nuclei (AGN) and Galactic black hole binaries, have yielded an unprecedented amount of information about the structure of these systems, detecting emission from material right down to the innermost stable orbit and even the event horizon, probing not only the mechanisms at work in liberating energy from the accretion flow but also the strong gravity regime close to the black hole itself.

The X-ray emission is highly variable and recent studies of this variability have added a further dimension to the studies of these systems. The narrow line Seyfert 1 galaxy 1H 0707-495 was the first AGN found to exhibit reverberation lags (Fabian et al., 2009), where the variability in the spectral band dominated by reflection from the accretion disc is found to lag behind that in the spectral band corresponding to direct emission from the coronal X-ray source by tens to hundreds of seconds (Zoghbi et al., 2010). Since then, reverberation lags have been discovered in a multitude of other AGN (Emmanoulopoulos et al., 2011; de Marco et al., 2011; Zoghbi & Fabian, 2011; Zoghbi et al., 2012; de Marco et al., 2012) and even in Galactic stellar mass X-ray binaries where the black hole mass and length scale invariance gives equivalent reverberation lags on timescales of millisec-

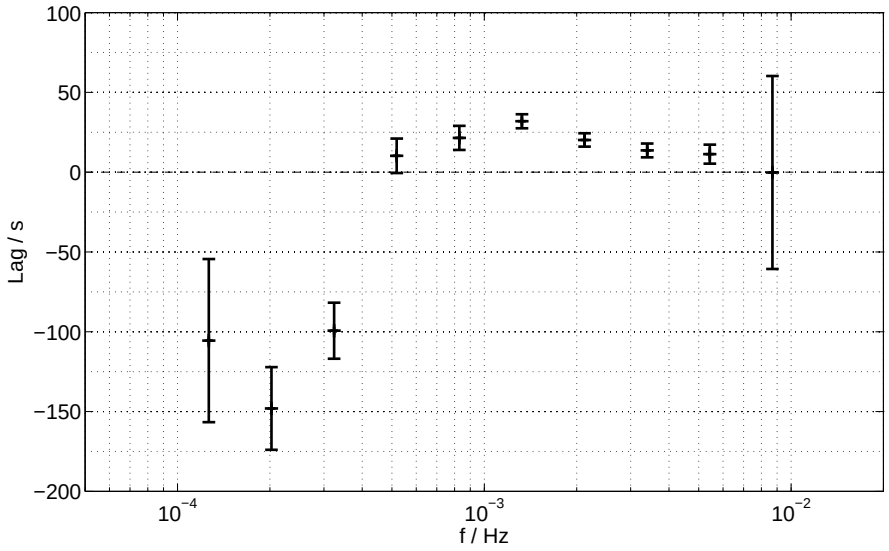

Figure 8.1: The lag spectrum from a 1 Ms lightcurve of 1H 0707-495 from Kara et al. (2012) showing the time lag for the variability at different Fourier frequencies between the hard (1.0-4.0 keV) band corresponding to the primary continuum emission and the soft (0.3-1.0 keV) band corresponding to reflection from the accretion disc. A positive lag indicates that variability in the soft (reflected) band lags behind that in the hard (primary) band.

onds (Uttley et al., 2011).

Measuring these phase lags measures the light travel time between the source and reflector and allows us to probe scales as small as 10 light-seconds in AGN. The reverberation of X-rays from the accretion disc is characterised by the lag spectrum (Nowak et al., 1999) which shows the time lag of variability at different frequencies between the energy bands. The lag spectrum of 1H 0707-495 was first obtained from a 500 ks lightcurve by Zoghbi et al. (2010) and then in more detail following observations with XMM Newton totalling 1.3 Ms by Kara et al. (2012). Such a lag spectrum, from a 1 Ms observation of 1H 0707-495 between the 'hard' (1.0-4.0 keV) band dominated by the primary continuum and the 'soft' (0.3-1.0 keV) band dominated by reflection from the accretion disc is shown in Fig. 8.1.

At temporal frequencies of around 10^{-3} Hz, a lag of around 30 s can be seen between the arrival of the X-ray continuum and the reflection from the accretion disc. Naïvely, this can be converted into the distance of the reflecting material from the primary X-ray source, which taking the mass of the black hole in 1H 0707-495 to be $2 \times 10^6\,\mathrm{M}_\odot$, (Zhou & Wang, 2005), gives a distance of $2\,r_\mathrm{g}$ (a gravitational radius, $1\,r_\mathrm{g} = \frac{GM}{c^2}$). This simple calculation, however, takes into account neither the multiple paths that X-rays may follow from the source to the reflector nor the effects of general relativity which are expected to be significant in such close proximity to the black hole. It is assumed that the

spectral energy bands correspond to detections of pure continuum and reflected emission, while in reality there will be contributions from both spectral components in each energy band. Finally, this analysis does not explain the full shape of the lag spectrum, rather it just looks at the longest time lag where the reflection follows the primary continuum.

The reverberation of of the iron Kα emission line from the accretion disc of an AGN due to a localised flare of X-ray emission from the corona was first considered by (Fabian et al., 1989) and by Stella (1990) in the context of measuring the mass of the central black hole. Gilfanov et al. (2000) quantified the effect of reverberation in the Galactic black hole binary Cygnus-X1, computing an approximate solution neglecting relativistic effects while Reynolds et al. (1999) accounted for the transport of the observed X-rays in general relativity to compute '2D transfer functions' giving the observed flux as a function of observed photon energy as time elapses from a single, localised, X-ray flare. Young & Reynolds (2000) related this work to observable signatures that may be detected by future generations of X-ray telescopes in the context of comparing observed reverberation of X-ray flares with a library of computed transfer functions to determine the mass of the black hole as well as the location of the X-ray flare.

Presented here is an analysis of X-ray reverberation applicable to the current state-of-the-art observations with XMM Newton. A systematic analysis of lag spectra computed theoretically for reflection of X-rays originating from a variety of X-ray sources of different sizes and geometries and in different locations allows us to understand the observed form of the lag spectra in AGN and to ask how much can be learned from these measurements about the energetics and geometry of the X-ray emitting corona. While applicable generally to X-ray sources exhibiting a reverberation lag, this study is motivated by the observed lag spectrum of 1H 0707-495. As well as the location and geometry of the X-ray source, observational constraints in separating the detection of the primary continuum and the reflected X-rays from the accretion disc are considered as well as how variations in luminosity may propagate through the expanse of the corona.

8.1 Lag Spectra

Following Nowak et al. (1999), time lags between spectral components or energy bands (with their own light curves recording the count rate as a function of time) are characterised by the lag spectrum, showing the phase (and hence time) lag between the Fourier frequency components that make up the light curves. The light curve, $F(t)$, is considered to be the sum over components of all frequencies:

$$F(t) = \int \tilde{F}(\omega) e^{i\omega t}\, d\omega$$

The amplitude and phase of each frequency component is given by the Fourier transform of the

light curve which can be written $\tilde{F}(\omega) = \left|\tilde{F}(\omega)\right| e^{i\varphi}$ and is computed by

$$\tilde{F}(\omega) = \int F(t) e^{-i\omega t}\, dt$$

The phase lag between two spectral components, say the hard and soft band light curves, $H(t)$ and $S(t)$ respectively, can be found by considering the complex form of their Fourier transforms $\tilde{H}(\omega) = \left|\tilde{H}(\omega)\right| e^{i\varphi}$ and $\tilde{S}(\omega) = \left|\tilde{S}(\omega)\right| e^{i\theta}$ and computing the cross spectrum

$$\tilde{C}(\omega) = \tilde{S}^*(\omega)\tilde{H}(\omega) = \left|\tilde{S}(\omega)\right| \left|\tilde{H}(\omega)\right| e^{i(\varphi-\theta)} \tag{8.1}$$

The argument of which gives the time lag, τ, since $\varphi = \omega t$ (and converting from angular to linear frequency, f)

$$\tau(f) = \frac{1}{2\pi f} \arg\left(\tilde{C}(f)\right) \tag{8.2}$$

Following this calculation (and sign convention), a positive time lag indicates that the variability in the soft energy band, $S(t)$, is lagging behind that in the hard energy band, $H(t)$, as would be expected if the hard band is dominated by an X-ray continuum which is reflecting off of the accretion disc and this reflected radiation dominates the soft band.

A warning is issued to the reader that this definition is the opposite sense of the time lag as adopted by Zoghbi et al. (2010) and Nowak et al. (1999) who define the soft band lagging behind the hard band to be the negative lag taking $\tilde{C} = \tilde{H}^*\tilde{S}$, though defining this as a positive lag is more instructive when considering the features of lag spectra arising from reverberation of X-ray variability from a reflecting accretion disc.

Detection of a time lag between spectral components requires the light curves to be coherent (*i.e.* there is a constant phase lag between the Fourier components over a given range in the two light curves, rather than a random one), although Kara et al. (2012) argue that total coherence is not required as uncorrelated (incoherent) variability will not contribute to the calculated lag as this part will average to zero when the cross spectrum is evaluated in finite-width frequency bins.

To explore the general features of reverberation lags, the lag spectrum was computed for the simplest case of a 'reflected' light curve exactly following the primary light curve but delayed in arrival by 30 s (*i.e.* shifting the time axis by 30 s). Such a lag spectrum, using the light curve of 1H 0707-495 in the 1-4 keV band as the input is shown in Fig. 8.2.

The lag spectrum shows a constant lag of approximately the input 30 s across all frequency components until the lag corresponds to a half-wave shift in phase at $f = \frac{1}{2\tau}$ (give or take the error introduced by the numerical, discrete Fourier transform of the real light curve and the temporal binning of the light curve, the combination of which causes the drift to a slightly longer lag at the lowest frequencies). Once $f = \frac{1}{2\tau}$, the waveform could have been shifted either forwards or backwards by half a wave and since the phase angle from which the lag is calculated is defined to be

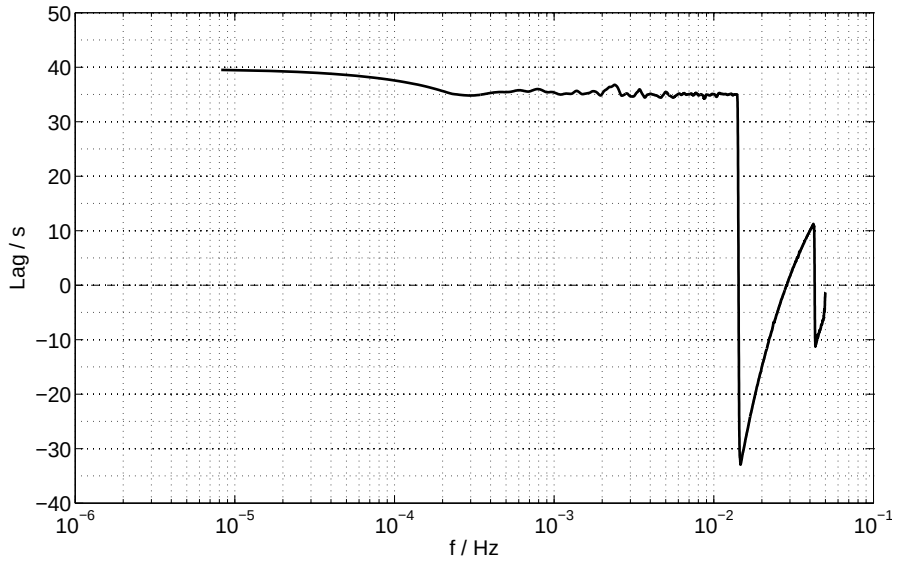

Figure 8.2: Lag spectrum between a primary light curve (taken from the light curve of 1H 0707-495 in the 1-4 keV band) and the same light curve delayed by 30 s. The lag spectrum shows a constant lag of approximately the input 30 s across all frequency components until phase-wrapping occurs when the lag corresponds to a half-wave shift in phase at $f = \frac{1}{2\tau}$. The drift to slightly a longer lag at the lowest frequencies is due to the error in the Fourier transform of the observed light curve.

in the range $-\pi < \varphi < \pi$, phase wrapping occurs. At higher frequencies, the phase continually wraps causing the lag to oscillate around zero until it decays away. It is not possible to measure lags longer than a shift of half a wavelength.

8.2 Simulating Lag Spectra for X-ray Reflection

8.2.1 The Transfer Function

The time lags between the observation of a change in the primary X-ray continuum and the corresponding change in the reflected flux from the accretion disc is characterised by the *transfer function*, $T(t)$. The transfer function is the response seen from the accretion disc to an instantaneous flash of light from the primary X-ray source.

The transfer function is calculated by general relativistic ray tracing simulations in two stages. Initially, rays are transferred from the source to the accretion disc, in the equatorial plane of the Kerr geometry around the central black hole with dimensionless spin parameter, a, as described in §5.

Initially, the X-ray source is assumed to be an isotropic point source, emitting equal power into equal solid angle in its own instantaneous rest frame. The photon's initial 4-momentum is transformed from the source's frame, a locally flat spacetime described by a tetrad of orthonormal basis vectors, to the global Boyer-Lindquist co-ordinate system to calculate the constants of motion of the ray, k, h and Q. The ray is then traced by numerical integration of the null geodesic equations (the equations of motion of a photon) in the Kerr spacetime. Taking $c = 1$ and $\frac{GM}{c^2} = 1$ to work in natrual units of $r_{\rm g} = \frac{GM}{c^2}$, the geodesic equations can be written:

$$\begin{aligned}
\dot{t} &= \frac{\left[(r^2 + a^2\cos^2\theta)(r^2 + a^2) + 2a^2 r \sin^2\theta\right] k - 2arh}{r^2\left(1 + \frac{a^2\cos^2\theta}{r^2} - \frac{2}{r}\right)(r^2 + a^2) + 2a^2 r\sin^2\theta} \\
\dot{\varphi} &= \frac{2ark\sin^2\theta + (r^2 + a^2\cos^2\theta - 2r)h}{(r^2 + a^2)(r^2 + a^2\cos^2\theta - 2r)\sin^2\theta + 2a^2 r\sin^4\theta} \\
\dot{\theta^2} &= \frac{Q + (ka\cos\theta - h\cot\theta)(ka\cos\theta + h\cot\theta)}{\rho^4} \\
\dot{r}^2 &= \frac{\Delta}{\rho^2}\left[k\dot{t} - h\dot{\varphi} - \rho^2\dot{\theta}^2\right]
\end{aligned}$$

Where the dots denote differentiation with respect to some affine parameter, σ.

Spatially extended X-ray sources are explored through Monte Carlo ray tracing simulations. Rays are started at random locations (with a uniform probability density function such that all locations are equally likely) within an allowed cylindrical source region (defined by a lower and upper height from the disc plane as well as an inner and outer radius) and are assigned random initial direction

cosines $\cos\alpha$ and β, again with uniform probability density. This will simulate the effect of an X-ray source of finite spatial extent that is optically thin to the X-rays it emits. Each local region of the source is taken to be co-rotating with the element of the accretion disc in a relativistic Keplerian orbit at the same radius. This model does, however, assume the surface brightness over the entire extent of the source varies simultaneously, which may be unphysical if the source region extends across multiple gravitational radii, as the light crossing time of the source is no longer negligible compared to the light travel time from the source to the reflector, however this model may be used to approximate the behaviour of an extended source and we will revisit the propagation of fluctuations in §8.5.

When the rays reach the accretion disc, their arrival time as measured by an observer at infinity (the t co-ordinate) as well as position (r, φ) are recorded and they are sorted into radial and azimuthal bins on the accretion disc.

The relative travel time of photons from each radial and azimuthal bin on the accretion disc to the telescope as well as their energy measured by an observer at infinity is determined by tracing parallel rays, travelling perpendicular to a flat image plane a large distance from the black hole, representing the area of the sky imaged by the X-ray telescope. Rays are started on a regular grid (the 'image plane') travelling perpendicular to this plane plane, a distance $10000\,r_{\mathrm{g}}$ from the black hole (to be certain the spacetime here is flat), inclined to the rotation axis of the black hole at the angle at which the telescope is observing the system, henceforth taken to be 53 deg, the measured inclination of 1H 0707-495. The image plane is centred on the black hole and spans the area of interest (*i.e.* the accretion disc, assumed to have a radius of $400\,r_{\mathrm{g}}$).

Due to the symmetry of the Kerr metric, propagating rays backwards in time (starting at the image plane to work out where they originated from on the accretion disc) is equivalent to propagating forwards in time, having reversed the direction of spin of the black hole. Propagating the rays from the image plane with the spin of the black hole reversed until they reach the equatorial plane will therefore give the position on the accretion disc (r and φ co-ordinates) from which the ray originated as well as the travel time of the ray from the disc to the telescope as measured by the observer at infinity (t co-ordinate). The rays are sorted into the radial and azimuthal bins upon the accretion disc and the average travel time of a ray is calculated for each bin. The number of rays landing in each bin is counted, which gives the area of that bin projected onto the image plane by gravitational lensing and will determine the flux received from each part of the accretion disc.

The energy and arrival rate of the photons arriving along a given ray measured by the observer at infinity is computed by the projection of the photon 4-momentum to the observers' timelike axes (which are their 4-velocities), though before doing so, since the photon under consideration is propagating backwards, the spacelike components of the 4-momentum are reversed (so that the photon is travelling in the correct direction with respect to the orbiting material in the accretion

disc and towards the observer allowing the correct Doppler shift to be computed).

$$g^{-1} \equiv \frac{\nu_{\mathrm{O}}}{\nu_{\mathrm{E}}} = \frac{\mathbf{v}_{\mathrm{O}} \cdot \mathbf{p}(\mathrm{O})}{\mathbf{v}_{\mathrm{E}} \cdot \mathbf{p}(\mathrm{E})} = \frac{g_{\mu\nu} v_O^{\mu} p^{\nu}(O)}{g_{\rho\sigma} v_E^{\rho} p^{\sigma}(E)} \tag{8.3}$$

The average energy shift for each bin on the accretion disc is computed from all the rays originating from it. It is assumed that the primary X-ray source is emitting photons of all energies and that this will excite emission lines and other spectral features from the disc. The energy shift of the observed photons is assumed to arise only from the transport of rays from the accretion disc to the observer, taking into account special relativistic Doppler shifts as well as gravitational redshifts. Material in the accretion disc is taken to be in a (relativistic) prograde Keplerian orbit in the equatorial plane around the black hole.

When a photon from the primary X-ray source lands in a specific bin on the accretion disc, the time from the disc to the observer as well as the energy of the photons measured at infinity is looked up from the values calculated for that bin from the rays traced from the image plane to the disc. The total arrival time of the ray from the primary X-ray source, via the disc, to the observer is the sum of the two computed times from the source to the disc and the disc to the observer. Pre-calculating the transfer from the disc to the observer and looking up the appropriate values when a photon from the source lands on the disc means that the reverberation X-rays from different sources can efficiently be calculated for the same configuration of the disc and observer.

Finally, the transfer function is computed by counting the number of rays that arrive at the observer as a function of time, $N(t, r, \varphi, E)$, integrating over all energies and positions on the disc. Assuming the X-ray source emits photons at an equal rate along each ray in its own rest frame (*i.e.* it is isotropic), the arrival rate of photons along each ray measured by the observer will vary according to the redshift, $\frac{\nu_{\mathrm{O}}}{\nu_{\mathrm{E}}} \equiv g^{-1}$, which is the product of the redshifts from the source to the disc (g_{SD}^{-1}) and from the disc to the observer (g_{DO}^{-1}).

$$T(t) = \int N(t, r, \varphi, E)\, g_{\mathrm{SD}}^{-1} g_{\mathrm{DO}}^{-1}\, r dr\, d\varphi\, dE \tag{8.4}$$

The ray tracing codes to compute these transfer functions as well as the lookup tables mapping the accretion disc to the observer were implemented to run rapidly on graphics processing units (GPUs) using the NVIDIA CUDA framework, allowing the paths of hundreds of rays to be computed in parallel.

8.2.2 The Arrival Time of the Primary Continuum

The ray tracing simulations described above give the photon arrival rate as a function of time since the initial flash of light left the primary X-ray source. However, when measuring reverberation in observations of AGN, it is the time lag between the arrival of the primary continuum and the

Table 8.1: Travel time (in natural units) as measured by an observer at infinity for a ray propagating from point sources at varying heights above the black hole on the rotation axis to an observer $10000\,r_{\rm g}$ away inclined at an angle of 53 deg to the rotation axis. The Shapiro delay is characterised by the difference between the travel time of the ray in general relativity and what it would be in classical, Euclidean space.

Source Height	Ray Travel Time	Delay
$1.235\,r_{\rm g}$	$10029\,GM/c^3$	$30\,GM/c^3$
$2\,r_{\rm g}$	$10020\,GM/c^3$	$21\,GM/c^3$
$5\,r_{\rm g}$	$10014\,GM/c^3$	$17\,GM/c^3$
$10\,r_{\rm g}$	$10008\,GM/c^3$	$14\,GM/c^3$
$20\,r_{\rm g}$	$10001\,GM/c^3$	$13\,GM/c^3$

reflected rays that is measured. One must therefore know the arrival time of the continuum X-ray emission at the observer to define the zero point in the time series of the transfer function.

For an infinitesimal point source, exactly one ray emitted from the source will end up at any given observer at infinity. Therefore the arrival time of the primary X-ray continuum may be computed by finding the one ray from the source that reaches the observer and timing its arrival. Table 8.1 shows the direct ray travel times (as measured by an observer at infinity) from point sources at varying heights above the black hole to an observer at a distance of $10000\,r_{\rm g}$ from the black hole inclined at 53 deg to the rotation axis. A source above the plane of the accretion disc should be closer to the observer than the black hole and classically, in natural units, light takes $1\,\frac{GM}{c^3}$ to travel $1\,r_{\rm g}$. These direct rays taking longer than 10,000 $\frac{GM}{c^3}$ to reach the observer illustrate the Shapiro delay where the passage of light is slowed down as it travels in the proximity of the black hole (Shapiro, 1964).

8.2.3 The Reflected Light Curve and Lag Spectrum

The transfer function describes the response seen in the reflection from the accretion disc due to an instantaneous flash of X-rays from the primary source. Hence, if the primary X-ray source, observed in a 'hard' band for the X-ray spectrum is varying as described by some light curve $H(t)$, the response in the reflection seen in a 'soft' band, $S(t)$, is given by the convolution of the primary light curve with the transfer function.

$$S(t) = H(t) \otimes T(t) = \int H(t')T(t-t')\,dt' \tag{8.5}$$

Ray tracing in the simulations is carried out in natural units, measuring time in units of $\frac{GM}{c^3}$. The time series of the transfer function is trivially converted to seconds for the mass of the black hole of interest.

In order to generate a realistic lag spectrum with the power spectral density (PSD) observed in the primary continuum of an AGN, the primary, hard light curve is taken to be the observed light curve of the narrow line Seyfert 1 galaxy, 1H 0707-495 in the 1-4 keV band in 10 s bins. Using the observed light curve of 1H 0707-495 also means that lag spectra are simulated with a realistic time resolution that is achievable with the current generation of X-ray telescopes. The mass of the black hole is taken to be $2 \times 10^6\,\mathrm{M}_\odot$, as quoted in the literature (see *e.g.* Zhou & Wang, 2005).

The primary light curve is convolved with the transfer function obtained from the ray tracing simulations in order to obtain the light curve of the reflected component. The Fourier transforms of both the primary and reflected light curves were then computed. The cross and lag spectra are calculated using Equations 8.1 and 8.2. The convolution, Fourier transforms (using the Fast Fourier Transform, FFT algorithm) and lag calculations were performed in MATLAB.

8.2.4 Extended Sources

For an extended corona, a range of rays following different paths will be observed by the telescope as the primary continuum. A transfer function (photon arrival rate vs. time) for an extended source region may be calculated in exactly the same way as the rays are traced from the observer to the accretion disc. If the source is said to extend radially at some height above the accretion disc, rays are traced from the image plane until they reach this plane and their time is measured if they intercept the region of the plane spanning the source.

In order to compute the lag spectrum arising from the reflection of X-rays originating from an extended source, the observed light curve is taken to be the 'intrinsic' variability of the X-ray source. This is permissible since the transfer functions do not impart any power on the variability spectrum, they just add a phase lag. This will mean the simulated variability has a physically realistic power spectrum. Simulated light curves that would be observed for the primary (hard) and reflected (soft) spectral components, $H(t)$ and $S(t)$ respectively, are computed by convolving the light curve with the calculated transfer functions for each component.

$$H(t) = H_{\mathrm{obs}}(t) \otimes T_{\mathrm{src}}(t) \tag{8.6}$$

$$S(t) = H_{\mathrm{obs}}(t) \otimes T_{\mathrm{ref}}(t) \tag{8.7}$$

The lag spectrum between the two spectral components is calculated as above.

8.3 Theoretical Lag Spectra

8.3.1 Lag Spectra for Point Sources

Initially, the transfer functions and lag spectra were computed for reflection from isotropic point sources located at varying heights on the rotation axis above the black hole, as shown in Fig. 8.3.

A striking feature of the transfer functions is the peak in X-rays after the initial arrival of the reflection from the accretion disc. This corresponds to the 're-emergence' of the redshifted, gravitationally lensed (and thus magnified) reflection from the far side of the accretion disc, travelling round the black hole to the observer as was noted by Reynolds et al. (1999).

Turning to the resulting lag spectra, a constant lag is observed at low frequencies, corresponding to the average time lag of the transfer function

$$\bar{t} = \frac{1}{\int T(t)\,dt} \int t\,T(t)\,dt \tag{8.8}$$

Towards higher frequencies, the contribution to the lag from the extended tail of the transfer function decreases as phase wrapping causes these contributions to the lag to average to zero. This decreases the average lag time at higher frequencies, until the peak in the transfer function is left to dominate, causing the lag spectrum to flatten off before the jump down where phase wrapping occurs for all timescales making up the transfer function.

The transfer functions roughly follow the form of those computed by Gilfanov et al. (2000) who calculated the transfer functions for point sources in Euclidean spacetime, taking into account no relativistic effects and only for accretion discs extending inward to $10\,r_{\rm g}$. Here, the fully relativistic transfer functions are computed for accretion discs extending all the way down to the innermost stable orbit for a maximally spinning black hole. As in the classical case, the transfer functions fall of as t^{-2} at long times, though the relativistic effects cause the initial peak in the transfer function to be steeper. Extending the accretion disc to the innermost stable orbit for a rapidly spinning black hole means the flattened part visible at early times in the transfer functions of Gilfanov et al. (2000) are not seen (consistent with their trend as the inner radius of the disc is decreased).

Considering, for illustration, the case of the point source at a height of $5\,r_{\rm g}$, the mean arrival time of rays in the transfer function is around 290 s after the arrival of the primary continuum from the source. This time can be compared with travel times computed for the equivalent source and reflector in flat, Euclidean spacetime. For the case of a point source at $5\,r_{\rm g}$, the primary continuum takes 168 s longer to reach the observer accounting for relativistic effects than it would in Euclidean spacetime and computing the transfer function using classical ray travel times (but keeping the relativistic formulation for the projection of areas on the accretion disc to the observer and the emissivity profile of the disc), the average arrival time is delayed by 173 s. Since the lag is measured

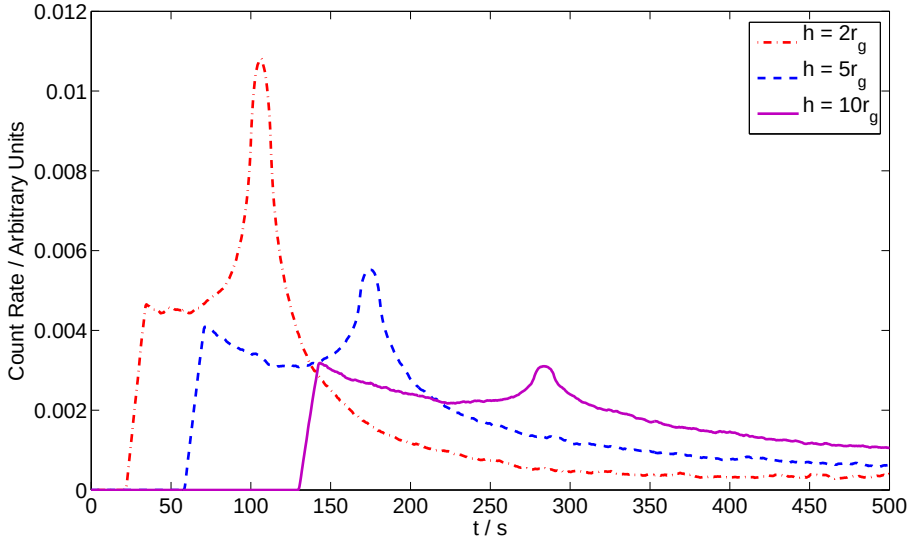

(a)

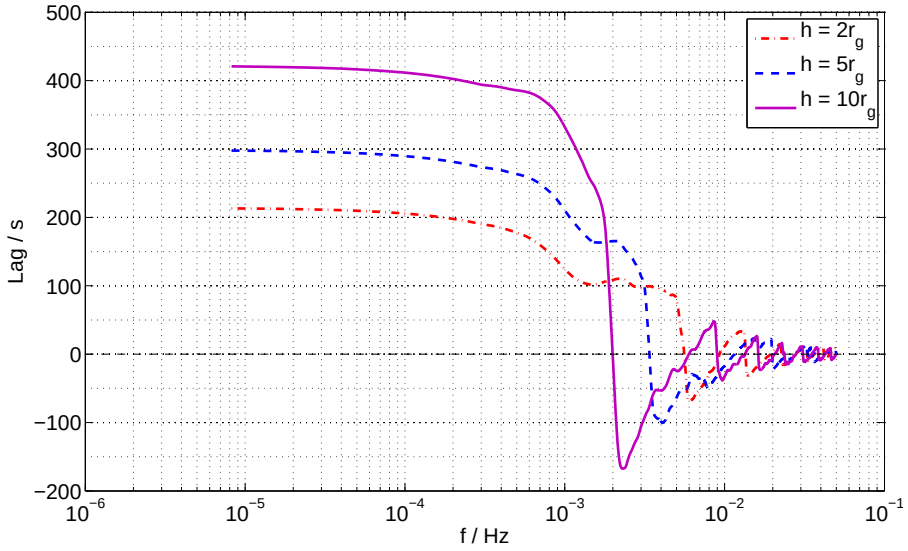

(b)

Figure 8.3: (a) Transfer functions and (b) lag spectra for reflection due to isotropic point sources at varying heights, stationary on the rotation axis above the black hole, mass $2 \times 10^6\,\mathrm{M}_\odot$. The accretion disc is observed at an inclination angle of 53 deg. A positive time lag indicates that variability in the reflected X-rays lag behind variability in the primary emission from the source.

between the arrival of the continuum and the reflection, relativistic effects on the light travel time increase the measured lag by around 4 s (the 'Shapiro delay'). When directly equating the lag to the light travel time from the source to the reflector, this means the source appears $0.5\,r_{\rm g}$ further from the accretion disc than it really is.

8.3.2 Lag Spectra for Extended Sources

Whilst it is instructive to consider the lag spectra arising from point sources in general relativity, observations of the relativistically broadened iron K line profile in 1H 0707-495 suggest that the X-ray source is radially extended out to around $35\,r_{\rm g}$ (§4 and §6). It is therefore important to understand the form of lag spectra arising from extended sources.

While the following analysis is generally applicable to X-ray reverberation from spatially extended sources, we are motivated by the observed lag spectrum of 1H 0707-495 and illustrate the effects with source geometries similar to that suggested by the emissivity profile observed in this object. Further more, we consider a source region whose luminosity is constant throughout its extent. While in reality the luminosity is likely to vary across the source, perhaps being concentrated in the central regions, we here elect to minimise the number of free parameters such that we may gain insight into the physical effects. When assuming a constant source luminosity, the modelled source extents will represent the bulk of the emitting material.

The transfer functions and lag spectra for reflection of X-rays from source regions of constant height and vertical extent but increasing in radial extent outward from the rotation axis are shown in Fig. 8.4. The most notable feature of the transfer function for extended sources is the extended tail to long reverberation times since from an extended X-ray source, there are many more possible light paths for the primary X-rays to reach the accretion disc.

In addition to the extended tail of the transfer function, some reflected rays (those originating from the edge of the X-ray source closest to the observer reflecting off the part of the disc immediately below) may reach the telescope before the mean arrival time of the continuum, meaning the transfer function begins before the time $t = 0$. As for the case of a point source, the reflected X-rays are seen to rise after their initial arrival owing to the re-emergence of X-rays from the far side of the accretion disc, lensed around the black hole, though this is less pronounced due to the increased range of ray paths now possible from an extended source.

Turning to the lag spectrum in Fig. 8.4(b), a constant lag is once again observed at low frequencies corresponding to the mean arrival time of reflected rays over the transfer function, though with an extended X-ray source, since more of the flux is in the extended tail of the transfer function, there is a much more pronounced decay of the lag measured in the higher frequency components. For the most extended sources, there is almost a continuous decay of the measured lag to zero in the

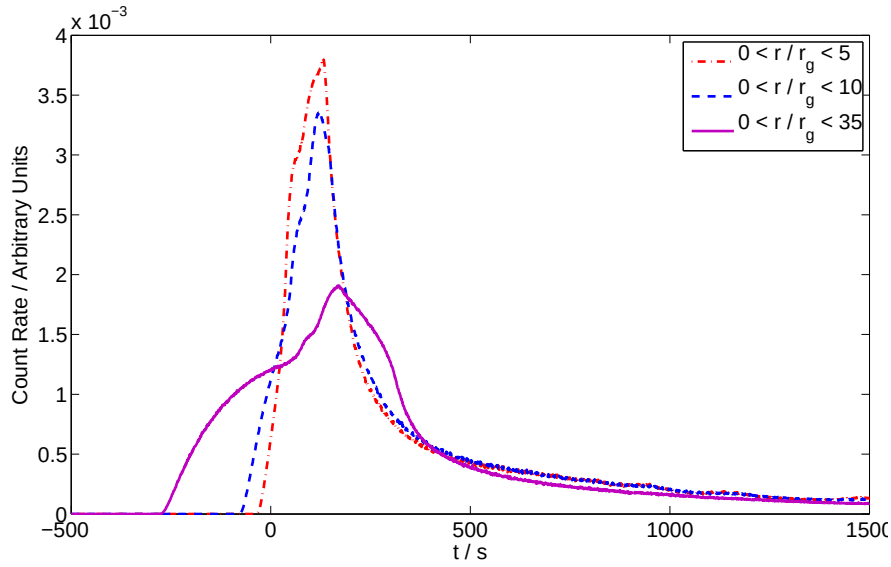

(a)

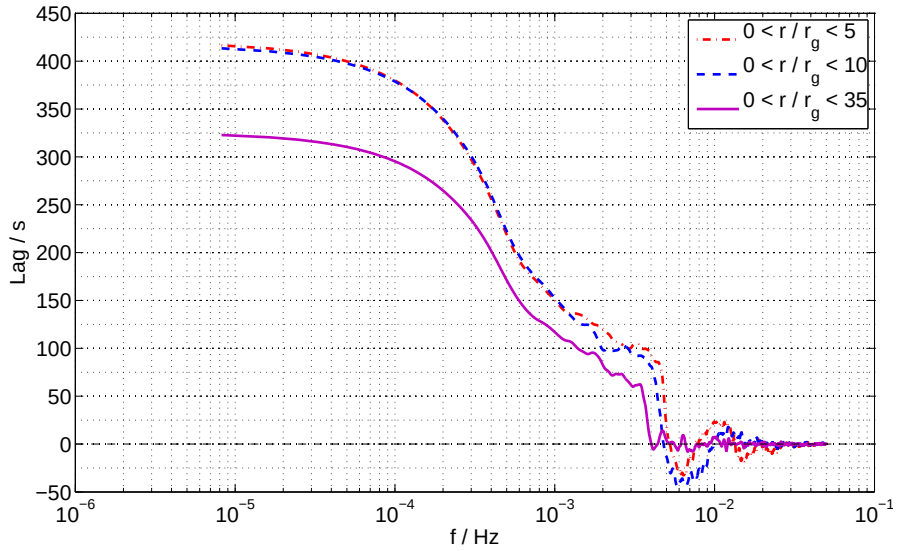

(b)

Figure 8.4: (a) Transfer functions and (b) lag spectra for the instantaneous illumination of X-ray sources extended vertically between $2\,r_{\rm g}$ and $2.5\,r_{\rm g}$ above the plane of the accretion disc and with different radial extents outward from the rotation axis.

high frequency components as the long timescale contributions to the transfer function phase-wrap and no oscillation about zero lag is seen at the highest frequencies. The extremes of the source being further from the black hole reduces the shortest possible light travel time to the observer since further from the black hole, the time delay due to spacetime curvature (the Shapiro delay) is reduced. This means that for the most radially extended sources, the observed lag is less than that measured for the sources more confined to the region around the central black hole but with the same vertical extent.

Increasing the vertical extent of the source region (Fig. 8.5) again increases the range of possible ray paths from the source to the disc, giving the transfer function an extended tail and causing the measured lag to decay away more for the higher frequency components of the variability. Increasing the vertical extent of the source above a fixed bottom also moves the mean source location away from the accretion disc, increasing the mean lag time measured for the lowest frequency components.

8.4 Dilution of Spectral Components

The preceding calculations of reverberation time lags assume that the light curves of the directly observed continuum and reflected emission can be measured directly. In reality, however, light curves are obtained in spectral bands which are merely *dominated* by either the continuum emission (the 'hard' band at 1-4 keV) or the reflection from the accretion disc (the 'soft' band at 0.3-1 keV). This means that the measured time lags will be 'diluted' as the measured 'reflection' will include promptly-arriving photons from the continuum and the 'continuum' will include late-arriving photons from the reflection.

Fig. 8.6 shows the X-ray spectrum of 1H 0707-495 modelled as the sum of a direct power law component, reflection from the accretion disc and black body emission from the disc. Integrating the number of photons detected from each of the components over each energy band reveals that the 0.3-1 keV band (dominated by the reflection component) contains a contribution from the primary continuum at 70 per cent of the number of photons detected in this band from the reflection. Likewise, the 1-4 keV band (dominated by the primary continuum) contains a contribution from the reflected emission at 60 per cent of the number of photons detected in this band from the power law. We assume the flux in the thermal, black body emission to be constant and therefore not to contribute to the lag.

To determine the effect of this dilution on the observed lag spectrum, a composite transfer function for the soft 'reflection' band was formed by summing the transfer functions due to reflection from the accretion disc and for the direct emission seen from the primary X-ray source, weighted such that the integrated photon counts in the constituents are split in the ratio observed in the spectrum (Fig. 8.7). Likewise, the transfer function in the hard 'primary' band is constructed as the sum of

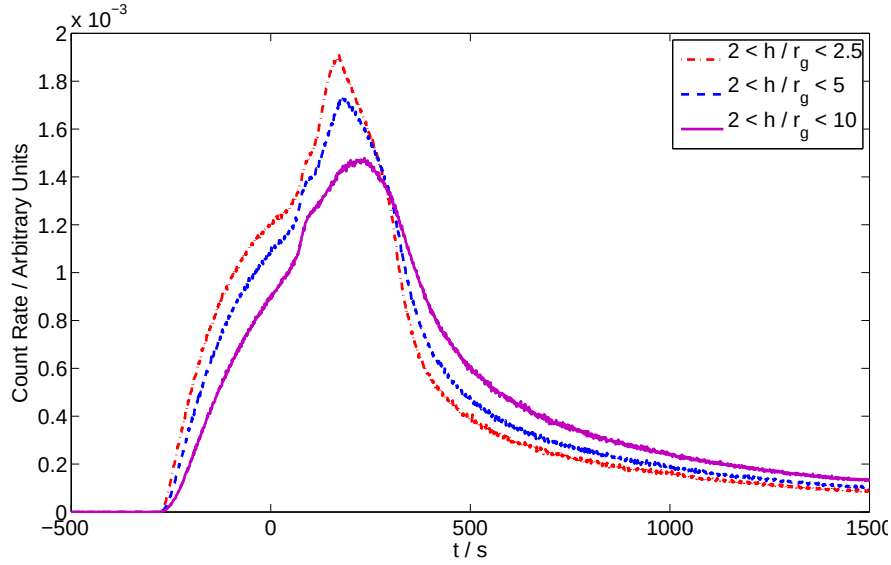

(a)

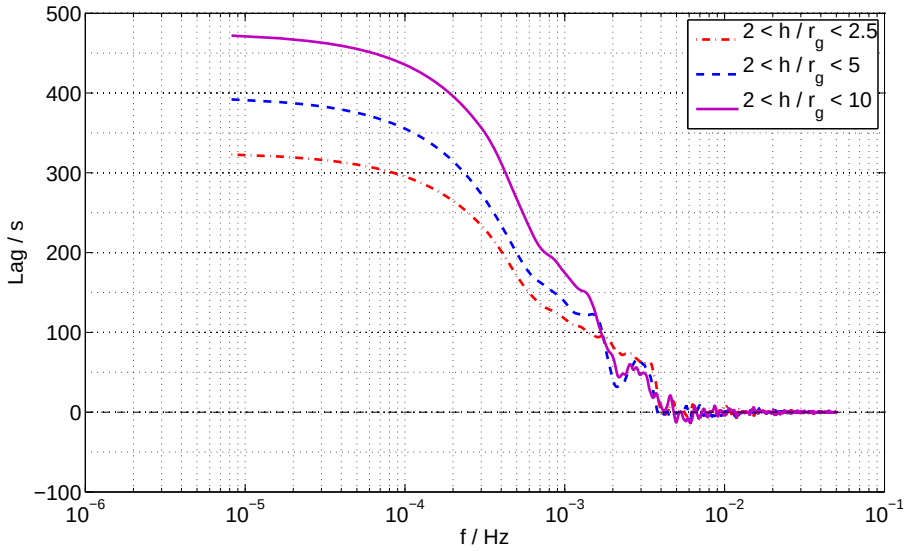

(b)

Figure 8.5: (a) Transfer functions and (b) lag spectra for X-ray sources extended vertically from $2\,r_{\rm g}$ to varying heights above the plane of the accretion disc. In each case, the X-ray source is extended radially out to $35\,r_{\rm g}$.

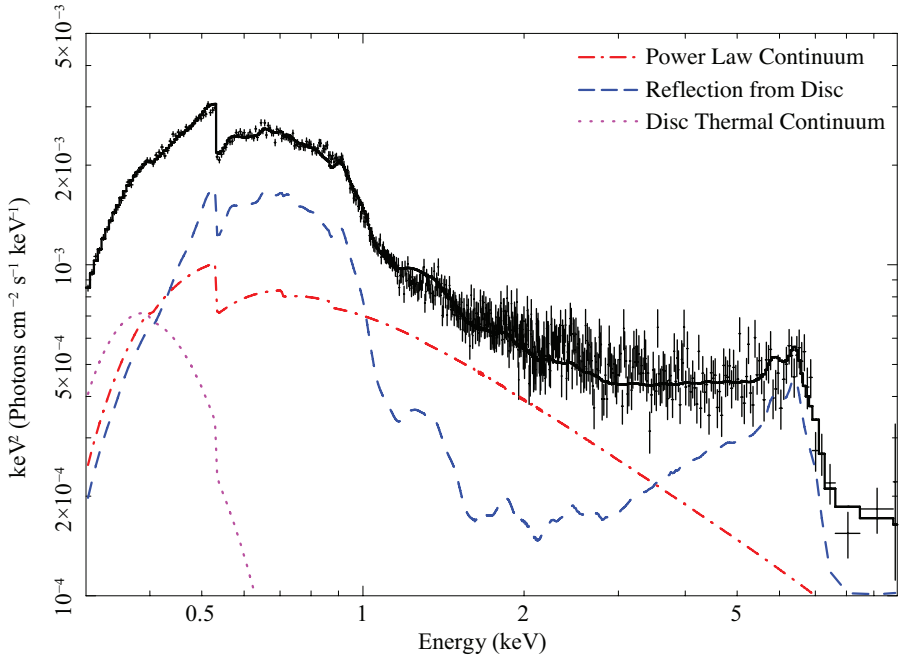

Figure 8.6: The time-averaged X-ray spectrum of 1H 0707-495 observed using the EPIC pn detector on XMM Newton in October 2008, modelled as the sum of a direct power law component, reflection from an ionised accretion disc (using the REFLIONX model of Ross & Fabian 2005) and black body emission from the disc.

Table 8.2: Contributions from the spectral components of 1H 0707-495 from the January 2008 XMM Newton observation in the hard and soft bands from which reverberation time lags are calculated. Photon counts are normalised to the component said to be dominating in that band.

Component	**0.3-1 keV**	**1-4 keV**
Power law continuum	0.7	1
Reflection	1	0.6
Black body	0.4	10^{-4}

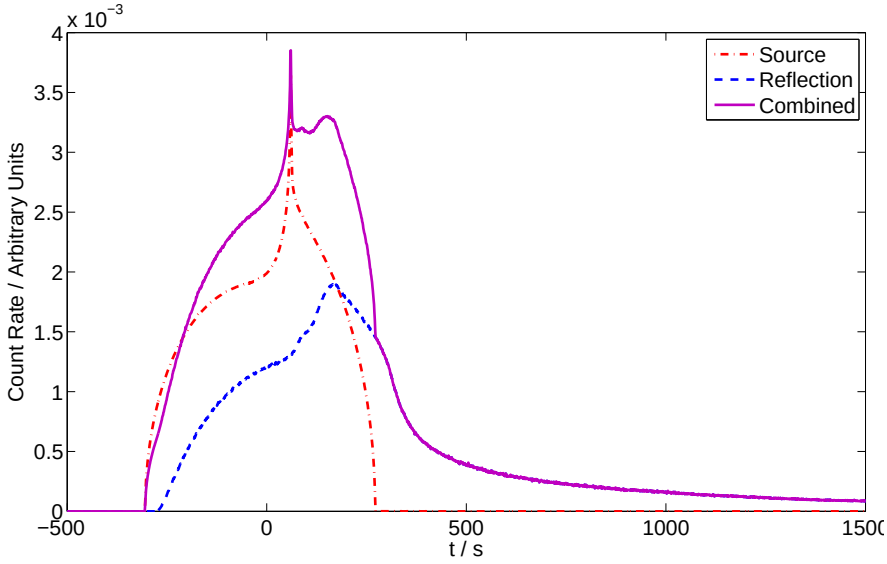

Figure 8.7: The combination of the transfer functions for reflection from the accretion disc and direct emission from the X-ray source, in the ratio found in 1H 0707-495, to give the overall transfer function for the soft (0.3-1.0 keV) band.

contributions from the direct continuum emission and reflection from the accretion disc. These combined transfer functions are used to obtain the light curves that would be observed in the hard and soft bands with Equations 8.6 and 8.7. Using the photon fluxes calculated above, the composite transfer functions are

$$T_{0.3-1.0\mathrm{keV}} = T_{\mathrm{reflection}} + 0.7T_{\mathrm{source}}$$
$$T_{1.0-4.0\mathrm{keV}} = T_{\mathrm{source}} + 0.6T_{\mathrm{reflection}}$$

Fig. 8.8 shows the effect of dilution of the spectral components in the 'primary' and 'reflection' energy bands on the lag spectrum. It is clear that when the contribution from the primary X-ray source is included in the 'reflection' band, the measured time lag is reduced by around 40 per cent compared to the 'actual' time lag that would be seen if it were possible to directly observe the primary and reflected light curves. When, in addition to this, the contribution of the reflected component is included in the primary continuum band, the measured time lag is further reduced. The observed time lag at 10^{-3} Hz can be reduced by up to 75 per cent from the 'actual' time lag.

It is evident that when interpreting the observed time lags between the primary continuum emission and reflection in terms of the light travel time to constrain the location of the X-ray source with respect to the reflector, it is important to interpret the observed 'hard' and 'soft' spectral bands as combinations of the primary and reflected emission, rather than simply using them as proxies for the respective components.

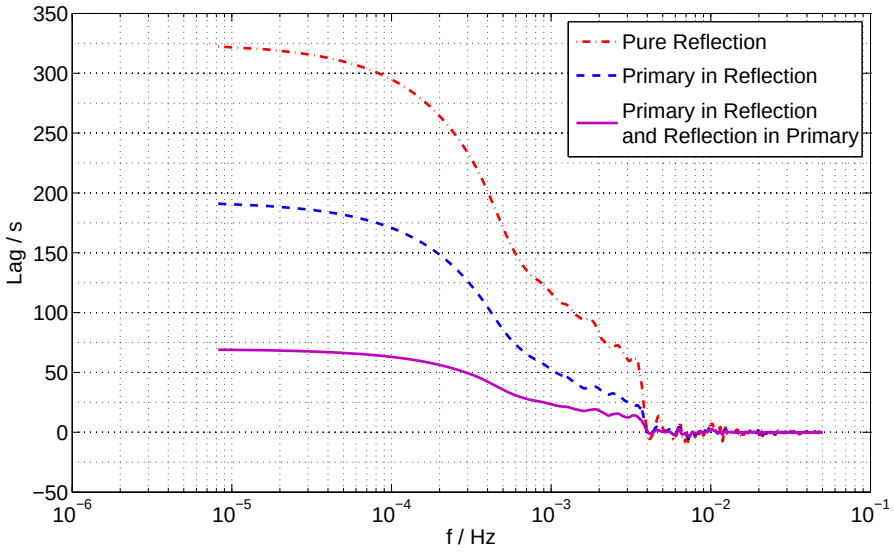

Figure 8.8: The effect of dilution of spectral components in the 'primary' and 'reflection' energy bands on the lag spectrum is illustrated by comparing the lag spectrum assuming a pure reflection component, the lag spectrum obtained using a reflection transfer function combined with a transfer function of the primary X-ray source contributing to this energy band and a lag spectrum also accounting for the reflection component contributing to the 'primary' energy band in the calculation of the observed arrival time of the direct emission. In each case, the source is taken to extend radially out to $35\,r_{\rm g}$ and vertically between 2.0 and $2.5\,r_{\rm g}$.

8.5 Propagation Effects

When considering X-ray sources spanning radially out to around $35\,r_{\mathrm{g}}$, it is not physically meaningful to consider the source varying instantaneously through its entire extent, as has been assumed to this point. However, in taking all of the rays were taken to originate from the X-ray source at the same time in evaluating the transfer functions provides a useful starting point for exploring the phenomena observed in the lag spectra. A fluctuation in the intensity of the primary X-ray source will propagate throughout its extent and in fact must do so in a time greater than the light travel time across the source region (which would be $35\,r_{\mathrm{g}}/c$ for a source spanning $35\,r_{\mathrm{g}}$). This will have a noticeable effect on the measured lag spectrum if the light travel time to the disc is less than the propagation time of a luminosity fluctuation through the corona.

There are a number of possible scenarios for the propagation of fluctuations in the intensity of the primary X-ray source, which can arise due to changes in the density or energy/temperature of the particles in the corona. It is possible that the fluctuations in the corona originate from the injection of energy by a process close to the central black hole and that fluctuations in the X-rays emitted from the corona originate near the centre and propagate outwards. Alternatively, it is possible that energy is injected into the corona from the surface of the accretion disc, either directly or through magnetic fields that are anchored to the accretion disc that accelerate the particles of the corona to high energies. In this case, one might expect that fluctuations arise from fluctuations in the accretion disc (for instance, variations in the mass accretion rate or in the magnetic flux density as field lines are 'accreted' inwards through the disc as per Beckwith et al. 2009 or McKinney et al. 2012). Such fluctuations are likely to propagate inwards through the accretion disc and will cause fluctuations in the corona that originate at the edge and move inwards. Finally, it could be that there is no ordered propagation of fluctuations through the corona, rather variations in the intensity of the primary X-ray source are stochastic in nature, occurring randomly throughout the source region (for example, they arise due to isolated magnetic flaring events with no change in the bulk properties of the corona over the time-scale of the observations).

We investigate whether it is possible to discriminate between these scenarios in the observed lag spectra by computing transfer functions for the primary X-ray source and the reflection from the accretion disc in which the rays originate from the source at variable times. The influence of propagation effects is investigated on the lag spectrum of an X-ray emitting region extending radially outward to $35\,r_{\mathrm{g}}$ and between 2 and $2.5\,r_{\mathrm{g}}$ above the plane of the accretion disc and the full effects of dilution of the spectral components in the two energy bands are considered with the dilution fractions as found in 1H 0707-495.

Random fluctuations in the X-ray source (if the changes in the observed X-ray luminosity originate in random flaring events throughout the source region whose net effect is to change the total count rate we observe; the variability arising probabilistically) are simulated by assigning a random start

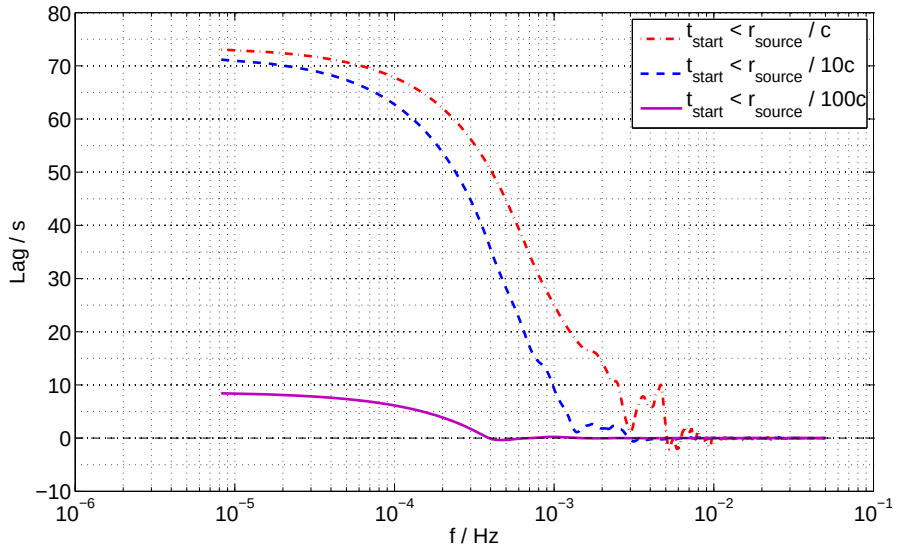

Figure 8.9: The lag spectrum between the hard (1.0-4.0 keV, dominated by the primary continuum) and soft (0.3-1.0 keV, dominated by reflection from the acctrion disc) X-ray bands, taking into account the contributions of both spectral components to each band, allowing the rays from the primary X-ray source to have random start times up to a maximum (as a function of the radius of the source). The emitting region is located between 2.0 and 2.5 $r_{\rm g}$ above the accretion disc and extends radially out to 35 $r_{\rm g}$.

time to the rays up to a maximum value (here taken to be a multiple of the light travel time from the centre to the edge of the source region) which defines a characteristic timescale over which variations occur throughout the source region. These rays make up the transfer function, so in this model, constructed to give insight into how such a system would manifest itself in reverberation measurements, the random fluctuations are not the cause of the variability, rather given the observed variability, they dictate its spatial propagation through the source region and therefore how it is passed into the X-ray reflection.

The lag spectrum arising from such a scenario, with increasing ranges in the ray start times in each transfer function, is shown in Fig. 8.9. Randomising the start times of rays through the source region results in the dilution of the measured lag between the arrival of the primary and reflected X-rays, with the lag between the primary and reflected components tending to zero when the timescale of the random flaring events is much greater than the light travel time between the X-ray source and the reflector.

To simulate the effect of fluctuations in the source luminosity propagating outwards from the centre of the source region, the start time of a ray is taken to be proportional to its originating radius within the region, where the constant of proportionality represents the speed at which fluctuations move

radially through the source region, corresponding to dynamical timescales within the corona, and is the same for all rays. Likewise, the effect of fluctuations propagating inwards from the edge of the X-ray source is simulated by setting the start time of the rays proportional to their initial radial distance from the edge of the source region.

The propagation of luminosity fluctuations inward from the edge of a defined source region delays the arrival time of the reflected radiation with respect to the primary continuum. The resulting lag spectrum is shown in Fig. 8.10(a). As the speed at which fluctuations propagate through the source region is decreased, the measured lag increases and the lag at high frequencies is damped to zero over a broader frequency range.

Conversely, Fig. 8.10(b) shows theoretical lag spectra in which the fluctuation in source intensity propagates outward from the centre at varying speeds. While the propagation of fluctuations outward throughout the source region reduces the apparent time lag between the primary continuum and reflection, the most notable effect is the turnover at low frequencies, $< 10^{-4}\,\mathrm{Hz}$, once the fluctuations propagate slower than approximately one tenth of the speed of light. In these situations, low frequency variations appear in the soft X-ray band, representing the 'reflection' before the hard band, representing the 'primary continuum.'

Due to the propagation delay, X-rays from the outer parts of the source, which due to their larger area make up the majority of the flux received from the primary X-ray source, are delayed in their emission and thus their arrival at the observer. On the other hand, X-rays emitted from parts of the source closer to the black hole are more likely to be reflected from the accretion disc rather than observed directly in the continuum as rays passing closer to the black hole will be focussed on to the accretion disc by the strong gravity. This means that, comparatively, the reflected X-rays originate from parts of the source region closer to the black hole than the observed continuum and since the propagation time of the fluctuation is greater than the light travel time to the reflector, the average arrival time of the soft X-ray band at the observer is slightly earlier than the average arrival time of the hard band once the full contribution of the continuum and reflection in each band (the dilution) is accounted for, resulting in the soft band slightly leading the hard band at the lowest variability frequencies (this effect is phase-wrapped out of the variability at higher frequencies due to its comparatively long timescale, so here the soft band is seen to lag behind the hard band).

If the speed at which the fluctuations propagate is further reduced, the low frequency variability in the observed hard X-ray band (dominated by the primary continuum) lags further behind that in the soft band while the high frequency part of the lag spectrum decays as the increasing lags cause these components to be phase-wrapped out.

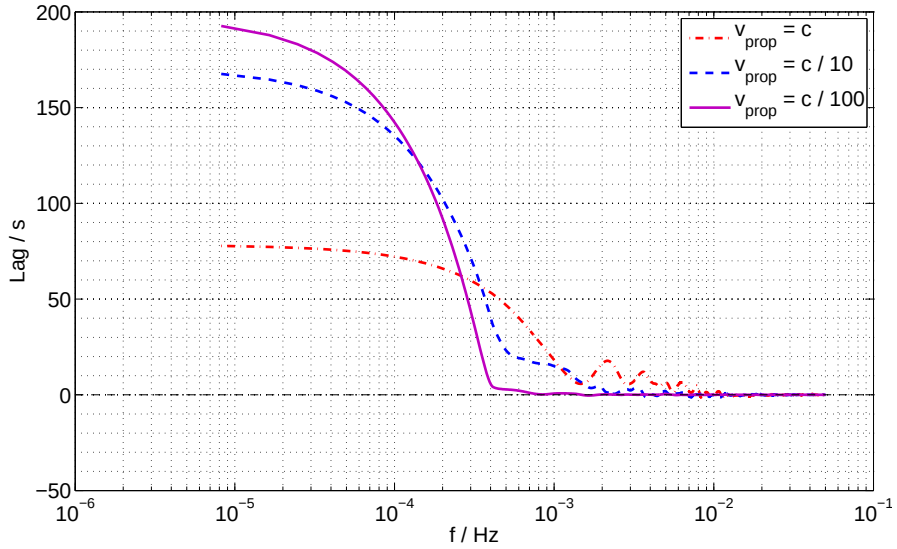

(a) Inward propagation

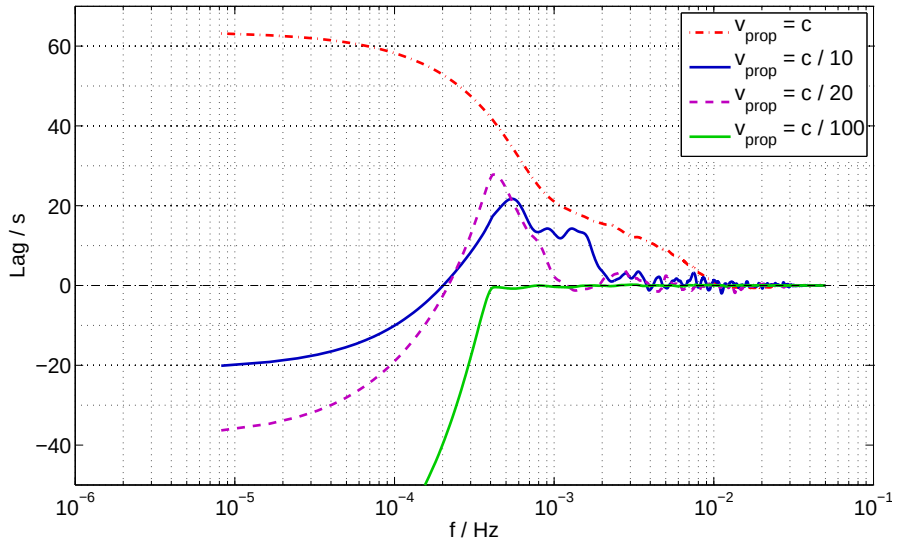

(b) Outward propagation

Figure 8.10: Lag spectra arising from fluctuations in the X-ray source luminosity propagating (a) inward from the edge of the defined source region and (b) outward from the centre. In each case, the lag spectra are shown for varying velocities at which the fluctuations propagate radially through the source region. The lag spectra are between the hard (1.0-4.0 keV, dominated by the primary continuum) and soft (0.3-1.0 keV, dominated by reflection from the acctrion disc) X-ray bands, taking into account the contributions of both spectral components to each band and the emitting region is located between 2.0 and 2.5 $r_{\rm g}$ above the accretion disc and extends radially out to 35 $r_{\rm g}$.

8.6 The Lag Spectrum of 1H 0707-495

The lag spectrum obtained for the narrow line Seyfert 1 galaxy, 1H 0707-495 (see Zoghbi et al., 2010, detailing the data reduction in the context of computing the lag spectrum) between the 1.0-4.0 keV band, dominated by the power law continuum, and the 0.3-1.0 keV band, dominated by reflection from the accretion disc, is compared to the theoretical lag spectra computed from the reflection of an X-ray continuum arising from an extended source by the accretion disc.

It is clear that the high frequency part of the lag spectrum ($> 10^{-3}$ Hz) in which the soft 'reflection' band lags behind the hard 'primary' band by around 30 s is explained naturally by an X-ray source extending outward from the rotation axis to $35\,r_{\rm g}$ and located around $2\,r_{\rm g}$ above the plane of the accretion disc which, once the effects of dilution are taken into account matches the lag of 30 s at 10^{-3} Hz as well as the decay of the lag towards higher frequencies (solid line in Fig. 8.8). This is consistent with the extent of the primary X-ray source derived in §6 from the observed emissivity profile of the reflected iron Kα line from the accretion disc. Considering the reverberation time lag, however, the average height of the emitting region, which is not well constrained by the emissivity profile alone, was found to be around $2\,r_{\rm g}$ above the disc plane. The two independent techniques compliment one another in placing constraints on the properties of the source.

It is assumed here that the X-ray source has a constant luminosity throughout its extent. In reality, it is likely that the X-ray emission will vary in luminosity throughout its volume, with, perhaps, the emission being concentrated towards the centre of the source region. Assuming constant source luminosity, however, minimised the number of free parameters in this model and finding the X-ray source under this assumption has allowed the data itself to constrain the location of the bulk of the X-ray emission. This result is the vital first step in more detailed modelling of the structure of the corona which must simultaneously satisfy the constraints from the observed lag spectrum, emissivity profile and energy spectrum.

The simple model does not, however, explain the lag spectrum at low frequencies where the hard band is seen to lag behind the soft band. Such a turnover in the lag spectrum may be, in part, accounted for by the propagation of luminosity fluctuations through the primary X-ray emitting region (in fact, fluctuations must propagate in a finite time through a spatially extended corona). If fluctuations in the X-ray source luminosity propagate outward from the centre of the source region at velocities of order one tenth of the speed of light, the low frequency variations in the soft band lead those in the hard band, while the high frequency variability shows the reverberation lag with the soft band lagging behind the hard, shown in Fig. 8.10(b).

The hard X-ray band lagging behind the soft band at low frequencies may suggest a scenario in which energy is injected into the corona at the centre, close to the black hole, then propagates outwards. It should be noted that this model does not make any assumptions about the origin of

the fluctuations in the X-ray source luminosity or their power spectral density (PSD). In fact, since the theoretical lag spectra have been computed by convolving the observed hard band light curve of 1H 0707-495 with the transfer functions corresponding to the X-ray source and the reflection, the observed PSD is accounted for inherently in the model. Neither are any assumptions made of the underlying energy transport mechanism between the accretion flow and the X-ray emitting region. Rather the observed lag spectra of AGN are accounted for in terms of the propagation of variations at a characteristic velocity (analogous to a dynamical timescale) through an X-ray emitting region which is also constrained by independent, spectral measurements of the accretion disc emissivity profile, and the response of the reflecting accretion disc.

In January 2011, 1H 0707-495 was observed to fall into a low flux state in which the spectrum was almost entirely dominated by reflection from the accretion disc with almost no flux observed from the power law continuum (§7). The reflection spectrum from the accretion disc was identified with a very steeply falling emissivity profile implying a small source concentrated close to the black hole. This can be reconciled with the energy that accelerates particles in the X-ray source originating from the central regions and then propagating outwards to form an extended source region. When the available energy decreases, particles are still accelerated close to the black hole, though since less energy is available, it is not propagated outwards meaning the source is unable to extend, reducing the detected continuum emission as the emitting volume is smaller and the emission closer to the black hole tends to be focussed on to the accretion disc to be detected after reflection.

It is possible that the fluctuations in the luminosity of the primary X-ray source are due to fluctuations into the mass accretion rate onto the central black hole (varying the energy that is released during the gravitational infall), with the fluctuations in accretion rate resulting from density fluctuations spiralling inwards through the accretion disc. Such a model is proposed by Kotov et al. (2001) and Arévalo & Uttley (2006) in which the X-ray variability of Galactic black hole binaries is explained by fluctuations in the accretion disc propagating inwards, modulating the luminosity of the X-ray emitting region as they do so. This model does not account for how the accretion disc is coupled to the corona and only finds time lags in different energy bands of the emission from the primary X-ray source with measurements in energy bands both dominated by the continuum. In the case of AGN, however, the dominant spectral component in the soft band is the reflection from the accretion disc with a characteristic lag spectrum resulting from reverberation of variability in the source.

The simple reverberation from a fluctuation that propagates outwards through the X-ray source does not, however, reproduce the entirety of the hard lag which is observed to be longer than the soft lag. Other physical effects are likely to contribute to this. As well as fluctuations propagating through the source, the coronal properties are likely to vary through its extent, such as its density and energy per particle, meaning that the luminosity and spectrum (characterised by the power law slope or photon index) of X-rays emitted from different parts of the source may change. A

greater Compton optical depth, up to unity, will result in the seed photons undergoing more scatterings and therefore reaching higher energies, producing a harder continuum spectrum. However, increasing the optical depth above unity will mean the photons undergo so many scatterings, the net effect is that energy is distributed more between the photons, resulting in a softer spectrum with more photons at lower energies. Likewise, increasing the average energy of the particles in the corona will produce a harder spectrum where more energy is transferred to the photons (see, *e.g.*, Titarchuk, 1994).

The observed hard lag at low frequencies can, alternatively, result from the X-ray source itself if the fluctuations reach parts of the source producing a harder spectrum after they reach parts of the source producing a soft spectrum. This will mean at low frequencies, variability in the hard X-ray band will lag behind that in the soft band. If this effect is to add to the hard lag produced intrinsically by the propagation of fluctuations through the source, the central regions of the X-ray source produce a softer power law continuum spectrum than the outer parts. This is possible if the average energy of the particles in the corona is greater in the outer parts. If it is only the higher energy particles that are able to travel out further from the central part into which the energy is injected from the accretion flow with the lower energy particles remaining in the centre, the average energy of particles in the outer parts of the source region will be greater, producing a harder spectrum here. Alternatively, a softer power law continuum could be produced by the innermost parts of the source if the density is much greater here such that the optical depth is greater than unity (such that the increasing density produces a softer spectrum), though it is unlikely a Compton-thick source extends further out than the innermost stable orbit of the accretion disc as this corona would obscure the reflected emission seen from the disc.

Finally, it is possible that the fluctuations in source luminosity propagate inwards from the edge of the source region and the inner parts of the X-ray source produce a harder power law continuum as the Compton depth and particle energy increases towards the centre, however for this to be the case, the variation in spectral slope must be sufficient across the source that the intrinsic time lag between the energy bands within the source is able to counteract the increased soft lag (the soft, reflection band lagging behind the hard, continuum band) that results from the fluctuations propagating inwards.

8.7 A Second Example: IRAS 13224-3809

Fabian et al. (2013) obtained the lag spectrum of the narrow line Seyfert 1 galaxy IRAS 13224-3809 from a long observation of the X-ray emission from this source with XMM Newton. The lag spectrum is of the same form as that of 1H 0707-495 with a reverberation lag (between the soft band corresponding to reflection from the accretion disc lagging behind the hard band corresponding

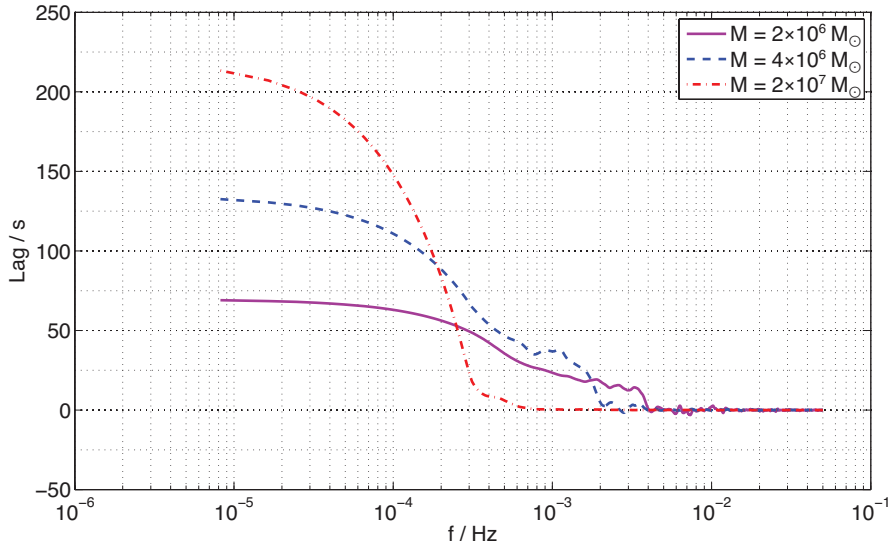

Figure 8.11: The effect of the black hole mass on the observed lag spectrum. In each case, the source is taken to extend radially out to $35\,r_{\rm g}$ from the black hole and vertically between 2 and $2.5\,r_{\rm g}$ above the plane of the accretion disc. The full effects of spectral dilution in the fractions observed in 1H 0707-495 are taken into account. The mass of the black hole in 1H 0707-495 is considered as well as twice and ten times that.

to the directly observed continuum) of around 100 s at a frequency of around 4×10^{-3} Hz and the turnover at low frequencies with the hard band lagging behind the soft.

The longer observed lag (once dilution has been taken into account) and the shift of the form of the lag spectrum to lower frequencies is consistent with the greater mass of the central black hole in IRAS 13224-3809 than in 1H 0707-495 (around $10^7\,{\rm M}_\odot$, though this is not as well determined as that of 1H 0707-495) and with the X-ray source being more compact. The emissivity profile of the accretion disc implies the X-ray source is contained within the innermost $10\,r_{\rm g}$, which, from Fig. 8.4(b), implies in itself a slight shift of the reverberation lag to lower frequencies and a longer reverberation lag than for the more extended source in 1H 0707-495 since there are fewer possible ray paths from an extended source and the rays pass closer to the central black hole, increasing the influence of the Shapiro delay. The increased mass of the black hole causes the light travel times to increase in the vicinity of the black hole as the characteristic scale-length on the spacetime ($r_{\rm g}$) increases in proportion to the black hole mass (notwithstanding the Shapiro delays in the vicinity of the black hole), both increasing the measured lag and decreasing the frequency at which the lag is seen, with more of the high frequency variability damped with longer time lags, as shown in Fig. 8.11.

8.8 Energy Dependence of Reverberation Lags

Reverberation lags arising from the reflection of the continuum X-rays by the accretion disc will be strongly energy dependent owing to the strong emission lines and other features in the reflection spectrum. It should therefore, in principle, be possible to measure the reverberation time lag as a function of energy rather than simply taking broad energy bands dominated by the reflection and continuum spectral components in order to simultaneously constrain the light travel times and the spectral features that arise from reflection. Zoghbi et al. (2010) and Kara et al. (2012) measure energy dependent reverberation lags in 1H 0707-495 and show that the iron L emission line at 0.9 keV and the iron K emission line at 6.4 keV both lag behind the continuum detected in the intermediate energy range, while Zoghbi et al. (2012) find there to be a shorter lag to the variability in the most redshifted parts of broadened emission lines originating from the innermost parts of the accretion disc than from the peaks of the lines originating further out.

In order to understand measurements of energy dependent time lags, it is necessary to know the reflection spectrum that is emitted from the accretion disc. Considering the simple case of a point source of X-rays above the plane of the accretion disc, the observed emission at any given energy will consist of both rest frame emission from the outer parts of the accretion disc, largely unaffected by relativistic effects but experiencing a long light travel time from the source, and highly redshifted emission from close to the black hole but with a much shorter time lag.

The rest frame emission from any part of the accretion disc is taken to be that described by the REFLIONX model of Ross & Fabian (2005). Rays are traced from the source to the disc and when each ray strikes the disc, the reflection spectrum from that location is then redshifted and timed to the image plane using the lookup table for that part of the accretion disc. These photons are the ones recorded by the telescope and are binned by energy and arrival time. The time-resolved reflection spectrum as would be observed by an ideal telescope with high energy and time resolution following an instantaneous flash of emission from the corona is shown in Fig. 8.12.

A first estimate of the energy-dependent lag spectrum can be computed by calculating the average arrival time of emission at each energy, taking the transfer function, $T(E,t)$ to be the number of photons arriving at time t with energy E;

$$\tau(E) = \frac{1}{\int T(E,t)dt} \int t\, T(E,t)\, dt \tag{8.9}$$

The average arrival time as a function of photon energy is shown in Fig. 8.13 for the case of a point source at $5\,r_{\rm g}$ above the black hole, where $t = 0$ is taken to be the arrival time of the continuum emitted from the point source. This lag-energy spectrum shows the extended redshifted wings of the emission line responding first since they arise from the inner parts of the accretion disc, closest to the black hole and also to the primary X-ray source. The latest response comes from line emission from the outermost parts of the accretion disc, seen here as two sharp peaks corresponding to the

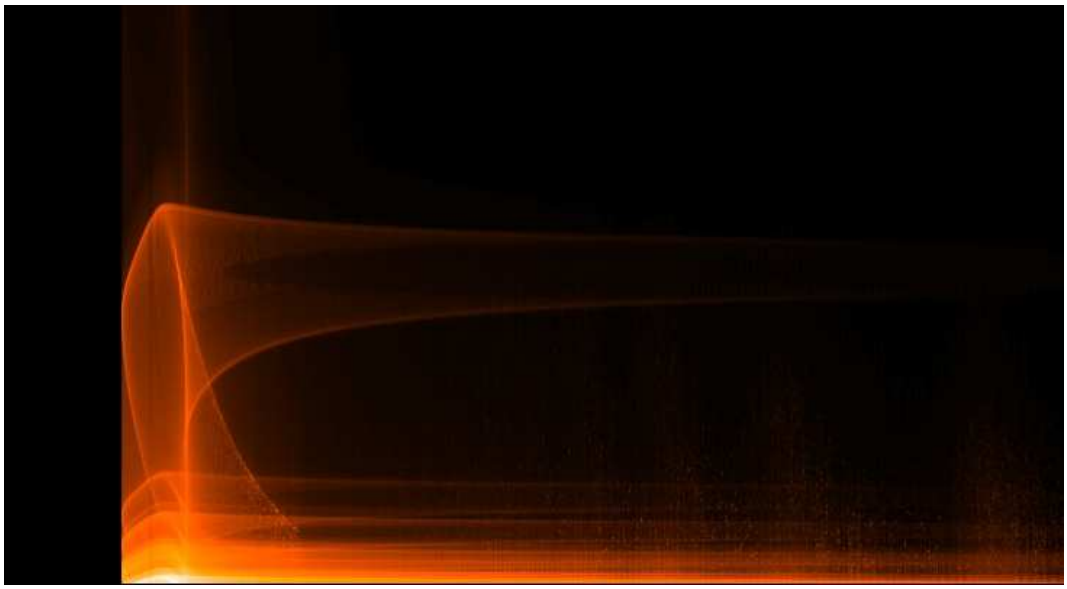

Figure 8.12: Time-resolved reflection spectrum as would be observed by an ideal telescope with high energy and time resolution following an instantaneous flash of emission from a point source at a height of $5\,r_{\rm g}$ above the plane of an accretion disc emitting according to the REFLIONX model. Photon energy runs from 0.3 keV at the bottom to 10 keV at the top. Time runs from left to right, starting at the arrival time of the continuum emission. Brighter shading corresponds to an increase in the detected photon count.

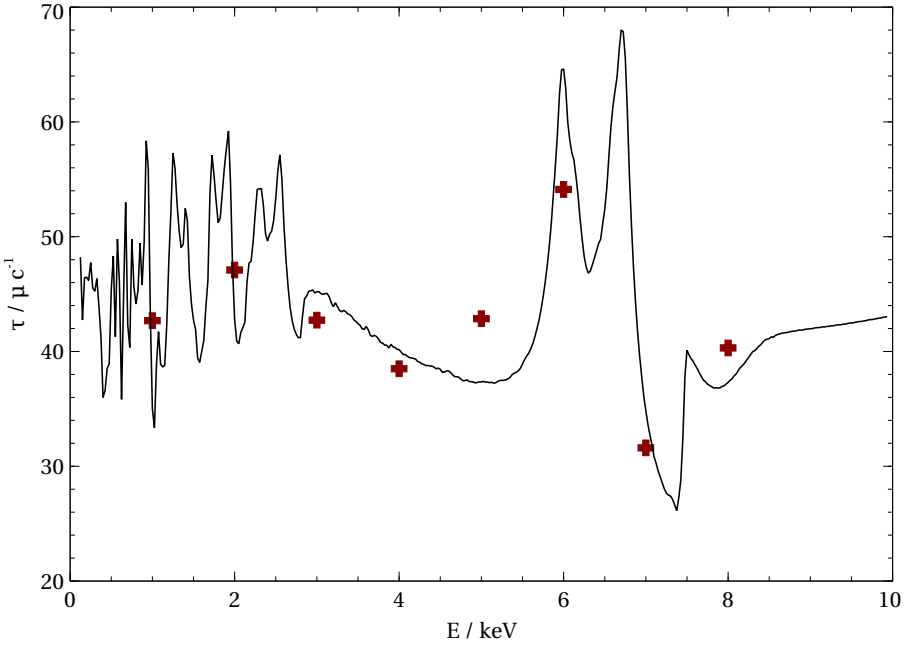

Figure 8.13: The average time lag as a function of photon energy for reverberation of X-rays emitted from a point source at a height of $5\,r_{\rm g}$ above the plane of an accretion disc that emits according to the REFLIONX model, both at high energy resolution (line) and an energy resolution currently achievable in energy-resolved variability analysis of long observations with XMM Newton (points). Energy runs from 0.3 keV at the bottom to 10 keV at the top while time runs from left to right.

Doppler shifted emission from the approaching and receding sides of the disc.

In reality, however, we do not measure the arrival times of rays in this way, rather lag spectra are computed as a function of Fourier frequency between the variability in two energy bands (the band of interest and some reference band). Recall that the lag spectrum is calculated from the phase lag; the argument of the cross spectrum of the two energy bands, $\tilde{C} = \tilde{S}^* \tilde{H}$. In the ideal case, with the hard band light curve, $H(t)$, corresponding to only the directly observed continuum emission and $S(t)$ being the light curve in whichever reflected energy band we are, interested in, the two light curves are simply related by the appropriate transfer function

$$S(E,t) = H(t) \otimes T(E,t)$$

In this case, the convolution theorem may be applied to obtain the cross spectrum:

$$\begin{aligned} \tilde{C} &= \tilde{S}^* \tilde{H} \\ &= \tilde{H}^* \tilde{H} \tilde{T}^* \\ &= \left|\tilde{H}\right|^2 \tilde{T}^* \end{aligned}$$

Thus, in the ideal case of knowing the (instantaneous) arrival time of the continuum, the phase lag is simply the argument of the Fourier transform of the transfer function. Fig. 8.14 shows the lag spectrum as a function of the variability frequency and the photon energy and is calculated by computing the Fourier transform of the transfer function in each energy band (the rays counted into time bins for that energy) using the Fastest Fourier Transform in the West (FFTW) library to perform the Fast Fourier Transform. As in the case of lag spectra computed from broad energy bands, the average time lag in the transfer function at each energy is equal to the time lag in the lowest frequency component (though not the zero frequency component whose phase is zero by definition of the FFT). Visible in the energy resolved lag spectrum are the two peaks of delayed emission from the broadened emission line which drift in photon energy on moving to higher frequency as the longer timescale components are phase-wrapped out of the observed lag; at higher frequency, the shorter lags seen by the more redshifted emission from the inner disc survive while the longer timescales from reflection from the outer parts of the disc, closer to the rest frame energy of the line are lost, causing the peak in lag to shift to lower photon energy. Also visible is the first phase wrap at sufficiently high frequency that the phase changes from π to $-\pi$ where the shading (corresponding to the lag) steps from light to dark.

In reality, of course, since every energy band contains contributions from both the reflection and directly observed continuum, lag spectra are computed between the energy band of interest and some reference band, also taken from the observation. Kara et al. (2012) take the 0.3-1.0 keV band as the reference for each energy band while Zoghbi et al. (2010) take the entire 0.3-10 keV band, though excluding the current band of interest such that noise is not correlated between the bands and is averaged out in computing the cross spectrum. Each energy band will be formed from its own transfer function (describing the arrival of both continuum and reflected photons) with which the light curve representing the underlying variability of the coronal emission is convolved. Let $L(t)$ be the underlying variability which will be convolved with transfer functions $T_1(t)$ and $T_R(t)$ to give the light curves in the energy band of interest and the reference band respectively. In this case, the cross spectrum is given by

$$\begin{aligned} \tilde{C} &= \tilde{L}^* \tilde{T_1}^* \tilde{L} \tilde{T_R} \\ &= \left|\tilde{L}\right|^2 \tilde{T_1}^* \tilde{T_R} \end{aligned}$$

Thus, the measured phase lag is the argument of the Fourier transform of the combined transfer function, $\tilde{T_1}^* \tilde{T_R}$ and the time lag is simply $\tau = \frac{\arg\left(\tilde{T_1}^* \tilde{T_R}\right)}{2\pi f}$. The energy and frequency resolved lag spectrum for X-ray reverberation from a point source at $5\,r_{\rm g}$ above the plane of the accretion disc is shown in Fig. 8.15. The earliest response is seen from energy bands dominated by the continuum and in the reflection-dominated bands, the response is led by the redshifted wings of the emission line from the inner parts of the disc, received before the peaks of the emission lines from the outer parts of the disc. Strong frequency dependence is now seen, with a 'beating' or oscillation of the lag at any given energy, most notably in bands dominated by the continuum emission. This beating

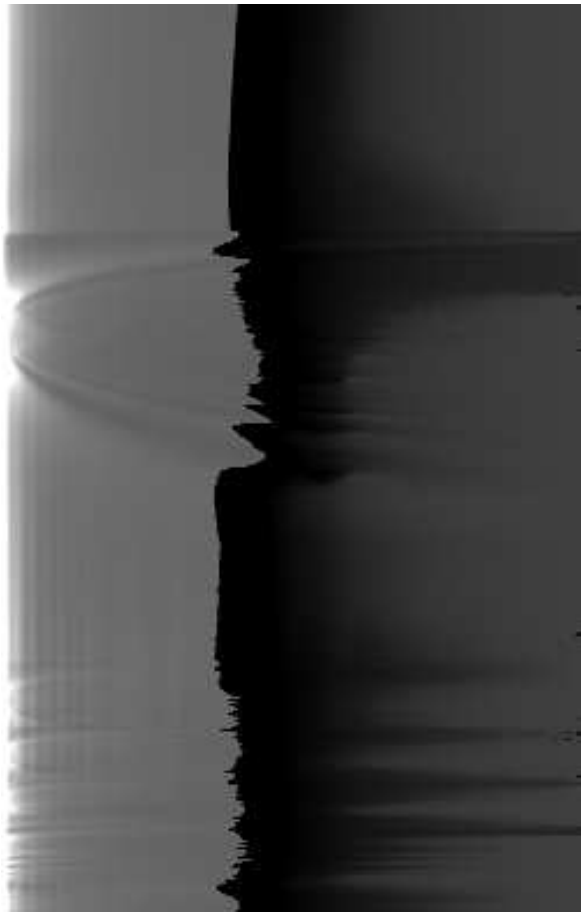

Figure 8.14: The energy resolved lag spectrum arising from reverberation of X-rays originating from a point source at a height of $5\,r_{\rm g}$ above the plane of the accretion disc, with times taken relative to the (instantaneous) arrival of the continuum. Photon energy runs from 0.3 keV at the bottom to 10 keV at the top. Variability frequency runs from left to right. Lighter shading corresponds to a longer time lag.

Figure 8.15: The energy resolved lag spectrum arising from reverberation of X-rays originating from a point source at a height of 5 $r_{\rm g}$ above the plane of the accretion disc, relative to the 0.3-1.0 keV energy band. Photon energy runs from 0.3 keV at the bottom to 10 keV at the top and variability frequency runs from left to right. Lighter shading corresponds to a longer time lag.

occurs where the lags between two relatively similar transfer functions are evaluated and is analogous to the beating of two similar waveforms that are added or subtracted. While this analysis is completed for an ideal instrument with infinite time and energy resolution, observations can be simulated for realistic instruments by convolving the transfer functions with realistic light curves (either real observations or light curves generated using simulated effective areas and background noise for an existing or proposed instrument) as in the preceding analysis of broadband lag spectra.

It is clear that the lag spectrum arising from reverberation of X-rays from an accretion disc described by the REFLIONX model has significant structure in both frequency and energy which must be understood in order to use such measurements as a probe of the accreting black hole. However, energy-resolved lag spectra are strongly dependent on both the underlying X-ray spectrum and relativistic blurring thereof, which is a function of position in the accretion disc as well as the light travel time from the X-ray source to that part of the disc. This means that given the lag spectrum at a given energy, the position of the X-ray source can be computed, in detail, with respect to positions on the accretion disc. It will be possible to probe the geometry of the X-ray emitting corona and accretion disc and even the propagation of variability through the corona along with

other properties of the corona and accretion disc in much more detail than is possible by separately considering measurements of the X-ray spectrum and variability.

Such analysis of energy-resolved lag spectra, however, requires a large number of photon counts in each time and energy bin, which in turn requires data taken using a telescope with a large collecting area. With the current generation of telescopes such as XMM Newton, trade-offs are made to maximise the number of photon counts available in the data analysis; either analysing time-averaged spectra or computing lag spectra in broad energy bands. The proposed European LOFT X-ray mission however promises a collecting area of $10\,\mathrm{m}^2$ with energy resolution between 2 and 10 keV comparable to that achieved by CCD detectors and may, for the first time, enable simultaneous fitting of models to energy and frequency resolved lag spectra to place these simultaneous constraints on models of emission in order to make significant advances in the understanding of accreting black holes.

8.9 Conclusions

In order to interpret reverberation lags and the observed lag spectra between the primary continuum and reflected X-ray emission in AGN, theoretical lag spectra were calculated for reflection of the X-ray continuum from the accretion disc by computing transfer functions in general relativistic ray tracing simulations which were convolved with the observed hard band X-ray light curve of 1H 0707-495. Lag spectra were computed for isotropic point sources at varying heights as well as a variety of spatially extended sources.

The Shapiro delay of light travelling close to the central black hole has a significant effect on the travel time of rays from the source to the reflector and to the observer. Therefore, when inferring the location and properties of the primary X-ray source from measurements of reverberation lags, it is important to account for general relativistic effects rather than directly equating the measured lag to a light travel time and the equivalent distance in flat, Euclidean space.

When interpreting observed reverberation lags, it is necessary to consider the contribution of all spectral components to the 'hard' and 'soft' bands rather than taking them to be direct proxies for the primary and reflected radiation. The 'hard' and 'soft' X-ray bands are seen to have significant contributions from both the primary continuum and reflected spectral components in AGN such as 1H 0707-495 which causes the observed time lag between the arrival of the primary continuum and reflection components to be diluted, reducing the observed lag by up to 75 per cent compared to the 'intrinsic' light travel time delay. It is therefore vital to have adequate spectral models to understand the contributions to the energy bands when interpreting reverberation lags.

By comparing the observed lag spectrum of 1H 0707-495 to theoretical predictions, the primary X-ray continuum is constrained to originating from a source region extending radially outwards to

around $35\,r_{\rm g}$ from the rotation axis, located around $2\,r_{\rm g}$ above the plane of the accretion disc. This is consistent with constraints on the location and extent of the X-ray source derived independently from the observed X-ray reflection emissivity profile of the accretion disc.

The propagation of luminosity fluctuations through an extended X-ray source is considered, since it is unphysical to think of the luminosity of a spatially extended source varying instantaneously. It is demonstrated that if the fluctuations in luminosity are allowed to propagate radially outward from the centre of the source at a velocity (corresponding to a dynamical timescale in the corona) of order a tenth of the speed of light, the resulting lag spectrum turns over at low frequencies, $< 10^{-4}\,{\rm Hz}$ and variability in the soft band (dominated by reflection) leads that in the hard band (dominated by the primary continuum) as is seen in AGN such as 1H 0707-495. This suggests that the hard lag could arise, in part, from a scenario in which energy is injected into the corona from the accretion flow very close to the central black hole and then propagates outwards into the spatially extended source region.

In this work, no assumptions are made as to the underlying physical processes through which energy is released from the accretion flow into the X-ray emitting corona. Rather, constraints are placed upon the properties the X-ray source must have to be consistent with observations in the context of the reverberation off an accretion disc surrounding a black hole in the framework of general relativity. These findings may be compared to more physical models of coronæ or indeed rays may be traced in the same framework from X-ray sources produced by these models to constrain the underlying physical processes. It is argued that the energetics of the X-ray emitting corona must be dominated by magnetic fields and coronae composed of magnetic flux loops emerging from the accretion disc due to the magneto-rotational instability have been studied extensively by, among others, Uzdensky & Goodman (2008). They describe the corona as a statistical ensemble of magnetic flux loops in (magnetic) pressure equilibrium with their surroundings, allowing them to undergo reconnection and predict that the magnetic energy density should be concentrated at low heights above the accretion disc (within a few times the scale height of the disc). Assuming a thin accretion disc with aspect ratio $H/r \sim 0.1$, this is roughly consistent with our findings from the reverberation lags that the bulk of the X-ray source is located within a few gravitational radii above the accretion disc, though more detailed theoretical work tailored to these observations would be required to place any firm constraints on the underlying process powering the corona.

9

Probing the Variability of the X-ray Source

The X-ray emission from accreting black holes is highly variable as is evident in the lightcurves shown in Fig. 9.1. For instance, the X-ray count rate observed from the AGN in IRAS 13224-3809 is seen to rise by a factor of three (from 2 to 6 $\mathrm{ct\,s^{-1}}$) on timescales of just half an hour; an increase at a rate of $7 \times 10^{40}\,\mathrm{erg\,s^{-2}}$ (assuming the spectral model for this source from §4.5.1) and even decrease by 50 per cent (from 6 to 3 $\mathrm{ct\,s^{-1}}$) in only a few hundred seconds; a rate approaching $10^{42}\,\mathrm{erg\,s^{-2}}$.

Variations in luminosity are widely attributed to fluctuations in the mass accretion rate onto the black hole, with over- and under-densities in the accretion flow that diffuse inwards on viscous timescales in the disc (*e.g.* Kotov et al., 2001; Arévalo & Uttley, 2006). The gravitational binding energy liberated by the accretion process is therefore modulated by the fluctuations in the density of the accretion disc, causing the luminosity we observe to fluctuate.

9.1 Reverberation Time Lags

Kara et al. (2013) obtain the lag spectrum of the 0.3-1.0 keV band, dominated by reflection from the accretion disc, relative to the 1.0-4.0 keV band, dominated by the directly observed continuum emitted from corona (§8) during periods in which the total observed flux from IRAS 13224-3809

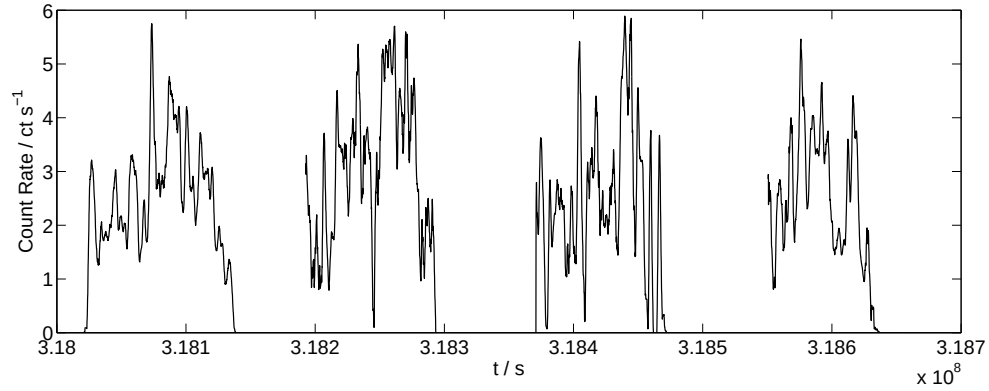

(a) 1H 0707-495 (January 2008)

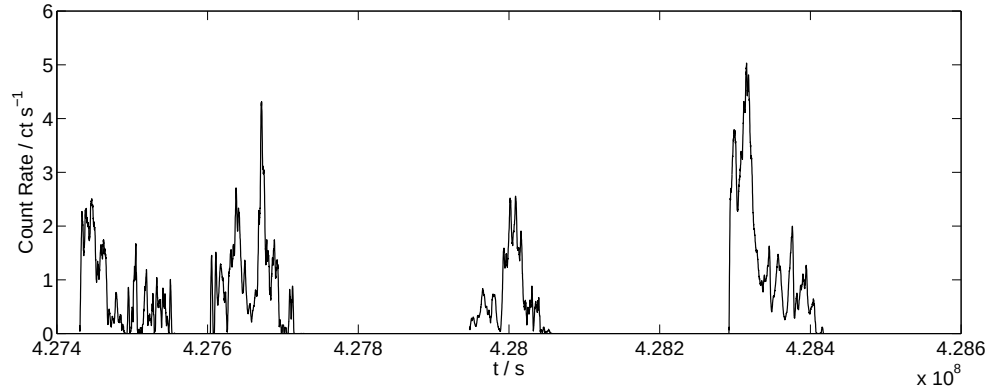

(b) IRAS 13224-3809 (July 2011)

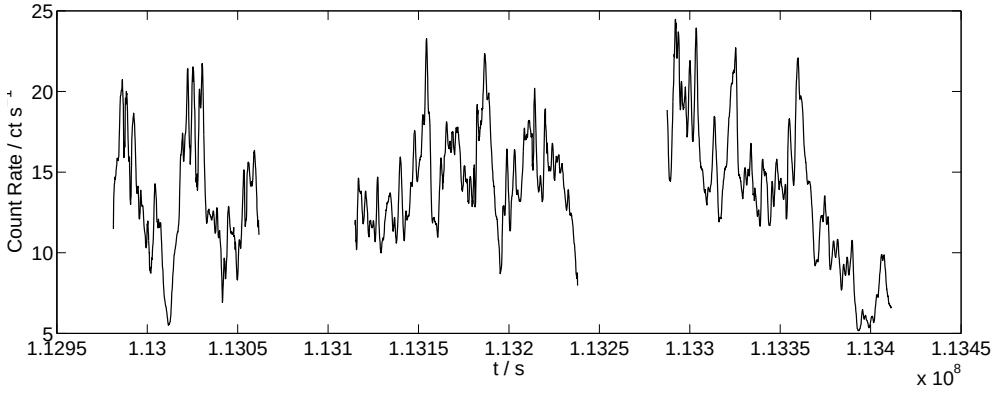

(c) MCG–6-30-15 (August 2001)

Figure 9.1: Background-subtracted X-ray lightcurves of the of the AGN (a) 1H 0707-495, (b) IRAS 13224-3809 and (c) MCG–6-30-15, recorded with the pn detector on board XMM Newton, illustrating the extreme X-ray variability exhibited by these accreting black holes.

is low, compared to the periods in which it flares. They find that the reverberation lag between variability in the 'primary' band and that in the 'reflected' band increases from around 230 s in the low flux state to around 660 s in the high flux state. The Fourier frequency at which the lag is seen decreases from 4.1×10^{-4} Hz to 1.8×10^{-4} Hz.

Interpreted in the context of X-rays emitted from a corona around the central black hole and reflecting off the accretion disc, such a result is due to the average light travel time between the source and the reflector increasing. Looking at theoretical lag spectra obtained in ray tracing simulations (§8.3.2), it can be seen that while increasing the radial extent of the coronal X-ray source decreases the observed lag time, increasing the vertical extent of the X-ray source increases the measured lag. This is not to say that the radial extent of the X-ray source is not also increasing, merely that the dominant effect is due to the increasing vertical extent of the source. It should be noted that like-for-like, the extra lag time due to increasing the vertical extent of the source is, in itself, a greater effect than that of increasing the radial extent of the source since the vertical extent of the source acts to extend the light path to the disc, while increasing the radial extent of the source decreases the effect of the Shapiro delay close to the black hole.

Analysis of reverberation lags through lag spectra requires continuous light curves. It is therefore only possible to compare the lag spectra during low and high flux states when there are extended, continuous periods during which the source can be found in such a state.

9.2 The Changing X-ray Spectrum

While there are not prolonged periods of high and low flux in other sources from which lag spectra can be extracted, it is possible to extract X-ray spectra from the different flux states. This is because the data produced by X-ray telescopes are essentially 'event lists' of all photons that reach the detector, recording the arrival time, position and energy of each. Spectra are produced by counting all of the photons that arrive during the exposure into energy bins, hence it is possible to produce spectra of the source in different flux states by only including photons that arrive when the total count rate from the source is within specified limits. Spectra are extracted across varying flux states of the narrow line Seyfert 1 galaxy 1H 0707-495 since archival observations of this source between October 2000 and September 2010 total more than 1 Ms, giving long accumulated time periods in each flux state.

9.2.1 Extracting Spectra in Varying Flux States

X-ray spectra in different flux limits were extracted from observations of 1H 0707-495 using the pn detector on board XMM Newton, a technique often employed in the analysis of the X-ray emission

Table 9.1: Flux cuts for which spectra were extracted from the observations of 1H 0707-495. The mean count rate was calculated from the light curve during each of the cuts and the error corresponds to the standard deviation of the rate within the cut. Also shown is the total exposure time selected by each filter.

GTI Count Rate	Mean Count Rate	Exposure
$0 - 3\,\mathrm{ct\,s^{-1}}$	$1.89 \pm 0.75\,\mathrm{ct\,s^{-1}}$	3.94×10^5 s
$0 - 4\,\mathrm{ct\,s^{-1}}$	$2.43 \pm 0.97\,\mathrm{ct\,s^{-1}}$	6.08×10^5 s
$0 - 5\,\mathrm{ct\,s^{-1}}$	$2.79 \pm 1.2\,\mathrm{ct\,s^{-1}}$	7.43×10^5 s
$3 - 4\,\mathrm{ct\,s^{-1}}$	$3.48 \pm 0.26\,\mathrm{ct\,s^{-1}}$	1.90×10^5 s
$3 - 5\,\mathrm{ct\,s^{-1}}$	$3.86 \pm 0.53\,\mathrm{ct\,s^{-1}}$	3.25×10^5 s
$4 - 5\,\mathrm{ct\,s^{-1}}$	$4.46 \pm 0.25\,\mathrm{ct\,s^{-1}}$	1.18×10^5 s
$4 - 6\,\mathrm{ct\,s^{-1}}$	$4.81 \pm 0.53\,\mathrm{ct\,s^{-1}}$	1.90×10^5 s
$4 - 10\,\mathrm{ct\,s^{-1}}$	$5.34 \pm 1.1\,\mathrm{ct\,s^{-1}}$	2.52×10^5 s
$5 - 10\,\mathrm{ct\,s^{-1}}$	$6.20 \pm 0.98\,\mathrm{ct\,s^{-1}}$	1.25×10^5 s
$6 - 10\,\mathrm{ct\,s^{-1}}$	$7.04 \pm 0.84\,\mathrm{ct\,s^{-1}}$	5.64×10^4 s

from accreting black holes. Data collected during individual orbits were reduced separately using the XMM Newton Science Analysis System (SAS).

After initial reduction of the event list and removal of background flares, the light curve recording the total count rate from the source (a circular region of the detector centred on the co-ordinates of the AGN, 35 arcsec in diameter) was extracted and used to create a *good time interval* (GTI) filter that selects the time periods during the orbit in which specified criteria are met. In this case, the time intervals were selected in which the total count rate from the source was within a given range.

This GTI filter was then used to extract the spectrum of the AGN counting only the photons that arrived during the time periods in which the count rate was within the required range. Thus, we obtain the average spectrum of the source over all times when the count rate is as required. Corresponding background spectra were extracted from a region of the same size, on the same chip as the source using photons from the same time periods. The photon redistribution matrices (RMF) and ancillary response matrices (ARF) were computed for each spectrum, then the spectra from all orbits in a given flux state were summed under average response matrices.

9.2.2 Spectral Analysis

Above 1.1 keV, the X-ray spectrum of 1H 0707-495 is composed entirely of the continuum emission from the coronal X-ray source (taking the form of a power law) and reflection from the accretion disc. We have seen in §4 and §6 that the emissivity profile of this reflection (the reflected flux as a

function of position on the disc) takes the form of a twice broken power law and that in the case of an X-ray emitting region extending radially over the disc, the outer break point of this function between the flattened middle region and the outer power law r^{-3} corresponds to the radial extent of the source (§6.2.4).

Clearly, the best way to determine the change in the extent of the X-ray source as the flux received from the source varies would be to determine the emissivity profile of the reflection component from each flux cut by decomposing the reflected iron Kα emission line into the contributions from successive radii (§4). The effective exposures, however, of the spectra in each of the flux cuts are only around 100 ks. This means that, particularly in the lower flux states, there were not a sufficient number of photons detected in the reflection component to properly constrain the emissivity profile in this way (§4.6).

Instead, we are guided by the emissivity profiles obtained from the total observations of 1H 0707-495 (as well as that of IRAS 13224-3809 and MCG–6-30-15) to assume that the emissivity profile takes the form of a twice broken power law and we fit the slopes of the three parts of the profile as well as the locations of the break radii, reducing the number of free parameters in the emissivity profile from 35 (the number of distinct annuli available in the KDBLUR convolution kernel) to five. The reflection spectrum as measured in the rest frame of the material in the accretion disc was computed with the REFLIONX code of Ross & Fabian (2005) and was convolved with the profile of a single emission line broadened by the relativistic effects from an orbiting accretion disc in the Kerr spacetime using a twice-broken power law form of the emissivity profile, itself computed using the KDBLUR3 model. The directly observed continuum emission from the corona was modelled as a power law, giving the total model spectrum

$$\mathrm{powerlaw} + \mathrm{kdblur3} \otimes \mathrm{reflionx} \tag{9.1}$$

The inclination of the accretion disc and the iron abundance were fixed at the previously found best-fit values as these certainly do not change during the observation. The ionisation parameter in the REFLIONX model was also assumed to remain constant between the high and low flux periods within the observations. While in reality, variation in the incident X-ray flux will likely change the ionisation state of the reflecting material, the value obtained in fitting to the whole observation will be the average ionisation parameter during this period. As seen in §4.7.3, errors in the estimate of the overall ionisation state of the accretion disc do not affect the shape of the recovered emissivity profile, though it is possible that gradients in ionisation across the disc will, though it is assumed that the shape of the ionisation profile of the disc does not greatly change on the timescales of these observations.

The slope of the power law continuum and the normalisations of the continuum and reflection are fit as free parameters to the spectrum and the slopes and break radii of the emissivity profile are fit, but constrained to be within reasonable ranges to give the expected shape of the emissivity profile

Table 9.2: Allowed ranges for the parameters of the twice-broken power law emissivity profile when fitting to find the extent of the X-ray source.

Parameter	**Fit Range**
Index 1	5 – 10
Break radius 1	3 – 5 $r_{\rm g}$
Index 2	0 – 2
Break radius 2	5 – 35 $r_{\rm g}$
Index 3	2 – 4

(*i.e.* a steep decline, followed by a flatter region before a slope close to r^{-3} over the outer parts of the disc) as shown in Table 9.2

9.2.3 The Extent of the X-ray Source

We first turn our attention to the variation of the emissivity profile with the total flux received. Fitting the emissivity profile to the observed spectrum (namely the profile of the relativistically broadened iron Kα emission line) as a twice-broken power law, the location of the outermost break radius (between the flat part of the emissivity profile and the approximate inverse-cube profile over the outer part of the disc) as a function of count rate for 1H 0707-495 is shown in Fig. 9.2(a).

Identifying the outer break radius of the emissivity profile with the outermost radial extent of the X-ray source in a plane parallel to the accretion disc (§6.2.4), we see evidence that the X-ray emitting corona expands as the luminosity increases then contracts as the luminosity decreases again (note we are finding the average extent of the source between all times of a given count rate rather than following the evolution of the source in time as the count rate varies). The increase in radius of the corona is slight with, at most, a 2σ variation between points at low and high count rates.

We saw in §8 that varying the radial extent of the X-ray emitting region above the accretion disc had only a slight effect on the measured reverberation lag seen in the reflection from the accretion disc. In fact, increasing the radial extent of the source decreased the reverberation lag since the X-rays emitted further from the central black hole do not experience such an extreme Shapiro delay which slows down their passage from the inner parts of the corona. Therefore, to explain the increasing lag time with increasing count rate observed by Kara et al. (2013), the source must also be expanding vertically (*i.e.* perpendicular to the plane of the accretion disc), though the vertical extent of the corona is not well constrained by the emissivity profile. That said, it is not physically unreasonable to picture a corona of accelerated particles expanding in all directions (either through more particles being accelerated or the accelerated particles being less confined) as more energy is injected into it to increase the luminosity.

9.2.4 The Continuum Spectrum

Turning to the photon index of the directly observed continuum emission from the corona, Γ (where the continuum spectrum takes the form $I_E(E) \propto E^{-\alpha}$ in terms of the spectral energy density or $N_E(E) \propto E^{-\Gamma}$ in terms of photon count rates, with $\Gamma = 1 + \alpha$), the best-fit value for the photon index of the continuum spectrum for each flux cut is shown in Fig. 9.2(b).

It is clear to see that as the luminosity of the X-ray source increases, the coronal emission becomes softer, with a more steeply falling spectrum such that fewer hard X-rays are emitted compared to the softer photons.

Comptonisation of thermal seed photons emitted from the accretion disc by high energy electrons in the corona has been widely explored as the means of producing the X-ray continuum seen from accreting black holes (see, *e.g.*, Galeev et al., 1979; Titarchuk, 1994). A softer continuum spectrum (with a greater photon index) is produced if the average energy of each individual electron in the corona is reduced, or if the number density of scattering electrons is increased such that the Compton optical depth of the corona increases above unity (Sunyaev & Trümper, 1979). Given that we see evidence of the corona expanding as the count rate increases and that we do detect relativistically blurred line emission from the inner parts of the accretion disc that would be beneath the corona we infer from the observed emissivity profile, the optical depth of the corona due to Compton scattering cannot be increasing much above unity as an optically thick corona should scatter the emission we detect from the inner parts of the disc and would require an enormous increase in the number of scattering particles for it to both expand and become optically thicker.

It is more likely that the as the corona expands, the energy per electron decreases, however more electrons are accelerated through a larger volume. This would produce the softer continuum spectrum and the increased number of scattering particles throughout a larger volume would provide a larger cross section for scattering seed photons emitted from the accretion disc, explaining the increase in count rate of X-ray photons emitted from the corona.

9.2.5 The Reflected vs. Direct Continuum Flux

A key prediction of models in which the increase in luminosity of an X-ray emitting corona corresponds to the spatial expansion of that corona is that a collapse of the corona into a more confined region around the central black hole not only leads to reduced overall luminosity but also must result in an increase in the number of photons hitting the disc to be reflected relative to the number that are able to escape to be observed in the continuum. This increase in the reflection fraction is due to emission from closer to the black hole being bent towards the black hole and thus focussed onto the accretion disc and was invoked to explain the simultaneous steepening of the iron line emissivity profile and disappearance of the continuum when 1H 0707-495 dropped into an extremely low

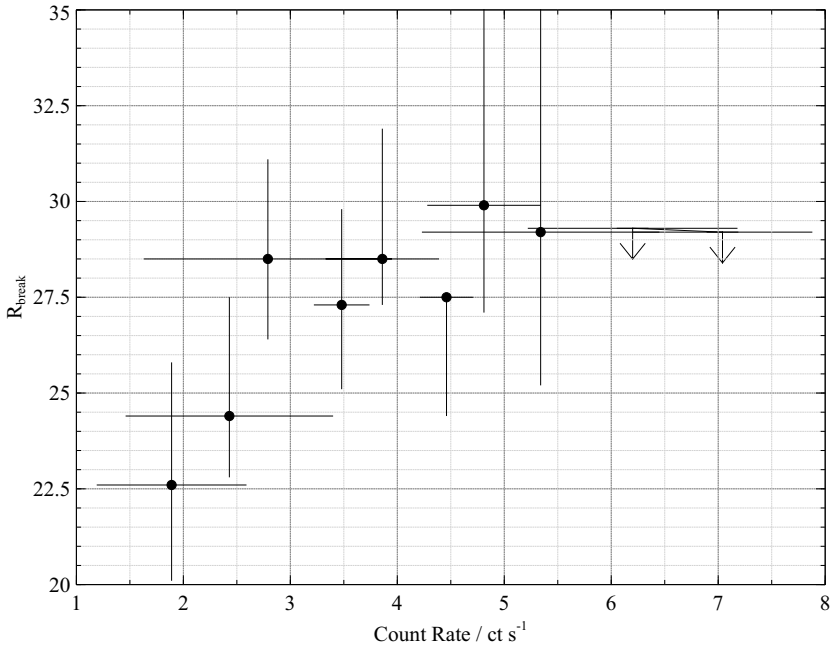

(a) Emissivity profile outer break radius

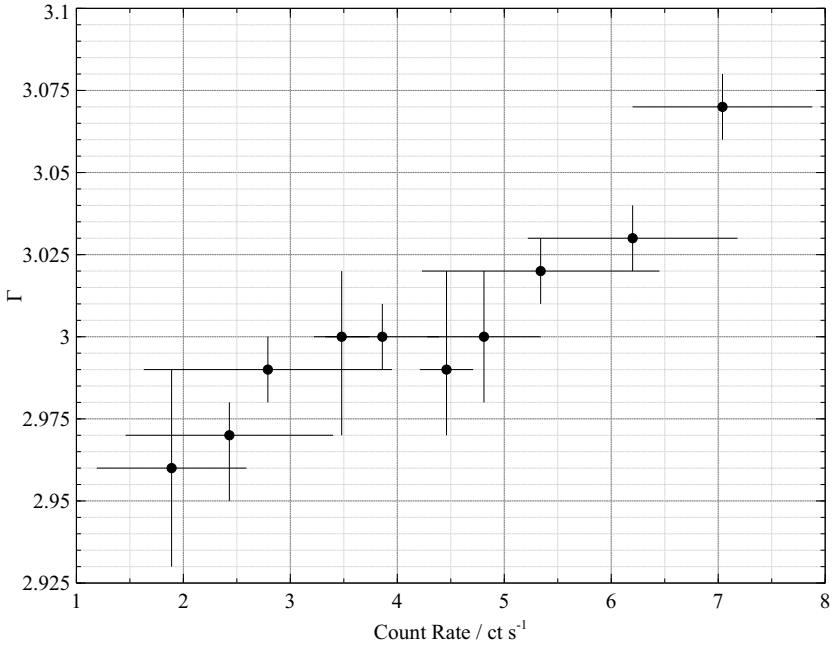

(b) Photon index of X-ray continuum

Figure 9.2: The outer break radius of the emissivity profile (assumed to be a twice-broken power law) of the X-ray reflection from the accretion disc and (b) the photon index of the continuum emission from the corona in 1H 0707-495 as a function of the total count rate from the source. Error bars correspond to 1σ.

flux state in January 2011 (§7).

Ray tracing simulations will predict the number of photons emitted from the corona that hit the disc compared to the number that escape to infinity. They do not, however, predict the number of photons that will be *observed* in the reflection component of the observed spectrum without inputting a detailed model of the (spatially resolved) properties of the disc material and the 'reflection' processes that take place when photons are incident upon the accretion disc (Compton scattering, photoelectric absorption, fluorescent line emission, bremsstrahlung, *etc.*). As such, the number of photons that are seen in the reflection spectrum is not directly indicative of the number of photons that hit the disc and cannot be directly compared to the number of photons detected in the continuum.

It is, however, possible to probe the variation in reflection fraction by measuring the photon flux seen in the reflection component of the spectrum *as a function of* the photon flux directly detected in continuum emission from the corona. This is achieved by fitting the model consisting of a power law continuum and reflection from the accretion disc described by the REFLIONX code as detailed above and then computing the flux (which can be found as both the photon flux and energy flux) that would be detected by the telescope in each of these spectral model components by folding the fitted model through the instrument responses. When considering reflection from the accretion disc, significant flux emerges in the 'Compton hump' around 30 keV and at soft X-ray energies, around 0.1 keV. It is therefore necessary to compute fluxes integrating photons over a wide energy range, here taken to be 0.1-100 keV and the instrument response is extrapolated from its limit at 12 keV up to 100 keV for the purposes of computing the flux represented by the model components.[1]

The models are fit to the data over both the energy bands 0.3-10 keV (the full energy range of the pn detector) and 1.1-10 keV (containing only the X-ray continuum and the iron Kα emission line). The ionisation parameter is allowed to vary as a free parameter in this instance as changes in the ionisation state of the disc could result in errors computing the fluxes. The data in the 1.1-10 keV energy band is better fit by the model, though the 0.3-10 keV band is included for completeness to ensure the ionisation parameter is well determined, as this is sensitive to the series of emission lines below 1 keV. Results are shown in Fig. 9.3 and it can be seen that the relationship between the reflected and continuum flux is broadly consistent between the two fits in the two energy bands, suggesting that in the case of 1H 0707-495, the reflected flux is related to the continuum flux as approximately $R \propto C^{0.4}$.

If the reflection fraction remained constant (*i.e.* the source geometry remained constant or reflection took place from distant material and experienced no gravitational light bending enhancing reflection as the X-ray source changes) and the reflected flux changed only due to the variations in

[1]The instrument response extrapolation and flux calculations are performed as part of the spectral fitting procedure in XSPEC.

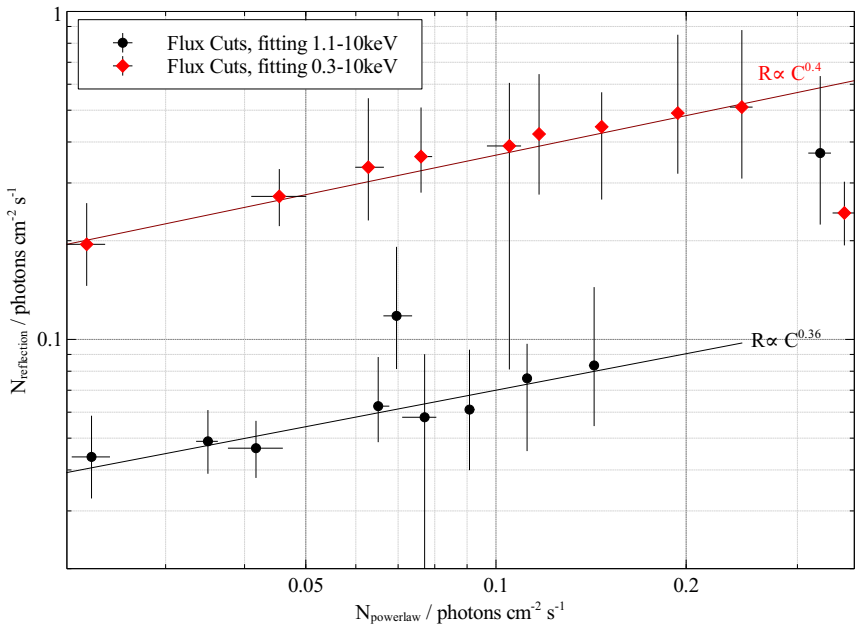

Figure 9.3: The relationship between the photon counts in the X-ray reflection from the accretion disc and the directly observed continuum emission in 1H 0707-495 obtained by fitting a model consisting of a power law continuum and reflection from the accretion disc described by the REFLIONX model of Ross & Fabian (2005) along with the best fitting power laws. Error bars correspond to 1σ.

the illuminating luminosity (the intrinsic variability in the source), one would expect the reflected photon flux to rise linearly with the continuum flux detected directly from the corona. This linear relation would hold no matter how the intrinsic luminosity of the source varies in time. At the other extreme, if the total photon count rate emitted from the source remains constant but its location or geometry changes, changing the fraction of the emitted photons that are reflected, the reflected photon flux would fall linearly as the continuum flux increases (*i.e.* the shape $y = 1 - x$ where y and x correspond respectively to the reflected and continuum flux). The total number of photons is conserved, they are just moved from one component to the other, except when the source is close to the black hole, when both the reflected and continuum fluxes would fall as a significant proportion of the photons emitted from the corona are lost into the black hole.

If the luminosity of the source is allowed to vary while it expands, the relationship between the continuum and reflected fluxes cannot be simply interpreted in terms of the extent or position of the corona. Instead, a simplified model is constructed to test if the data we obtain are consistent with the picture of an expanding corona giving rise to increased X-ray luminosity. While we do not know how the intrinsic luminosity of the X-ray source changes, we are guided by the observation that the radial extent of the source, r increases as the source becomes brighter, to approximate the total luminosity as a power law in the radius of the emitting region, $L \propto r^{\beta}$. We also know that the vertical extent of the source, Δz must increase to explain the observed increase in the reverberation lag time measured in the high flux state.

Ray tracing simulations are used to compute the fraction of the emitted photons that hit the accretion disc, are able to escape to be observed as the continuum and that are lost into the black hole event horizon as a function of the source radius, with the vertical extent of the source either being held constant or defined to increase linearly with the radius within the limits of the coronal geometry inferred in emissivity and reverberation lag measurements (though it turns out that the functional form of reflection fraction is not greatly altered by how the vertical extent of the source varies with radius). Multiplying these fractions by the total luminosity of the source using the above parametrisation, we find that in order to produce the observed flux-flux relation for 1H 0707-495, $R \propto C^{0.36}$, for instance, the total count rate emitted from the entire volume of the corona obeys $L \propto r^{0.35}$ (Fig. 9.4) in this simple model.

Naïvely, if the average energy density of the corona remained constant and it simply grew, the luminosity of an axisymmetric corona will follow $L \propto r^2 \Delta z$ or $L \propto r^3$ if the height were to increase linearly with the radial extent. Finding such a low power law index relating the luminosity to the radial extent of the source implies that the average energy density of the corona *decreases* as it expands. The energy density would decrease during the expansion of the corona if the corona was the most luminous in its central regions and the expanding and contracting outer parts of the corona were made up of less energetic particles. The decrease in the average energy density of the corona as it increases in volume would also explain the softening of the power law continuum seen

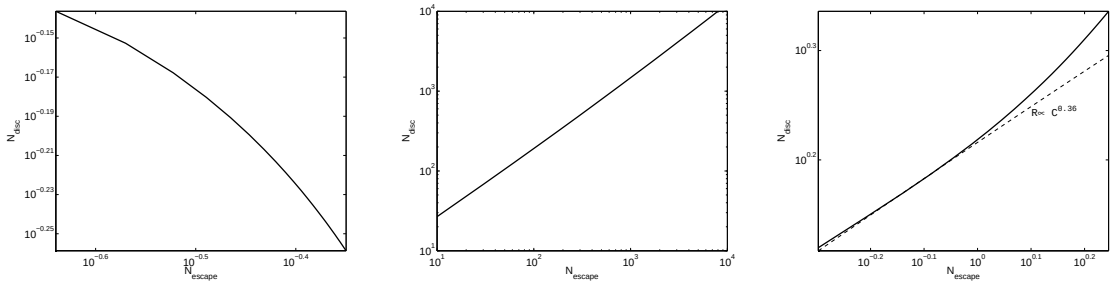

(a) Constant photon count (b) $L \propto r^2\,\Delta z$ (c) $L \propto r^{0.35}$

Figure 9.4: The relationship between the photon counts in the X-ray reflection from the accretion disc and the directly observed continuum emission computed from ray tracing simulations counting the rays that hit the disc and that are able to escape to infinity from a corona with varying radial extent from 2 to 50 r_g whose vertical extent varies linearly with the radial extent from 0.5 r_g to 5 r_g for (a) constant source luminosity where the total photon count is constant and photons are just shifted between the two groups giving a $y = 1 - x$ relationship, except for the most confined sources where a substantial fraction of the photons is lost into the black hole, (b) the source luminosity varying proportional to its volume, $r^2\,\Delta z$. In this case the significant intrinsic variability outweighs the change in reflection fraction resulting in the reflected flux rising linearly with the continuum flux. In (c), the intrinsic, total luminosity of the source is taken to vary as $r^{0.35}$ to reproduce the $R \propto C^{0.36}$ relationship seen in 1H 0707-495 over the source radii up to around 30 r_g. At larger source radii, the reflection fraction becomes approximately constant and the reflected flux starts to rise linearly with the continuum flux.

in the lower flux states, since if this is produced by the Comptonisation of thermal photons emitted from the accretion disc, lower energies per scattering particle will produce a softer spectrum while a larger corona covering more of the disc will have a greater cross section for scattering photons so the continuum will be brighter.

9.3 Conclusions

By analysing spectra obtained for the narrow line Seyfert 1 galaxy 1H 0707-495 in states of high and low flux, evidence has been found for the expansion of the X-ray emitting corona as the coronal luminosity increases and contraction to a more confined region around the black hole as the luminosity decreases again. The emissivity profile of the accretion disc, obtained by fitting a twice-broken power law emissivity profile to the relativistically broadened iron Kα emission line implies that the radial extent of the corona in 1H 0707-495 above the plane of the accretion disc varies by 25 to 30 per cent on timescales of hours as the total flux received varies by a factor of two to three. Combined with measurements of an increasing reverberation lag during prolonged high-flux periods of IRAS 13224-3809 and the low state of 1H 0707-495 discussed in §7, a picture is emerging of X-ray emitting corona that expands and contracts both radially and vertically above the plane of the accretion disc as more or less energy is injected from the accretion flow.

It is observed that as the flux received from the source increases, the continuum spectrum becomes softer, while in order to reproduce the observed relationship between the primary continuum and reflected fluxes by simply following the changing reflection fraction as the corona expands and contracts it is required that the total luminosity of the corona expands only as a weak function of its radius rather than scaling with its volume. These observations suggest that as the corona expands, the energy per scattering particle decreases though there being more scattering particles in a larger corona explains the increase in luminosity if the corona is said to arise from the inverse-Compton scattering of thermal seed photons emitted from the accretion discs.

This analysis demonstrates the understanding that can be gained of the processes at work in the X-ray emitting corona around a black hole through detailed analysis of the observed data combined with insight gained from theoretical predictions. These conclusions are, however, limited by the quality of data available with these results derived from the long total exposure time of 1H 0707-495. It will be possible to draw firmer conclusions from longer observations of other objects such that high quality spectra can be obtained in many different states of the system.

10

Conclusions and Looking Ahead

X-ray reflection from accretion discs surrounding black holes was analysed in the context of probing the central regions of accreting black holes; both in active galactic nuclei and X-ray binaries.

A method was devised for obtaining the emissivity profile of the accretion disc, that is the reflected flux as a function of radius, using the profile of relativistically broadened emission lines seen in the X-ray spectrum. This method exploits the varying Doppler and gravitational redshift of emission from different radii, fitting the contributions from successive radii in the accretion disc to the overall line profile and proved successful in recovering the emissivity profiles of the accretion discs in the narrow line Seyfert 1 galaxies 1H 0707-495, IRAS 13224-3809 and MCG–6-30-15 as well as the Galactic X-ray binary Cygnus X-1. Measuring the emissivity profile was found to be a powerful tool in constraining the location and extent of the corona that gives rise to the X-ray continuum emission.

A formalism was developed in which fully relativistic ray tracing simulations could be carried out from a general X-ray source in the corona to the accretion disc where X-rays are reflected to be finally observed by a telescope at infinity. Simulations were started from the fewest possible assumptions, based upon emission of X-rays from isotropic point sources and extended coronae with simple geometries as well as the idealised reflection of all X-rays from a plane to discover the

intrinsic effects that are inevitable in the emission and reflection of X-rays in the curved spacetime around a black hole, before being extended to more realistic models. Simulations were tailored to give predictions that can be directly compared with observed data of real black holes.

Calculation of theoretical emissivity profiles of accretion discs illuminated by both X-ray point sources and simple extended coronae confirmed that the emissivity profiles measured from X-ray spectra of accreting black holes (steeply falling over the inner part of the accretion disc then flattening before the reflected flux decreases as r^{-3} over the outer part of the accretion disc) arise naturally from relativistic effects on the propagation of rays in the curved space time around the black hole as well as on the relative passage of time for observers at different radii in the disc. It was determined that the break point between the flat part of the emissivity profile and the r^{-3} fall off over the outer disc corresponds to the outermost radial extent of the X-ray source allowing the X-ray emitting corona to be located. The corona in 1H 0707-495 was found to extend radially out to $30 \sim 35\,r_{\rm g}$ above the plane of the accretion disc while in both IRAS 13224-3809 and MCG–6-30-15 the corona extends to around $10\,r_{\rm g}$. The Galactic X-ray binary Cygnus X-1 was found to have a much more compact corona, within $5\,r_{\rm g}$ of the black hole, perhaps corresponding to the base of the jet.

Measurement of the accretion disc emissivity profile enabled the low flux state that 1H 0707-495 was seen to drop in to in January 2011 to be understood in the context of the X-ray emitting corona collapsing down to a confined region within $2\,r_{\rm g}$ of the black hole. Such a compact corona explains the steeply falling emissivity profile that was measured as well as the disappearance of the directly observed continuum emission from the corona since many of the photons emitted from such a compact source are focussed towards the black hole and onto the accretion disc.

The rapid variability of X-ray emission from accreting black holes in AGN was exploited in the measurement of reverberation time lags. Variability in the reflection from the accretion disc is seen to lag behind that in the directly observed continuum from the corona and can be understood in the context of the additional light travel time from the source to the reflector. X-ray reverberation was analysed in the Kerr spacetime and the Shapiro delay of light rays travelling close to a black hole as well as the dilution of the measured time lag by multiple spectral components contributing to observed energy bands were found to be important in analysing X-ray reverberation. Measurement of reverberation time lags provides an independent means of constraining the extent and location of the X-ray source and the coronal geometry derived from analysis of the lag spectrum of 1H 0707-495 was found to be consistent with that found from analysis of the measured accretion disc emissivity profile while the height of the corona was able to be better constrained to around $2\,r_{\rm g}$ above the plane of the accretion disc. Reverberation lag spectra were also found to depend upon the means by which fluctuations in luminosity propagate through the extent of the corona. It was found that lag between the low energy and higher energy X-ray emission seen at low variability frequencies could be produced by fluctuations in luminosity propagating outward through the corona from the central regions, suggesting mechanisms by which the energy is liberated from the accretion flow

and injected into the corona.

By analysing spectra extracted from observations of 1H 0707-495 during time intervals in which the flux received from the source was at different levels, evidence was found for the X-ray emitting corona expanding as the luminosity increases then contracting as it decreases again on timescales of hours. Furthermore, the changing slope of the continuum spectrum between these different flux states as well as the observed relationship between the continuum and reflected flux suggest that as the corona expands, while its total energy increases, the average energy density decreases.

There are exciting prospects for further detailed studies of accreting black holes with the next generation of X-ray telescopes. The NuSTAR telescope, launched in 2012, offers imaging and the capability to measure X-ray spectra up to 79 keV, which will allow the measured reflection spectra to include the prominent Compton hump. Including this strong spectral feature will enable much tighter constraints to be placed on the observed reflection to improve measurements of the reflected flux from which constraints were placed on the evolution of the corona as the X-ray luminosity varies as well as measurements of reverberation time lags between the continuum and reflected emission. The Japanese-led, Astro-H, due to launch in 2015 will offer vastly improved energy resolution, as low as a few eV through a microcalorimeter spectrometer, giving much more detail in the measured spectra of accreting black holes than has been achieved before. Improved energy resolution will not only allow better measurements of emissivity profiles and other quantities from spectra, but will also allow the physical processes at work in the corona and on the accretion disc to be probed in more detail. Proposed missions also bring exciting prospects for probing accreting black holes; the LOFT mission with its large area detector would enable energy resolved analysis of the variability while a future large X-ray observatory will offer both high energy resolution and a larger collecting area to obtain high quality spectra and perform high quality timing analysis.

Having said that, the power of the existing X-ray observatories; notably XMM Newton and Suzaku for the study of black holes, but also Chandra, should not be underestimated. Vast archives of observations coupled with insight gained from theoretical predictions guiding detailed data analysis and the interpretation thereof hold the potential to make great advances in understanding. At the same time, while great advances have been made comparing models of X-ray reflection from fairly simple coronae, perhaps representing the time average or the bulk of the X-ray emission, simulations can be extended to include more physically realistic models of X-ray emitting coronae and the processes therein, perhaps from magneto-hydrodynamic simulations of particle acceleration followed by Comptonisation of photons from the accretion disc to discover the roles such models play in interpreting observations of black holes. Detailed analyses of X-ray reflection and the structure of the corona can also be compared to other observed phenomena such as the acceleration of jets, state transitions in Galactic X-ray binaries and even more general properties of the system such as the accretion rate to really gain an understanding of how these phenomena are linked by the liberation of energy from the accretion flow.

Research to date has revealed a tantalising amount of information about the structure and physical mechanisms at work in accreting black holes right down to the innermost few gravitational radii. By connecting observational data with theroetical insights gained from ray tracing simulations it has been possible to not only locate the X-ray emitting corona, but to observe how it varies as the luminosity of the X-ray source fluctuates and even to start to understand how fluctuations propagate through its extent, constraining mechanisms by which energy is injected from the accretion flow. Through detailed analysis of vast archives of observations, coupled with further development of theoretical modelling and the advances promised by the next generation X-ray observatories, great advances lie ahead in understanding the physical processes powering some of the brightest objects in the Universe.

Bibliography

Agol E., Krolik J. H., 2000, ApJ, 528, 161

Arévalo P., Uttley P., 2006, MNRAS, 367, 801

Arnaud K. A., 1996, in Astronomical Society of the Pacific Conference Series, Vol. 101, Jacoby G. H., Barnes J., ed, Astronomical Data Analysis Software and Systems V, p. 17

Beckwith K., Hawley J. F., Krolik J. H., 2008, MNRAS, 390, 21

Beckwith K., Hawley J. F., Krolik J. H., 2009, ApJ, 707, 428

Blandford R. D., Payne D. G., 1982, MNRAS, 199, 883

Blandford R. D., Rees M. J., 1974, MNRAS, 169, 395

Blandford R. D., Znajek R. L., 1977, MNRAS, 179, 433

Blustin A. J., Fabian A. C., 2009, MNRAS, 399, L169

Brenneman L. W., Reynolds C. S., 2006, ApJ, 652, 1028

Chandrasekhar S., 1983, The Mathematical Theory of Black Holes. Oxford

Chiang C.-Y., Fabian A. C., 2011, MNRAS, 414, 2345

Cunningham C., 1976, ApJ, 208, 534

Cunningham C. T., 1975, ApJ, 202, 788

Dabrowski Y., Lasenby A. N., 2001, MNRAS, 321, 605

Dauser T., Wilms J., Reynolds C. S., Brenneman L. W., 2010, MNRAS, 1460

de Marco B., Ponti G., Cappi M., Dadina M., Uttley P., Cackett E. M., Fabian A. C., Miniutti G., 2012, ArXiv e-prints

de Marco B., Ponti G., Uttley P., Cappi M., Dadina M., Fabian A. C., Miniutti G., 2011, MNRAS, 417, L98

Dovčiak M., Karas V., Yaqoob T., 2004, ApJS, 153, 205

Emmanoulopoulos D., McHardy I. M., Papadakis I. E., 2011, MNRAS, 416, L94

Fabian A. C. et al., 2013, MNRAS, 429, 2917

Fabian A. C., Rees M. J., Stella L., White N. E., 1989, MNRAS, 238, 729

Fabian A. C., Vaughan S., 2003a, MNRAS, 340, L28

Fabian A. C., Vaughan S., 2003b, MNRAS, 340, L28

Fabian A. C. et al., 2002, MNRAS, 335, L1

Fabian A. C. et al., 2009, Nat, 459, 540

Fabian A. C. et al., 2011, MNRAS, 1970

Galeev A. A., Rosner R., Vaiana G. S., 1979, ApJ, 229, 318

George I. M., Fabian A. C., 1991, MNRAS, 249, 352

Gilfanov M., Churazov E., Revnivtsev M., 2000, MNRAS, 316, 923

Goyder R., Lasenby A. N., 2004, MNRAS, 353, 338

Guilbert P. W., Rees M. J., 1988, MNRAS, 233, 475

Haardt F., Maraschi L., 1991, ApJ, 380, L51

Halpern J. P., 1984, ApJ, 281, 90

Kara E., Fabian A. C., Cackett E. M., Miniutti G., Uttley P., 2013, MNRAS, 430, 1408

Kara E., Fabian A. C., Cackett E. M., Steiner J., Uttley P., Wilkins D. R., Zoghbi A., 2012, MNRAS submitted

Kerr R., 1963, Phys. Rev. Let., 11, 237

Kotov O., Churazov E., Gilfanov M., 2001, MNRAS, 327, 799

Laor A., 1991, ApJ, 376, 90

Martocchia A., Karas V., Matt G., 2000, MNRAS, 312, 817

Matt G., Fabian A. C., Reynolds C. S., 1997, MNRAS, 289, 175

McKinney J. C., Tchekhovskoy A., Blandford R. D., 2012, MNRAS, 423, 3083

Merloni A., Fabian A. C., 2001, MNRAS, 328, 958

Miller L., Turner T. J., Reeves J. N., 2008, A&A, 483, 437

Miller L., Turner T. J., Reeves J. N., Braito V., 2010, MNRAS, 408, 1928

Miniutti G., Fabian A. C., Goyder R., Lasenby A. N., 2003, MNRAS, 344, L22

Novikov I. D., Thorne K. S., 1973, in C. Dewitt & B. S. Dewitt , ed, Black Holes (Les Astres Occlus), p. 343

Nowak M. A., Vaughan B. A., Wilms J., Dove J. B., Begelman M. C., 1999, ApJ, 510, 874

Reynolds C. S., Young A. J., Begelman M. C., Fabian A. C., 1999, ApJ, 514, 164

Ross R. R., Fabian A. C., 2005, MNRAS, 358, 211

Ross R. R., Fabian A. C., Ballantyne D. R., 2002, MNRAS, 336, 315

Shakura N. I., Sunyaev R. A., 1973, A&A, 24, 337

Shapiro I. I., 1964, Phys. Rev. Lett., 13, 789

Stella L., 1990, Nat, 344, 747

Suebsuwong T., Malzac J., Jourdain E., Marcowith A., 2006, A&A, 453, 773

Sunyaev R. A., Trümper J., 1979, Nat, 279, 506

Svoboda J., Dovčiak M., Goosmann R. W., Jethwa P., Karas V., Miniutti G., Guainazzi M., 2012, A&A, 545, A106

Svoboda J., Dovčiak M., Goosmann R. W., Karas V., 2010, in American Institute of Physics Conference Series, Vol. 1248, A. Comastri, L. Angelini, & M. Cappi , ed, American Institute of Physics Conference Series, p. 515

Tanaka Y. et al., 1995, Nat, 375, 659

Titarchuk L., 1994, ApJ, 434, 570

Uttley P., Wilkinson T., Cassatella P., Wilms J., Pottschmidt K., Hanke M., Böck M., 2011, MNRAS, 414, L60

Uzdensky D. A., Goodman J., 2008, ApJ, 682, 608

Vaughan S., Edelson R., 2001, ApJ, 548, 694

Young A. J., Reynolds C. S., 2000, ApJ, 529, 101

Zhou X.-L., Wang J.-M., 2005, ApJ, 618, L83

Zoghbi A., Fabian A. C., 2011, MNRAS, 418, 2642

Zoghbi A., Fabian A. C., Reynolds C. S., Cackett E. M., 2012, MNRAS, 422, 129

Zoghbi A., Fabian A. C., Uttley P., Miniutti G., Gallo L. C., Reynolds C. S., Miller J. M., Ponti G., 2010, MNRAS, 401, 2419